Magnetoelastic interactions and condensation of magnons in yttrium-iron garnet films

Dissertation
zur Erlangung des Doktorgrades
der Naturwissenschaften

vorgelegt beim Fachbereich Physik der
Goethe-Universität Frankfurt
in Frankfurt am Main

von
Andreas Rückriegel
aus
Gelnhausen

Frankfurt (2016)
(D30)

vom Fachbereich Physik der

Goethe Universität Frankfurt

als Dissertation angenommen.

Dekan: Prof. Dr. Rene Reifarth

Gutachter: Prof. Dr. Peter Kopietz
Priv.-Doz. Dr. Axel Pelster
Prof. Dr. Achim Rosch

Datum der Disputation: 05.09.2016

Contents

Abstract

Magnetism is a beautiful example of a macroscopic quantum phenomenon. While known at least since the ancient Greeks, a microscopic theoretical explanation of magnetism could only be achieved with the advent of quantum mechanics at the beginning of the 20th century. Then it was understood that in a certain class of solids the famous Pauli exclusion principle leads to an effective interaction between the microscopic magnetic moments, i.e., the spins, which favors an ordered, and hence macroscopically magnetic, state. Nowadays, magnetic phenomena are used in a host of applications, and are especially relevant for information storage and processing technologies.

Despite the long history of the field, magnetic phenomena are still an active research topic. In particular, in the last decade the fields of spintronics and spin-caloritronics emerged, which manipulate the microscopic spins via charge and heat currents respectively. This opens new avenues to potential applications; including the possibility to use the magnetic spin degrees of freedom instead of charges as carriers of information, which could provide a number of advantages such as reduced losses and further miniaturization.

In this thesis we do not delve any further into the realm of possible applications. Instead we use sophisticated theories to explore the microscopic spin dynamics which is the basis of all such applications. We also focus on a particular compound: Yttrium-iron garnet (YIG), which is a ferrimagnetic insulator. This material has been widely used in experiments on magnetism over the last decades, and is a popular candidate for spintronic devices. Microscopically, the low-energy magnetic properties of YIG can be described by a ferromagnetic Heisenberg model. For spintronics and spin-caloritronics applications, it is however insufficient to only consider the magnetic degrees of freedom; one should also include the coupling of the spins to the elastic lattice vibrations, i.e., the phonons. In YIG these magnetoelastic interactions can currently only be modeled phenomenologically, because they stem from relativistic effects which cannot be taken into account in a spin model. Besides giving an overview on techniques used throughout the thesis, the introductory Ch. 1 provides a discussion of the microscopic Hamiltonian used to model the coupled spin-phonon system in the subsequent chapters.

The topic of Ch. 2 are the consequences of the magnetoelastic coupling on the low-energy magnon excitations in YIG. Starting from the microscopic spin-

phonon Hamiltonian, we rigorously derive the magnon-phonon hybridization and scattering vertices in a controlled spin wave expansion. For the experimentally relevant case of thin YIG films at room temperature, these vertices are then used to compute the magnetoelastic modes as well as the magnon damping. In the course of this work, the damping of magnons in this system was also investigated experimentally using Brillouin light scattering spectroscopy. While comparison to the experimental data shows that the magnetoelastic interactions do not dominate the total magnon relaxation in the experimentally accessible regime, we are able to show that the spin-lattice relaxation time is strongly momentum dependent, thereby providing a microscopic explanation of a recent experiment.

In the final Ch. 3, we investigate a different phenomenon occurring in thin YIG films: Room temperature condensation of magnons. Prior work attributed this condensation process to quantum mechanics, i.e., it was interpreted as Bose-Einstein condensation. However, this is not satisfactory because at room temperature, the magnons in YIG behave as purely classical waves. In particular, the quantum Bose-Einstein distribution reduces to the classical Rayleigh-Jeans distribution in this case. In addition, the effective spin $S \approx 14$ in YIG is very large. Therefore we start from the hypothesis that the room temperature magnon condensation is actually a new example of the kinetic condensation of classical waves, which has so far only been observed by imaging classical light in a photorefractive crystal. To distinguish this classical condensation from the quantum mechanical Bose-Einstein one, we refer to it as Rayleigh-Jeans condensation. To prove our claim, we consider the classical equations of motion of the coupled spin-phonon system. By eliminating the phonon degrees of freedom, we microscopically derive a non-Markovian stochastic Landau-Lifshitz-Gilbert equation (LLG) for the classical spin vectors. Under the assumption that the phonons are initially in thermal equilibrium, this LLG contains a random magnetic field generating thermal noise, and a damping kernel, which depends on the microscopic phonon dynamics; both are connected via the fluctuation-dissipation theorem. We then use this LLG to perform numerical simulations of the magnon dynamics, with all parameters fixed by experiments. These simulations accurately reproduce all stages of the magnon time evolution observed in experiments, including the appearance of the magnon condensate at the bottom of the magnon spectrum. Also, the time scales extracted from the simulation are in excellent agreement with the experiments. The condensate in these simulations is immersed in a cloud of thermal magnons, which are distributed in momentum space according to a Rayleigh-Jeans distribution with a chemical potential equal to the minimum magnon energy. In this way we confirm our initial hypothesis that the magnon condensation is a classical Rayleigh-Jeans condensation, which is unrelated to quantum mechanics.

Chapter 1

Introduction

This introductory chapter serves a twofold purpose: Firstly, after a brief discussion of the phenomenon of magnetic ordering in Sec. 1.1, we characterize in Sec. 1.2 the low energy magnetic and elastic properties of thin films of the insulating magnet yttrium-iron garnet; thereby setting the stage for the remainder of this thesis. The aim of the following Secs. 1.3, 1.4, and 1.5 is to familiarize the reader with the basic concepts and methods used throughout the rest of this thesis.

A note on unit conventions: Throughout this thesis we always use Gaussian cgs units, and set both the (reduced) Planck and Boltzmann constants equal to unity, $\hbar = 1 = k_B$. Consequently energies, temperatures, and frequencies have the same dimensions, and will be measured either in degree K or GHz, with the conversion factor $1\,\mathrm{K} \approx 131\,\mathrm{GHz}$.

1.1 Magnetic ordering

In some solids the elementary ions have a finite average magnetic moment even in the absence of external magnetic fields. This spontaneous magnetization cannot be explained on the basis of classical mechanics, since the Bohr-van Leeuwen theorem states that the thermal equilibrium magnetization of all classical systems vanishes [1]. Therefore magnetism in solids is a purely quantum effect, based on the interaction of the elementary magnetic moments of the localized ions. We shall always refer to these moments as spins, although they will in general also include contributions from orbital angular momentum.

The most basic interaction between two spins $\boldsymbol{S}_1$ and $\boldsymbol{S}_2$ with magnetic moment μ and spatial separation $\boldsymbol{r} = r\hat{\boldsymbol{r}}$ is the dipole-dipole interaction

$$\mathcal{H}_{\mathrm{dd}} = -\frac{\mu^2}{r^3}\left[3\left(\boldsymbol{S}_1 \cdot \hat{\boldsymbol{r}}\right)\left(\boldsymbol{S}_2 \cdot \hat{\boldsymbol{r}}\right) - \boldsymbol{S}_1 \cdot \boldsymbol{S}_2\right]. \tag{1.1}$$

However, a simple energy estimation shows that the dipolar interaction cannot be responsible for magnetic ordering [2, 3]. Assuming that as in the case of free electrons the magnetic moment is $\mu = 2\mu_B$, where μ_B is the Bohr

magneton, and the typical distance of ions in a solid is $r \approx 2\,\text{Å}$, we find $\mathcal{H}_{\text{dd}} \approx (2\mu_B)^2/r^3 \approx 0.3\,\text{K}$. Thus one would expect that the spontaneous magnetization is destroyed by thermal fluctuation for temperatures above a few degrees Kelvin. Contrary to that, the Curie temperature T_C above which the spontaneous magnetization vanishes is in many magnetic solids of the order of hundreds of Kelvin.

On the other hand the electrostatic Coloumb energy of two electrons at the same distance is $e^2/r \approx 8 \times 10^4\,\text{K}$, where e is the electron charge. As this is much greater than the observed values of T_C, the Coloumb interaction is a good candidate to explain spontaneous magnetization, although it is actually spin independent. The spin dependence enters via the Pauli exclusion principle, which states that two electrons cannot occupy the same quantum mechanical state. This constraint results in a spin dependence of the electronic wavefunctions, which in turn implies that the mean Coloumb energy of two electrons contains a part which depends on the spin configuration of the electrons. This energy is called exchange energy and is responsible for the spontaneous magnetization. It corresponds to a spin Hamiltonian [2, 3]

$$\mathcal{H}_{\text{ex}} = -J\boldsymbol{S}_1 \cdot \boldsymbol{S}_2, \tag{1.2}$$

where J is called the exchange interaction. Depending on the sign of J we distinguish two types of magnetic order:

- For $J > 0$ parallel orientation of the spins is favored, resulting in a finite net magnetic moment. Systems of this kind are called ferromagnetic.
- For $J < 0$ antiparallel orientation of the spins is favored, resulting in a vanishing net magnetic moment. Systems of this kind are called antiferromagnetic.

If there are different kinds of magnetic ions in a solid there is a third possibility: ferrimagnetism. In ferrimagnetic systems the nearest neighbor exchange is antiferromagnetic but since the magnetic moments do not have the same magnitude the net magnetic moment is nonzero. Fig. 1.1 shows an illustration of these three types of magnetic order for a one dimensional spin chain.

Lastly, let us note that the exchange interaction between nearest neighbor ions considered above, which is known as direct exchange, is often not the most important exchange type interaction. When two magnetic ions are separated by a nonmagnetic ion it is nonetheless possible for them to interact via the electrons of the nonmagnetic ions. This is called superexchange. In metallic systems, there is also the indirect exchange via conduction electrons and the itinerant exchange among the conduction electrons themselves [2, 3].

1.2 Yttrium-iron garnet

Yttrium-iron garnet (YIG), with stochiometric formula $Y_3Fe_2\,(FeO_4)_3$, has been in the focus of experimental and theoretical research on magnetism for

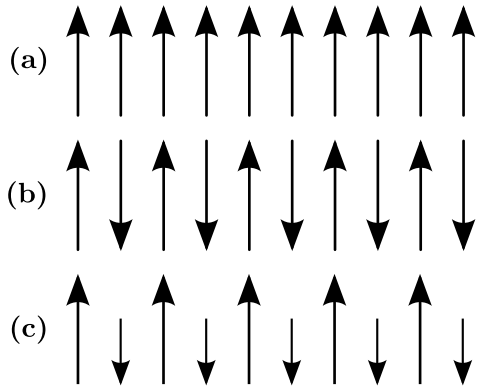

Figure 1.1: *Sketch of the three types of magnetic ordering for a one dimensional spin chain, showing (a) ferromagnetic, (b) antiferromagnetic, and (c) ferrimagnetic order.*

many decades [3, 4]. There are three main reasons for this [4]: First of all, YIG has a very narrow ferromagnetic resonance and consequently a very low spin wave damping. This in turn implies that YIG is a suitable model system to study magnetic properties of solids. Second, it can be grown in very pure crystals, so that the acoustic damping is low. The third reason is that the Curie temperature of YIG is $T_C = 560\,\mathrm{K}$. Therefore experiments probing magnetic properties can conveniently be performed at room temperature.

The crystal structure of YIG is quite complicated. It belongs to the cubic group $Ia3d$, with 160 atoms per primitive elementary cell [4, 5, 6]. Such a cell is schematically shown in Fig. 1.2. The magnetic moment is carried solely by the Fe ions, which occupy two inequivalent positions: The 16 octahedral sites a and the 24 tetrahedral sites d, see Fig. 1.2. The exchange interaction between these Fe ions is mediated by the neighboring O ions, therefore it is a superexchange interaction. It has turned out that the exchange interaction in YIG is antiferromagnetic [4]. However, due to the unequal number of magnetic Fe ions in a and d positions there is a finite net magnetization, so that YIG is a ferrimagnet.

1.2.1 Magnetic Hamiltonian

Since YIG is a ferrimagnet it has both ferro- and antiferromagnetic magnon bands, the lowest being ferromagnetic [4]. In the center of the Brillouin zone this lowest band is well separated from the higher antiferromagnetic bands [4]. Therefore it is generally believed [4, 6, 8, 9, 10, 11, 12, 13] that only this lowest ferromagnetic magnon band is relevant to the experiments [14, 15, 16, 17, 18, 19, 20, 21, 22, 23, 24] we aim to describe. This band can conveniently be described with an effective Heisenberg model on a simple cubic lattice with lattice spacing [5, 6, 11, 12]

$$a = 12.376\,\text{Å}. \tag{1.3}$$

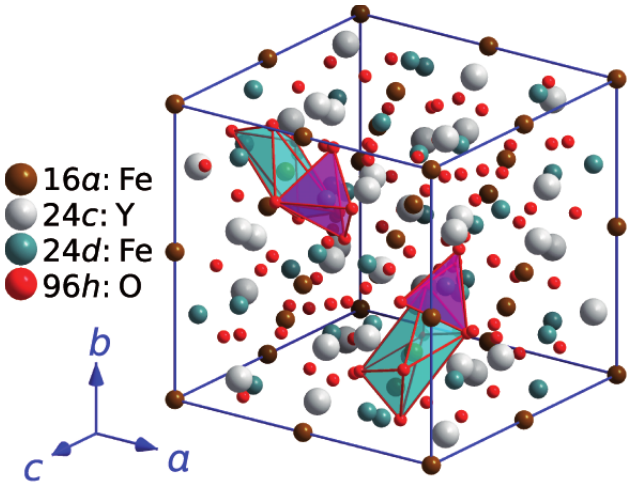

Figure 1.2: *Schematic depiction of the elementary unit cell of YIG; taken from [7]. YIG is a ferrimagnet because there is an antiferromagnetic superexchange interaction between the iron ions in the inequivalent a and d positions.*

In order to correctly describe the long-wavelength behavior we also have to include dipolar interactions [4, 6, 8, 10, 11, 12, 13]. Thus our effective magnetic Hamiltonian is given by [6, 8, 11, 12, 13]

$$\mathcal{H}_{\mathrm{m}}(t) = -\frac{1}{2}\sum_{ij}\sum_{\alpha\beta}\left[J_{ij}\delta^{\alpha\beta} + D_{ij}^{\alpha\beta}\right] S_i^{\alpha} S_j^{\beta} - \boldsymbol{H}(t)\cdot\sum_i \boldsymbol{S}_i. \tag{1.4}$$

Here and in the following, the roman subscripts denote lattice sites whereas Greek superscripts are the three spatial components x, y, z. The $\boldsymbol{S}_i$ are spin operators satisfying the commutation relation

$$\left[S_i^{\alpha}, S_j^{\beta}\right] = i\delta_{ij}\epsilon^{\alpha\beta\gamma}S_i^{\gamma}, \tag{1.5}$$

with length

$$\boldsymbol{S}_i^2 = S(S+1). \tag{1.6}$$

The ferromagnetic exchange interaction $J_{ij} = J(\boldsymbol{R}_i - \boldsymbol{R}_j)$ decays sufficiently fast with distance so that we only need to take nearest neighbors into account [4, 6, 8, 11, 12, 13],

$$J_{ij} = \begin{cases} J > 0 & \text{if } \boldsymbol{R}_i - \boldsymbol{R}_j \text{ connects nearest neighbor lattice sites,} \\ 0 & \text{otherwise.} \end{cases} \tag{1.7}$$

$D_{ij}^{\alpha\beta} = D^{\alpha\beta}(\boldsymbol{R}_i - \boldsymbol{R}_j)$ are the components of the dipolar interaction tensor and are explicitly given by

$$D_{ij}^{\alpha\beta} = (1-\delta_{ij})\,\frac{\mu^2}{|\boldsymbol{R}_{ij}|^3}\left[3\hat{R}_{ij}^{\alpha}\hat{R}_{ij}^{\beta} - \delta^{\alpha\beta}\right], \tag{1.8}$$

where $\boldsymbol{R}_{ij} = \boldsymbol{R}_i - \boldsymbol{R}_j$ and $\hat{\boldsymbol{R}}_{ij} = \boldsymbol{R}_{ij}/|\boldsymbol{R}_{ij}|$. The magnetic moment is given by $\mu = g\mu_B$, with effective g-factor equal to two [3, 6, 8, 11, 12, 13, 25]. The last term in the Hamiltonian (1.4) is the Zeeman energy associated with the external magnetic field $\boldsymbol{H}(t)/\mu$, which may be time dependent.

The remaining free parameters are fixed experimentally. The measured saturation magnetization of YIG at room temperature is [6, 25]

$$4\pi M_s = 1750\,\mathrm{G}. \tag{1.9}$$

For the effective spin this implies

$$S = \frac{M_s a^3}{\mu} \approx 14.2. \tag{1.10}$$

The strength J of the exchange interaction can be fixed via the experimentally accessible spin stiffness [3, 5, 6]

$$\rho_s = JSa^2 = 5.17 \times 10^{-9}\,\mathrm{Oe\,cm^2} \times \mu, \tag{1.11}$$

yielding $J \approx 3.19\,\mathrm{K}$.

1.2.2 Elastic Hamiltonian

In any solid the ions are not fixed at the Bravais lattice sites $\boldsymbol{R}_i$. Due to quantum as well as thermal fluctuations they will in general oscillate, with mean positions given by the $\boldsymbol{R}_i$. The actual ionic positions are then given by

$$\boldsymbol{r}_i = \boldsymbol{R}_i + \boldsymbol{X}_i, \tag{1.12}$$

where the $\boldsymbol{X}_i$ are the lattice displacement vectors. They describe deviations of the ion positions from their equilibrium values $\boldsymbol{R}_i$.

In the harmonic approximation, the oscillations of the lattice deviations $\boldsymbol{X}_i$ can be expanded in terms of normal modes $X_{\boldsymbol{k}\lambda}$, also called phonons, with momentum $\boldsymbol{k}$ and polarization $\boldsymbol{e}_{\boldsymbol{k}\lambda}$ [2],

$$\boldsymbol{X}_i = \boldsymbol{X}(\boldsymbol{R}_i) = \frac{1}{\sqrt{N}} \sum_{\boldsymbol{k}\lambda} e^{i\boldsymbol{k}\cdot\boldsymbol{R}_i} X_{\boldsymbol{k}\lambda} \boldsymbol{e}_{\boldsymbol{k}\lambda}. \tag{1.13}$$

Here λ labels the three acoustic phonon branches with dispersions in the long-wavelength limit given by

$$\omega_{\boldsymbol{k}\lambda} = c_\lambda |\boldsymbol{k}|, \tag{1.14}$$

where c_λ are the sound velocities.

Note that since the lattice displacement $\boldsymbol{X}_i$ must be Hermitian we have the symmetries

$$X^\dagger_{\boldsymbol{k}\lambda} = X_{-\boldsymbol{k}\lambda}, \tag{1.15a}$$

$$\boldsymbol{e}^*_{\boldsymbol{k}\lambda} = \boldsymbol{e}_{-\boldsymbol{k}\lambda}. \tag{1.15b}$$

Also, the polarization vectors have to satisfy the following orthogonality and completeness relations,

$$\boldsymbol{e}^*_{\boldsymbol{k}\lambda} \cdot \boldsymbol{e}_{\boldsymbol{k}\lambda'} = \delta_{\lambda\lambda'}, \tag{1.16a}$$

$$\sum_\lambda \boldsymbol{e}_{\boldsymbol{k}\lambda} \boldsymbol{e}^\dagger_{\boldsymbol{k}\lambda} = \mathbf{1}, \tag{1.16b}$$

where $\mathbf{1}$ is the 3×3 unit matrix.

The dynamics of these phonons is governed by the elastic Hamiltonian [2]

$$\mathcal{H}_\mathrm{e} = \sum_{\boldsymbol{k}\lambda} \left[\frac{P_{-\boldsymbol{k}\lambda} P_{\boldsymbol{k}\lambda}}{2M} + \frac{M}{2} \omega^2_{\boldsymbol{k}\lambda} X_{-\boldsymbol{k}\lambda} X_{\boldsymbol{k}\lambda} \right]. \tag{1.17}$$

Here M is the effective ionic mass and $P_{\boldsymbol{k}\lambda}$ is the canonical conjugate momentum of the normal mode $X_{\boldsymbol{k}\lambda}$, i.e., they satisfy the commutation relation

$$[X_{\boldsymbol{k}\lambda}, P_{\boldsymbol{k}'\lambda'}] = i\delta_{\boldsymbol{k},-\boldsymbol{k}'}\delta_{\lambda\lambda'}. \tag{1.18}$$

For YIG the situation is actually more complex because of the large number of atoms in the unit cell. This allows for the appearance of optical phonon modes with dispersions that do not vanish for $|\boldsymbol{k}| \to 0$. However, the energy scale associated with these optical branches is in the THz regime [26, 27], which is three orders of magnitude larger than the energy of the long-wavelength magnons we are considering. Therefore optical phonons can safely be ignored and we can again effectively consider YIG as a simple cubic lattice with lattice spacing a given in Eq. (1.3). From the mass density $\rho = 5.17\,\mathrm{g/cm^3}$ [3] of YIG we can then obtain the effective ionic mass

$$M = \rho a^3 = 9.8 \times 10^{-21}\mathrm{g}. \tag{1.19}$$

For isotropic systems it is also always possible to choose the polarization for a given $\boldsymbol{k}$ such that one is parallel to $\boldsymbol{k}$, i.e., longitudinal, while the other two are transversal. The corresponding longitudinal and transverse sound velocities of YIG at room temperature are [3]

$$c_\parallel = 7.209 \times 10^5\,\mathrm{cm/s}, \tag{1.20a}$$

$$c_\perp = 3.843 \times 10^5\,\mathrm{cm/s}. \tag{1.20b}$$

1.2.3 Magnetoelastic interaction

There are two main sources of coupling between magnetic and elastic degrees of freedom [3]: The dependence of the exchange and dipolar interactions between spins on the actual ionic positions, and relativistic spin-orbit coupling. To take into account the former, one may expand exchange and dipolar interactions in

powers of the phonon displacements $\boldsymbol{X}_i$ around the equilibrium Bravais lattice positions $\boldsymbol{R}_i$ as [28]

$$J_{ij} = J(\boldsymbol{R}_{ij}) + \sum_{n=1}^{\infty} \frac{1}{n!} \left(\boldsymbol{X}_{ij} \cdot \nabla_{\boldsymbol{r}}\right)^n J(\boldsymbol{r})\Big|_{\boldsymbol{r}=\boldsymbol{R}_{ij}}, \tag{1.21a}$$

$$D_{ij}^{\alpha\beta} = D^{\alpha\beta}(\boldsymbol{R}_{ij}) + \sum_{n=1}^{\infty} \frac{1}{n!} \left(\boldsymbol{X}_{ij} \cdot \nabla_{\boldsymbol{r}}\right)^n D^{\alpha\beta}(\boldsymbol{r})\Big|_{\boldsymbol{r}=\boldsymbol{R}_{ij}}, \tag{1.21b}$$

where $\boldsymbol{R}_{ij} = \boldsymbol{R}_i - \boldsymbol{R}_j$ and $\boldsymbol{X}_{ij} = \boldsymbol{X}_i - \boldsymbol{X}_j$. Formally the above expansions (1.21) generate an infinite number of spin-phonon interactions, but since the lattice deviations $\boldsymbol{X}_i$ are usually small one can often terminate the series after the first few terms.

For collinear magnets like YIG however, the position dependence of the exchange and dipolar interactions is not the dominant mechanism of magnetoelastic interaction. Instead one has to consider spin-orbit coupling [3]. As these effects involve the charge degrees of freedom, they cannot be included in our effective spin Hamiltonian (1.4) in a straightforward manner.

To overcome these difficulties, we employ the semiclassical phenomenological theory of magnetoelastic interaction [3, 29, 30, 31, 32, 33], which relies solely on symmetry considerations. This theory is formulated in terms of the macroscopic magnetization $\boldsymbol{M}(\boldsymbol{r})$ and the elastic strain tensor $X^{\alpha\beta}(\boldsymbol{r})$, which can be defined in terms of the phonon displacement field $\boldsymbol{X}(\boldsymbol{r})$ as

$$X^{\alpha\beta}(\boldsymbol{r}) = \frac{1}{2}\left[\frac{\partial X^{\alpha}(\boldsymbol{r})}{\partial r^{\beta}} + \frac{\partial X^{\beta}(\boldsymbol{r})}{\partial r^{\alpha}}\right]. \tag{1.22}$$

To lowest order in these fields the classical magnetoelastic energy is then given by [3, 29, 30, 31, 32, 33]

$$\begin{aligned} E_{\mathrm{me}}[\boldsymbol{M}, \boldsymbol{X}] =& \frac{n}{M_s^2} \int \mathrm{d}^3 r \sum_{\alpha\beta} \Bigg[B^{\alpha\beta} M^{\alpha}(\boldsymbol{r}) M^{\beta}(\boldsymbol{r}) \\ &+ \tilde{B}^{\alpha\beta} \frac{\partial \boldsymbol{M}(\boldsymbol{r})}{\partial r^{\alpha}} \cdot \frac{\partial \boldsymbol{M}(\boldsymbol{r})}{\partial r^{\beta}} \Bigg] X^{\alpha\beta}(\boldsymbol{r}), \end{aligned} \tag{1.23}$$

where M_s is the saturation magnetization and n the density of magnetic ions. Note that terms of first order in the magnetization components are forbidden since the magnetization $\boldsymbol{M}(\boldsymbol{r})$ is a pseudovector. The coupling tensors $B^{\alpha\beta}$ and $\tilde{B}^{\alpha\beta}$ are known as magnetoelastic constants. The first term of the magnetoelastic energy (1.23) describes the effects of dipole-dipole and relativistic spin-orbit interactions, whereas the second term is the contribution of the exchange interaction. For cubic lattices the coupling tensors have the form [3, 30, 31, 34, 35]

$$B^{\alpha\beta} = \delta^{\alpha\beta} B_{\parallel} + \left(1 - \delta^{\alpha\beta}\right) B_{\perp}, \tag{1.24a}$$

$$\tilde{B}^{\alpha\beta} = \delta^{\alpha\beta} \tilde{B}_{\parallel} + \left(1 - \delta^{\alpha\beta}\right) \tilde{B}_{\perp}. \tag{1.24b}$$

As mentioned above, relativistic spin-orbit coupling is the dominant source of magnetoelastic interaction for systems like YIG, therefore we set $\tilde{B}^{\alpha\beta} = 0$. For YIG at room temperature the remaining coupling constants are experimentally found to be [3, 34, 35]

$$B_{\parallel} = 3.48 \times 10^6\,\mathrm{erg/cm^3} \times a^3 = 47.8\,\mathrm{K}, \tag{1.25a}$$
$$B_{\perp} = 6.69 \times 10^6\,\mathrm{erg/cm^3} \times a^3 = 95.6\,\mathrm{K}. \tag{1.25b}$$

In the semiclassical approach [3, 29, 30, 31, 32, 33], quantum effects are incorporated by promoting the classical fields $\boldsymbol{M}(\boldsymbol{r})$ and $X^{\alpha\beta}(\boldsymbol{r})$ as well as the magnetoelastic energy (1.23) to their corresponding quantum operators.

To connect with the lattice models for spins and phonons in YIG introduced in Sec. 1.2.1 and Sec. 1.2.2 respectively, we discretize the magnetoelastic energy (1.23) according to the prescription

$$n \int \mathrm{d}^3 r \to \sum_i, \tag{1.26a}$$
$$\boldsymbol{M}(\boldsymbol{r}) \to \frac{\mu}{a^3} \boldsymbol{S}_i, \tag{1.26b}$$
$$X^{\alpha\beta}(\boldsymbol{r}) \to X_i^{\alpha\beta} = X^{\alpha\beta}(\boldsymbol{R}_i), \tag{1.26c}$$

yielding the magnetoelastic Hamiltonian

$$\mathcal{H}_{\mathrm{me}} = \frac{1}{S^2} \sum_i \sum_{\alpha\beta} B^{\alpha\beta} S_i^{\alpha} S_i^{\beta} X_i^{\alpha\beta}. \tag{1.27}$$

1.2.4 Thin film geometry

In this thesis we will only consider tangentially magnetized thin YIG films, see Fig. 1.3. In this geometry, translational invariance holds only in the y-z plane, while the spatial extension in x direction, the thickness d, remains finite. In the experiments [14, 15, 16, 17, 18, 19, 20, 21, 22, 23, 24] we are aiming at this is satisfied very well, with d being of the order of microns, while the width and length of the sample are of the order of millimeters. The film is magnetized via an in-plane magnetic field $\boldsymbol{H}_0 = H_0 \boldsymbol{e}_z$, ensuring that the ground state is indeed a saturated ferromagnet.

Previously [6] it has been shown that the lowest magnon band of YIG in the thin film geometry can be described in the so-called uniform mode approximation. This amounts to taking an effectively two-dimensional in-plane version of the magnetic Hamiltonian (1.4), which is obtained by replacing all quantities by their average over the width d of the sample. The corresponding in-plane momenta will be parametrized as

$$\boldsymbol{k} = |\boldsymbol{k}| \left(\cos\theta_{\boldsymbol{k}} \boldsymbol{e}_z + \sin\theta_{\boldsymbol{k}} \boldsymbol{e}_y \right). \tag{1.28}$$

Effects of the finite thickness d enter via the dipolar tensor, since it contains long-range interactions. The explicit calculation of the components of the

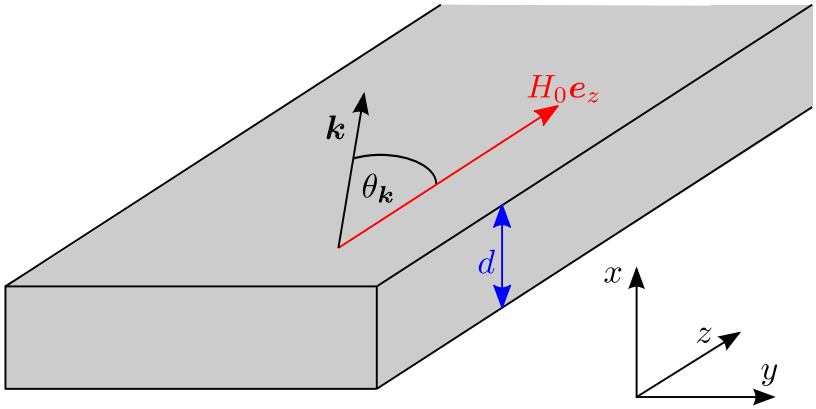

Figure 1.3: *Geometry of a YIG film with thickness d, in the presence of a bias magnetic field $\boldsymbol{H}_0 = H_0 \boldsymbol{e}_z$ in the film plane. In the uniform mode approximation, we only consider magnons with in-plane momenta of the form $\boldsymbol{k} = |\boldsymbol{k}| (\cos\theta_{\boldsymbol{k}} \boldsymbol{e}_z + \sin\theta_{\boldsymbol{k}} \boldsymbol{e}_y)$.*

dipolar tensor in uniform mode approximation is rather complicated, we refer to Ref. [6] for further details. Here we only state the results for the Fourier transforms of the dipolar tensor components,

$$D^{xx}_{\boldsymbol{k}} = \frac{\Delta}{S}\left[\frac{1}{3} - f_{\boldsymbol{k}}\right], \tag{1.29a}$$

$$D^{yy}_{\boldsymbol{k}} = \frac{\Delta}{S}\left[\frac{1}{3} + \sin^2\theta_{\boldsymbol{k}}\,(f_{\boldsymbol{k}} - 1)\right], \tag{1.29b}$$

$$D^{zz}_{\boldsymbol{k}} = \frac{\Delta}{S}\left[\frac{1}{3} + \cos^2\theta_{\boldsymbol{k}}\,(f_{\boldsymbol{k}} - 1)\right], \tag{1.29c}$$

$$D^{xy}_{\boldsymbol{k}} = D^{yz}_{\boldsymbol{k}} = D^{zx}_{\boldsymbol{k}} = 0, \tag{1.29d}$$

where we defined the form factor

$$f_{\boldsymbol{k}} = \frac{1 - \exp(-|\boldsymbol{k}|d)}{|\boldsymbol{k}|d}, \tag{1.30}$$

and the characteristic energy scale of dipolar interactions,

$$\Delta = 4\pi\mu M_s. \tag{1.31}$$

For the phonon sector, we only have to define a proper set of polarization vectors $\boldsymbol{e}_{\boldsymbol{k}\lambda}$. A suitable choice for the thin film geometry is[1]

$$\boldsymbol{e}_{\boldsymbol{k}\parallel} = i\,(\cos\theta_{\boldsymbol{k}} \boldsymbol{e}_z + \sin\theta_{\boldsymbol{k}} \boldsymbol{e}_y), \tag{1.32a}$$

$$\boldsymbol{e}_{\boldsymbol{k}\perp 1} = i\,(\sin\theta_{\boldsymbol{k}} \boldsymbol{e}_z - \cos\theta_{\boldsymbol{k}} \boldsymbol{e}_y), \tag{1.32b}$$

$$\boldsymbol{e}_{\boldsymbol{k}\perp 2} = \boldsymbol{e}_x. \tag{1.32c}$$

[1] In order to satisfy $\boldsymbol{e}^*_{\boldsymbol{k}\lambda} = \boldsymbol{e}_{-\boldsymbol{k}\lambda}$ one should set the longitudinal phonon polarization vector to $\boldsymbol{e}_{\boldsymbol{k}\parallel} = i\hat{\boldsymbol{k}}$; see p. 316 of Ref. [36] for a discussion of this point.

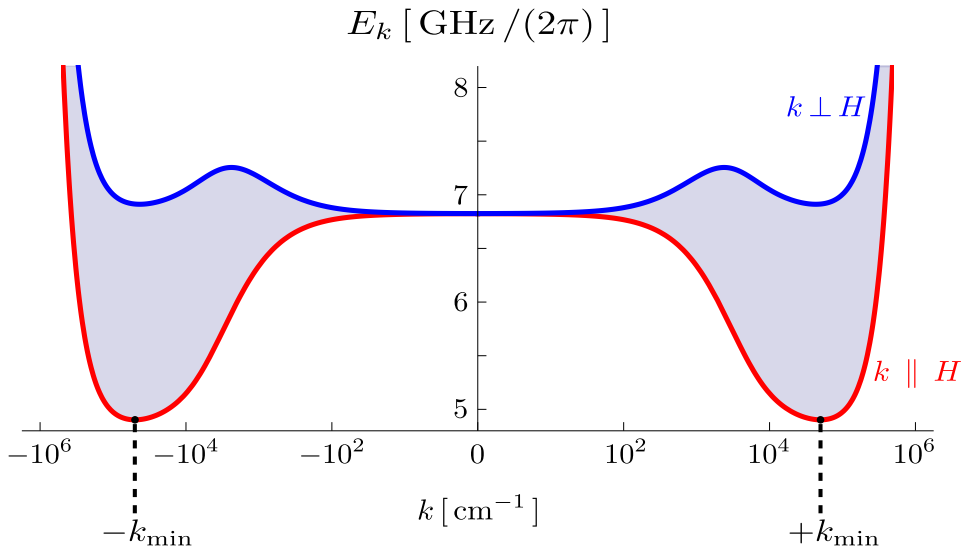

Figure 1.4: *Plot of the magnon dispersion relation (1.33) of a YIG film with thickness $d = 6.7\,\mu$m, for a bias magnetic field $H_0 = 1710\,\mathrm{Oe}\times\mu$. The magnon branches with momenta parallel ($\theta_{\boldsymbol{k}} = 0$) and perpendicular ($\theta_{\boldsymbol{k}} = \pi/2$) to the in-plane bias field are shown as red and blue lines respectively; the shaded area in between denotes the allowed frequency range of magnons with arbitrary angle $\theta_{\boldsymbol{k}}$. Note that the dispersion acquires its minimum value at finite momenta $\boldsymbol{k} = \pm k_{\min}\boldsymbol{e}_z$ parallel to the bias field, with $k_{\min} \approx 5 \times 10^4\,\mathrm{cm}^{-1}$.*

In conclusion, let us remark that due to the interplay of long-range dipolar and short-range exchange interactions as well as finite size effects, the long-wavelength dispersion of linear spin waves deviates strongly from the $\boldsymbol{k}^2$ form of exchange-dominated spin waves. Explicitly it is given by [6]

$$E_{\boldsymbol{k}} = \sqrt{\left[H_0 + \rho_s \boldsymbol{k}^2 + \Delta\,(1 - f_{\boldsymbol{k}})\sin^2\theta_{\boldsymbol{k}}\right]\left[H_0 + \rho_s \boldsymbol{k}^2 + \Delta f_{\boldsymbol{k}}\right]}, \tag{1.33}$$

as will be derived in two different ways later on. An important feature that has to be taken into account for the correct description of experiments in the thin film geometry is that the magnon dispersion (1.33) displays two degenerate minima at finite momenta $\boldsymbol{k} = \pm k_{\min}\boldsymbol{e}_z$ parallel to the bias magnetic field $\boldsymbol{H}_0$, compare Fig. 1.4. These minima appear because of the competition of the exchange and dipolar interactions that dominate the short- and long-wavelength momentum regimes respectively.

1.2.5 Parametric instability

The main experimental technique to excite magnons with well-defined energy and momentum in thin YIG films is the instability mechanism of parallel parametric pumping [13]; in particular it is widely used in the magnon condensation experiments [15, 16, 17, 18, 19, 20, 21, 22, 23, 24] we aim to describe in Ch.

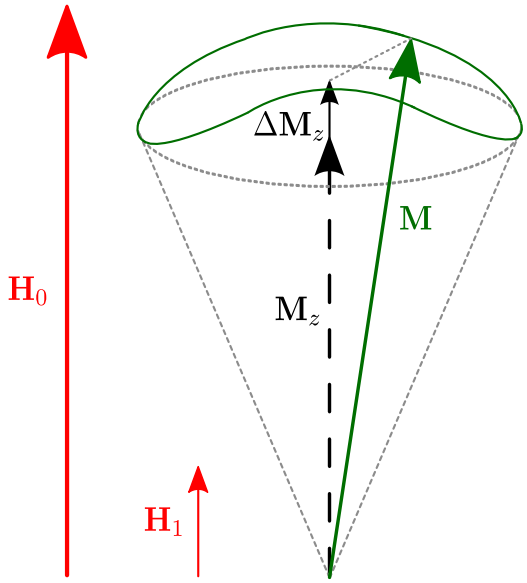

Figure 1.5: *Semiclassical picture of the parametric resonance: For elliptical spin waves, an alternating magnetic field* $\boldsymbol{H}_1$ *parallel to the bias field* $\boldsymbol{H}_0$ *couples to the longitudinal magnetization component* M_z*, inducing an alternating contribution* ΔM_z*. As the total length of the magnetization vector* $\boldsymbol{M}$ *is a conserved quantity, such an elliptical precession of* $\boldsymbol{M}$ *excites also the transverse magnetization, and hence magnon modes.*

3 to increase the density of the magnon gas in thin YIG films above the critical threshold of condensation. Therefore we will now discuss the theoretical foundations of this effect.

In the parallel parametric pumping geometry, a comparatively small oscillating magnetic field with amplitude H_1 is added parallel to the bias magnetic field H_0, so that the total magnetic field is given by

$$\boldsymbol{H}(t) = [H_0 + H_1 \cos(2\omega_\mathrm{p} t)]\, \boldsymbol{e}_z. \tag{1.34}$$

Since the goal is to excite magnons with frequencies typically in the range of several GHz, the frequency $2\omega_\mathrm{p}$ of the pumping field has to be in the microwave regime. In the semiclassical picture, illustrated in Fig 1.5, the oscillating microwave field in z-direction can induce an oscillation of the same frequency $2\omega_\mathrm{p}$ in the z-component of the magnetization. As the length of the magnetization vector is conserved, such an oscillation of the z-component entails an oscillation of the transverse component with exactly half the frequency; i.e., spin waves with energy $E_{\boldsymbol{k}} = \omega_\mathrm{p}$ are generated. Note that this process requires the spin waves to be elliptic; otherwise, the projection of the magnetization on the z-axis is itself conserved and cannot be excited by the pumping field. In corpuscular language, this effect can also be understood as coherent decay of a photon of the microwave field into two elliptic magnons. Because the momentum of the microwave photon is essentially zero (compared to the

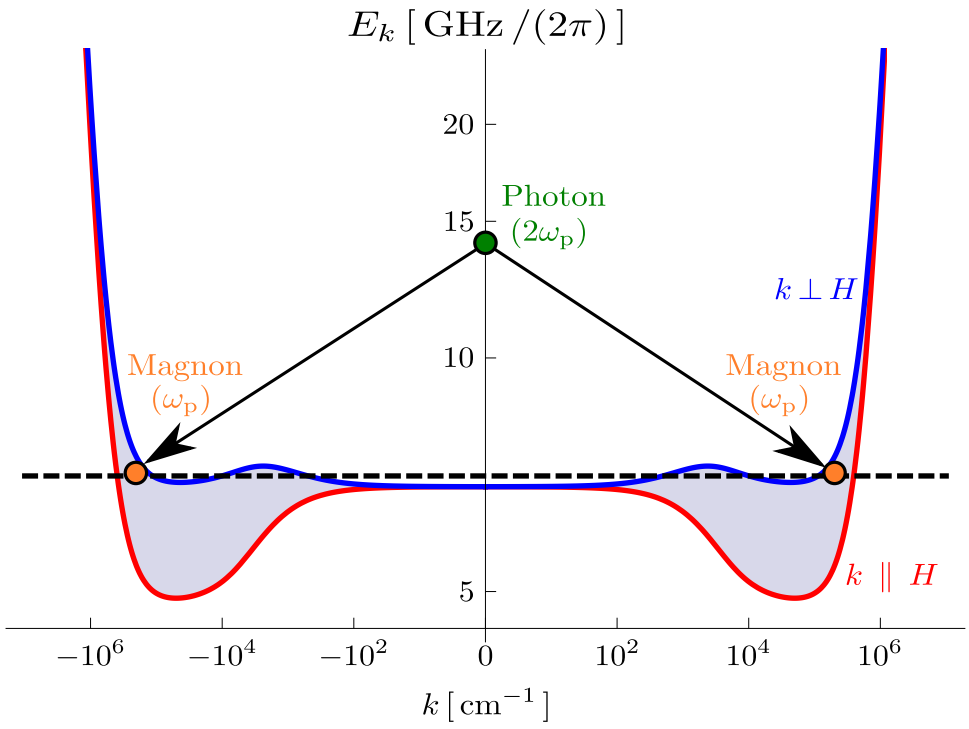

Figure 1.6: *Visualization of the parametric instability mechanism for a thin YIG film. A microwave photon with frequency $2\omega_\mathrm{p}$ and (approximately) zero momentum coherently decays into two magnons with frequencies $E_{\boldsymbol{k}} = \omega_\mathrm{p}$ and momenta $\pm\boldsymbol{k}$. The magnon branches with momenta parallel and perpendicular to the in-plane magnetic field $\boldsymbol{H}_0$ are shown as red and blue lines respectively; the shaded area in between denotes the frequency range that can be populated with magnons. Parametric excitation of magnons is possible whenever the black dashed line denoting the pumping frequency ω_p crosses the magnon dispersion. The plot is for the same set of parameters as Fig. 1.4; the pumping frequency is chosen to be $\omega_\mathrm{p} = 2\pi \times 7.046\,\mathrm{GHz}$.*

magnon momentum scale), momentum conservation requires that the two excited magnons have momentum $+\boldsymbol{k}$ and $-\boldsymbol{k}$. Energy conservation for such a process demands in addition that

$$E_{\boldsymbol{k}} + E_{-\boldsymbol{k}} = 2\omega_\mathrm{p}, \tag{1.35}$$

and hence $E_{\boldsymbol{k}} = \omega_\mathrm{p}$ for systems with inversion symmetry. This decay mechanisms is sketched in Fig. 1.6.

To theoretically describe the parametric instability, it is sufficient to study the classical equations of motion of the magnetization linearized around the classical ground state $\boldsymbol{S}_i = S\boldsymbol{e}_z$, and neglect all magnetoelastic and thermal noise effects. Writing the deviation from said classical ground state as $\boldsymbol{m}_i = (\boldsymbol{S}_i - S\boldsymbol{e}_z)/S$ then leads to the following linear system for the transverse

magnetization in momentum space:

$$\dot{m}^x_{\boldsymbol{k}} = \left[\omega^y_{\boldsymbol{k}} + H_1 \cos\left(2\omega_\mathrm{p} t\right)\right] m^y_{\boldsymbol{k}}, \tag{1.36a}$$
$$\dot{m}^y_{\boldsymbol{k}} = -\left[\omega^x_{\boldsymbol{k}} + H_1 \cos\left(2\omega_\mathrm{p} t\right)\right] m^x_{\boldsymbol{k}}, \tag{1.36b}$$

which will be derived in detail in Ch. 3. Here the elliptic precession of the linear spin waves is described by the two frequencies $\omega^x_{\boldsymbol{k}}$ and $\omega^y_{\boldsymbol{k}}$; for thin YIG films they are given in terms of the Fourier transforms of the exchange interaction and the components of the dipolar tensor as

$$\omega^x_{\boldsymbol{k}} = H_0 + S\left(J_{\boldsymbol{k}=0} - J_{\boldsymbol{k}} + D^{zz}_{\boldsymbol{k}=0} - D^{xx}_{\boldsymbol{k}}\right), \tag{1.37a}$$
$$\omega^y_{\boldsymbol{k}} = H_0 + S\left(J_{\boldsymbol{k}=0} - J_{\boldsymbol{k}} + D^{zz}_{\boldsymbol{k}=0} - D^{yy}_{\boldsymbol{k}}\right). \tag{1.37b}$$

The effect of the parametric pumping on the linear system (1.36) is most apparent if one expresses the transverse magnetization in terms of the complex normal modes of the unpumped system, given by

$$\phi_{\boldsymbol{k}} = \left(\frac{\omega^x_{\boldsymbol{k}}}{\omega^y_{\boldsymbol{k}}}\right)^{1/4} m^x_{\boldsymbol{k}} + i \left(\frac{\omega^y_{\boldsymbol{k}}}{\omega^x_{\boldsymbol{k}}}\right)^{1/4} m^y_{\boldsymbol{k}}. \tag{1.38}$$

These normal modes satisfy the equation of motion

$$i\dot{\phi}_{\boldsymbol{k}} = \left[E_{\boldsymbol{k}} + U_{\boldsymbol{k}} H_1 \cos\left(2\omega_\mathrm{p} t\right)\right] \phi_{\boldsymbol{k}} + 2V_{\boldsymbol{k}} H_1 \cos\left(2\omega_\mathrm{p} t\right) \phi^*_{-\boldsymbol{k}}, \tag{1.39}$$

where $E_{\boldsymbol{k}} = \sqrt{\omega^x_{\boldsymbol{k}} \omega^y_{\boldsymbol{k}}}$ is the dispersion of the unpumped magnons, $U_{\boldsymbol{k}} = \sqrt{1 + 4|V_{\boldsymbol{k}}|^2}$, and

$$V_{\boldsymbol{k}} = \frac{\omega^y_{\boldsymbol{k}} - \omega^x_{\boldsymbol{k}}}{4E_{\boldsymbol{k}}} = S\frac{D^{xx}_{\boldsymbol{k}} - D^{yy}_{\boldsymbol{k}}}{4E_{\boldsymbol{k}}} \tag{1.40}$$

is proportional to the ellipticity of the spin wave. Let us now move to a reference frame rotating with the pumping frequency by setting

$$\phi_{\boldsymbol{k}}(t) = e^{-i\omega_\mathrm{p} t} \varphi_{\boldsymbol{k}}(t). \tag{1.41}$$

In this rotating reference frame the equation of motion (1.39) becomes

$$i\dot{\varphi}_{\boldsymbol{k}} = \left[E_{\boldsymbol{k}} - \omega_\mathrm{p} + U_{\boldsymbol{k}} H_1 \cos\left(2\omega_\mathrm{p} t\right)\right] \varphi_{\boldsymbol{k}} + V_{\boldsymbol{k}} H_1 \left(e^{4i\omega_\mathrm{p} t} + 1\right) \varphi^*_{-\boldsymbol{k}}. \tag{1.42}$$

To obtain the parametric instability it is sufficient to retain the resonant terms while dropping all oscillatory contributions to the equation of motion (1.42). Thus we are left with

$$i\dot{\varphi}_{\boldsymbol{k}} = \left(E_{\boldsymbol{k}} - \omega_\mathrm{p}\right) \varphi_{\boldsymbol{k}} + V_{\boldsymbol{k}} H_1 \varphi^*_{-\boldsymbol{k}}. \tag{1.43}$$

Differentiating above equation of motion (1.43) again with respect to time yields the harmonic oscillator equation

$$\ddot{\varphi}_{\boldsymbol{k}} = -\left(|E_{\boldsymbol{k}} - \omega_\mathrm{p}|^2 - |V_{\boldsymbol{k}} H_1|^2\right) \varphi_{\boldsymbol{k}}. \tag{1.44}$$

For sufficiently strong pumping field H_1, it now obvious from above oscillator equation (1.44) that the frequency of oscillation of the normal modes can become imaginary close to the resonance $E_{\boldsymbol{k}} = \omega_\mathrm{p}$; signifying the parametric instability. In particular, magnon modes which satisfy

$$|E_{\boldsymbol{k}} - \omega_\mathrm{p}| < |V_{\boldsymbol{k}} H_1| \tag{1.45}$$

diverge exponentially,

$$\varphi_{\boldsymbol{k}} \propto e^{\alpha_{\boldsymbol{k}} t}, \tag{1.46}$$

where

$$\alpha_{\boldsymbol{k}}^2 = |V_{\boldsymbol{k}} H_1|^2 - |E_{\boldsymbol{k}} - \omega_\mathrm{p}|^2 > 0. \tag{1.47}$$

Note also that only elliptic spin waves can be parametrically unstable, because otherwise the coupling coefficient $V_{\boldsymbol{k}}$ vanishes.

In reality, this exponential increase is of course bounded by nonlinear interaction effects. The most basic such effect is the conservation of the length of the magnetization vector, which prohibits an unbounded growth. However, usually the parametric instability saturates far below the values at which this constraint on the magnetization vector becomes important [3]. The dominant interaction processes that limit the parametric growth have been identified in the 1960's and 70's by V. E. Zakharov and co-workers, and the theory they developed subsequently came to be known as S-theory [37, 38, 39]. In this theory, nonlinear interactions between wave pairs satisfying the energy conservation law

$$E_{\boldsymbol{k}} + E_{-\boldsymbol{k}} = E_{\boldsymbol{k}'} + E_{-\boldsymbol{k}'}, \tag{1.48}$$

which do not take the spin waves out of parametric resonance, are taken into account on a self-consistent mean field level. Such processes naturally arise in a spin wave expansion when one considers the interaction of the transverse magnetization with the uniform mode of the longitudinal magnetization. In Refs. [38, 39], the authors are able to show that such interactions conserve phase correlations within each parametrically excited magnon pair, and effectively lead to a self-consistent renormalization of the pumping field, thereby limiting the parametric growth.

1.3 Spin wave theory

Spin waves, or magnons, are collective low-energy excitations of magnetically ordered systems [2, 3]. In a classical picture they correspond to a precession of the ionic spins around the classical magnetization, resulting in a lowering of the average magnetic moment. Due to the exchange interaction between spins, this precession travels as a wave through the ionic lattice, see Fig. 1.7.

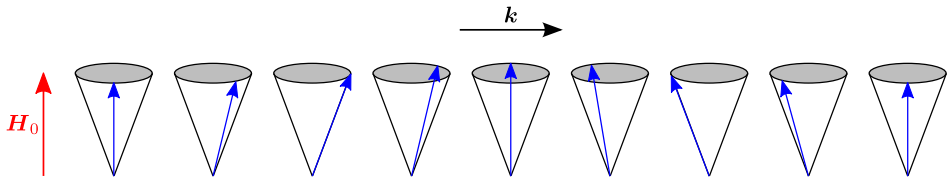

Figure 1.7: *Classical visualization of a spin wave in a one dimensional ferromagnetic spin chain. The spin vectors precess around the direction of the external bias field $\boldsymbol{H}_0$; because of the exchange interaction, this precession travels along the spin chain with momentum $\boldsymbol{k}$.*

1.3.1 Holstein-Primakoff bosonization

A spin Hamiltonian like Eq. (1.4) is notoriously difficult to solve because of the complicated spin algebra (1.5). In particular the spin components at a given lattice site do not commute and therefore have no common eigenbasis. These problems may be circumvented by mapping the spins to bosonic degrees of freedom which describe the spin waves directly. There are several bosonization techniques to achieve this: Holstein-Primakoff [40] and Dyson-Maleev [41] transformations, and Schwinger Bosons [42]. Each of these have their own advantages and drawbacks, for a discussion see for example [43]. For our purposes the Holstein-Primakoff bosonization technique is the most useful. For a ferromagnet with saturation magnetization pointing in z direction, it amounts to setting

$$S_i^+ = S_i^x + iS_i^y = \sqrt{2S}\sqrt{1 - \frac{b_i^\dagger b_i}{2S}}\, b_i, \tag{1.49a}$$

$$S_i^- = S_i^x - iS_i^y = \sqrt{2S}\, b_i^\dagger \sqrt{1 - \frac{b_i^\dagger b_i}{2S}}, \tag{1.49b}$$

$$S_i^z = S - b_i^\dagger b_i, \tag{1.49c}$$

where the magnon operators obey the bosonic commutation relation

$$\left[b_i, b_j^\dagger\right] = \delta_{ij}. \tag{1.50}$$

The Holstein-Primakoff transformation (1.49) explicitly fulfills the spin algebra (1.5) while also preserving the length of the spin (1.6) and the Hermiticity of the spin operators. However, for practical calculations one has to expand the squareroots in Eqs. (1.49a) and (1.49b), yielding

$$S_i^+ = \sqrt{2S}\left[b_i - \frac{b_i^\dagger b_i b_i}{4S} + \mathcal{O}(1/S^2)\right], \tag{1.51a}$$

$$S_i^- = \sqrt{2S}\left[b_i^\dagger - \frac{b_i^\dagger b_i^\dagger b_i}{4S} + \mathcal{O}(1/S^2)\right]. \tag{1.51b}$$

Therefore the Holstein-Primakoff bosonization amounts to an expansion in powers of the inverse spin quantum number, and a general spin Hamiltonian can be written as

$$\mathcal{H}_{\text{spin}} = \sum_{n=0}^{\infty} \mathcal{H}_n. \tag{1.52}$$

where $\mathcal{H}_n$ denotes a term containing n magnon operators. Thus the original spin system can be mapped to a system of interacting bosons. Truncating the expansion (1.52) at $n = 2$ yields free magnons, whereas the higher order terms can be interpreted as magnon-magnon interactions. For the expansion (1.51) to be meaningful, one has to require that

$$\langle b_i^\dagger b_i \rangle \ll S, \tag{1.53}$$

i.e., that the average magnon number is small compared to the overall length of the spin operator. This is satisfied either for low temperatures or a large spin quantum number.

1.3.2 Stochastic Landau-Lifshitz-Gilbert equation

For large spin and high temperatures it is often possible to neglect the quantum nature of the spin operators entirely and instead work with a classical spin model [44]. Then one has to work with classical three-component vectors $\boldsymbol{S}_i$. Their equations of motion can be obtained by invoking the classical-quantum correspondence principle for spins [45, 46], yielding

$$\dot{\boldsymbol{S}}_i = \boldsymbol{S}_i \times \left[-\frac{\partial \mathcal{H}(\{\boldsymbol{S}_i\})}{\partial \boldsymbol{S}_i} \right], \tag{1.54}$$

where $\mathcal{H}(\{\boldsymbol{S}_i\})$ denotes the classical Hamiltonian, which is a function of the spin configuration $\{\boldsymbol{S}_i\}$. The above equation of motion describes the precession of the local spins around an effective magnetic field $-\partial\mathcal{H}(\{\boldsymbol{S}_i\})/\partial\boldsymbol{S}_i$. In addition to the external magnetic field, this effective field also contains contributions generated by the internal spin-spin interactions. Note that the structure of the equation of motion (1.54) guarantees the conservation of the length of the spins,

$$\frac{\mathrm{d}}{\mathrm{d}t}\boldsymbol{S}_i^2 = 0. \tag{1.55}$$

Since the equation of motion (1.54) is a Hamiltonian time evolution for an isolated spin system, it contains no dissipation. As every real system is in some way in contact with an environment, it is usually a poor approximation to ignore dissipative effects. These then lead to a transfer of energy from the spins to other degrees of freedom, most notably to the phonons [3, 47, 48]. In principle these dissipative effects can be modeled by including the dynamics of the environment, i.e., the phonons, and solving the equations of motion of the coupled spin-phonon system [48]. Such an approach will be constructed

in Ch. 3. However, conventionally dissipation is added phenomenologically to the spin equation of motion, in such a way as to produce the desired statistical properties and preserve the conservation of the length of the spin [47, 49, 50]. As it is a phenomenological procedure, there are different ways to achieve this, see for example [47, 50]. For our purposes the most relevant is the stochastic Landau-Lifshitz-Gilbert equation (LLG) [49],

$$\dot{\boldsymbol{S}}_i = \boldsymbol{S}_i \times \left[-\frac{\partial \mathcal{H}(\{\boldsymbol{S}_i\})}{\partial \boldsymbol{S}_i} + \delta \boldsymbol{h}_i(t) - \gamma \dot{\boldsymbol{S}}_i \right], \tag{1.56}$$

where $\delta \boldsymbol{h}_i(t)$ is a random magnetic field with vanishing mean, $\langle \delta \boldsymbol{h}_i(t) \rangle = 0$, and γ is the phenomenological damping constant. They are connected via the fluctuation-dissipation theorem [51]

$$\left\langle \delta h_i^\alpha(t) \delta h_j^\beta(t') \right\rangle = 2\gamma T \delta_{ij} \delta^{\alpha\beta} \delta(t - t'), \tag{1.57}$$

where T is the temperature[2]. The fact that the random field correlations are assumed to be white, i.e., delta-correlated in time, reflects the basic assumption that the spin dynamics is much slower than the dynamics of the environment variables, allowing us to neglect the memory of the environment entirely [48, 49, 50]. This assumption should be critically reexamined for every system whose dynamics we want to model with the LLG (1.56) [48], as we will do in the context of YIG in Ch. 3. On general grounds, because of the singular nature of the white noise, it is unlikely that the LLG (1.56) will produce the correct physics on short time scales [48].

Finally, let us note that the LLG (1.56) is a stochastic differential equation [52]. A precise definition of this type of equation will be given below in Sec. 1.5. For now it is sufficient to remark that when interpreted in the sense of Stratonovich [52], the fluctuation-dissipation theorem (1.57) ensures that the probability distribution function of the spin configuration has the Boltzmann distribution as equilibrium solution [47],

$$\rho_{\text{eq}}(\{\boldsymbol{S}_i\}) \propto \exp\left[-\mathcal{H}(\{\boldsymbol{S}_i\})/T\right]. \tag{1.58}$$

1.4 Many-body methods

This section serves to introduce the many-body methods that will be used in Ch. 2. As many-body theory is a vast field, we cannot hope to give any kind of self-contained introduction including all derivations and subtleties. Therefore we will mainly state the results necessary for our purposes, and refer the interested reader to the excellent textbooks [53, 54, 55, 56, 57, 58, 59] covering this topic. To this end we will consider a generic Bose system with Hamiltonian

$$\mathcal{H} = \sum_{\boldsymbol{k}} \epsilon_{\boldsymbol{k}} a_{\boldsymbol{k}}^\dagger a_{\boldsymbol{k}} + \frac{1}{2} \sum_{\boldsymbol{k}_1 \boldsymbol{k}_2 \boldsymbol{k}_3 \boldsymbol{k}_4} V_{\boldsymbol{k}_1 \boldsymbol{k}_2; \boldsymbol{k}_3 \boldsymbol{k}_4} a_{\boldsymbol{k}_1}^\dagger a_{\boldsymbol{k}_2}^\dagger a_{\boldsymbol{k}_3} a_{\boldsymbol{k}_4}, \tag{1.59}$$

[2]Usually it is additionally assumed that all higher cumulants of the random field vanish, i.e., that it is Gaussian white noise [49].

where the $a_{\boldsymbol{k}}^\dagger$ and $a_{\boldsymbol{k}}$ are bosonic creation and destruction operators respectively. The single-particle dispersion (which may also include a chemical potential) is denoted by $\epsilon_{\boldsymbol{k}}$, whereas $V_{\boldsymbol{k}_1\boldsymbol{k}_2;\boldsymbol{k}_3\boldsymbol{k}_4}$ is the amplitude of two-body scattering.

1.4.1 Matsubara technique

Mathematically, all properties of the interacting many-body system (1.59) are encoded in correlation functions of the Bose operators $a_{\boldsymbol{k}}^\dagger$ and $a_{\boldsymbol{k}}$. Such correlation functions are known as Green functions in this context. We will only be concerned with single-particle properties of systems in thermal equilibrium at temperature $T = 1/\beta$. In this case it is most convenient to consider the imaginary-time single-particle Green function defined as

$$G(\boldsymbol{k}, \tau - \tau') = -\left\langle \mathcal{T}\left(a_{\boldsymbol{k}}(\tau) a_{\boldsymbol{k}}^\dagger(\tau')\right)\right\rangle \tag{1.60}$$

where the expectation value is defined as $\langle \ldots \rangle = \operatorname{Tr}\left(e^{-\beta\mathcal{H}} \ldots\right) / \operatorname{Tr} e^{-\beta\mathcal{H}}$ and the imaginary-time operators are

$$a_{\boldsymbol{k}}(\tau) = e^{\mathcal{H}\tau} a_{\boldsymbol{k}} e^{-\mathcal{H}\tau}, \tag{1.61a}$$

$$a_{\boldsymbol{k}}^\dagger(\tau) = e^{\mathcal{H}\tau} a_{\boldsymbol{k}}^\dagger e^{-\mathcal{H}\tau}, \tag{1.61b}$$

which can be obtained from the Heisenberg time evolution by performing the Wick rotation $\tau = it$ to imaginary times τ. In thermal equilibrium this greatly facilitates calculations because the oscillatory complex exponentials of the real-time evolution are avoided altogether. The time-ordering symbol $\mathcal{T}$ entering the Green function (1.60) is defined via

$$\mathcal{T}\left(a_{\boldsymbol{k}}(\tau) a_{\boldsymbol{k}}^\dagger(\tau')\right) = \begin{cases} a_{\boldsymbol{k}}(\tau) a_{\boldsymbol{k}}^\dagger(\tau') & \text{if } \tau > \tau', \\ a_{\boldsymbol{k}}^\dagger(\tau') a_{\boldsymbol{k}}(\tau) & \text{if } \tau' \geq \tau. \end{cases} \tag{1.62}$$

From the condition that the trace in the definition of the Green function (1.60) is convergent one can show that $\tau - \tau'$ must lie in $[-\beta, \beta]$, and from the cyclic invariance of said trace that $G(\boldsymbol{k}, \tau)$ satisfies the so-called Kubo-Martin-Schwinger boundary conditions, which relate $G(\boldsymbol{k}, -\tau)$ to $G(\boldsymbol{k}, \tau)$. This allows us to define the Fourier transformation to imaginary-frequency space as

$$G(\boldsymbol{k}, \tau) = \sum_{n=-\infty}^{\infty} e^{-i\omega_n \tau} G(\boldsymbol{k}, i\omega_n), \tag{1.63a}$$

$$G(\boldsymbol{k}, i\omega_n) = \frac{1}{\beta} \int_0^\beta e^{i\omega_n \tau} G(\boldsymbol{k}, \tau), \tag{1.63b}$$

where the bosonic Matsubara frequencies are given by

$$\omega_n = \frac{2\pi n}{\beta}, \; n \in \mathbb{Z}. \tag{1.64}$$

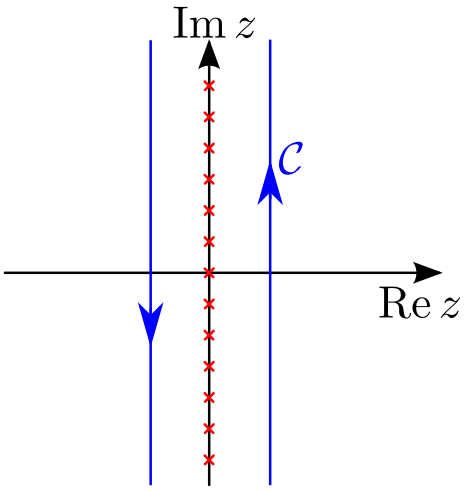

Figure 1.8: *Integration contour $\mathcal{C}$ in the complex plane for evaluating generic Matsubara sums (1.65). The (bosonic) Matsubara frequencies $i\omega_n$ are depicted as red crosses on the imaginary axis; the contour $\mathcal{C}$ encircles all Matsubara frequencies and is closed at infinity.*

When working in this representation one often encounters Matsubara sums, i.e., sums of a given $F(i\omega_n)$ on all Matsubara frequencies. They can always be calculated using the residue theorem of complex analysis,

$$\frac{1}{\beta}\sum_{n=-\infty}^{\infty} F(i\omega_n) = -\frac{1}{2\pi i}\int_{\mathcal{C}} \mathrm{d}z\, \frac{F(z)}{1-e^{\beta z}} \tag{1.65}$$

where the contour $\mathcal{C}$ circles around all Matsubara frequencies, as shown in Fig. 1.8.

Physical properties may be extracted from the Matsubara Green function $G(\boldsymbol{k}, i\omega_n)$ by analytic continuation to the real frequency axis. For example the retarded and advanced Green functions $G^{R/A}(\boldsymbol{k}, \omega)$, which carry information about the spectrum of single-particle excitations, can be obtained as

$$G^{R/A}(\boldsymbol{k}, \omega) = G(\boldsymbol{k}, i\omega_n \to \omega \pm i\eta), \tag{1.66}$$

where $\eta = 0^+$ is an infinitesimal regularization.

1.4.2 Coherent state functional integral

Many-body calculations in the operator formalism are usually quite cumbersome because of the time-ordering and non-commutativity of operators. Instead, one can use a functional integral representation which naturally keeps track of the time-ordering and, in the bosonic case, only employs complex fields. The most convenient way to define the many-body functional integral is in terms of coherent states, which for bosons are defined via the eigenvalue equation

$$a_{\boldsymbol{k}}|\psi_{\boldsymbol{k}}\rangle = \psi_{\boldsymbol{k}}|\psi_{\boldsymbol{k}}\rangle, \tag{1.67}$$

where $\psi_{\boldsymbol{k}}$ is a complex number. With them the partition function of a bosonic many-body system can be written as a functional integral on the fields $\psi_{\boldsymbol{k}}$ and their complex conjugates $\bar{\psi}_{\boldsymbol{k}}$:

$$\mathcal{Z} = \operatorname{Tr} e^{-\beta\mathcal{H}} = \int \mathcal{D}[\bar{\psi},\psi]\, e^{-S[\bar{\psi},\psi]}. \tag{1.68}$$

For our model Hamiltonian (1.59), the euclidean action $S[\bar{\psi},\psi]$ is given by

$$S[\bar{\psi},\psi] = S_0[\bar{\psi},\psi] + S_1[\bar{\psi},\psi], \tag{1.69}$$

where the noninteracting part is

$$S_0[\bar{\psi},\psi] = -\beta \sum_K \left(i\omega_n - \epsilon_{\boldsymbol{k}}\right) \bar{\psi}(K)\psi(K), \tag{1.70}$$

and the interaction contribution is

$$S_1[\bar{\psi},\psi] = \frac{\beta}{2} \sum_{K_1K_2K_3K_4} \delta_{n_1+n_2,n_2+n_3} V_{\boldsymbol{k}_1\boldsymbol{k}_2;\boldsymbol{k}_3\boldsymbol{k}_4} \bar{\psi}(K_1)\bar{\psi}(K_2)\psi(K_3)\psi(K_4), \tag{1.71}$$

and we collected momentum and Matsubara frequency into a collective label $K = (\boldsymbol{k}, i\omega_n)$.

Functional averages may now be defined as

$$\langle \ldots \rangle = \frac{1}{\mathcal{Z}} \int \mathcal{D}[\bar{\psi},\psi] \ldots e^{-S[\bar{\psi},\psi]}, \tag{1.72}$$

and the Matsubara Green function (1.60) becomes

$$G(K) = -\beta \langle \psi(K)\bar{\psi}(K) \rangle. \tag{1.73}$$

In the noninteracting limit, this yields for our model system (1.59)

$$G_0(K) = \frac{1}{i\omega_n - \epsilon_{\boldsymbol{k}}}. \tag{1.74}$$

1.4.3 Diagrammatic perturbation theory

The functional integration necessary to calculate the Matsubara Green function (1.73) can only be performed exactly for noninteracting systems, i.e. when it is Gaussian. For weakly interacting systems, on may expand

$$e^{-S[\bar{\psi},\psi]} = e^{-S_0[\bar{\psi},\psi]} e^{-S_1[\bar{\psi},\psi]} = e^{-S_0[\bar{\psi},\psi]} \sum_{\nu=0}^{\infty} \frac{(-1)^\nu}{\nu!} \left(S_1[\bar{\psi},\psi]\right)^\nu. \tag{1.75}$$

This is known as the perturbation expansion and amounts to an expansion in the amplitudes of the many-body interaction processes ($V_{\boldsymbol{k}_1\boldsymbol{k}_2;\boldsymbol{k}_3\boldsymbol{k}_4}$ for our model Hamiltonian (1.59)). If these amplitudes are small, it is often possible

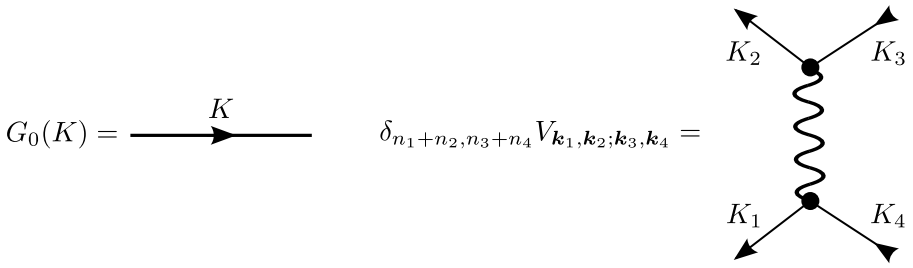

Figure 1.9: *Diagrammatic representation of noninteracting Green function and interaction vertex for the model Hamiltonian (1.59); these two objects constitute the basic building blocks of diagrammatic perturbation theory.*

to truncate the expansion (1.75) after the first few terms. In order to calculate correlation functions like the Matsubara Green function (1.73) in this approximation, one only needs to calculate noninteracting averages, i.e., Gaussian integrals, on products of the fields. By virtue of the Wick theorem such averages factorize into products of noninteracting Green functions. Therefore the perturbation expansion (1.75) contains only two kinds of objects: Noninteracting Green functions and interaction amplitudes. Representing noninteracting Green functions by directed lines and interaction amplitudes by vertices, as in Fig. 1.9, the terms of the perturbation expansion (1.75) may be translated into diagrams. The exact translation procedure, called the Feynman rules, depends on the model system chosen, therefore we will not state them here.

The advantage of the diagrammatic representation is that one can classify and sort all terms of the perturbation expansion in a clear way. In particular it allows one to resum the expansion (1.75) in such a way that the number of diagrams that have to be calculated is significantly reduced. For the Matsubara Green function (1.73) this is achieved by introducing the one-particle irreducible self-energy $\Sigma(K)$, which contains all diagrams which cannot be reduced to two parts by cutting a single line. Then one can write

$$\begin{aligned} G(K) =& G_0(K) + G_0(K)\Sigma(K)G_0(K) + G_0(K)\Sigma(K)G_0(K)\Sigma(K)G_0(K) + \dots \\ =& G_0(K) + G_0(K)\Sigma(K)G(K), \end{aligned} \tag{1.76}$$

which is known as Dyson equation and shown diagrammatically in Fig. 1.10. An equivalent version of the Dyson equation (1.76) is

$$G(K) = \frac{1}{G_0^{-1}(K) - \Sigma(K)} = \frac{1}{i\omega_n - \epsilon_{\boldsymbol{k}} - \Sigma(\boldsymbol{k}, i\omega_n)}, \tag{1.77}$$

which shows that the self-energy enters as correction to the single-particle dispersion. From the Dyson equation (1.77) it is obvious that once the self-energy is known in some approximation, e.g. in perturbation theory, one has obtained a partial resummation of the whole perturbation expansion for the interacting Green function $G(K)$.

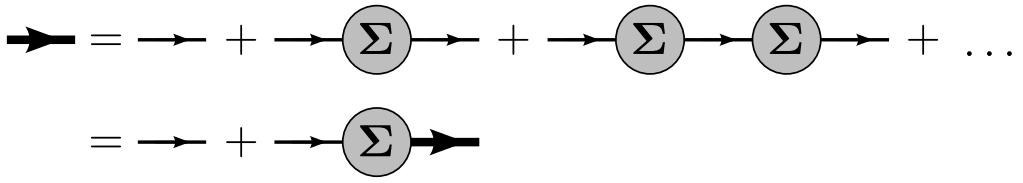

Figure 1.10: *Diagrammatic representation of the Dyson equation (1.76). Thick and thin directed lines denote interacting and noninteracting Green functions respectively.*

1.5 Stochastic methods

In this section we will introduce the notions of stochastic processes, ergodicity, and stochastic differential equations, to be used in Ch. 3. The following discussion will neither be mathematically rigorous nor exhaustive, it is rather intended to familiarize the reader with the concepts and tools necessary to describe physical systems in terms of stochastic variables, as done in Ch. 3. For more complete and rigorous treatments we refer to the textbooks [52, 60, 61].

1.5.1 Stochastic process

A stochastic process is a family of random variables $X(t)$ which depends on a real parameter t, which is the physical time. In physics, such a stochastic process is usually considered as an ensemble of identical, noninteracting copies of the system. Each realization $x(t)$ of the process $X(t)$ then describes the measurement of the property $X(t)$ on a single system. The outcome of such measurements cannot be predicted in general as it fluctuates randomly. Instead we can only assign probabilities by repeatedly measuring $X(t)$, i.e., by averaging on the whole ensemble. This ensemble average, denoted by $\langle \ldots \rangle$, yields smooth functions out of the original stochastic fluctuations. An illustration of this procedure is given in Fig. 1.11.

Stochastic processes can be characterized by specifying their simultaneous probability densities ρ_n, defined as

$$\rho_n(x_n, t_n; \ldots; x_1, t_1) = \langle \delta(x_n - X(t_n)) \ldots \delta(x_1 - X(t_1)) \rangle . \tag{1.78}$$

$\rho_n(x_n, t_n; \ldots; x_1, t_1)\mathrm{d}x_1 \ldots \mathrm{d}x_n$ gives the probability that the value of $X(t_i)$ lies in the interval $[x_i, x_i + \mathrm{d}x_i]$ for $i = 1, \ldots, n$. For $t_n > t_{n-1} > \ldots > t_1$, it also turns out to be useful to define the conditional probability density $\rho_{r|n-r}$ such that $\rho_{r|n-r}(x_n, t_n; \ldots; x_{n-r+1}, t_{n-r+1}|x_{n-r}, t_{n-r}; \ldots; x_1, t_1)\mathrm{d}x_{n-r+1} \ldots \mathrm{d}x_n$ is the probability that $X(t_i)$ assumes values in $[x_i, x_i + \mathrm{d}x_i]$ for $i = n - r + 1, \ldots, n$, while $X(t_1), \ldots, X(t_{n-r})$ have the fixed values $x_1, \ldots, x_{n-r}$. According to Bayes' theorem it is given by

$$\begin{aligned} &\rho_{r|n-r}(x_n, t_n; \ldots; x_{n-r+1}, t_{n-r+1}|x_{n-r}, t_{n-r}; \ldots; x_1, t_1) \\ =&\rho_n(x_n, t_n; \ldots; x_1, t_1)/\rho_{n-r}(x_{n-r}, t_{n-r}; \ldots; x_1, t_1). \end{aligned} \tag{1.79}$$

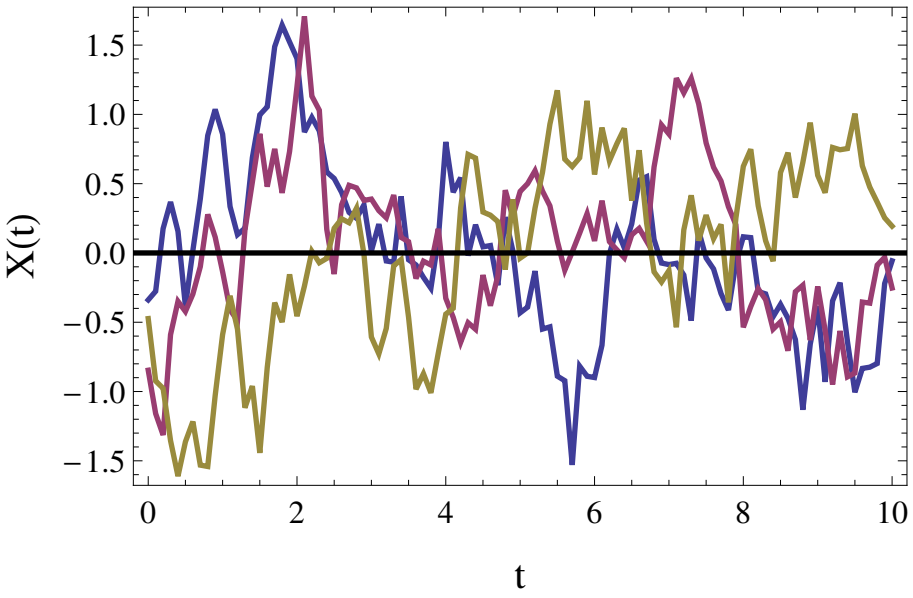

Figure 1.11: *Three stochastic trajectories of a random variable $X(t)$. While the individual realizations fluctuate erratically, the ensemble average $\langle X(t)\rangle$, which is shown as black line, is constant.*

For physical applications, the three most important classes of stochastic processes are Gaussian, Markovian and stationary processes:

- For a Gaussian process, all simultaneous probability densities ρ_n are (multivariate) Gaussian distributions. Thus they are completely specified by their first two moments $\langle X(t)\rangle$ and $\langle X(t_1)X(t_2)\rangle$. Gaussian processes are particularly important in physics because of the central limit theorem, which states that every macroscopically additive random variable of the form $A(t) = \sum_{i=1}^{N} X_i(t)$ becomes a Gaussian process in the limit $N \to \infty$.

- A Markovian process is a process in which the conditional probability $\rho_{1|n-1}$ for time t_n depends only on the prior time step t_{n-1},

$$\rho_{1|n-1}(x_n, t_n | x_{n-1}, t_{n-1}; \ldots; x_1, t_1) = \rho_{1|1}(x_n, t_n | x_{n-1}, t_{n-1}). \tag{1.80}$$

  Hence such a process contains no memory of its own history and is completely specified by the transition probability $\rho_{1|1}$, which by Bayes' theorem (1.79) depends only on ρ_1 and ρ_2.

- A stationary process is invariant with respect to arbitrary shifts τ of all time variables,

$$\rho_n(x_n, t_n + \tau; \ldots; x_1, t_1 + \tau) = \rho_n(x_n, t_n; \ldots; x_1, t_1). \tag{1.81}$$

  This implies that the stochastic properties of stationary processes do not change with time. In particular the first moment $\langle X(t)\rangle$ has to be

independent of time t, whereas the second moment $\langle X(t_1)X(t_2)\rangle$ can only depend on the time difference $|t_1 - t_2|$.

Since every physical process only has a limited duration, there are no truly stationary processes in nature. However, very often that duration is so long compared to the time scale of the dynamics one is interested in that one can practically consider it as infinite, thereby approximately recovering a stationary process.

1.5.2 Ergodic hypothesis

The ergodic hypothesis is central to all of statistical mechanics. It states that for a certain class of stationary stochastic processes, called ergodic, all statistical properties can be deduced from a sufficiently long sample of the process. The reasoning behind this is as follows: A measurement of the property $A(X(t))$ at time t_0 on a certain system necessarily only gives a time average,

$$\overline{A(t_0)} = \frac{1}{\tau}\int_0^\tau \mathrm{d}t\, A\left(X(t_0+t)\right) \tag{1.82}$$

$$= \int \mathrm{d}x\, \rho(x, t_0; \tau) A(x), \tag{1.83}$$

where τ is the temporal resolution of the measurement device, which is large compared to all microscopic time scales, and the distribution function $\rho(x, t_0; \tau)$ is given by

$$\rho(x, t_0; \tau) = \frac{1}{\tau}\int_0^\tau \mathrm{d}t\, \delta\left(x - X(t_0+\tau)\right). \tag{1.84}$$

As the process is assumed to be stationary, we can choose τ arbitrarily large. In particular, we can consider the limit $\tau \to \infty$. For an ergodic process we then have

$$\lim_{\tau\to\infty} \rho(x, t_0; \tau) = \rho_1(x, t_0). \tag{1.85}$$

so that the time average in Eq. (1.83) turns into an ensemble average

$$\overline{A(t_0)} = \int \mathrm{d}x\, \rho_1(x, t_0) A(x) = \langle A\left(X(t_0)\right)\rangle. \tag{1.86}$$

This is hard to justify mathematically; however, it can easily be understood on physical grounds: Given a very long sample of a stationary stochastic process, we can cut it into smaller samples, which are still long compared to the time scales of the microscopic fluctuations. Since the process is stationary, the smaller samples have the same statistical properties as the original one and thus define an ensemble for the stochastic process. Therefore the time average can be replaced by an ensemble average.

By virtue of the ergodic hypothesis, it is possible to introduce the concept of the Gibbsian ensembles in statistical mechanics. This amounts to turning

the microscopic degrees of freedom into stochastic processes. Thermodynamic averages are then stochastic ensemble averages with special equilibrium probability densities, which justifies using the same symbol, $\langle \ldots \rangle$, for both.

1.5.3 Stochastic differential equations

A stochastic differential equation (SDE) is any differential equation in which coefficients are stochastic processes. Here we will only consider SDEs of the form

$$\dot{y}_i = A_i\left(\boldsymbol{y}, t\right) + \sum_k B_{ik}\left(\boldsymbol{y}, t\right) L_k(t) \tag{1.87}$$

where $\boldsymbol{y} = \left(y_1, \ldots, y_n\right)^T$ is the system variable we are interested in, $\boldsymbol{A} = \left(A_1, \ldots, A_n\right)^T$ is the drift vector, B_{ik} the diffusion matrix, and $L_k(t)$ is a random process. Note that since $L_k(t)$ is a random process, so is $\boldsymbol{y}(t)$. If the random process is Gaussian white noise, i.e.,

$$\langle L_k(t) \rangle = 0, \tag{1.88a}$$

$$\langle L_k(t) L_{k'}(t') \rangle = \delta_{kk'} \delta(t - t'), \tag{1.88b}$$

and all higher cumulants are zero, the SDE (1.87) is called the Langevin equation. There exists a wide literature on solving the Langevin equation, see for example [52, 60, 61]. The most notable analytical techniques are the Fokker-Planck approach [52, 60, 61], which derives a continuity equation (the Fokker-Planck equation) for the probability density $\rho_1(\boldsymbol{y}, t)$, and the Martin-Siggia-Rose/Jansen-De Dominicis [62, 63, 64] approach, which employs a functional integral formulation.

When using the Langevin equation (1.87), one should always keep in mind that the white noise (1.88) cannot describe the physical reality correctly. This is due to the fact that the $\delta(t - t')$ introduces an infinitely high and narrow peak, while the physical correlation function always has to have finite width and height. Mathematically, this singularity leads to complications in the interpretation of the noise term. This can be seen by visualizing the white noise $L_k(t)$ as a sequence of delta peaks arriving at random times. The Langevin equation (1.87) now states that each delta peak arriving causes a jump in the variable $\boldsymbol{y}(t)$. In consequence, the value of $\boldsymbol{y}$ at the time the delta function arrives is undetermined, and thus also the value of the diffusion matrix $B_{ik}\left(\boldsymbol{y}, t\right)$. The SDE (1.87) alone does not specify whether on should insert the value of $\boldsymbol{y}$ before or after the jump or some combination of both into the diffusion matrix $B_{ik}\left(\boldsymbol{y}, t\right)$. Hence, the Langevin equation (1.87) with the white noise (1.88) is not uniquely defined without also supplying an interpretation rule for the noise term. Such interpretation rules are called stochastic calculus; the two most common being Itô and Stratonovich calculus.

The Itô interpretation assumes that only the state of the system before the

jump is important, so that the SDE (1.87) is interpreted as

$$y_i(t+\Delta t) - y_i(t) = A_i\left(\boldsymbol{y}(t), t\right)\Delta t + \sum_k B_{ik}\left(\boldsymbol{y}(t), t\right)\int_t^{t+\Delta t} \mathrm{d}s\, L_k(s). \quad (1.89)$$

In mathematics, the Itô interpretation is favored since it allows to prove some general theorems. However, usage of Itô calculus also entails serious drawbacks: First of all, if one accepts the interpretation (1.89) of the Langevin equation (1.87) one is invariably lead to the conclusion that the chain rule of ordinary calculus is not valid for stochastic processes; it is replaced by Itô's lemma, which states that the time derivative of any function $F\left(\boldsymbol{y}(t)\right)$ is given by

$$\dot{F}\left(\boldsymbol{y}(t)\right) = \sum_i \frac{\partial F(\boldsymbol{y})}{\partial y_i}\dot{y}_i + \frac{1}{2}\sum_{ikl} B_{ik}(\boldsymbol{y}, t)B_{lk}(\boldsymbol{y}, t)\frac{\partial^2 F(\boldsymbol{y})}{\partial y_i \partial y_l}. \quad (1.90)$$

The second drawback is that the Itô interpretation (1.89) can only be formulated as long as the noise consists of singular delta peaks; as soon as one considers the physically more adequate picture of peaks with finite widths, Itô calculus can no longer be applied.

The most important alternative to the Itô interpretation (1.89) is the Stratonovich interpretation, which employs a midpoint rule to evaluate the diffusion matrix at the jump:

$$\begin{aligned} y_i(t+\Delta t) - y_i(t) = {} & A_i\left(\boldsymbol{y}(t), t\right)\Delta t \\ & + \sum_k B_{ik}\left(\frac{\boldsymbol{y}(t) + \boldsymbol{y}(t+\Delta t)}{2}, t + \frac{\Delta t}{2}\right)\int_t^{t+\Delta t} \mathrm{d}s\, L_k(s). \end{aligned} \quad (1.91)$$

It has been shown [65] that when starting from finite noise peaks, as in the physical situation, and then taking the white noise limit, one arrives at the Stratonovich interpretation (1.91) of the Langevin equation (1.87). Therefore Stratonovich calculus is dominant in physics. Another advantage of Stratonovich calculus is that the chain rule of ordinary calculus holds even for random processes, in contrast to Itô calculus where one has to use the more complicated Itô's lemma (1.90). However, every Stratonovich SDE can be translated into an Itô SDE and vice versa by modifying the drift vector $\boldsymbol{A}\left(\boldsymbol{y}, t\right)$ according to

$$A_i^{\mathrm{Strat}}\left(\boldsymbol{y}, t\right) = A_i^{\mathrm{Itô}}\left(\boldsymbol{y}, t\right) - \frac{1}{2}\sum_{kl} B_{kl}\left(\boldsymbol{y}, t\right)\frac{\partial B_{il}\left(\boldsymbol{y}, t\right)}{\partial y_k}, \quad (1.92)$$

where $A_i^{\mathrm{Strat}}\left(\boldsymbol{y}, t\right)$ are the components of the drift vector of the Stratonovich SDE that is equivalent to the Itô SDE with drift vector components $A_i^{\mathrm{Itô}}\left(\boldsymbol{y}, t\right)$. In particular, note that the conversion rule (1.92) implies that for additive noise, i.e., when the diffusion matrix $B_{ik}\left(\boldsymbol{y}, t\right) = B_{ik}\left(t\right)$ is independent of the system variable $\boldsymbol{y}(t)$, Stratonovich and Itô interpretation coincide.

If the random process $L_k(t)$ is not described by Gaussian white noise (1.88), it is called colored noise. In this case there is no ambiguity as to which stochastic calculus to use, since the noise correlations are not given by singular distributions. Despite this, the theory of colored-noise driven stochastic differential equations is far less developed than the white noise case. However, in some relevant cases it is possible to simulate the colored noise by a Langevin equation which only contains white noise [66, 67]; we will employ such an approach in the course of Ch. 3.

Chapter 2

Magnetoelastic modes and lifetime of magnons

2.1 Motivation and outline

The coupling of the magnetic and the elastic sector in magnetic insulators, i.e., of magnons and phonons, is often negligible [3]. However, sometimes the magnetoelastic coupling is also essential for the understanding of the experiments. One such example are ultrasound experiments, where the properties of the spin degrees of freedom are deduced from measurements of the propagation and attenuation of sound waves [68]. Although the theory of magnetoelastic effects in magnetic insulators has been developed more than half a century ago by Abrahams and Kittel [29, 30, 31], and by Kaganov and Tsukernik [32], there have only been a few theoretical studies of magnetoelastic effects in the past decades [3, 33, 69, 70, 71, 72]. In recent years however, the emerging fields of spintronics and spin-caloritronics [73, 74], where spin degrees of freedom are manipulated by charge and heat currents respectively, have incited new interest in magnetoelastic effects.

The work presented in this chapter is motivated by the experiment [14] of Agrawal *et al.*. There, the magnetoelastic coupling in a thin YIG film was investigated via a spatially resolved measurement of the temperature T_m of short-wavelength exchange magnons in the presence of a thermal gradient. It was found that the magnon and phonon temperatures T_m and T_p are almost exactly equal. This seems to contradict earlier studies on the spin Seebeck effect [73], in which a spin current is believed to be generated by the difference $\Delta T = T_\mathrm{m} - T_\mathrm{p}$ of magnon and phonon temperatures. In an effort to reconcile their findings with these experiments, the authors of [14] suggested that the magnon temperature is spectrally nonuniform, i.e., $T_\mathrm{m} = T_\mathrm{m}(\boldsymbol{k})$. Then it would be possible that the dipolar magnons, which could not be observed in the experiment, thermalize more slowly than the observed exchange magnons. Thus the temperature difference required for the spin Seebeck effect could be maintained between the long-wavelength dipolar magnons and the phonon

bath. In this chapter we present a microscopic explanation for such a spectrally nonuniform magnon temperature: We show that the spin-lattice relaxation time $\tau(\boldsymbol{k})$ in thin YIG films is strongly momentum dependent. In particular, we show that $\tau(\boldsymbol{k})$ exhibits a pronounced minimum in the exchange regime, whereas it is two orders of magnitude larger in the dipolar regime. Due to this longer lifetime, dipolar magnons thermalize slower than exchange magnons to the phonon bath and therefore a temperature difference can persist for longer times.

This calculation is supplemented by a Brillouin light scattering (BLS) spectroscopy [75] measurement of the total damping rate of dipolar magnons. As function of in-plane momenta, the measured damping rate qualitatively agrees with the theoretical prediction, but is three orders of magnitude larger. Since our calculation only takes magnon-phonon scattering into account, which determines the aforementioned temperature equilibration, this indicates that in the long-wavelength dipolar regime other scattering channels are dominant, for example magnon-magnon or elastic magnon-impurity scattering. We also calculate the magnetoelastic hybridization of dipolar magnons and acoustic phonons, which is shown to give rise to a characteristic minimum in the spin dynamic structure factor.

The theoretical part of the work presented in this chapter was done together with Peter Kopietz, whereas the experimental part was done by Dmytro A. Bozhko, Alexander A. Serga, and Burkard Hillebrands. It was published in [P2].

The remainder of this chapter is organized as follows: In Sec. 2.2 and Sec. 2.3 we will carefully derive the magnon and magnetoelastic Hamiltonian in a leading order spin wave expansion. Then, in Sec. 2.4 we will employ a functional integral representation to integrate out the phonon degrees of freedom, thereby generating effective magnon-magnon interactions. The structure of the magnon Green function and the leading order self-energies will be discussed in Sec. 2.5. In Sec. 2.6, we then proceed to calculate the magnetoelastic modes in leading order from the poles of the magnon Green function. We also calculate the resulting spectral functions and the transverse dynamic spin structure factor, which is proportional to the BLS cross section. The calculation of the leading order magnon damping rate will be presented in Sec. 2.7, together with the BLS measurement of the total damping rate of dipolar magnons. Finally, Sec. 2.8 provides a summary and concluding discussion of our results.

2.2 Linear spin wave theory

The Hamiltonian of the magnetic degrees of freedom in thin YIG films has already been introduced in Sec. 1.2.1. In the presence of a static magnetic

field H_0 pointing in z direction, it is given by

$$\mathcal{H}_{\mathrm{m}} = -\frac{1}{2}\sum_{ij}\sum_{\alpha\beta}\left[J_{ij}\delta^{\alpha\beta} + D_{ij}^{\alpha\beta}\right] S_i^{\alpha} S_j^{\beta} - H_0 \sum_i S_i^z. \tag{2.1}$$

Magnons are now introduced via the Holstein-Primakoff bosonization discussed in Sec. 1.3.1. As the effective spin $S \approx 14.2$ is rather large, we retain only the leading terms in the $1/S$ expansion of the Holstein-Primakoff transformation (1.51), so that

$$S_i^x \approx \frac{\sqrt{2S}}{2}\left(b_i + b_i^{\dagger}\right), \tag{2.2a}$$

$$S_i^y \approx \frac{\sqrt{2S}}{2i}\left(b_i - b_i^{\dagger}\right), \tag{2.2b}$$

$$S_i^z = S - b_i^{\dagger} b_i. \tag{2.2c}$$

In the thin film geometry described in Sec. 1.2.4, Fourier transforms are defined via

$$b_{\boldsymbol{k}} = \frac{1}{\sqrt{N}}\sum_i e^{-i\boldsymbol{k}\cdot\boldsymbol{R}_i} b_i, \tag{2.3}$$

where $\boldsymbol{k} = k_z\boldsymbol{e}_z + k_y\boldsymbol{e}_y = |\boldsymbol{k}|\cos\theta_{\boldsymbol{k}}\boldsymbol{e}_z + |\boldsymbol{k}|\sin\theta_{\boldsymbol{k}}\boldsymbol{e}_y$ is the in-plane momentum and N the number of lattice sites in the y-z plane. Keeping only terms quadratic in the bosonic operators yields the Hamiltonian

$$\mathcal{H}_{\mathrm{m}}^{(2)} = \sum_{\boldsymbol{k}}\left[A_{\boldsymbol{k}} b_{\boldsymbol{k}}^{\dagger} b_{\boldsymbol{k}} + \frac{B_{\boldsymbol{k}}}{2}\left(b_{\boldsymbol{k}}^{\dagger} b_{-\boldsymbol{k}}^{\dagger} + b_{-\boldsymbol{k}} b_{\boldsymbol{k}}\right)\right], \tag{2.4}$$

where the energies $A_{\boldsymbol{k}}$ and $B_{\boldsymbol{k}}$ can be expressed in terms of the Fourier transforms $J_{\boldsymbol{k}}$ and $D_{\boldsymbol{k}}^{\alpha\beta}$ of exchange and dipolar interaction as follows [6]:

$$A_{\boldsymbol{k}} = H_0 + S\left(J_{\boldsymbol{k}=0} - J_{\boldsymbol{k}}\right) + S\left(D_{\boldsymbol{k}=0}^{zz} - \frac{D_{\boldsymbol{k}}^{xx} + D_{\boldsymbol{k}}^{yy}}{2}\right), \tag{2.5a}$$

$$B_{\boldsymbol{k}} = -S\frac{D_{\boldsymbol{k}}^{xx} - D_{\boldsymbol{k}}^{yy}}{2}. \tag{2.5b}$$

The quadratic Hamiltonian (2.4) can be diagonalized by means of a canonical Bogoliubov transformation [54],

$$\begin{pmatrix} b_{\boldsymbol{k}} \\ b_{-\boldsymbol{k}}^{\dagger} \end{pmatrix} = \begin{pmatrix} u_{\boldsymbol{k}} & -v_{\boldsymbol{k}} \\ -v_{\boldsymbol{k}}^{*} & u_{\boldsymbol{k}} \end{pmatrix} \begin{pmatrix} \beta_{\boldsymbol{k}} \\ \beta_{-\boldsymbol{k}}^{\dagger} \end{pmatrix}, \tag{2.6}$$

where $\beta_{\boldsymbol{k}}^{\dagger}$ and $\beta_{\boldsymbol{k}}$ are, respectively, the magnon quasiparticle creation and destruction operators. The transformation coefficients are explicitly given by

$$u_{\boldsymbol{k}} = \sqrt{\frac{A_{\boldsymbol{k}} + E_{\boldsymbol{k}}}{2E_{\boldsymbol{k}}}}, \tag{2.7a}$$

$$v_{\boldsymbol{k}} = \frac{B_{\boldsymbol{k}}}{|B_{\boldsymbol{k}}|}\sqrt{\frac{A_{\boldsymbol{k}} - E_{\boldsymbol{k}}}{2E_{\boldsymbol{k}}}}, \tag{2.7b}$$

with the magnon dispersion

$$E_{\boldsymbol{k}} = \sqrt{A_{\boldsymbol{k}}^2 - |B_{\boldsymbol{k}}|^2}. \tag{2.8}$$

In terms of this new magnon operators the Hamiltonian (2.4) is diagonal,

$$\mathcal{H}_{\mathrm{m}}^{(2)} = \sum_{\boldsymbol{k}} \left[E_{\boldsymbol{k}} \beta_{\boldsymbol{k}}^\dagger \beta_{\boldsymbol{k}} + \frac{A_{\boldsymbol{k}} - E_{\boldsymbol{k}}}{2E_{\boldsymbol{k}}} \right]. \tag{2.9}$$

To explicitly evaluate the magnon dispersion (2.8) we need the Fourier transforms of dipolar and exchange interaction; the former was already stated in the introductory Sec. 1.2.4, whereas the latter is given by

$$J_{\boldsymbol{k}} = 2J \left[\cos\left(k_z a\right) + \cos\left(k_y a\right) \right]. \tag{2.10}$$

Because we are mostly interested in long-wavelength magnons with $|\boldsymbol{k}|a \ll 1$, we may expand the exchange interaction in this limit as

$$J_{\boldsymbol{k}} \approx 4J - \frac{\rho_s}{S} \boldsymbol{k}^2, \tag{2.11}$$

with the spin stiffness $\rho_s = JSa^2$. Thus we find that the magnon dispersion $E_{\boldsymbol{k}}$ of a thin film with thickness d is in the long-wavelength limit explicitly given by [6]

$$E_{\boldsymbol{k}} = \sqrt{\left[H_0 + \rho_s \boldsymbol{k}^2 + \Delta \left(1 - f_{\boldsymbol{k}}\right) \sin^2 \theta_{\boldsymbol{k}} \right] \left[H_0 + \rho_s \boldsymbol{k}^2 + \Delta f_{\boldsymbol{k}} \right]}, \tag{2.12}$$

with the form factor

$$f_{\boldsymbol{k}} = \frac{1 - \exp\left(-|\boldsymbol{k}|d\right)}{|\boldsymbol{k}|d}. \tag{2.13}$$

Recall that the magnon dispersion relation (2.12) was already discussed in Sec. 1.2.4 and that it has two degenerate minima at finite momenta $\boldsymbol{k} = \pm k_{\min} \boldsymbol{e}_z$ parallel to the external magnetic field, see also Fig. 1.4.

2.3 Magnon-phonon Hamiltonian

Our starting point for the derivation of magnon-phonon interactions is the phenomenological magnetoelastic Hamiltonian introduced in Sec. 1.2.3,

$$\mathcal{H}_{\mathrm{me}} = \frac{1}{S^2} \sum_i \sum_{\alpha\beta} B^{\alpha\beta} S_i^\alpha S_i^\beta X_i^{\alpha\beta}. \tag{2.14}$$

Applying the linearized Holstein-Primakoff transformation (2.2) and as before retaining terms up to quadratic order in the magnon operators yields two separate contributions,

$$\mathcal{H}_{\mathrm{me}} \approx \mathcal{H}_{\mathrm{me}}^{(2)} + \mathcal{H}_{\mathrm{me}}^{(3)}, \tag{2.15}$$

where the superscript indicates the number of operators involved. $\mathcal{H}_{\text{me}}^{(2)}$ contains one magnon and one phonon operator, and thus describes the hybridization of magnons and phonons, indicating the existence of magnetoelastic modes. On the other hand, $\mathcal{H}_{\text{me}}^{(3)}$ contains two magnon and one phonon operator and therefore describes magnon-phonon scattering processes, so that the magnons acquire a finite lifetime. Note that the Hamiltonian (2.15) is also an expansion in $1/S$, with the leading order contributions $\mathcal{H}_{\text{me}}^{(2)} \propto 1/\sqrt{S}$, and $\mathcal{H}_{\text{me}}^{(3)} \propto 1/S$.

Since the spins couple to elastic strain tensor $X_i^{\alpha\beta}$, we will need an expression for the Fourier transform $X_{\boldsymbol{k}}^{\alpha\beta}$ in terms of the phonon operator $\boldsymbol{X}_{\boldsymbol{k}} = \sum_\lambda X_{\boldsymbol{k}\lambda}\boldsymbol{e}_{\boldsymbol{k}\lambda}$. From the definition (1.22) of the strain tensor in terms of derivatives of the phonon displacement, it follows that

$$X_{\boldsymbol{k}}^{\alpha\beta} = \frac{i}{2}\boldsymbol{k}_{\alpha\beta}\cdot\boldsymbol{X}_{\boldsymbol{k}}, \quad \boldsymbol{k}_{\alpha\beta} = k_\alpha \boldsymbol{e}_\beta + k_\beta \boldsymbol{e}_\alpha. \tag{2.16}$$

In general it is also possible to map the phonon coordinates $X_{\boldsymbol{k}\lambda}$ and momenta $P_{\boldsymbol{k}\lambda}$ to bosonic creation and annihilation operators $a_{\boldsymbol{k}\lambda}^\dagger$ and $a_{\boldsymbol{k}\lambda}$ by setting

$$X_{\boldsymbol{k}\lambda} = \frac{1}{\sqrt{2M\omega_{\boldsymbol{k}\lambda}}}\left(a_{\boldsymbol{k}\lambda} + a_{-\boldsymbol{k}\lambda}^\dagger\right), \tag{2.17a}$$

$$P_{\boldsymbol{k}\lambda} = \frac{1}{i}\sqrt{\frac{M\omega_{\boldsymbol{k}\lambda}}{2}}\left(a_{\boldsymbol{k}\lambda} - a_{-\boldsymbol{k}\lambda}^\dagger\right). \tag{2.17b}$$

Then the noninteracting elastic Hamiltonian becomes

$$\begin{aligned}\mathcal{H}_{\text{e}} &= \sum_{\boldsymbol{k}\lambda}\left[\frac{P_{-\boldsymbol{k}\lambda}P_{\boldsymbol{k}\lambda}}{2M} + \frac{M}{2}\omega_{\boldsymbol{k}\lambda}^2 X_{-\boldsymbol{k}\lambda}X_{\boldsymbol{k}\lambda}\right] \\ &= \sum_{\boldsymbol{k}\lambda}\omega_{\boldsymbol{k}\lambda}\left[a_{\boldsymbol{k}\lambda}^\dagger a_{\boldsymbol{k}\lambda} + \frac{1}{2}\right].\end{aligned} \tag{2.18}$$

However, as magnons always couple to the phonon displacement operator $X_{\boldsymbol{k}\lambda}$ in our magnetoelastic Hamiltonian (2.14), it is advantageous for our purposes to keep the coordinate-momentum representation.

2.3.1 Magnon-phonon hybridization

In the Holstein-Primakoff basis, the magnon-phonon hybridization Hamiltonian takes the form

$$\mathcal{H}_{\text{me}}^{(2)} = \sum_{\boldsymbol{k}}\left[\boldsymbol{X}_{\boldsymbol{k}}^\dagger\cdot\boldsymbol{\Gamma}_{\boldsymbol{k}}b_{\boldsymbol{k}} + \boldsymbol{X}_{\boldsymbol{k}}\cdot\boldsymbol{\Gamma}_{\boldsymbol{k}}^* b_{\boldsymbol{k}}^\dagger\right], \tag{2.19a}$$

$$= \sum_{\boldsymbol{k}}\boldsymbol{X}_{-\boldsymbol{k}}\cdot\left[\boldsymbol{\Gamma}_{\boldsymbol{k}}b_{\boldsymbol{k}} + \boldsymbol{\Gamma}_{-\boldsymbol{k}}^* b_{-\boldsymbol{k}}^\dagger\right], \tag{2.19b}$$

where we used in the second line that $\boldsymbol{X}_{\boldsymbol{k}}$ is the Fourier transform of a Hermitian operator and therefore satisfies $\boldsymbol{X}_{\boldsymbol{k}}^\dagger = \boldsymbol{X}_{-\boldsymbol{k}}$. The vector vertex function is

explicitly given by

$$\boldsymbol{\Gamma}_{\boldsymbol{k}} = -\frac{B_\perp}{\sqrt{2S}}\left(\boldsymbol{k}_{yz} + i\boldsymbol{k}_{xz}\right) \tag{2.20a}$$

$$= -\frac{B_\perp}{\sqrt{2S}}\left[\left(k_y + ik_x\right)\boldsymbol{e}_z + k_z\left(\boldsymbol{e}_y + i\boldsymbol{e}_x\right)\right]. \tag{2.20b}$$

Expanding phonon operator and the vertex function in the basis of phonon polarization vectors as

$$\boldsymbol{X}_{\boldsymbol{k}} = \sum_\lambda X_{\boldsymbol{k}\lambda}\boldsymbol{e}_{\boldsymbol{k}\lambda}, \quad X_{\boldsymbol{k}\lambda} = \boldsymbol{e}^*_{\boldsymbol{k}\lambda}\cdot\boldsymbol{X}_{\boldsymbol{k}}, \tag{2.21a}$$

$$\boldsymbol{\Gamma}_{\boldsymbol{k}} = \sum_\lambda \Gamma_{\boldsymbol{k}\lambda}\boldsymbol{e}_{\boldsymbol{k}\lambda}, \quad \Gamma_{\boldsymbol{k}\lambda} = \boldsymbol{e}^*_{\boldsymbol{k}\lambda}\cdot\boldsymbol{\Gamma}_{\boldsymbol{k}}, \tag{2.21b}$$

allows to write the hybridization Hamiltonian (2.19) as

$$\mathcal{H}^{(2)}_{\mathrm{me}} = \sum_{\boldsymbol{k}\lambda}\left[\Gamma_{\boldsymbol{k}\lambda}X^\dagger_{\boldsymbol{k}\lambda}b_{\boldsymbol{k}} + \Gamma^*_{\boldsymbol{k}\lambda}X_{\boldsymbol{k}\lambda}b^\dagger_{\boldsymbol{k}}\right], \tag{2.22a}$$

$$= \sum_{\boldsymbol{k}\lambda} X_{-\boldsymbol{k}\lambda}\left[\Gamma_{\boldsymbol{k}\lambda}b_{\boldsymbol{k}} + \Gamma^*_{-\boldsymbol{k}\lambda}b^\dagger_{-\boldsymbol{k}}\right]. \tag{2.22b}$$

With the phonon polarization vectors for the thin film geometry given in Eqs. (1.32) we explicitly obtain for the projections of the vertex function,

$$\Gamma_{\boldsymbol{k}\parallel} = i\frac{B_\perp}{\sqrt{2S}}\frac{2k_yk_z}{|\boldsymbol{k}|} = i\frac{B_\perp}{\sqrt{2S}}|\boldsymbol{k}|\sin(2\theta_{\boldsymbol{k}}), \tag{2.23a}$$

$$\Gamma_{\boldsymbol{k}\perp 1} = i\frac{B_\perp}{\sqrt{2S}}\frac{k_y^2 - k_z^2}{|\boldsymbol{k}|} = -i\frac{B_\perp}{\sqrt{2S}}|\boldsymbol{k}|\cos(2\theta_{\boldsymbol{k}}), \tag{2.23b}$$

$$\Gamma_{\boldsymbol{k}\perp 2} = -i\frac{B_\perp}{\sqrt{2S}}k_z = -i\frac{B_\perp}{\sqrt{2S}}|\boldsymbol{k}|\cos(\theta_{\boldsymbol{k}}). \tag{2.23c}$$

As it is our aim to calculate magnon spectral properties, it is advantageous to apply the Bogoliubov transformation (2.6) to obtain the hybridization Hamiltonian in the magnon quasiparticle basis,

$$\mathcal{H}^{(2)}_{\mathrm{me}} = \sum_{\boldsymbol{k}\lambda} X_{-\boldsymbol{k}\lambda}\left[\Gamma^\beta_{\boldsymbol{k}\lambda}\beta_{\boldsymbol{k}} + \Gamma^{\bar\beta}_{-\boldsymbol{k}\lambda}\beta^\dagger_{-\boldsymbol{k}}\right], \tag{2.24}$$

where the hybridization vertices are given by

$$\Gamma^\beta_{\boldsymbol{k}\lambda} = u_{\boldsymbol{k}}\Gamma_{\boldsymbol{k}\lambda} - v^*_{\boldsymbol{k}}\Gamma^*_{-\boldsymbol{k}\lambda}, \tag{2.25a}$$

$$\Gamma^{\bar\beta}_{\boldsymbol{k}\lambda} = u_{\boldsymbol{k}}\Gamma^*_{\boldsymbol{k}\lambda} - v_{\boldsymbol{k}}\Gamma_{-\boldsymbol{k}\lambda} = \left(\Gamma^\beta_{\boldsymbol{k}\lambda}\right)^*. \tag{2.25b}$$

2.3.2 Magnon-phonon scattering

To leading order in $1/S$, the magnon-phonon scattering Hamiltonian is in the Holstein-Primakoff basis given by

$$\begin{aligned}\mathcal{H}_{\text{me}}^{(3)} =&\frac{1}{\sqrt{N}}\sum_{\boldsymbol{k}\boldsymbol{k}'}\Bigg[\boldsymbol{\Gamma}^{\bar{b}b}_{\boldsymbol{k},\boldsymbol{k}'}\cdot\boldsymbol{X}_{\boldsymbol{k}-\boldsymbol{k}'}b^\dagger_{\boldsymbol{k}}b_{\boldsymbol{k}'}\\ &+\frac{1}{2!}\left(\boldsymbol{\Gamma}^{bb}_{\boldsymbol{k},\boldsymbol{k}'}\cdot\boldsymbol{X}_{-\boldsymbol{k}-\boldsymbol{k}'}b_{\boldsymbol{k}}b_{\boldsymbol{k}'}+\boldsymbol{\Gamma}^{\bar{b}\bar{b}}_{\boldsymbol{k},\boldsymbol{k}'}\cdot\boldsymbol{X}_{\boldsymbol{k}+\boldsymbol{k}'}b^\dagger_{\boldsymbol{k}}b^\dagger_{\boldsymbol{k}'}\right)\Bigg] &\text{(2.26a)}\\ =&\frac{1}{\sqrt{N}}\sum_{\boldsymbol{k}\boldsymbol{q}}\boldsymbol{X}_{-\boldsymbol{q}}\cdot\left[\boldsymbol{U}_{-\boldsymbol{q}}b^\dagger_{\boldsymbol{k}}b_{\boldsymbol{k}+\boldsymbol{q}}+\frac{1}{2!}\left(\boldsymbol{V}_{-\boldsymbol{q}}b_{-\boldsymbol{k}}b_{\boldsymbol{k}+\boldsymbol{q}}+\boldsymbol{V}^*_{\boldsymbol{q}}b^\dagger_{\boldsymbol{k}}b^\dagger_{-\boldsymbol{k}-\boldsymbol{q}}\right)\right], &\text{(2.26b)}\end{aligned}$$

where we defined the vector vertices

$$\begin{aligned}\boldsymbol{\Gamma}^{\bar{b}b}_{\boldsymbol{k},\boldsymbol{k}'} =&\boldsymbol{U}_{\boldsymbol{k}-\boldsymbol{k}'}, &\text{(2.27a)}\\ \boldsymbol{\Gamma}^{bb}_{\boldsymbol{k},\boldsymbol{k}'} =&\boldsymbol{V}_{-\boldsymbol{k}-\boldsymbol{k}'}, &\text{(2.27b)}\\ \boldsymbol{\Gamma}^{\bar{b}\bar{b}}_{\boldsymbol{k},\boldsymbol{k}'} =&\boldsymbol{V}^*_{-\boldsymbol{k}-\boldsymbol{k}'}, &\text{(2.27c)}\end{aligned}$$

with

$$\begin{aligned}\boldsymbol{U}_{\boldsymbol{q}} =&\frac{iB_\parallel}{S}\left(q_x\boldsymbol{e}_x+q_y\boldsymbol{e}_y-2q_z\boldsymbol{e}_z\right), &\text{(2.28a)}\\ \boldsymbol{V}_{\boldsymbol{q}} =&\frac{iB_\parallel}{S}\left(q_x\boldsymbol{e}_x-q_y\boldsymbol{e}_y\right)+\frac{B_\perp}{S}\boldsymbol{q}_{xy}\\ =&\frac{iB_\parallel}{S}\left(q_x\boldsymbol{e}_x-q_y\boldsymbol{e}_y\right)+\frac{B_\perp}{S}\left(q_x\boldsymbol{e}_y+q_y\boldsymbol{e}_x\right). &\text{(2.28b)}\end{aligned}$$

In the magnon quasiparticle basis, the cubic Hamiltonian 2.26 becomes

$$\begin{aligned}\mathcal{H}_{\text{me}}^{(3)} =&\frac{1}{\sqrt{N}}\sum_{\boldsymbol{k}\boldsymbol{k}'}\Bigg[\boldsymbol{\Gamma}^{\bar{\beta}\beta}_{\boldsymbol{k},\boldsymbol{k}'}\cdot\boldsymbol{X}_{\boldsymbol{k}-\boldsymbol{k}'}\beta^\dagger_{\boldsymbol{k}}\beta_{\boldsymbol{k}'}\\ &+\frac{1}{2!}\left(\boldsymbol{\Gamma}^{\beta\beta}_{\boldsymbol{k},\boldsymbol{k}'}\cdot\boldsymbol{X}_{-\boldsymbol{k}-\boldsymbol{k}'}\beta_{\boldsymbol{k}}\beta_{\boldsymbol{k}'}+\boldsymbol{\Gamma}^{\bar{\beta}\bar{\beta}}_{\boldsymbol{k},\boldsymbol{k}'}\cdot\boldsymbol{X}_{\boldsymbol{k}+\boldsymbol{k}'}\beta^\dagger_{\boldsymbol{k}}\beta^\dagger_{\boldsymbol{k}'}\right)\Bigg], &\text{(2.29)}\end{aligned}$$

where the interaction vertices are

$$\begin{aligned}\boldsymbol{\Gamma}^{\bar{\beta}\beta}_{\boldsymbol{k},\boldsymbol{k}'} =&u_{\boldsymbol{k}}u_{\boldsymbol{k}'}\boldsymbol{\Gamma}^{\bar{b}b}_{\boldsymbol{k},\boldsymbol{k}'}+v_{\boldsymbol{k}}v^*_{\boldsymbol{k}'}\boldsymbol{\Gamma}^{\bar{b}b}_{-\boldsymbol{k}',-\boldsymbol{k}}-v_{\boldsymbol{k}}u_{\boldsymbol{k}'}\boldsymbol{\Gamma}^{bb}_{-\boldsymbol{k},\boldsymbol{k}'}-u_{\boldsymbol{k}}v_{\boldsymbol{k}'}*\boldsymbol{\Gamma}^{\bar{b}\bar{b}}_{\boldsymbol{k},-\boldsymbol{k}'}\\ =&\left(u_{\boldsymbol{k}}u_{\boldsymbol{k}'}+v_{\boldsymbol{k}}v^*_{\boldsymbol{k}'}\right)\boldsymbol{U}_{\boldsymbol{k}-\boldsymbol{k}'}-v_{\boldsymbol{k}}u_{\boldsymbol{k}'}\boldsymbol{V}_{\boldsymbol{k}-\boldsymbol{k}'}-u_{\boldsymbol{k}}v^*_{\boldsymbol{k}'}\boldsymbol{V}^*_{\boldsymbol{k}'-\boldsymbol{k}}, &\text{(2.30a)}\\ \boldsymbol{\Gamma}^{\beta\beta}_{\boldsymbol{k},\boldsymbol{k}'} =&u_{\boldsymbol{k}}u_{\boldsymbol{k}'}\boldsymbol{\Gamma}^{bb}_{\boldsymbol{k},\boldsymbol{k}'}+v^*_{\boldsymbol{k}}v^*_{\boldsymbol{k}'}\boldsymbol{\Gamma}^{\bar{b}\bar{b}}_{-\boldsymbol{k},-\boldsymbol{k}'}-v^*_{\boldsymbol{k}}u_{\boldsymbol{k}'}\boldsymbol{\Gamma}^{\bar{b}b}_{-\boldsymbol{k},\boldsymbol{k}'}-u_{\boldsymbol{k}}v^*_{\boldsymbol{k}'}\boldsymbol{\Gamma}^{\bar{b}b}_{-\boldsymbol{k}',\boldsymbol{k}}\\ =&u_{\boldsymbol{k}}u_{\boldsymbol{k}'}\boldsymbol{V}_{-\boldsymbol{k}-\boldsymbol{k}'}+v^*_{\boldsymbol{k}}v^*_{\boldsymbol{k}'}\boldsymbol{V}^*_{\boldsymbol{k}+\boldsymbol{k}'}-\left(v^*_{\boldsymbol{k}}u_{\boldsymbol{k}'}+u_{\boldsymbol{k}}v^*_{\boldsymbol{k}'}\right)\boldsymbol{U}_{-\boldsymbol{k}-\boldsymbol{k}'}, &\text{(2.30b)}\\ \boldsymbol{\Gamma}^{\bar{\beta}\bar{\beta}}_{\boldsymbol{k},\boldsymbol{k}'} =&u_{\boldsymbol{k}}u_{\boldsymbol{k}'}\boldsymbol{\Gamma}^{\bar{b}\bar{b}}_{\boldsymbol{k},\boldsymbol{k}'}+v_{\boldsymbol{k}}v_{\boldsymbol{k}'}\boldsymbol{\Gamma}^{bb}_{-\boldsymbol{k},-\boldsymbol{k}'}-u_{\boldsymbol{k}}v_{\boldsymbol{k}'}\boldsymbol{\Gamma}^{\bar{b}b}_{\boldsymbol{k},-\boldsymbol{k}'}-v_{\boldsymbol{k}}u_{\boldsymbol{k}'}\boldsymbol{\Gamma}^{\bar{b}b}_{\boldsymbol{k}',-\boldsymbol{k}}\\ =&u_{\boldsymbol{k}}u_{\boldsymbol{k}'}\boldsymbol{V}^*_{-\boldsymbol{k}-\boldsymbol{k}'}+v_{\boldsymbol{k}}v_{\boldsymbol{k}'}\boldsymbol{V}_{\boldsymbol{k}+\boldsymbol{k}'}-\left(u_{\boldsymbol{k}}v_{\boldsymbol{k}'}+v_{\boldsymbol{k}}u_{\boldsymbol{k}'}\right)\boldsymbol{U}_{\boldsymbol{k}+\boldsymbol{k}'}. &\text{(2.30c)}\end{aligned}$$

Note that the Hermiticity of the Hamiltonian implies the symmetries

$$\boldsymbol{\Gamma}^{\bar{\beta}\beta}_{\boldsymbol{k},\boldsymbol{k}'} = \left(\boldsymbol{\Gamma}^{\bar{\beta}\beta}_{\boldsymbol{k}',\boldsymbol{k}}\right)^*, \tag{2.31a}$$

$$\boldsymbol{\Gamma}^{\beta\beta}_{\boldsymbol{k},\boldsymbol{k}'} = \left(\boldsymbol{\Gamma}^{\bar{\beta}\bar{\beta}}_{\boldsymbol{k},\boldsymbol{k}'}\right)^*. \tag{2.31b}$$

The interaction processes with scattering amplitude $\boldsymbol{\Gamma}^{\bar{\beta}\beta}_{\boldsymbol{k},\boldsymbol{k}'}$ describe the scattering of one magnon by one phonon, and consequently conserve the magnon number. They are known as Cherenkov scattering [3]. On the other hand, the vertices $\boldsymbol{\Gamma}^{\beta\beta}_{\boldsymbol{k},\boldsymbol{k}'}$ and $\boldsymbol{\Gamma}^{\bar{\beta}\bar{\beta}}_{\boldsymbol{k},\boldsymbol{k}'}$ do not conserve the magnon number. $\boldsymbol{\Gamma}^{\beta\beta}_{\boldsymbol{k},\boldsymbol{k}'}$ is the amplitude for the confluence of two magnons into one phonon, while the complex conjugate $\boldsymbol{\Gamma}^{\bar{\beta}\bar{\beta}}_{\boldsymbol{k},\boldsymbol{k}'}$ is the amplitude for the inverse process, i.e., the creation of two magnons from one phonon.

For the calculation of the effective magnon action and the magnon damping in Secs. 2.4 and 2.7 below, we shall also need the projections of the cubic interactions vertices on the phonon polarization basis, defined as

$$\Gamma^{\bar{\beta}\beta}_{\boldsymbol{k},\boldsymbol{k}',\lambda} = \boldsymbol{e}^*_{\boldsymbol{k}'-\boldsymbol{k},\lambda} \cdot \boldsymbol{\Gamma}^{\bar{\beta}\beta}_{\boldsymbol{k},\boldsymbol{k}'}, \tag{2.32a}$$

$$\Gamma^{\beta\beta}_{\boldsymbol{k},\boldsymbol{k}',\lambda} = \boldsymbol{e}^*_{\boldsymbol{k}'+\boldsymbol{k},\lambda} \cdot \boldsymbol{\Gamma}^{\beta\beta}_{\boldsymbol{k},\boldsymbol{k}'}, \tag{2.32b}$$

or, equivalently, in terms of shifted momenta,

$$\Gamma^{\bar{\beta}\beta}_{\boldsymbol{k},\boldsymbol{k}+\boldsymbol{q},\lambda} = \boldsymbol{e}^*_{\boldsymbol{q},\lambda} \cdot \boldsymbol{\Gamma}^{\bar{\beta}\beta}_{\boldsymbol{k},\boldsymbol{k}+\boldsymbol{q}}, \tag{2.33a}$$

$$\Gamma^{\beta\beta}_{\boldsymbol{k},-\boldsymbol{k}+\boldsymbol{q},\lambda} = \boldsymbol{e}^*_{\boldsymbol{q},\lambda} \cdot \boldsymbol{\Gamma}^{\beta\beta}_{\boldsymbol{k},-\boldsymbol{k}+\boldsymbol{q}}. \tag{2.33b}$$

Let us remark that these magnon-phonon scattering vertices could also serve as starting point for kinetic theories dealing with the nonequilibrium dynamics of magnons in YIG. In Ref. [76] for example, the magnon dynamics was calculated in a nonequilibrium Functional Renormalization Group approach, taking into account magnon-phonon scattering. However, only the Cherenkov-type vertices $\boldsymbol{\Gamma}^{\bar{\beta}\beta}_{\boldsymbol{k},\boldsymbol{k}'}$ were included, and only in a simple phenomenological approximation. Using the interaction vertices we derived microscopically in this work should give a more realistic description of the magnon dynamics in YIG.

2.4 Effective magnon action

The effect of the lattice vibrations, i.e., the phonons, on the magnon system can be conveniently studied using a functional integral approach as described in Sec. 1.4. All operators are then replaced by complex fields depending on momentum $\boldsymbol{k}$ and (bosonic) Matsubara frequency $i\omega_n$, which we collect into the single label $K = (\boldsymbol{k}, i\omega_n)$. The action of the combined magnon-phonon system is given by

$$S_{\mathrm{me}}[\bar{\beta},\beta,X,P] = S^{(2)}_{\mathrm{m}}[\bar{\beta},\beta] + S^{(2)}_{\mathrm{e}}[X,P] + S^{(2)}_{\mathrm{me}}[\bar{\beta},\beta,X] + S^{(3)}_{\mathrm{me}}[\bar{\beta},\beta,X], \tag{2.34}$$

where

$$S_{\mathrm{m}}^{(2)}[\bar{\beta},\beta] = -\frac{1}{T}\sum_{K}\left(i\omega_n - E_{\boldsymbol{k}}\right)\bar{\beta}_K\beta_K, \tag{2.35a}$$

$$S_{\mathrm{e}}^{(2)}[X,P] = \frac{1}{2T}\sum_{K\lambda}\Bigg[\frac{1}{M}P_{-K\lambda}P_{K\lambda} + M\omega_{\boldsymbol{k}\lambda}^2 X_{-K\lambda}X_{K\lambda} - \omega_n\left(P_{-K\lambda}X_{K\lambda} - X_{-K\lambda}P_{K\lambda}\right)\Bigg], \tag{2.35b}$$

$$S_{\mathrm{me}}^{(2)}[\bar{\beta},\beta,X] = \frac{1}{T}\sum_{K\lambda}X_{-K\lambda}\left[\Gamma_{\boldsymbol{k}\lambda}^{\beta}\beta_K + \Gamma_{-\boldsymbol{k}\lambda}^{\bar{\beta}}\bar{\beta}_{-K}\right], \tag{2.35c}$$

$$S_{\mathrm{me}}^{(3)}[\bar{\beta},\beta,X] = \frac{1}{T\sqrt{N}}\sum_{KQ\lambda}X_{-Q\lambda}\Bigg[\Gamma_{\boldsymbol{k},\boldsymbol{k}+\boldsymbol{q},\lambda}^{\bar{\beta}\beta}\bar{\beta}_K\beta_{K+Q} + \frac{1}{2!}\left(\Gamma_{-\boldsymbol{k},\boldsymbol{k}+\boldsymbol{q},\lambda}^{\beta\beta}\beta_{-K}\beta_{K+Q} + \Gamma_{\boldsymbol{k},-\boldsymbol{k}-\boldsymbol{q},\lambda}^{\bar{\beta}\bar{\beta}}\bar{\beta}_K\bar{\beta}_{-K-Q}\right)\Bigg]. \tag{2.35d}$$

As the phonon variables $X_{K\lambda}$ and $P_{K\lambda}$ enter at most quadratically, they can be integrated out exactly,

$$\int\mathcal{D}[X,P]\,e^{-S_{\mathrm{me}}[\bar{\beta},\beta,X,P]} = \mathrm{const}\times e^{-S[\bar{\beta},\beta]}, \tag{2.36}$$

yielding an effective magnon action $S[\bar{\beta},\beta]$ which includes all magnetoelastic interactions implicitly. The constant does not affect any functional average and will henceforth be ignored. Explicitly, the effective magnon action is given by

$$S[\bar{\beta},\beta] = S_2[\bar{\beta},\beta] + S_3[\bar{\beta},\beta] + S_4[\bar{\beta},\beta], \tag{2.37}$$

with the quadratic part

$$S_2[\bar{\beta},\beta] = -\frac{1}{T}\sum_{K}\Bigg\{\left[i\omega_n - E_{\boldsymbol{k}} - \Sigma_1(K)\right]\bar{\beta}_K\beta_K - \frac{1}{2}\left[\Pi_1(K)\beta_{-K}\beta_K + \Pi_1^*(K)\bar{\beta}_K\bar{\beta}_{-K}\right]\Bigg\}. \tag{2.38}$$

Here we defined the first order normal and anomalous self-energies

$$\Sigma_1(K) = -\sum_{\lambda}|\Gamma_{\boldsymbol{k}\lambda}^{\beta}|^2 F_{K\lambda}, \tag{2.39a}$$

$$\Pi_1(K) = -\sum_{\lambda}\Gamma_{\boldsymbol{k}\lambda}^{\beta}\Gamma_{-\boldsymbol{k}\lambda}^{\beta}F_{K\lambda}, \tag{2.39b}$$

and the symmetric phonon propagator

$$F_{K\lambda} = \frac{1}{M\left(\omega_n^2 + \omega_{\boldsymbol{k}\lambda}^2\right)}. \tag{2.40}$$

Interference of the magnon-phonon hybridization and scattering terms generates the cubic contribution,

$$\begin{aligned} S_3[\bar\beta,\beta] = &-\frac{1}{T\sqrt{N}}\sum_{K_1K_2K_3}\delta_{K_1+K_2+K_3,0} \\ &\times\Big[\frac{1}{2!}\Gamma^{\bar\beta\beta\beta}_{1;23}\bar\beta_{-1}\beta_2\beta_3+\frac{1}{2!}\Gamma^{\bar\beta\bar\beta\beta}_{12;3}\bar\beta_{-1}\bar\beta_{-2}\beta_3 \\ &+\frac{1}{3!}\Gamma^{\beta\beta\beta}_{123}\beta_1\beta_2\beta_3+\frac{1}{3!}\Gamma^{\bar\beta\bar\beta\bar\beta}_{123}\bar\beta_{-1}\bar\beta_{-2}\bar\beta_{-3}\Big], \end{aligned} \tag{2.41}$$

where we abbreviated $\beta_{K_1}\equiv\beta_1$, $\Gamma^{\bar\beta\beta\beta}_{K_1;K_2K_3}\equiv\Gamma^{\bar\beta\beta\beta}_{1;23}$, and similarly for the other labels. The properly symmetrized cubic interaction vertices are given by

$$\Gamma^{\bar\beta\beta\beta}_{1;23}=\sum_\lambda\Big[F_{1\lambda}\Gamma^{\bar\beta}_{-1\lambda}\Gamma^{\beta\beta}_{2,3,\lambda}+F_{2\lambda}\Gamma^{\beta}_{2\lambda}\Gamma^{\bar\beta\beta}_{-1,3,\lambda}+F_{3\lambda}\Gamma^{\beta}_{3\lambda}\Gamma^{\bar\beta\beta}_{-1,2,\lambda}\Big], \tag{2.42a}$$

$$\Gamma^{\bar\beta\bar\beta\beta}_{12;3}=\sum_\lambda\Big[F_{1\lambda}\Gamma^{\bar\beta}_{-1\lambda}\Gamma^{\bar\beta\beta}_{-2,3,\lambda}+F_{2\lambda}\Gamma^{\bar\beta}_{-2\lambda}\Gamma^{\bar\beta\beta}_{-1,3,\lambda}+F_{3\lambda}\Gamma^{\beta}_{3\lambda}\Gamma^{\bar\beta\bar\beta}_{-1,-2,\lambda}\Big], \tag{2.42b}$$

$$\Gamma^{\beta\beta\beta}_{123}=\sum_\lambda\Big[F_{1\lambda}\Gamma^{\beta}_{1\lambda}\Gamma^{\beta\beta}_{2,3,\lambda}+(1\leftrightarrow2)+(1\leftrightarrow3)\Big], \tag{2.42c}$$

$$\Gamma^{\bar\beta\bar\beta\bar\beta}_{123}=\sum_\lambda\Big[F_{1\lambda}\Gamma^{\bar\beta}_{-1\lambda}\Gamma^{\bar\beta\bar\beta}_{-2,-3,\lambda}+(1\leftrightarrow2)+(1\leftrightarrow3)\Big]. \tag{2.42d}$$

Finally, the quartic contribution to the effective action (2.37) is generated from the square of the magnon-phonon scattering terms via exchange of a virtual phonon,

$$\begin{aligned} S_4[\bar\beta,\beta] = &-\frac{1}{TN}\sum_{K_1\ldots K_4}\delta_{K_1+\ldots+K_4,0}\Big[\frac{1}{(2!)^2}\Gamma^{\bar\beta\bar\beta\beta\beta}_{12;34}\bar\beta_{-1}\bar\beta_{-2}\beta_3\beta_4 \\ &+\frac{1}{3!}\Gamma^{\bar\beta\beta\beta\beta}_{1;234}\bar\beta_{-1}\beta_2\beta_3\beta_4+\frac{1}{3!}\Gamma^{\bar\beta\bar\beta\bar\beta\beta}_{123;4}\bar\beta_{-1}\bar\beta_{-2}\bar\beta_{-3}\beta_4 \\ &+\frac{1}{4!}\Gamma^{\beta\beta\beta\beta}_{1234}\beta_1\beta_2\beta_3\beta_4+\frac{1}{4!}\Gamma^{\bar\beta\bar\beta\bar\beta\bar\beta}_{1234}\bar\beta_{-1}\bar\beta_{-2}\bar\beta_{-3}\bar\beta_{-4}\Big], \end{aligned} \tag{2.43}$$

with properly symmetrized interaction vertices

$$\Gamma^{\bar\beta\bar\beta\beta\beta}_{12;34} = \sum_\lambda \Big[F_{1+2,\lambda} \Gamma^{\bar\beta\bar\beta}_{-1,-2,\lambda} \Gamma^{\beta\beta}_{3,4,\lambda} + F_{2+3,\lambda} \Gamma^{\bar\beta\beta}_{-2,3,\lambda} \Gamma^{\bar\beta\beta}_{-1,4,\lambda} + F_{3+1,\lambda} \Gamma^{\bar\beta\beta}_{-1,3,\lambda} \Gamma^{\bar\beta\beta}_{-2,4,\lambda} \Big], \tag{2.44a}$$

$$\Gamma^{\bar\beta\beta\beta\beta}_{1;234} = \sum_\lambda \Big[F_{1+2,\lambda} \Gamma^{\bar\beta\beta}_{-1,2,\lambda} \Gamma^{\beta\beta}_{3,4,\lambda} + (2 \leftrightarrow 3) + (2 \leftrightarrow 4) \Big], \tag{2.44b}$$

$$\Gamma^{\bar\beta\bar\beta\bar\beta\beta}_{123;4} = \sum_\lambda \Big[F_{1+2,\lambda} \Gamma^{\bar\beta\bar\beta}_{-1,-2,\lambda} \Gamma^{\bar\beta\beta}_{-3,4,\lambda} + (2 \leftrightarrow 3) + (1 \leftrightarrow 3) \Big], \tag{2.44c}$$

$$\Gamma^{\beta\beta\beta\beta}_{1234} = \sum_\lambda \Big[F_{1+2,\lambda} \Gamma^{\beta\beta}_{1,2,\lambda} \Gamma^{\beta\beta}_{3,4,\lambda} + (2 \leftrightarrow 3) + (2 \leftrightarrow 4) \Big], \tag{2.44d}$$

$$\Gamma^{\bar\beta\bar\beta\bar\beta\bar\beta}_{1234} = \sum_\lambda \Big[F_{1+2,\lambda} \Gamma^{\bar\beta\bar\beta}_{-1,-2,\lambda} \Gamma^{\bar\beta\bar\beta}_{-3,-4,\lambda} + (2 \leftrightarrow 3) + (2 \leftrightarrow 4) \Big]. \tag{2.44e}$$

2.5 Green functions and self-energies

The existence of the anomalous terms proportional to $\beta_{-K}\beta_K$ and $\bar\beta_K\bar\beta_{-K}$ in the quadratic part of the action (2.38) entails a matrix structure of the magnon Green function,

$$\hat G(K) = \begin{pmatrix} G(K) & P(K) \\ P^*(K) & G(-K) \end{pmatrix}, \tag{2.45}$$

with normal and anomalous components

$$G(K) = -\frac{1}{T}\langle \beta_K \bar\beta_K \rangle, \tag{2.46a}$$

$$P(K) = -\frac{1}{T}\langle \beta_K \beta_{-K} \rangle. \tag{2.46b}$$

In the noninteracting limit, these reduce to

$$G_0(K) = \frac{1}{i\omega_n - E_{\boldsymbol{k}}}, \tag{2.47a}$$

$$P_0(K) = 0. \tag{2.47b}$$

Interaction effects may now be incorporated conveniently via the (matrix) Dyson equation,

$$\hat G^{-1}(K) = \hat G_0^{-1}(K) - \hat\Sigma(K), \tag{2.48}$$

where we introduced the self-energy matrix

$$\hat\Sigma(K) = \begin{pmatrix} \Sigma(K) & \Pi^*(K) \\ \Pi(K) & \Sigma(-K) \end{pmatrix}. \tag{2.49}$$

Explicit matrix inversion of the Dyson equation (2.48) yields for normal and anomalous magnon Green function

$$G(K) = -\frac{i\omega_n + E_{\boldsymbol{k}} + \Sigma_+(K) - \Sigma_-(K)}{D(K)}, \tag{2.50a}$$

$$P(K) = \frac{\Pi^*(K)}{D(K)}, \tag{2.50b}$$

where

$$\Sigma_\pm(K) = \frac{1}{2}\left[\Sigma(K) \pm \Sigma(-K)\right], \tag{2.51}$$

and

$$D(K) = \det \hat{G}^{-1} = \left[E_{\boldsymbol{k}} + \Sigma_+(K)\right]^2 - \left[i\omega_n - \Sigma_-(K)\right]^2 - |\Pi(K)|^2. \tag{2.52}$$

The normal and anomalous self-energies can be calculated in perturbation theory as expansion in powers of the small parameter $1/S$,

$$\Sigma(K) = \Sigma_1(K) + \Sigma_2(K) + \ldots, \tag{2.53a}$$

$$\Pi(K) = \Pi_1(K) + \Pi_2(K) + \ldots. \tag{2.53b}$$

The first order self-energies are generated from the magnetoelastic hybridization and are already given in Eqs. (2.39). For calculating the leading order magnon damping in Sec. 2.7 below, we only need the $1/S^2$ correction to the normal magnon self-energy, given by

$$\Sigma_2(K) = \frac{T}{N}\sum_{K'} \Gamma^{\bar{\beta}\bar{\beta}\beta\beta}_{-K,-K';K',K} G_0(K') \tag{2.54a}$$

$$= \frac{T}{N}\sum_{K'} \left[|\Gamma^{\bar{\beta}\beta}_{\boldsymbol{k},\boldsymbol{k}',\lambda}|^2 F_{K-K',\lambda} + |\Gamma^{\beta\beta}_{\boldsymbol{k},\boldsymbol{k}',\lambda}|^2 F_{K+K',\lambda}\right] G_0(K'). \tag{2.54b}$$

The Matsubara frequency sum in this expression can be explicitly evaluated by virtue of Eq. (1.65), using the Residue theorem,

$$\Sigma_2(K) = \frac{1}{N}\sum_{\boldsymbol{k}'\lambda}\left\{ \frac{|\Gamma^{\bar{\beta}\beta}_{\boldsymbol{k},\boldsymbol{k}',\lambda}|^2}{2M\omega_{\boldsymbol{k}-\boldsymbol{k}'\lambda}} \left[\frac{b(\omega_{\boldsymbol{k}-\boldsymbol{k}'\lambda}) - b(E_{\boldsymbol{k}'})}{i\omega_n + \omega_{\boldsymbol{k}-\boldsymbol{k}'\lambda} - E_{\boldsymbol{k}'}} + \frac{1 + b(\omega_{\boldsymbol{k}-\boldsymbol{k}'\lambda}) + b(E_{\boldsymbol{k}'})}{i\omega_n - \omega_{\boldsymbol{k}-\boldsymbol{k}'\lambda} - E_{\boldsymbol{k}'}}\right] \right.$$
$$\left. - \frac{|\Gamma^{\beta\beta}_{\boldsymbol{k},\boldsymbol{k}',\lambda}|^2}{2M\omega_{\boldsymbol{k}+\boldsymbol{k}'\lambda}} \left[\frac{1 + b(\omega_{\boldsymbol{k}+\boldsymbol{k}'\lambda}) + b(E_{\boldsymbol{k}'})}{i\omega_n + \omega_{\boldsymbol{k}+\boldsymbol{k}'\lambda} + E_{\boldsymbol{k}'}} + \frac{b(\omega_{\boldsymbol{k}+\boldsymbol{k}'\lambda}) - b(E_{\boldsymbol{k}'})}{i\omega_n - \omega_{\boldsymbol{k}+\boldsymbol{k}'\lambda} + E_{\boldsymbol{k}'}}\right] \right\}, \tag{2.55}$$

where we introduced the Bose function

$$b(\omega) = \frac{1}{\exp(\omega/T) - 1}. \tag{2.56}$$

2.6 Magnetoelastic modes

The spectrum of magnetoelastic modes can be obtained from the real part of the poles of the matrix Green function (2.45) after analytic continuation to the real frequency axis, i.e., from

$$\mathrm{Re}\, D(\boldsymbol{k}, i\omega_n \to \omega + i\eta) = 0, \tag{2.57}$$

with infinitesimal positive η. Explicitly, this yields

$$\begin{aligned} &\omega^2 - E_{\boldsymbol{k}}^2 - 2\omega \mathrm{Re}\, \Sigma_-(\boldsymbol{k}, \omega + i\eta) - 2E_{\boldsymbol{k}} \mathrm{Re}\, \Sigma_+(\boldsymbol{k}, \omega + i\eta) \\ =&\mathrm{Re}\, \left[\Sigma_+(\boldsymbol{k}, \omega + i\eta)\right]^2 - \mathrm{Re}\, \left[\Sigma_-(\boldsymbol{k}, \omega + i\eta)\right]^2 - |\Pi(\boldsymbol{k}, \omega + i\eta)|^2. \end{aligned} \tag{2.58}$$

Since the effective spin $S \approx 14.2$ is rather large, we may evaluate the above Eq. (2.58) to leading order in $1/S$. Therefore we approximate $\Sigma(K) \approx \Sigma_1(K)$, $\Pi(K) \approx \Pi_1(K)$, and neglect the right-hand side entirely, since it involves squares of the self-energies and is therefore at least of order $1/S^2$ [1]. From the explicit expressions of the first order self-energies, Eqs. (2.39) it is immediately obvious that $\Sigma_-(K) = 0$ and thus $\Sigma_+(K) = \Sigma_1(K)$ in this approximation. Then we are left with

$$\omega^2 - E_{\boldsymbol{k}}^2 = 2E_{\boldsymbol{k}} \mathrm{Re}\, \Sigma_1(\boldsymbol{k}, \omega + i\eta). \tag{2.59}$$

To make the equation (2.59) determining the spectrum of magnetoelastic modes more tractable analytically, let us further suppose that either the energy of the longitudinal or of the transverse phonon mode is close to the magnon energy $E_{\boldsymbol{k}}$. In the first case we may approximate

$$\Sigma_1(\boldsymbol{k}, \omega + i\eta) \approx \frac{|\Gamma^\beta_{\boldsymbol{k}\parallel}|^2}{M\left(\omega^2 - \omega^2_{\boldsymbol{k}\parallel} + 2i\eta\omega\right)}, \tag{2.60}$$

whereas in the latter

$$\Sigma_1(\boldsymbol{k}, \omega + i\eta) \approx \frac{|\Gamma^\beta_{\boldsymbol{k}\perp}|^2}{M\left(\omega^2 - \omega^2_{\boldsymbol{k}\perp} + 2i\eta\omega\right)}, \tag{2.61}$$

where we defined

$$|\Gamma^\beta_{\boldsymbol{k}\perp}|^2 = |\Gamma^\beta_{\boldsymbol{k}\perp 1}|^2 + |\Gamma^\beta_{\boldsymbol{k}\perp 2}|^2, \tag{2.62}$$

since the two transverse phonon modes are degenerate. Then Eq. (2.59) is biquadratic with solutions

$$\Omega^2_{\boldsymbol{k}\lambda\pm} = \frac{\omega^2_{\boldsymbol{k}\lambda} + E^2_{\boldsymbol{k}}}{2} \pm \sqrt{\frac{\left(\omega^2_{\boldsymbol{k}\lambda} - E^2_{\boldsymbol{k}}\right)^2}{4} + \Delta^4_{\boldsymbol{k}\lambda}}, \tag{2.63}$$

[1] Without neglecting the right-hand side Eq. (2.58) amounts to finding the roots of a sixth order polynomial within our approximations. We have checked numerically that keeping these terms does not significantly affect the solutions for the parameters of YIG.

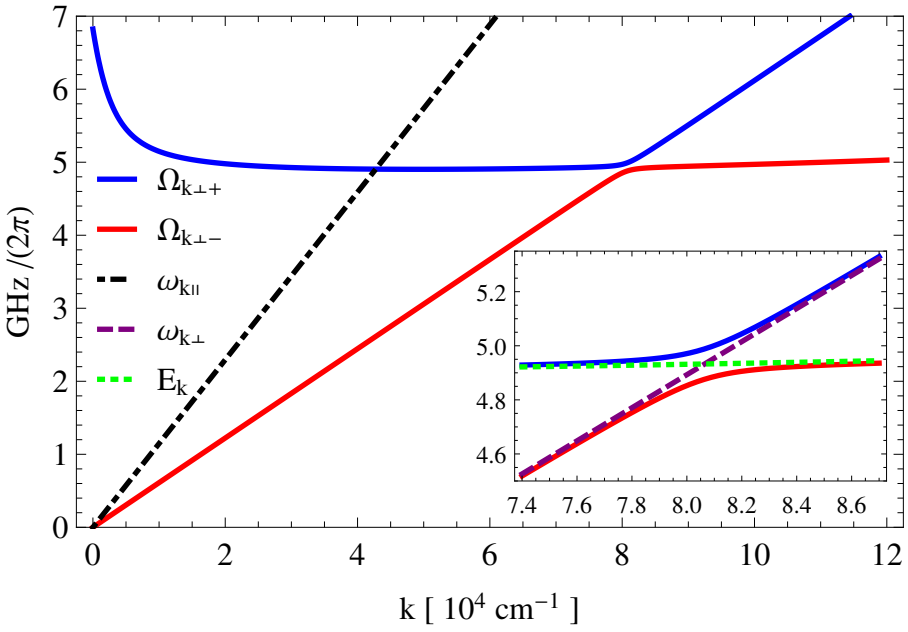

Figure 2.1: *Plot of the magnetoelastic dispersion relations (2.63) of a YIG film with thickness $d = 6.7\,\mu$m in an external magnetic field $H_0 = 1710\,\mathrm{Oe} \times \mu$, for momenta $\boldsymbol{k} = k\boldsymbol{e}_z$ parallel to the in-plane magnetic field. The inset shows a magnified view of the hybridization at the crossing of magnon and transverse phonon branches; axes are the same as in the main plot.*

where the hybridization energy scale is given by

$$\Delta^4_{\boldsymbol{k}\lambda} = 2\frac{E_{\boldsymbol{k}}}{M}|\Gamma^{\beta}_{\boldsymbol{k}\lambda}|^2. \tag{2.64}$$

A plot of the dispersion relation (2.63) of the magnetoelastic modes is displayed in Fig. 2.1, for in-plane momenta $\boldsymbol{k} = k\boldsymbol{e}_z$ parallel to the external magnetic field. Note that for this propagation direction the longitudinal phonons do not hybridize, since the relevant hybridization vertex $\Gamma_{\boldsymbol{k}\parallel}$ given in Eq. (2.23a) vanishes for $k_y = 0$, i.e., $\theta_{\boldsymbol{k}} = 0$.

2.6.1 Spectral functions

The normal and anomalous spectral functions of the magnons can be obtained from their corresponding Matsubara Green functions after analytical continuation to real frequencies,

$$A(\boldsymbol{k},\omega) = -\frac{1}{\pi}\mathrm{Im}\,G(\boldsymbol{k}, i\omega_n \to \omega + i\eta), \tag{2.65a}$$

$$B(\boldsymbol{k},\omega) = -\frac{1}{\pi}\mathrm{Im}\,P(\boldsymbol{k}, i\omega_n \to \omega + i\eta). \tag{2.65b}$$

Including first order corrections in $1/S$, the normal and anomalous Green functions are given by

$$G(\boldsymbol{k}, i\omega_n) = \frac{i\omega_n + E_{\boldsymbol{k}} + \Sigma_1(\boldsymbol{k}, i\omega_n)}{(i\omega_n)^2 - E_{\boldsymbol{k}}^2 - 2E_{\boldsymbol{k}}\Sigma_1(\boldsymbol{k}, i\omega_n)}, \tag{2.66a}$$

$$P(\boldsymbol{k}, i\omega_n) = \frac{\Pi_1^*(\boldsymbol{k}, i\omega_n)}{(i\omega_n)^2 - E_{\boldsymbol{k}}^2 - 2E_{\boldsymbol{k}}\Sigma_1(\boldsymbol{k}, i\omega_n)}. \tag{2.66b}$$

As in the calculation of the spectrum of the magnetoelastic modes, we may now assume that $i\omega_n$ is close to either $\omega_{\boldsymbol{k}\parallel}$ or $\omega_{\boldsymbol{k}\perp}$ and neglect the other polarization. Then we obtain for the normal and anomalous magnon Green functions

$$G(\boldsymbol{k}, i\omega_n) \approx \frac{[i\omega_n + E_{\boldsymbol{k}}]\,[(i\omega_n)^2 - \omega_{\boldsymbol{k}\lambda}^2] + |\Gamma_{\boldsymbol{k}\lambda}^{\beta}|^2/M}{[(i\omega_n)^2 - E_{\boldsymbol{k}}^2]\,[(i\omega_n)^2 - \omega_{\boldsymbol{k}\lambda}^2] - 2E_{\boldsymbol{k}}|\Gamma_{\boldsymbol{k}\lambda}^{\beta}|^2/M}, \tag{2.67a}$$

$$P(\boldsymbol{k}, i\omega_n) \approx \frac{-\Gamma_{\boldsymbol{k}\lambda}^{\bar{\beta}}\Gamma_{-\boldsymbol{k}\lambda}^{\bar{\beta}}/M}{[(i\omega_n)^2 - E_{\boldsymbol{k}}^2]\,[(i\omega_n)^2 - \omega_{\boldsymbol{k}\lambda}^2] - 2E_{\boldsymbol{k}}|\Gamma_{\boldsymbol{k}\lambda}^{\beta}|^2/M}, \tag{2.67b}$$

where we again take the degeneracy of transverse phonon modes into account by defining

$$\Gamma_{\boldsymbol{k}\perp}^{\bar{\beta}}\Gamma_{-\boldsymbol{k}\perp}^{\bar{\beta}} = \Gamma_{\boldsymbol{k}\perp 1}^{\bar{\beta}}\Gamma_{-\boldsymbol{k}\perp 1}^{\bar{\beta}} + \Gamma_{\boldsymbol{k}\perp 2}^{\bar{\beta}}\Gamma_{-\boldsymbol{k}\perp 2}^{\bar{\beta}}. \tag{2.68}$$

Analytical continuation in this approximation yields the spectral functions

$$A(\boldsymbol{k}, \omega) \approx Z_{\boldsymbol{k}\lambda}(\omega) \sum_{s=\pm} s\left[\delta(\omega - \Omega_{\boldsymbol{k}\lambda s}) + \delta(\omega + \Omega_{\boldsymbol{k}\lambda s})\right], \tag{2.69a}$$

$$B(\boldsymbol{k}, \omega) \approx Y_{\boldsymbol{k}\lambda}(\omega) \sum_{s=\pm} s\left[\delta(\omega - \Omega_{\boldsymbol{k}\lambda s}) + \delta(\omega + \Omega_{\boldsymbol{k}\lambda s})\right], \tag{2.69b}$$

where the weighing factors are given by

$$Z_{\boldsymbol{k}\lambda}(\omega) = \frac{[\omega + E_{\boldsymbol{k}}]\,[\omega^2 - \omega_{\boldsymbol{k}\lambda}^2] + |\Gamma_{\boldsymbol{k}\lambda}^{\beta}|^2/M}{2\omega\left[\Omega_{\boldsymbol{k}\lambda+}^2 - \Omega_{\boldsymbol{k}\lambda-}^2\right]}, \tag{2.70a}$$

$$Y_{\boldsymbol{k}\lambda}(\omega) = -\frac{\Gamma_{\boldsymbol{k}\lambda}^{\bar{\beta}}\Gamma_{-\boldsymbol{k}\lambda}^{\bar{\beta}}}{2M\omega\left[\Omega_{\boldsymbol{k}\lambda+}^2 - \Omega_{\boldsymbol{k}\lambda-}^2\right]}. \tag{2.70b}$$

An intensity plot of the normal magnon spectral function (2.69a) for in-plane momenta $\boldsymbol{k} = k\boldsymbol{e}_z$ is presented in Fig. 2.2, clearly showing the transfer of spectral weight from magnons to transverse acoustic phonon in the vicinity of the resonance $E_{\boldsymbol{k}} \approx \omega_{\boldsymbol{k}\perp}$.

2.6.2 Dynamic structure factor

The intensity measured in Brillouin light scattering experiments is actually proportional to the transverse dynamic spin structure factor [77, 78], defined as

$$S_{\perp}(\boldsymbol{k}, \omega) = \int_{-\infty}^{\infty} \frac{\mathrm{d}t}{2\pi}\, e^{i\omega t} \left\langle S_{-\boldsymbol{k}}^x(0) S_{\boldsymbol{k}}^x(t) + S_{-\boldsymbol{k}}^y(0) S_{\boldsymbol{k}}^y(t) \right\rangle. \tag{2.71}$$

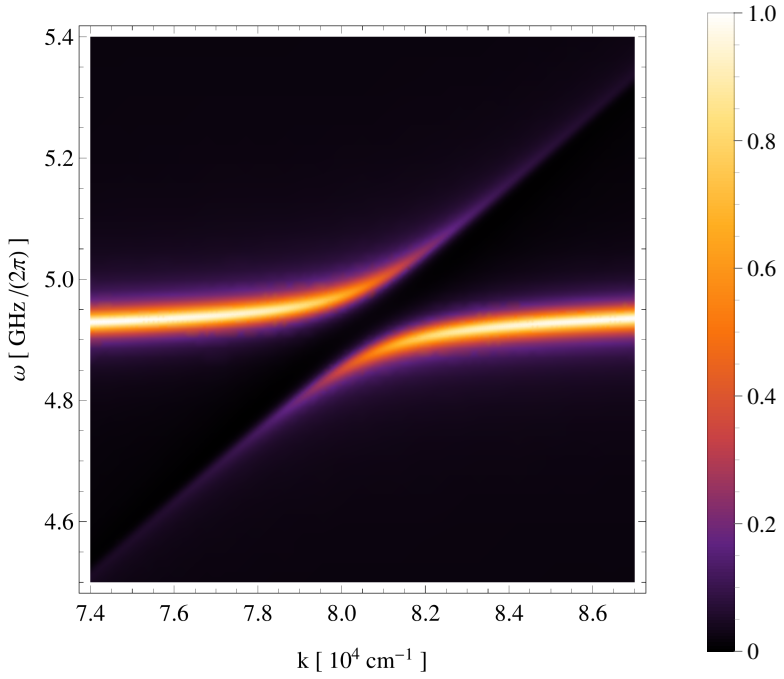

Figure 2.2: *Normalized intensity plot of the normal magnon spectral function (2.69a) of a YIG film with thickness* $d = 6.7\,\mu\mathrm{m}$ *in an external magnetic field* $H_0 = 1710\,\mathrm{Oe}\times\mu$*, for momenta* $\boldsymbol{k} = k\boldsymbol{e}_z$ *parallel to the in-plane magnetic field. For the purpose of plotting, the delta distributions are modeled as Lorentzians with a finite lifetime of* 10 ns*.*

In thermal equilibrium, this spin structure factor can be calculated via analytical continuation as

$$S_\perp(\boldsymbol{k},\omega) = -\frac{1}{\pi}\frac{1}{1-e^{\omega/T}}\mathrm{Im}\,\chi_\perp(\boldsymbol{k}, i\omega_n \to \omega + i\eta), \tag{2.72}$$

where the imaginary-time dynamic susceptibility is given by

$$\chi_\perp(K) = -\int_0^{1/T} \mathrm{d}\tau\, e^{i\omega_n\tau}\left\langle S^x_{-\boldsymbol{k}}(0)S^x_{\boldsymbol{k}}(\tau) + S^y_{-\boldsymbol{k}}(0)S^y_{\boldsymbol{k}}(\tau)\right\rangle. \tag{2.73}$$

Applying the linearized Holstein-Primakoff transformation (2.2) allows to express the above susceptibility via magnon Green functions,

$$\begin{aligned}\chi_\perp(K) =& S\big\{\left(u_{\boldsymbol{k}}^2 + |v_{\boldsymbol{k}}|^2\right)\left[G(-\boldsymbol{k}, i\omega_n) + G(\boldsymbol{k}, -i\omega_n)\right]\\ &- 2u_{\boldsymbol{k}}v^*_{\boldsymbol{k}}P(\boldsymbol{k}, i\omega_n) - 2u_{\boldsymbol{k}}v_{\boldsymbol{k}}P^*(\boldsymbol{k}, i\omega_n)\big\}.\end{aligned} \tag{2.74}$$

Thus we arrive at the following expression for the transverse spin structure factor,

$$\begin{aligned}S_\perp(\boldsymbol{k},\omega) =& \frac{S}{1-e^{\omega/T}}\big\{\left(u_{\boldsymbol{k}}^2 + |v_{\boldsymbol{k}}|^2\right)\left[A(-\boldsymbol{k},\omega) - A(\boldsymbol{k},-\omega)\right]\\ &- 2\left(u_{\boldsymbol{k}}v^*_{\boldsymbol{k}} + u_{\boldsymbol{k}}v_{\boldsymbol{k}}\right)B(\boldsymbol{k},\omega)\big\}.\end{aligned} \tag{2.75}$$

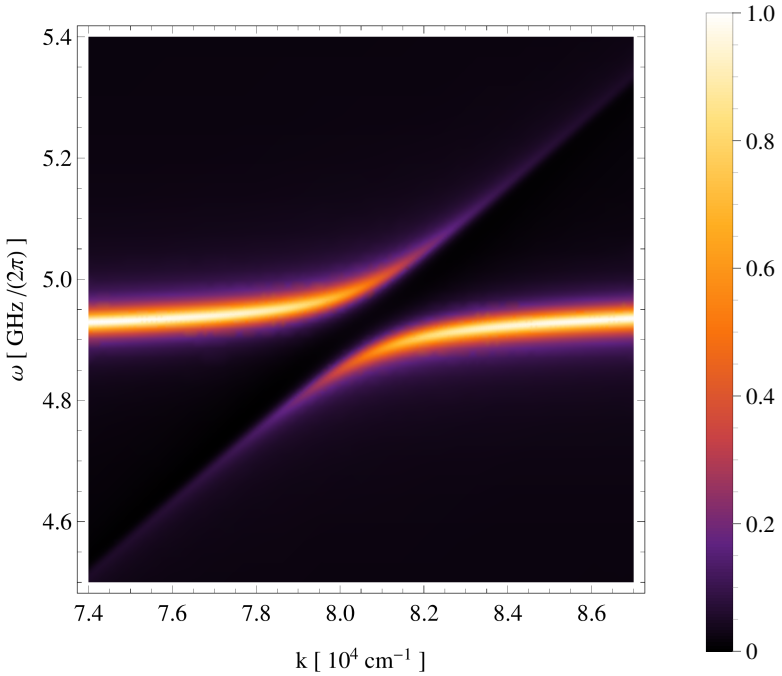

Figure 2.3: *Normalized intensity plot of transverse dynamic spin structure factor (2.75) of a YIG film with thickness* $d = 6.7\,\mu\mathrm{m}$ *in an external magnetic field* $H_0 = 1710\,\mathrm{Oe} \times \mu$ *and at temperature* $T = 300\,\mathrm{K}$*, for momenta* $\boldsymbol{k} = k\boldsymbol{e}_z$ *parallel to the in-plane magnetic field. For the purpose of plotting, the delta distributions are modeled as Lorentzians with a finite lifetime of* 10 ns*.*

Employing the approximate expressions (2.69) for the spectral functions, we show an intensity plot of the transverse dynamic spin structure factor (2.75) in Fig. 2.3. Note that due to the smallness of the Bogoliubov coefficient $v_{\boldsymbol{k}}$ in (almost) the entire Brillouin zone, the qualitative behavior as function of momentum of the spin structure factor is very similar to that of the normal magnon spectral function, see Fig. 2.2.

2.7 Magnon damping

The damping rate $\gamma(\boldsymbol{k})$ of a magnon with momentum $\boldsymbol{k}$ and energy $E_{\boldsymbol{k}}$ due to magnetoelastic interactions can be extracted from the determinant (2.52) of the inverse magnon Green function after analytical continuation to real frequencies,

$$\gamma(\boldsymbol{k}) = -\frac{1}{2E_{\boldsymbol{k}}}\mathrm{Im}\, D(\boldsymbol{k}, i\omega_n \to E_{\boldsymbol{k}} + i\eta). \tag{2.76}$$

Note that the first order self-energies (2.39) do not contribute to the damping (2.76) provided the renormalization of the magnon energies, i.e., the appearance of magnetoelastic modes, is correctly taken into account. Therefore the

first nonvanishing contribution to the damping is of order $1/S^2$. Neglecting all higher orders, the damping rate (2.76) reduces to

$$\gamma_2(\boldsymbol{k}) = -\mathrm{Im}\,\Sigma_2(\boldsymbol{k}, i\omega_n \to E_{\boldsymbol{k}} + i\eta), \tag{2.77}$$

where the second order self-energy $\Sigma_2(K) = \Sigma_2(\boldsymbol{k}, i\omega_n)$ is given in Eq. (2.55). The damping may then be split into three separate contributions,

$$\gamma_2(\boldsymbol{k}) = \gamma_{2a}^{\mathrm{Che}}(\boldsymbol{k}) + \gamma_{2b}^{\mathrm{Che}}(\boldsymbol{k}) + \gamma_2^{\mathrm{con}}(\boldsymbol{k}), \tag{2.78}$$

where

$$\gamma_{2a}^{\mathrm{Che}}(\boldsymbol{k}) = \frac{\pi}{N}\sum_{\boldsymbol{q}\lambda} \frac{|\Gamma^{\bar{\beta}\beta}_{\boldsymbol{k},\boldsymbol{k}+\boldsymbol{q},\lambda}|^2}{2M\omega_{\boldsymbol{q}\lambda}} \delta\left(E_{\boldsymbol{k}} - E_{\boldsymbol{k}+\boldsymbol{q}} + \omega_{\boldsymbol{q}\lambda}\right)\left[b(E_{\boldsymbol{k}+\boldsymbol{q}} - E_{\boldsymbol{k}}) - b(E_{\boldsymbol{k}+\boldsymbol{q}})\right], \tag{2.79a}$$

$$\gamma_{2b}^{\mathrm{Che}}(\boldsymbol{k}) = \frac{\pi}{N}\sum_{\boldsymbol{q}\lambda} \frac{|\Gamma^{\bar{\beta}\beta}_{\boldsymbol{k},\boldsymbol{k}-\boldsymbol{q},\lambda}|^2}{2M\omega_{\boldsymbol{q}\lambda}} \delta\left(E_{\boldsymbol{k}} - E_{\boldsymbol{k}-\boldsymbol{q}} - \omega_{\boldsymbol{q}\lambda}\right)\left[b(E_{\boldsymbol{k}-\boldsymbol{q}}) - b(E_{\boldsymbol{k}-\boldsymbol{q}} - E_{\boldsymbol{k}})\right], \tag{2.79b}$$

$$\gamma_2^{\mathrm{con}}(\boldsymbol{k}) = \frac{\pi}{N}\sum_{\boldsymbol{q}\lambda} \frac{|\Gamma^{\beta\beta}_{\boldsymbol{k},\boldsymbol{q}-\boldsymbol{k},\lambda}|^2}{2M\omega_{\boldsymbol{q}\lambda}} \delta\left(E_{\boldsymbol{k}} + E_{\boldsymbol{q}-\boldsymbol{k}} - \omega_{\boldsymbol{q}\lambda}\right)\left[b(E_{\boldsymbol{q}-\boldsymbol{k}}) - b(E_{\boldsymbol{q}-\boldsymbol{k}} + E_{\boldsymbol{k}})\right]. \tag{2.79c}$$

$\gamma_{2a}^{\mathrm{Che}}(\boldsymbol{k})$ and $\gamma_{2b}^{\mathrm{Che}}(\boldsymbol{k})$ respectively describe Cherenkov processes in which one magnon with energy $E_{\boldsymbol{k}}$ absorbs or emits a phonon with energy $\omega_{\boldsymbol{q}\lambda}$ and decays into a magnon with energy $E_{\boldsymbol{k}\pm\boldsymbol{q}}$. On the other hand, the last term $\gamma_2^{\mathrm{con}}(\boldsymbol{k})$ arises due to the confluence of two magnons with energies $E_{\boldsymbol{k}}$ and $E_{\boldsymbol{q}-\boldsymbol{k}}$ into one phonon with energy $\omega_{\boldsymbol{q}\lambda}$. These three types of damping mechanisms are depicted graphically as Feynman diagrams in Fig. 2.4. Since we are interested in room temperature physics, it is also permissible to approximate the Bose functions by their high temperature limit, $b(\omega) \approx T/\omega$, yielding

$$\gamma_{2a}^{\mathrm{Che}}(\boldsymbol{k}) = \frac{\pi T E_{\boldsymbol{k}}}{2MN}\sum_{\boldsymbol{q}\lambda} \frac{|\Gamma^{\bar{\beta}\beta}_{\boldsymbol{k},\boldsymbol{k}+\boldsymbol{q},\lambda}|^2}{E_{\boldsymbol{k}+\boldsymbol{q}}\omega_{\boldsymbol{q}\lambda}^2} \delta\left(E_{\boldsymbol{k}} - E_{\boldsymbol{k}+\boldsymbol{q}} + \omega_{\boldsymbol{q}\lambda}\right), \tag{2.80a}$$

$$\gamma_{2b}^{\mathrm{Che}}(\boldsymbol{k}) = \frac{\pi T E_{\boldsymbol{k}}}{2MN}\sum_{\boldsymbol{q}\lambda} \frac{|\Gamma^{\bar{\beta}\beta}_{\boldsymbol{k},\boldsymbol{k}-\boldsymbol{q},\lambda}|^2}{E_{\boldsymbol{k}-\boldsymbol{q}}\omega_{\boldsymbol{q}\lambda}^2} \delta\left(E_{\boldsymbol{k}} - E_{\boldsymbol{k}-\boldsymbol{q}} - \omega_{\boldsymbol{q}\lambda}\right), \tag{2.80b}$$

$$\gamma_2^{\mathrm{con}}(\boldsymbol{k}) = \frac{\pi T E_{\boldsymbol{k}}}{2MN}\sum_{\boldsymbol{q}\lambda} \frac{|\Gamma^{\beta\beta}_{\boldsymbol{k},\boldsymbol{q}-\boldsymbol{k},\lambda}|^2}{E_{\boldsymbol{q}-\boldsymbol{k}}\omega_{\boldsymbol{q}\lambda}^2} \delta\left(E_{\boldsymbol{k}} + E_{\boldsymbol{q}-\boldsymbol{k}} - \omega_{\boldsymbol{q}\lambda}\right). \tag{2.80c}$$

In the thermodynamic limit $\frac{1}{N}\sum_{\boldsymbol{k}} = \left(\frac{a}{2\pi}\right)^2 \int \mathrm{d}^2k$, above Eqs. (2.80) can be directly evaluated numerically. The results of such a numerical solution are

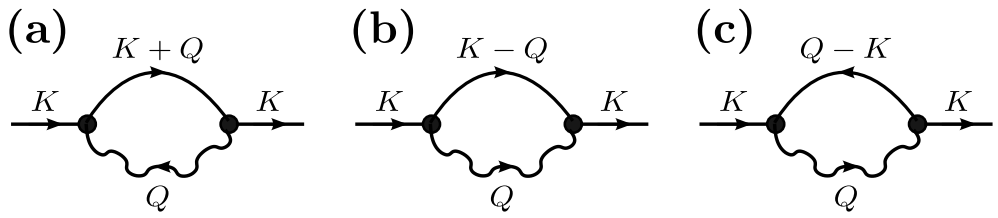

Figure 2.4: *The three Feynman diagrams generating the different contributions (2.79) to the magnon decay rate $\gamma_2(\boldsymbol{k})$: (a) Cherenkov process with absorption of a virtual phonon, (b) Cherenkov process with emission of a virtual phonon, and (c) confluent process. Solid and wavy directed lines respectively represent magnon and phonon Green functions, with the arrows pointing in the direction of the energy-momentum flow. Black dots denote the relevant components of the magnon-phonon scattering vertices $\boldsymbol{\Gamma}^{\bar{\beta}\beta}$ and $\boldsymbol{\Gamma}^{\beta\beta}$ defined in Eqs. (2.30).*

shown in Figs. 2.6 and 2.8 below[2]. However, for comparison it will also be instructive to obtain analytical estimates. In order to do so, we may employ the fact that the Bogoliubov transformation has only a small effect on the interaction vertices in YIG almost everywhere in the Brillouin zone. Thus we approximate in the following calculations

$$|\Gamma^{\bar{\beta}\beta}_{\boldsymbol{k},\boldsymbol{k}\pm\boldsymbol{q},\lambda}|^2 = |\boldsymbol{e}^*_{\boldsymbol{q}\lambda}\cdot\boldsymbol{\Gamma}^{\bar{\beta}\beta}_{\boldsymbol{k},\boldsymbol{k}\pm\boldsymbol{q}}|^2 \approx |\boldsymbol{e}^*_{\boldsymbol{q}\lambda}\cdot\boldsymbol{\Gamma}^{\bar{b}b}_{\boldsymbol{k},\boldsymbol{k}\pm\boldsymbol{q}}|^2 = |\boldsymbol{e}^*_{\boldsymbol{q}\lambda}\cdot\boldsymbol{U}_{\mp\boldsymbol{q}}|^2 \equiv |\boldsymbol{q}|^2 U^2_\lambda(\hat{\boldsymbol{q}}), \tag{2.81a}$$

$$|\Gamma^{\beta\beta}_{\boldsymbol{k},\boldsymbol{q}-\boldsymbol{k},\lambda}|^2 = |\boldsymbol{e}^*_{\boldsymbol{q}\lambda}\cdot\boldsymbol{\Gamma}^{\beta\beta}_{\boldsymbol{k},\boldsymbol{q}-\boldsymbol{k}}|^2 \approx |\boldsymbol{e}^*_{\boldsymbol{q}\lambda}\cdot\boldsymbol{\Gamma}^{bb}_{\boldsymbol{k},\boldsymbol{q}-\boldsymbol{k}}|^2 = |\boldsymbol{e}^*_{\boldsymbol{q}\lambda}\cdot\boldsymbol{V}_{-\boldsymbol{q}}|^2 \equiv |\boldsymbol{q}|^2 V^2_\lambda(\hat{\boldsymbol{q}}), \tag{2.81b}$$

where

$$U^2_\lambda(\hat{\boldsymbol{q}}) = \frac{B^2_\parallel}{S^2}\left|\boldsymbol{e}^*_{\boldsymbol{q}\lambda}\cdot(\hat{q}_x\boldsymbol{e}_x + \hat{q}_y\boldsymbol{e}_y - 2\hat{q}_z\boldsymbol{e}_z)\right|^2, \tag{2.82a}$$

$$V^2_\lambda(\hat{\boldsymbol{q}}) = \frac{B^2_\parallel}{S^2}\left|\boldsymbol{e}^*_{\boldsymbol{q}\lambda}\cdot(\hat{q}_x\boldsymbol{e}_x - \hat{q}_y\boldsymbol{e}_y)\right|^2 + \frac{B^2_\perp}{S^2}\left|\boldsymbol{e}^*_{\boldsymbol{q}\lambda}\cdot(\hat{q}_x\boldsymbol{e}_y + \hat{q}_y\boldsymbol{e}_x)\right|^2. \tag{2.82b}$$

Here we defined the unit vector in $\boldsymbol{q}$-direction, $\hat{\boldsymbol{q}} = \boldsymbol{q}/|\boldsymbol{q}|$, with Cartesian components $\hat{q}_\alpha = \hat{\boldsymbol{q}}\cdot\boldsymbol{e}_\alpha$. Using the phonon polarization basis (1.32) for the thin film geometry, we explicitly find[3]

$$U^2_\parallel(\hat{\boldsymbol{q}}) = \frac{B^2_\parallel}{S^2}\left(\hat{q}_y^2 - 2\hat{q}_z^2\right)^2 = \frac{B^2_\parallel}{S^2}\left(1 - 3\cos^2\theta_{\boldsymbol{q}}\right)^2, \tag{2.83a}$$

$$U^2_{\perp 1}(\hat{\boldsymbol{q}}) = \frac{B^2_\parallel}{S^2}\left(3\hat{q}_y\hat{q}_z\right)^2 = \frac{B^2_\parallel}{S^2}\frac{9}{4}\sin^2(2\theta_{\boldsymbol{q}}), \tag{2.83b}$$

$$U^2_{\perp 2}(\hat{\boldsymbol{q}}) = 0, \tag{2.83c}$$

[2]For the numerical evaluation of the integrals on Dirac delta distributions appearing in Eqs. (2.80), the triangle integration scheme outlined in App. A.3 is used.

[3]Note that $q_x = 0$ in the thin film geometry, as discussed in Sec. 1.2.4.

and

$$V_{\parallel}^2(\hat{\boldsymbol{q}}) = \frac{B_{\parallel}^2}{S^2}\hat{q}_y^4 = \frac{B_{\parallel}^2}{S^2}\sin^4\theta_{\boldsymbol{q}}, \tag{2.84a}$$

$$V_{\perp 1}^2(\hat{\boldsymbol{q}}) = \frac{B_{\parallel}^2}{S^2}\left(\hat{q}_y\hat{q}_z\right)^2 = \frac{B_{\parallel}^2}{S^2}\frac{1}{4}\sin^2\left(2\theta_{\boldsymbol{q}}\right), \tag{2.84b}$$

$$V_{\perp 2}^2(\hat{\boldsymbol{q}}) = \frac{B_{\perp}^2}{S^2}\hat{q}_y^2 = \frac{B_{\perp}^2}{S^2}\sin^2\theta_{\boldsymbol{q}}, \tag{2.84c}$$

where we set $\hat{q}_z = \cos\theta_{\boldsymbol{q}}$, and $\hat{q}_y = \sin\theta_{\boldsymbol{q}}$.

2.7.1 Dipolar regime: Theory

The dipolar regime is the long-wavelength region in $\boldsymbol{k}$-space around the minima of the magnon dispersion (2.12), where said dispersion deviates significantly from the $\boldsymbol{k}^2$-behavior of exchange-dominated magnons, i.e., where $|\boldsymbol{k}| \lesssim \sqrt{\Delta/\rho_s}$. As can be clearly seen from Fig. 2.1, the magnon dispersion is, compared to the phonon ones, very flat in a substantial region around the dispersion minima. Therefore the magnitude of the magnon velocity $\boldsymbol{v}(\boldsymbol{k}) = \nabla_{\boldsymbol{k}} E_{\boldsymbol{k}}$ is small compared to the sound velocities c_λ, allowing to obtain reasonable results in an expansion in the small parameter $|\boldsymbol{v}(\boldsymbol{k})|/c_\lambda$. However, note that for very small momenta, there is a momentum space region with $|\boldsymbol{v}(\boldsymbol{k})| > c_\lambda$, where we expect such an expansion to break down. This region where the magnon velocity exceeds the sound velocities is shown in Fig. 2.5.

To analytically evaluate the damping rates (2.80) for momenta $\boldsymbol{k}$ close the dispersion minima, we thus expand

$$E_{\boldsymbol{k}+\boldsymbol{q}} \approx E_{\boldsymbol{k}} + \boldsymbol{q}\cdot\boldsymbol{v}(\boldsymbol{k}). \tag{2.85}$$

Then the energy conserving Dirac deltas of the Cherenkov processes (2.80a) and (2.80b) become

$$\begin{aligned}\delta\left(E_{\boldsymbol{k}} - E_{\boldsymbol{k}\pm\boldsymbol{q}} \pm \omega_{\boldsymbol{q}\lambda}\right) \approx& \delta\left(\pm c_\lambda|\boldsymbol{q}|\left[1 - \hat{\boldsymbol{q}}\cdot\frac{\boldsymbol{v}(\boldsymbol{k})}{c_\lambda}\right]\right)\\ =& \frac{\delta\left(|\boldsymbol{q}|\right)}{|1 - \hat{\boldsymbol{q}}\cdot\boldsymbol{v}(\boldsymbol{k})/c_\lambda|},\end{aligned} \tag{2.86}$$

where we used in the second line that $|\boldsymbol{v}(\boldsymbol{k})|/c_\lambda < 1$ in this regime. From above Eq. (2.86) it immediately follows that the Cherenkov damping processes are kinematically suppressed in the momentum region around the dispersion minima, i.e.,

$$\gamma_{2a}^{\mathrm{Che}}(\boldsymbol{k}) = 0 = \gamma_{2b}^{\mathrm{Che}}(\boldsymbol{k}), \tag{2.87}$$

since an acoustic phonon cannot carry zero momentum. Therefore the magnon damping rate is dominated by the confluent damping process (2.80c) in the

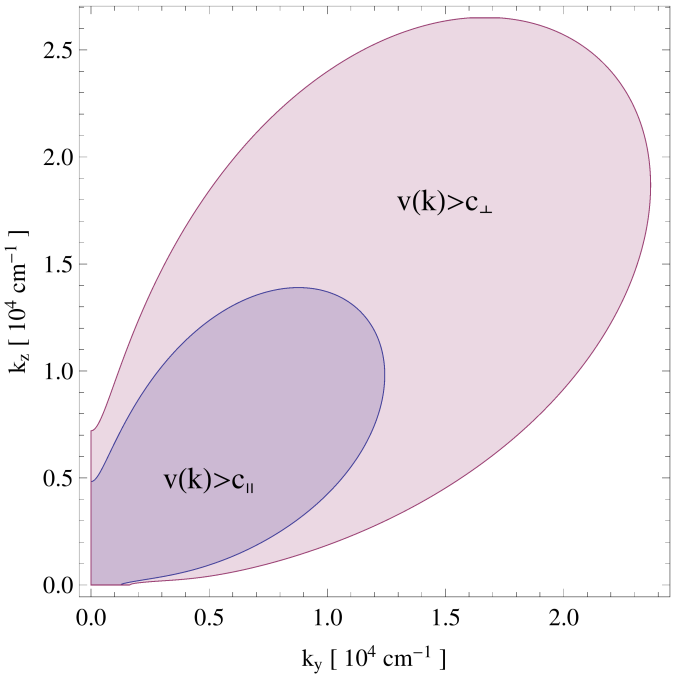

Figure 2.5: *In the shaded areas the group velocity* $v(\boldsymbol{k}) = |\boldsymbol{v}(\boldsymbol{k})|$ *of the magnons exceeds either the longitudinal or the transverse sound velocity. The plot is for a YIG film with thickness* $d = 6.7\,\mu\mathrm{m}$ *in an external magnetic field* $H_0 = 1710\,\mathrm{Oe} \times \mu$.

dipolar regime. For this confluent process, we have to evaluate the energy conservation

$$\begin{aligned}\delta\left(E_{\boldsymbol{k}} + E_{\boldsymbol{q}-\boldsymbol{k}} - \omega_{\boldsymbol{q}\lambda}\right) \approx& \delta\left(2E_{\boldsymbol{k}} - c_\lambda|\boldsymbol{q}|\left[1 + \hat{\boldsymbol{q}}\cdot\frac{\boldsymbol{v}(\boldsymbol{k})}{c_\lambda}\right]\right)\\ =& \frac{|\boldsymbol{q}|}{2E_{\boldsymbol{k}}}\delta\left(|\boldsymbol{q}| - \frac{2E_{\boldsymbol{k}}}{c_\lambda}\frac{1}{1+\hat{\boldsymbol{q}}\cdot\boldsymbol{v}(\boldsymbol{k})/c_\lambda}\right).\end{aligned} \tag{2.88}$$

With above Eq. 2.88) we can carry out the integration on $|\boldsymbol{q}|$ in the expression (2.80c) for the confluent damping rate, yielding

$$\gamma_2^{\mathrm{con}}(\boldsymbol{k}) = \frac{TE_{\boldsymbol{k}}}{2M}\sum_\lambda \frac{a^2}{c_\lambda^2}\int_0^{2\pi}\frac{\mathrm{d}\theta_{\boldsymbol{q}}}{2\pi}\,\frac{V_\lambda^2(\hat{\boldsymbol{q}})}{1-[\hat{\boldsymbol{q}}\cdot\boldsymbol{v}(\boldsymbol{k})/c_\lambda]^2} \tag{2.89a}$$

$$= \frac{TE_{\boldsymbol{k}}}{2M}\sum_\lambda \frac{a^2}{c_\lambda^2}\int_0^{2\pi}\frac{\mathrm{d}\theta_{\boldsymbol{q}}}{2\pi}\,V_\lambda^2(\hat{\boldsymbol{q}})\left[1 + \left(\hat{\boldsymbol{q}}\cdot\frac{\boldsymbol{v}(\boldsymbol{k})}{c_\lambda}\right)^2\right], \tag{2.89b}$$

where we expanded the denominator to the first nonvanishing order in $|\boldsymbol{v}(\boldsymbol{k})|/c_\lambda$ in the second line. The remaining angular integration in above Eq. (2.89b) is only on powers of trigonometric functions and can thus be carried

out easily, yielding the confluent damping to second order in $|\boldsymbol{v}(\boldsymbol{k})|/c_\lambda$,

$$\gamma_2^{\mathrm{con}}(\boldsymbol{k}) = \frac{TE_{\boldsymbol{k}}}{4S^2}\frac{a^2}{M}\left[\frac{B_\perp^2}{c_\perp^4}\left(1+\frac{3}{4}\frac{v_y^2(\boldsymbol{k})}{c_\perp^2}+\frac{v_z^2(\boldsymbol{k})}{4c_\perp^2}\right)+\frac{B_\parallel^2}{4c_\perp^4}\left(1+\frac{v_y^2(\boldsymbol{k})}{2c_\perp^2}+\frac{v_z^2(\boldsymbol{k})}{2c_\perp^2}\right)\right.$$
$$\left.+\frac{3}{4}\frac{B_\parallel^2}{c_\parallel^4}\left(1+\frac{5}{6}\frac{v_y^2(\boldsymbol{k})}{c_\parallel^2}+\frac{v_z^2(\boldsymbol{k})}{6c_\parallel^2}\right)\right]. \tag{2.90}$$

The analytical approximation (2.90) to the confluent contribution of the high temperature damping rate is shown as a thin dotted red line in Fig. 2.6, whereas the direct numerical evaluation of Eq. (2.80c) for the confluent damping process is shown as a thick red dotted line. Note that both agree very well in the region around the minima of the magnon dispersion where our approximations are valid. The Cherenkov damping rate calculated numerically from Eqs. (2.80a) and (2.80b) is displayed as a thick dashed green line. As expected by our analytical approximation, the Cherenkov processes only contribute for small momenta and vanish in the regime where the magnon dispersion is flat, i.e., where $|\boldsymbol{v}(\boldsymbol{k})| < c_\lambda$ (compare also Fig. 2.5). The total damping due to magnetoelastic interaction processes is shown as a thick blue line. Similar to the magnon dispersion, the damping in the dipolar regime depends only weakly on momentum, apart from the enhancement for small momenta $k \lesssim 2\times10^4\,\mathrm{cm}^{-1}$.

2.7.2 Dipolar regime: Experiment

For comparison, we also provide a measurement of the damping rate in the dipolar regime. However, one should keep in mind that our theoretical predictions of Sec. 2.7.1 only take the (comparatively weak, see [3]) magnon-phonon interactions into account. A measurement on the other hand necessarily contains all channels of magnon damping, such as magnon-magnon interactions and elastic magnon-impurity scattering. Therefore our calculation can only give a lower bound to the total damping rate measured in an actual experiment. As it turns out, our measurement results, presented in Fig. 2.7 below, reveal that magnon-phonon interactions are not the dominant source of magnon decay in the dipolar regime.

The relaxation time of magnons was obtained experimentally by measuring the spectral distribution of the density of the magnon gas as a function of frequency and momentum, using time- and wave-vector-resolved BLS spectroscopy [75] (see also App. A.2). For technical reasons, only in-plane momenta up to $k_z^{\max} = 11\times10^4\,\mathrm{cm}^{-1}$ are accessible with the experimental apparatus. Therefore the measurement is restricted to the long-wavelength dipolar part of the magnon spectrum. The YIG film employed in the measurement had a thickness of $6.7\,\mu$m, and was liquid-phase epitaxialy grown on a $500\,\mu$m thick gallium gadolinium garnet substrate, and a bias magnetic field of $H_0 = 1710\,\mathrm{Oe}$ was applied.

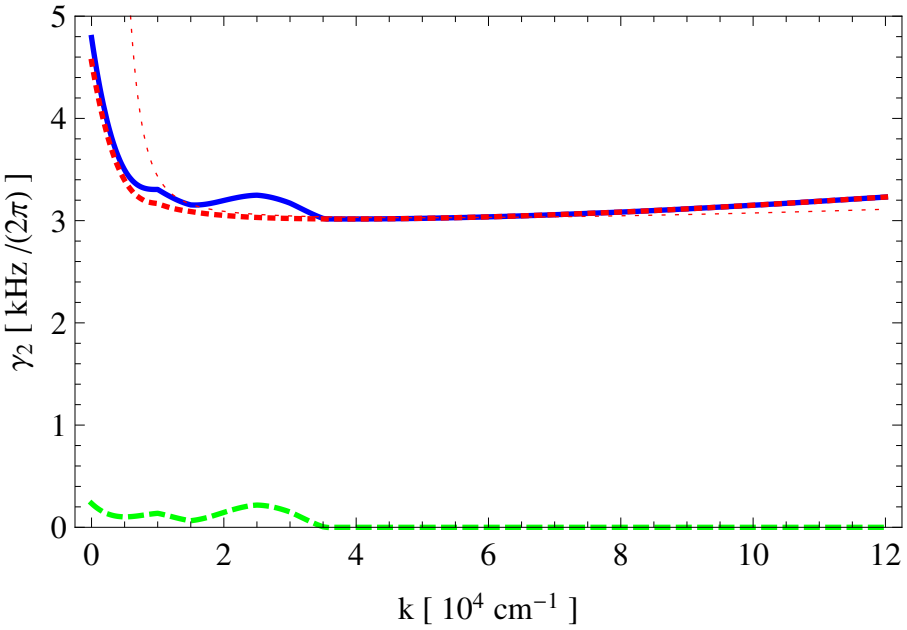

Figure 2.6: *Numerical evaluation of the magnon damping rates (2.80) for a YIG film at temperature $T = 300\,\mathrm{K}$, in the dipolar momentum regime. The plot is for a film with thickness $d = 6.7\,\mu\mathrm{m}$ in an external magnetic field $H_0 = 1710\,\mathrm{Oe} \times \mu$, for momenta $\boldsymbol{k} = k\boldsymbol{e}_z$ parallel to the in-plane magnetic field. The solid blue line corresponds to the total damping rate, while the dashed green and dotted red lines respectively represent the contributions from the Cherenkov and the confluent processes. The thin dotted red line is the approximation (2.90) for the confluent damping rate in the dipolar momentum regime.*

In order to populate the magnon spectrum, the technique of parametric pumping [13] described in Sec. 1.2.5 was used to inject magnons at the pumping frequency $\omega_\mathrm{p} = \pi \times 13.62\,\mathrm{GHz}$. This pumping frequency was tuned such that the parametric magnons were excited at the ferromagnetic resonance frequency, so that direct transitions to the bottom of the magnon spectrum are forbidden by conservation laws. Thereby high efficiency of the multistage two-body magnon-magnon scattering necessary for thermalization and thus population of the magnon spectrum is ensured. This procedure is also known as intensive thermalization [15, 20, 76].

The redistribution of thermalized magnons along the fundamental backward-volume magnetostatic spin wave mode was measured as a function of time and momentum. After the pumping was switched off, the magnons relaxed freely to thermal equilibrium. The total damping rate γ_tot of dipolar magnons as a function of the in-plane momentum k_z shown in Fig. 2.7 was then obtained by exponential fitting of the relaxation time of different groups of thermalized magnons. Comparing to the theoretical prediction for

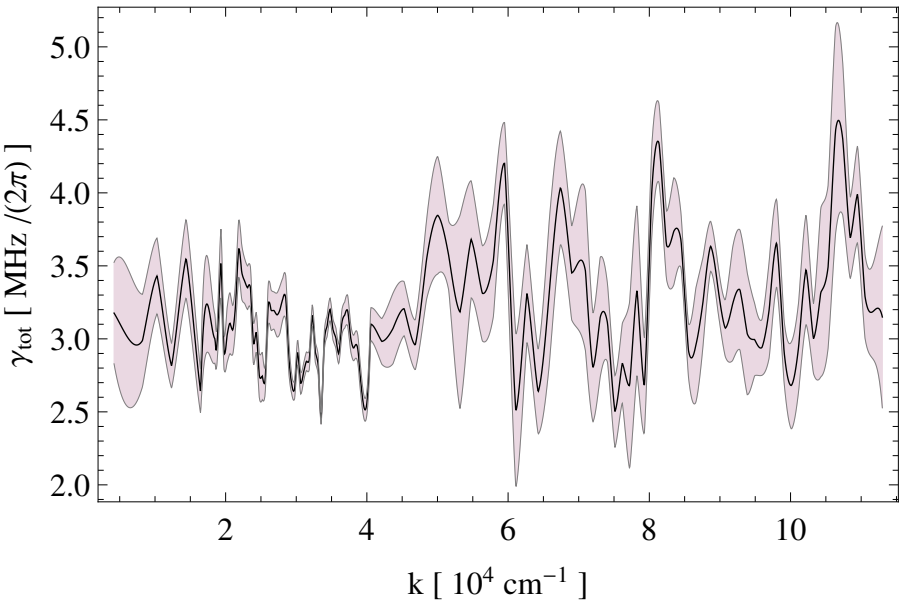

Figure 2.7: *Experimentally determined dependence of the total magnon damping rate γ_{tot} on the in-plane momentum in the dipolar momentum regime, in which the magnon dispersion is dominated by the competition between the dipole-dipole and exchange interactions. The shaded regions represent the estimated experimental uncertainties.*

the damping rate due to spin-phonon interactions displayed in Fig. 2.6, we see that the total damping is roughly three orders of magnitude larger. Thus, we conclude that other relaxation channels than magnon-phonon scattering, in particular magnon-magnon scattering (see Refs. [3, 79, 80, 81, 82, 83]), dominate the magnon damping in the dipolar momentum regime at room temperature. Also, note that the momentum dependence of the measured total damping presented in Fig. 2.7 is rather irregular, suggesting that impurity scattering might play an important role in this regime. However, taking into account the tolerance limits of the experiment, shown by the shaded region in Fig. 2.7, the total damping rate has only a weak dependence on the in-plane momenta in the entire experimentally accessible range. In this respect, the experimental result agrees with our theoretical prediction of the damping rate due to magnetoelastic interaction processes displayed in Fig. 2.6, which also shows only weak momentum dependence in this regime.

A more complete theoretical calculation of the damping rates at room temperature, taking magnon-magnon and magnon-impurity scattering microscopically into account, is unfortunately not yet available for the momentum range that has been investigated experimentally. On the other hand, let us emphasize that while other scattering channels might dominate the magnon decay at room temperature, the equilibration of the temperatures of the magnon and

the phonon subsystems, which we initially set out to explore, is governed solely by the magnetoelastic interaction processes.

2.7.3 Exchange regime

For short-wavelength magnons with $\|\boldsymbol{k}| \gg \sqrt{\Delta/\rho_s}$, the contribution of dipole-dipole interactions to the magnon dispersion (2.12) becomes negligible compared to the exchange contribution. In this regime we may therefore approximate

$$E_{\boldsymbol{k}} \approx H_0 + \frac{\boldsymbol{k}^2}{2m_s}, \tag{2.91}$$

where we defined the effective mass $m_s = 1/(2\rho_s)$ of exchange-magnons.

The exchange approximation (2.91) for the magnon dispersion considerably simplifies the evaluation of the damping rate integrals (2.80). It is then convenient to parametrize the angle dependence of the unit vector in direction of the momentum transfer $\boldsymbol{q}$ as

$$\hat{\boldsymbol{q}}_\varphi = [\hat{v}_y(\boldsymbol{k})\cos\varphi - \hat{v}_z(\boldsymbol{k})\sin\varphi]\,\boldsymbol{e}_y + [\hat{v}_z(\boldsymbol{k})\cos\varphi + \hat{v}_y(\boldsymbol{k})\sin\varphi]\,\boldsymbol{e}_z. \tag{2.92}$$

Here $\hat{v}_\alpha(\boldsymbol{k}) = \hat{\boldsymbol{v}}(\boldsymbol{k})\cdot\boldsymbol{e}_\alpha$ are the Cartesian components of the unit vector in direction of the magnon velocity, which is in the exchange approximation explicitly given by

$$\boldsymbol{v}(\boldsymbol{k}) = v(\boldsymbol{k})\hat{\boldsymbol{v}}(\boldsymbol{k}) = \nabla_{\boldsymbol{k}} E_{\boldsymbol{k}} \approx \frac{\boldsymbol{k}}{m_s}. \tag{2.93}$$

The energy conserving Dirac deltas of the Cherenkov damping rates (2.80a) and (2.80b) can thus be evaluated analytically,

$$\begin{aligned}\delta\left(E_{\boldsymbol{k}} - E_{\boldsymbol{k}\pm\boldsymbol{q}} \pm \omega_{\boldsymbol{q}\lambda}\right) \approx& \delta\left(\frac{\boldsymbol{q}^2}{2m_s} \mp |\boldsymbol{q}|\left[c_\lambda - v(\boldsymbol{k})\cos\varphi\right]\right)\\ =& \frac{\delta(|\boldsymbol{q}|)}{|c_\lambda - v(\boldsymbol{k})\cos\varphi|} + \frac{2m_s}{|\boldsymbol{q}|}\delta\left(|\boldsymbol{q}| \mp 2m_s\left[c_\lambda - v(\boldsymbol{k})\cos\varphi\right]\right).\end{aligned} \tag{2.94}$$

Therefore the integral on $|\boldsymbol{q}|$ can be directly performed, yielding the Cherenkov damping rate

$$\begin{aligned}\gamma_2^{\mathrm{Che}}(\boldsymbol{k}) \equiv& \gamma_{2a}^{\mathrm{Che}}(\boldsymbol{k}) + \gamma_{2b}^{\mathrm{Che}}(\boldsymbol{k})\\ =& \frac{TE_{\boldsymbol{k}}}{2}\frac{m_s}{M}\sum_\lambda \frac{a^2}{c_\lambda^2}\int_0^{2\pi}\frac{\mathrm{d}\varphi}{2\pi}\,\frac{U_\lambda^2(\hat{\boldsymbol{q}}_\varphi)}{E_{\boldsymbol{k}} + 2m_s c_\lambda\left[c_\lambda - v(\boldsymbol{k})\cos\varphi\right]}.\end{aligned} \tag{2.95}$$

Although the remaining angular integral in the above Eq. (2.95) can in principle be carried out analytically, the resulting expression is quite cumbersome and not very transparent, and will consequently not be stated here. Instead, we show the results of numerically integrating the Cherenkov damping rate

(2.95) as a thin dashed green line in Fig. 2.8. For comparison, we also integrated Eqs. (2.80a) and (2.80b) for the Cherenkov damping rate directly, displayed as a thick dashed green line in the same Fig. 2.8. For the confluent damping rate (2.80c), the energy conserving Dirac delta can also be evaluated analytically in the exchange approximation,

$$\begin{aligned}\delta\left(E_{\boldsymbol{k}}+E_{\boldsymbol{q}-\boldsymbol{k}}-\omega_{\boldsymbol{q}\lambda}\right)\approx&\delta\left(\frac{\boldsymbol{q}^2}{2m_s}-|\boldsymbol{q}|\left[c_\lambda+v(\boldsymbol{k})\cos\varphi\right]-2E_{\boldsymbol{k}}\right)\\=&\frac{\Theta\left[|c_\lambda+v(\boldsymbol{k})\cos\varphi|-\sqrt{\frac{4E_{\boldsymbol{k}}}{m_s}}\right]}{\sqrt{\left[c_\lambda+v(\boldsymbol{k})\cos\varphi\right]^2-\frac{4E_{\boldsymbol{k}}}{m_s}}}\\&\times\left[\delta\left(|\boldsymbol{q}|-q_+\right)+\delta\left(|\boldsymbol{q}|-q_-\right)\right],\end{aligned}\tag{2.96}$$

where

$$q_\pm=m_s\left[c_\lambda+v(\boldsymbol{k})\cos\varphi\right]\pm m_s\sqrt{\left[c_\lambda+v(\boldsymbol{k})\cos\varphi\right]^2-\frac{4E_{\boldsymbol{k}}}{m_s}}.\tag{2.97}$$

Thus, after carrying out the $|\boldsymbol{q}|$-integration, we obtain for the confluent damping rate

$$\begin{aligned}\gamma_2^{\mathrm{con}}(\boldsymbol{k})=&\frac{TE_{\boldsymbol{k}}}{4}\frac{a^2}{M}\sum_\lambda\int_0^{2\pi}\frac{\mathrm{d}\varphi}{2\pi}\,\frac{V_\lambda^2(\hat{\boldsymbol{q}}_\varphi)}{c_\lambda^3}\,\frac{\Theta\left[|c_\lambda+v(\boldsymbol{k})\cos\varphi|-\sqrt{\frac{4E_{\boldsymbol{k}}}{m_s}}\right]}{\sqrt{\left[c_\lambda+v(\boldsymbol{k})\cos\varphi\right]^2-\frac{4E_{\boldsymbol{k}}}{m_s}}}\\&\times\left[\frac{c_\lambda q_+}{c_\lambda q_+-E_{\boldsymbol{k}}}+\frac{c_\lambda q_-}{c_\lambda q_--E_{\boldsymbol{k}}}\right].\end{aligned}\tag{2.98}$$

Again, we integrated both Eq. (2.80c) for the confluent damping rate and the corresponding exchange approximation (2.98) numerically, with the results respectively being shown as the thick and thin dotted red lines in Fig. 2.8. Finally, the sum of Cherenkov and confluent damping rates, i.e., the total damping rate due to magnetoelastic interactions, in the exchange regime is also presented in Fig. 2.8, with the thick blue line being the result of direct numerical integration of the original expressions (2.80), and the thin blue line the corresponding exchange approximations (2.95) and (2.98). Note that our exchange approximation captures both qualitative and quantitative behavior of the exact results very well. One can also clearly see that the magnon damping rate is strongly momentum dependent, with peaks in the vicinity of the crossing points of magnon and phonon dispersions as well as velocities. From dipolar long-wavelength to exchange short-wavelength regimes, respectively dominated by confluent and Cherenkov processes, the damping even increases by two orders of magnitude. For the magnon lifetime $\tau(\boldsymbol{k})=1/\gamma(\boldsymbol{k})$ due to magnon-phonon interactions, i.e., the spin-lattice relaxation time, this implies values of the order of $50\,\mu$s in the dipolar momentum range, while it can be as low as 480 ns for exchange momenta.

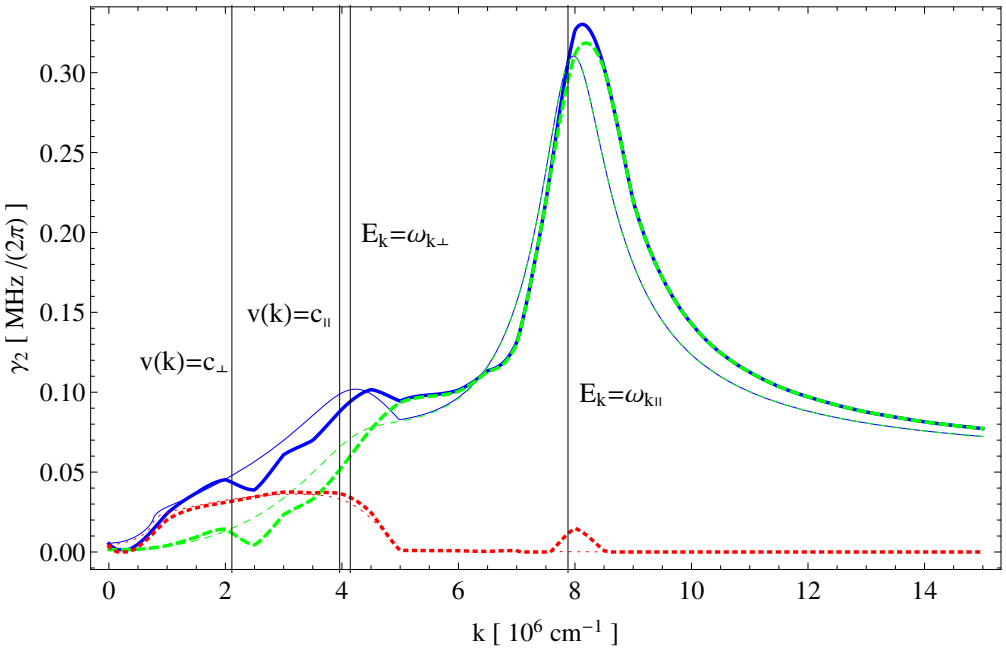

Figure 2.8: *Numerical evaluation of the magnon damping rates (2.80) for a YIG film at temperature $T = 300\,\mathrm{K}$, in the exchange momentum regime. The plot is for a film with thickness $d = 6.7\,\mu\mathrm{m}$ in an external magnetic field $H_0 = 1710\,\mathrm{Oe}\times\mu$, for momenta $\boldsymbol{k} = k\boldsymbol{e}_z$ parallel to the in-plane magnetic field. Solid blue lines correspond to the total damping rate, while the dashed green and dotted red lines respectively represent the contributions from the Cherenkov and the confluent processes. The corresponding thin lines are the approximations (2.95) and (2.98) in the exchange momentum regime.*

2.8 Summary and conclusions

In this chapter, we have studied the effect of lattice vibrations on the magnon degrees of freedom in experimentally relevant thin films of the magnetic insulator YIG. To correctly describe the coupling of magnons to phonons in YIG, we have followed a semiphenomenological approach relying on the quantization of a suitably chosen classical magnetoelastic energy [3, 29, 30, 31, 32]. This was necessary because there is no microscopic spin model which can take the dominant, relativistic sources of magnetoelastic coupling in collinear magnets like YIG into account [3]. Starting from the properly quantized magnetoelastic energy, we have then carefully derived the momentum dependence of the magnon-phonon interaction vertices to leading order in the conventional $1/S$ expansion for ordered quantum spin systems. With these vertices, both the magnetoelastic hybridization and the damping rate of magnons due to magnon-phonon interactions have been computed to leading order in $1/S$. It has been demonstrated that the hybridization coupling gives rise to a distinct minimum in the experimentally observable transverse dynamic spin structure

factor, where spectral weight is transferred from the magnons to the transverse phonon mode. The position of this minimum quantitatively agrees with a recent observation of the transverse magnetoelastic mode by the group of B. Hillebrands [84].

The calculated magnon damping rate at room temperature has turned out to be strongly dependent on the magnon momentum. In the long-wavelength dipolar regime, the magnon damping rate is rather flat and almost exclusively driven by confluent processes, in which two magnons decay into on phonon or vice versa. For this regime, we have also presented the total magnon damping rate, which we have extracted from time- and wave-vector resolved BLS spectroscopy measurements performed in the group of B. Hillebrands. Comparison of theoretical prediction and actual measurement reveals that magnon-phonon scattering is not the dominant magnon relaxation channel in YIG at room temperature, since the measured damping rate is roughly three orders of magnitude larger than the computed one. However, the irregular behavior of the measured total damping rate has lead us to suggest elastic scattering of magnons from impurities is a major source of magnon damping. In the short-wavelength exchange regime on the other hand, the calculated magnon damping is dominated by magnon number conserving Cherenkov scattering and displays a strong dependence on momentum, with pronounced peaks close to the crossings of magnon and phonon velocities and energy dispersions. Also, the damping rate in the short-wavelength exchange regime is two orders of magnitude larger than in the long-wavelength dipolar regime. Since in contrast to the overall damping of magnons, the equilibration of magnon and phonon temperatures is determined solely by the magnetoelastic interactions considered in this work, this agrees very well with the conclusion of the experiment by Agrawal *et al.*, reported in Ref. [14]. There the authors speculated that for their results to be compatible with prior experiments on the spin Seebeck effect [73], the spin-lattice relaxation in the dipolar momentum regime should be much slower than in the exchange regime. Our theoretical calculation of the magnon-phonon damping proves that this is indeed the case.

To conclude this chapter, let us remark that there are two obvious ways to extend the present work: On the theoretical side, the damping rate of dipolar magnons due to other relaxation channels, like spin-spin interactions or elastic impurity scattering, could be computed. This should allow us to identify the dominant relaxation mechanism in this regime and to reproduce the measured damping rate of Fig. 2.7 not only qualitatively but also quantitatively. In this context, let us note that spontaneous decay of $\boldsymbol{k} = 0$ magnons in YIG due to magnon-magnon interactions in high-magnetic fields has been considered recently by Chernyshev [83]. On the experimental side, it would be useful to extend the measurements of the magnon relaxation to the short-wavelength exchange regime, so that a comparison to the theoretical prediction shown in Fig. 2.8 would become possible.

Chapter 3

Rayleigh-Jeans condensation of pumped magnons

3.1 Motivation and outline

In the last decade, the nonequilibrium time evolution of magnons in thin YIG films and at room temperature has been in the focus of many experimental studies [15, 16, 17, 18, 19, 20, 21, 22, 23, 24]. In the seminal experiment [15], the magnon gas was subjected to parametric pumping (see Sec. 1.2.5), which employs a parametric instability mechanism to inject magnons with well-defined energy and momentum into the system. The nonequilibrium time evolution of these excess magnons was then studied by means of frequency-resolved BLS spectroscopy. It was found that the overpopulated magnon gas thermalizes to a quasiequilibrium state with finite chemical potential. For sufficient pumping powers, this chemical potential attained its maximal value given by the minimum energy of the magnons. At this point, an additional, sharply peaked contribution at the bottom of the magnon spectrum appeared: A magnon condensate had formed. As magnons are bosons, this condensation was immediately interpreted as Bose-Einstein condensation (BEC) [85] of magnons at room temperature. Numerous experiments have since then confirmed the existence and extended our knowledge of this nonequilibrium magnon condensation phenomenon [16, 17, 18, 19, 20, 21, 22, 23, 24]. In particular, using time- and wave-vector-resolved BLS spectroscopy ([75], see also App. A.2) it has become possible to directly observe the nonequilibrium magnon dynamics in momentum space.

These discoveries renewed the interest in parametrically pumped magnon gases and sparked many theoretical works on magnon condensation [8, 9, 10, 11, 12, 76, 86, 87, 88, 89, 90]. However, until now none of these theories was able to give a completely satisfactory theoretical description of the nonequilibrium time evolution and eventual condensation of magnons. While the so-called S-theory [37, 38, 39, 91], originally developed in the 1960's and 70's, and its extensions [9, 10, 11, 92, 93, 94] are able to satisfactorily describe the growth

and subsequent saturation of the parametrically excited magnons, it does take the magnon-magnon interactions into account only on a mean field level; consequently it cannot describe the cascade of relaxation processes leading to the formation of a magnon condensate. In contrast, theories focusing on the condensation usually ignore the pumping dynamics and start out from some given quasiequilibrium state that can be identified with the ground state of some effective quantum mechanical Hamiltonian [8, 12, 86, 88, 89]. Phenomenological approaches of the Ginzburg-Landau type have also been employed to study condensate dynamics [87]. Finally, theories dealing with the relaxation processes and kinetics of excited magnons so far did not include the possibility of a genuine magnon condensation [76, 90, 95, 96, 97].

In this chapter, we follow a radically different approach: We set out from the observation that at room temperature, the magnons are actually classical waves rather than quantum mechanical particles. Consequently, we derive a non-Markovian stochastic Landau-Lifshitz-Gilbert equation (LLG), which is an equation of motion for the classical spin vector and contains thermal noise originating from microscopic spin-lattice interactions. Performing simulations of the stochastic time evolution generated by this LLG equation, we are then able to accurately reproduce all experimentally observed stages of the nonequilibrium magnon time evolution, including the formation of a magnon condensate. However, as we are dealing only with classical waves, this condensate cannot be a BEC, which is a macroscopic manifestation of quantum mechanics. Instead, we use our simulations to reinterpret the condensation observed in the experiments [15, 16, 17, 18, 19, 20, 21, 22, 23, 24] as a form of classical kinetic condensation [98, 99, 100], which we refer to as Rayleigh-Jeans condensation [101].

The work presented in this chapter was done together with Peter Kopietz, and the main results were published in [P3].

The remainder of this chapter is organized as follows: The introductory part is concluded by Sec. 3.1.1, where the question whether magnons in YIG at room temperature should be regarded as classical or quantum objects is discussed in more detail, and Sec. 3.1.2, in which we introduce the basic concept and mechanism of Rayleigh-Jeans condensation. In Sec. 3.2 we then derive the aforementioned LLG equation, starting from a microscopic Hamiltonian, which includes parametric pumping, and spin-spin as well as spin-phonon interactions. Following that, we will use a spin wave approach in Sec. 3.3 to obtain an equation of motion for the magnon normal modes, within a reasonable approximation. In Sec. 3.4 we then proceed to transform our non-Markovian LLG into a Langevin equation containing only Gaussian white noise in a formally exact manner, by introducing additional fields simulating the non-Markovian noise correlation. Then, in Sec. 3.5 we will explain the details of our numerical implementation, before presenting our simulation results

in the central Sec. 3.6. The final Sec. 3.7 serves to summarize and conclude this chapter.

3.1.1 Quantum or classical?

The quantum mechanical equilibrium distribution of magnons with energy $E_{\boldsymbol{k}}$ is the Bose-Einstein distribution,

$$b(E_{\boldsymbol{k}}) = \frac{1}{\exp\left(E_{\boldsymbol{k}}/T\right) - 1}. \tag{3.1}$$

However, the relevant energies $E_{\boldsymbol{k}}$ of long-wavelength magnons in YIG films are of the order of 0.25 K, which is three orders of magnitude smaller than the energy scale of room temperature $T = 300\,\mathrm{K}$. Consequently, it is permissible to expand the exponential in the denominator of the Bose function (3.1) to first order in the small parameter $E_{\boldsymbol{k}}/T$, yielding

$$b(E_{\boldsymbol{k}}) \approx \frac{T}{E_{\boldsymbol{k}}}. \tag{3.2}$$

But the high temperature limit (3.2) of the Bose function is nothing else than the Rayleigh-Jeans distribution, which is the equilibrium distribution function of classical waves. Starting out from a classical ensemble of waves, it can be obtained directly using the arguments of statistical mechanics, in particular the equipartition of energy [102]; see also App. B.1. Indeed, as shown in Fig. 3.1, at room temperature the quantum mechanical Bose-Einstein and the classical Rayleigh-Jeans distribution, Eqs. (3.1) and (3.2) respectively, are virtually indistinguishable for a wide range of momenta. Significant deviations appear only close to the Brillouin zone edge, which does not play any role in the experiments [15, 16, 17, 18, 19, 20, 21, 22, 23, 24] we aim to describe. Therefore, it seems reasonable to directly start from a classical wave theory in order to develop a theoretical foundation sufficient for explaining the room temperature experiments [15, 16, 17, 18, 19, 20, 21, 22, 23, 24].

Another indication that a classical theory is adequate for YIG at room temperature is the large effective spin $S \approx 14$. Quantum fluctuations in spin systems always scale with $1/S$[1]. Thus, for a large spin as in YIG, quantum fluctuations are in general negligible (or at most subdominant), and it is sufficient to retain only the classical dynamics.

3.1.2 Rayleigh-Jeans condensation

It is a not very well-known fact that completely classical waves may undergo a condensation transition completely analogous to the BEC of quantum systems [98, 99, 100]. There are only two very general requirements:

[1] This can, for example, be shown by setting up a proper quantum spin wave expansion [P1], or by considering the quantum corrections to the semiclassical (truncated Wigner) approximation for spin systems [46].

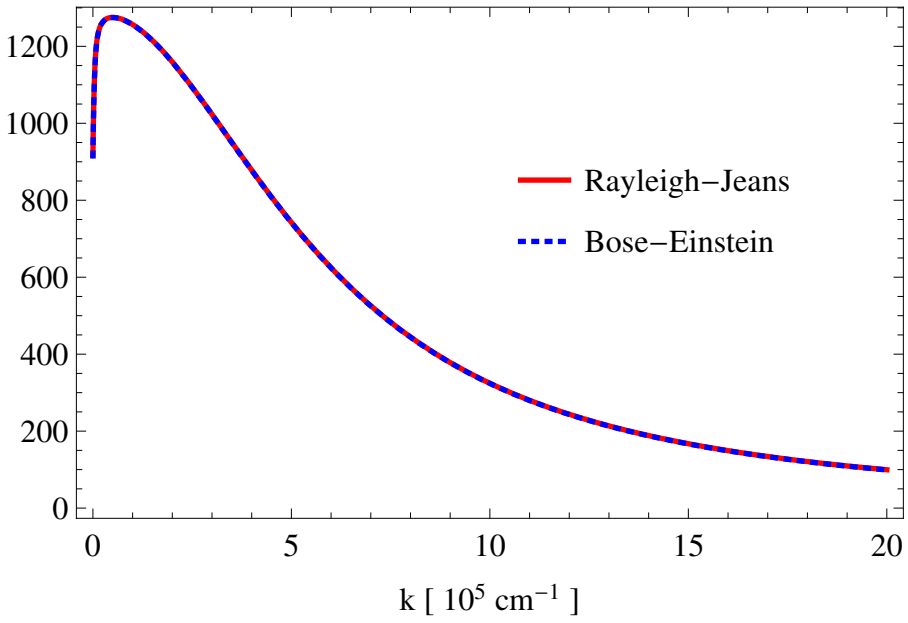

Figure 3.1: *Thermal equilibrium Rayleigh-Jeans (3.2) and Bose-Einstein (3.1) distributions for long-wavelength magnons in YIG at room temperature* $T = 300\,\mathrm{K}$. *The plot is for a film with thickness* $d = 6.7\,\mu\mathrm{m}$ *in an external magnetic field* $H_0 = 1710\,\mathrm{Oe} \times \mu$, *for momenta* $\boldsymbol{k} = k\boldsymbol{e}_z$ *parallel to the in-plane magnetic field.*

- A random ensemble of waves, and
- nonlinear mode coupling.

The former is necessary for the application of statistical arguments; and the latter for interaction processes which allow thermalization of the waves. For room temperature magnons in YIG, the required randomness is naturally provided by thermal fluctuations. The magnon number for a given state with momentum $\boldsymbol{k}$ can be mapped to the classical amplitude of the normal mode oscillations with said momentum. In an overpopulated system, turbulent wave mixing can lead to the formation of a large scale coherent structure, i.e., a condensate, in the lowest allowed energy state. However, this process is ruled by underlying Hamiltonian dynamics, and is therefore microscopically reversible. Despite that, entropy principles dictate that the system evolves to a equilibrium state of maximum disorder. Thus, the information necessary to reverse the condensation is stored in a sea of small scale fluctuations immersing the condensate. These thermal fluctuations correspond to the uncondensed particles of quantum systems. As the thermal distribution of uncondensed waves is the classical Rayleigh-Jeans distribution, this classical kinetic condensation should be called Rayleigh-Jeans condensation, in analogy to the

BEC of quantum mechanics. However, let us also emphasize that in the classical Rayleigh-Jeans scenario, the condensate corresponds to a classical wave with macroscopic amplitude, which is accompanied by a thermal ensemble of equally classical random waves [98, 99, 100]. In stark contrast to that, the condensate of the BEC is described by a macroscopic quantum wave function, which can only be interpreted in a probabilistic sense [85]. Such an interpretation of the condensed wave as probability amplitude is completely absent in the classical Rayleigh-Jeans condensation.

For a recent discussion of the concept of Rayleigh-Jeans condensation as opposed to BEC, see Ref. [101]. Experimentally, Rayleigh-Jeans condensation has so far only been observed by Sun *et al.*, by imaging classical light dynamics in a photorefractive crystal [100]. However, in this chapter we demonstrate that the condensation of magnons in YIG films at room temperature, observed in the experiments [15, 16, 17, 18, 19, 20, 21, 22, 23, 24], is in fact another example of classical Rayleigh-Jeans condensation.

3.2 Non-Markovian stochastic Landau-Lifshitz-Gilbert equation

In this section we microscopically derive the non-Markovian LLG, along the lines proposed by Heinonen, Rossi, and MacDonald in Ref. [48]. Our starting point are the magnetic, elastic, and magnetoelastic Hamiltonians of thin YIG films as introduced in Sec. 1.2, so that the total quantum Hamiltonian is given by

$$\mathcal{H}(t) = \mathcal{H}_{\mathrm{m}}(t) + \mathcal{H}_{\mathrm{e}} + \mathcal{H}_{\mathrm{me}}. \tag{3.3}$$

Here, the magnetic sector is

$$\mathcal{H}_{\mathrm{m}} = -\frac{1}{2}\sum_{ij} \boldsymbol{S}_i \mathbb{K}_{ij} \boldsymbol{S}_j - \boldsymbol{H}(t) \cdot \sum_i \boldsymbol{S}_i \tag{3.4}$$

where $\mathbb{K}_{ij}$ is a matrix in the spin components. It collects both exchange and dipole-dipole interactions, and has components

$$\mathbb{K}_{ij}^{\alpha\beta} = J_{ij}\delta^{\alpha\beta} + D_{ij}^{\alpha\beta}. \tag{3.5}$$

The magnetic field is explicitly time dependent,

$$\boldsymbol{H}(t) = \left[H_0 + H_1 \cos\left(2\omega_{\mathrm{p}} t\right)\right] \boldsymbol{e}_z, \tag{3.6}$$

with a large in-plane bias magnetic field H_0, and a comparatively small parallel parametric pumping field $H_1 \ll H_0$, which oscillates with twice the parametric excitation frequency ω_{p}. The elastic sector is taken to be

$$\mathcal{H}_{\mathrm{e}} = \frac{1}{N}\sum_{\boldsymbol{k}\lambda} \left[\frac{P_{-\boldsymbol{k}\lambda} P_{\boldsymbol{k}\lambda}}{2M} + \frac{M}{2}\omega_{\boldsymbol{k}\lambda}^2 X_{-\boldsymbol{k}\lambda} X_{\boldsymbol{k}\lambda} \right]. \tag{3.7}$$

Note that we normalized the phonon normal modes differently than in the preceding chapters[2] ; i.e., we defined the Fourier expansion as in continuum theory,

$$\boldsymbol{X}(\boldsymbol{R}_i) = \frac{1}{N}\sum_{\boldsymbol{k}\lambda} e^{i\boldsymbol{k}\cdot\boldsymbol{R}_i} X_{\boldsymbol{k}\lambda}\boldsymbol{e}_{\boldsymbol{k}\lambda}. \tag{3.8}$$

Lastly, the magnetoelastic interaction Hamiltonian is again given by

$$\mathcal{H}_{\text{me}} = \frac{1}{S^2}\sum_i\sum_{\alpha\beta} B^{\alpha\beta} S_i^\alpha S_i^\beta X_i^{\alpha\beta}. \tag{3.9}$$

As first step, a straightforward calculation yields the Heisenberg equations of motion for the spin and phonon operators from the Hamiltonian (3.3). For the spin operator, the Heisenberg equation is explicitly given by

$$\dot{\boldsymbol{S}}_i = \boldsymbol{S}_i \times \Big[\boldsymbol{H}(t) + \sum_j \mathbb{K}_{ij}\boldsymbol{S}_j\Big] + \frac{1}{2}\Big[\boldsymbol{S}_i \times \boldsymbol{F}_i(t) - \boldsymbol{F}_i(t)\times \boldsymbol{S}_i\Big], \tag{3.10}$$

where the vector operator $\boldsymbol{F}_i(t)$ describing the magnetic field induced by magnetoelastic coupling to the phonons is

$$\boldsymbol{F}_i(t) = -\frac{2}{S^2}\sum_{\alpha\beta} \boldsymbol{e}_\alpha B^{\alpha\beta} X_i^{\alpha\beta}(t) S_i^\beta(t). \tag{3.11}$$

The phonons themselves satisfy the Heisenberg equations

$$\dot{X}_{\boldsymbol{k}\lambda} = \frac{P_{\boldsymbol{k}\lambda}}{M}, \tag{3.12a}$$

$$\dot{P}_{\boldsymbol{k}\lambda} = -M\omega_{\boldsymbol{k}\lambda}^2 X_{\boldsymbol{k}\lambda} + MA_{\boldsymbol{k}\lambda}(t), \tag{3.12b}$$

where the magnetoelastic acceleration exerted by the spins on the phonons is given by the operator

$$A_{\boldsymbol{k}\lambda}(t) = \frac{i}{2MS^2}\sum_i\sum_{\alpha\beta} e^{-i\boldsymbol{k}\cdot\boldsymbol{R}_i} B^{\alpha\beta}\boldsymbol{k}_{\alpha\beta}\cdot\boldsymbol{e}_{-\boldsymbol{k}\lambda} S_i^\alpha(t) S_i^\beta(t). \tag{3.13}$$

The two operator equations of motion (3.12) for the phonon normal modes can be combined into a single second order equation of motion,

$$\ddot{X}_{\boldsymbol{k}\lambda} + \omega_{\boldsymbol{k}\lambda}^2 X_{\boldsymbol{k}\lambda} = A_{\boldsymbol{k}\lambda}(t), \tag{3.14}$$

[2] As compared to Chs. 1 and 2, we rescaled $X_{\boldsymbol{k}\lambda} \to X_{\boldsymbol{k}\lambda}/\sqrt{N}$ and $P_{\boldsymbol{k}\lambda} \to P_{\boldsymbol{k}\lambda}/\sqrt{N}$, so that the canonical commutation relation of phonons changes to $[X_{\boldsymbol{k}\lambda}, P_{\boldsymbol{k}'\lambda'}] = iN\delta_{\boldsymbol{k},-\boldsymbol{k}'}\delta_{\lambda\lambda'}$. This rescaling is necessary to obtain sensible thermodynamic limits of integrations and delta distributions in all expressions; i.e., $\frac{1}{N}\sum_{\boldsymbol{k}} = \left(\frac{a}{2\pi}\right)^2 \int \mathrm{d}^2k$ and $N\delta_{\boldsymbol{k}\boldsymbol{k}'} = \left(\frac{2\pi}{a}\right)^2 \delta(\boldsymbol{k}-\boldsymbol{k}')$.

which describes a quantum mechanical harmonic oscillator that is externally driven by the spin degrees of freedom. Formally, this differential equation can be solved exactly,

$$\begin{aligned} X_{\boldsymbol{k}\lambda}(t) =& X_{\boldsymbol{k}\lambda}(0)\cos\left(\omega_{\boldsymbol{k}\lambda}t\right) + \frac{P_{\boldsymbol{k}\lambda}(0)}{M\omega_{\boldsymbol{k}\lambda}}\sin\left(\omega_{\boldsymbol{k}\lambda}t\right) \\ &+ \int_0^t \mathrm{d}t'\,\frac{\sin\left[\omega_{\boldsymbol{k}\lambda}\left(t-t'\right)\right]}{\omega_{\boldsymbol{k}\lambda}} A_{\boldsymbol{k}\lambda}(t') \qquad (3.15) \\ =& \tilde{X}_{\boldsymbol{k}\lambda}(0)\cos\left(\omega_{\boldsymbol{k}\lambda}t\right) + \frac{P_{\boldsymbol{k}\lambda}(0)}{M\omega_{\boldsymbol{k}\lambda}}\sin\left(\omega_{\boldsymbol{k}\lambda}t\right) + \frac{A_{\boldsymbol{k}\lambda}(t)}{\omega_{\boldsymbol{k}\lambda}^2} \\ &- \int_0^t \mathrm{d}t'\,\frac{\cos\left[\omega_{\boldsymbol{k}\lambda}\left(t-t'\right)\right]}{\omega_{\boldsymbol{k}\lambda}^2}\frac{\mathrm{d}A_{\boldsymbol{k}\lambda}(t')}{\mathrm{d}t'}, \qquad (3.16) \end{aligned}$$

where in the second step we integrated by parts and introduced the shifted initial phonon positions

$$\tilde{X}_{\boldsymbol{k}\lambda}(0) = X_{\boldsymbol{k}\lambda}(0) - \frac{A_{\boldsymbol{k}\lambda}(0)}{\omega_{\boldsymbol{k}\lambda}^2}. \qquad (3.17)$$

At this point, we make the transition from quantum to classical dynamics, i.e., we replace all quantum mechanical vector operators by classical vectors. On the level of the equations of motion, this amounts to ignoring that the different components of the spin do not commute. Then we can write the magnetic field $\boldsymbol{F}_i(t)$ generated by the magnetoelastic interactions as

$$\boldsymbol{F}_i(t) = \bar{\boldsymbol{h}}_i(t) + \delta\boldsymbol{h}_i(t) - \int_0^t \mathrm{d}t'\,\mathbb{G}_{ij}(t,t')\dot{\boldsymbol{S}}_j(t'). \qquad (3.18)$$

Here, the first two contributions are instantaneous magnetic fields, whereas the third part is non-Markovian, i.e., it depends on the history of the system, and couples to the rate of change of the spin vector. Thus, we identify it with a damping term, describing the dissipation of energy from the magnetic degrees of freedom to the phonon bath. The first contribution is explicitly given by

$$\begin{aligned} \bar{\boldsymbol{h}}_i(t) =& \frac{1}{2S^4}\sum_{\alpha\beta}\sum_{\mu\nu}\boldsymbol{e}_\alpha B^{\alpha\beta}B^{\mu\nu}\sum_j S_i^\beta(t)S_j^\mu(t)S_j^\nu(t) \\ &\times \frac{1}{N}\sum_{\boldsymbol{k}\lambda} e^{i\boldsymbol{k}\cdot(\boldsymbol{R}_i-\boldsymbol{R}_j)}\frac{\left(\boldsymbol{k}_{\alpha\beta}\cdot\boldsymbol{e}_{\boldsymbol{k}\lambda}\right)\left(\boldsymbol{k}_{\mu\nu}\cdot\boldsymbol{e}_{-\boldsymbol{k}\lambda}\right)}{M\omega_{\boldsymbol{k}\lambda}^2}. \qquad (3.19) \end{aligned}$$

Note that it does not depend on the phonon dynamics, so that it is merely a small correction to the total magnetic field. Henceforth it will be neglected. On the other hand, the second contribution to the magnetoelastic field (3.18) is the magnetic field induced by the initial distribution of the phonon subsystem,

$$\begin{aligned} \delta\boldsymbol{h}_i(t) =& -\frac{i}{S^2}\sum_{\alpha\beta}\boldsymbol{e}_\alpha B^{\alpha\beta}S_i^\beta(t)\frac{1}{N}\sum_{\boldsymbol{k}\lambda} e^{i\boldsymbol{k}\cdot\boldsymbol{R}_i}\boldsymbol{k}_{\alpha\beta}\cdot\boldsymbol{e}_{\boldsymbol{k}\lambda} \\ &\times\left[\tilde{X}_{\boldsymbol{k}\lambda}(0)\cos\left(\omega_{\boldsymbol{k}\lambda}t\right) + \frac{P_{\boldsymbol{k}\lambda}(0)}{M\omega_{\boldsymbol{k}\lambda}}\sin\left(\omega_{\boldsymbol{k}\lambda}t\right)\right]. \qquad (3.20) \end{aligned}$$

Finally, the components of the non-Markovian damping kernel are given by

$$\begin{aligned}\mathbb{G}_{ij}^{\alpha\beta}(t,t') =& \frac{1}{S^4}\sum_{\mu\nu} B^{\alpha\mu}B^{\beta\nu}S_i^{\mu}(t)S_j^{\nu}(t')\frac{1}{N}\sum_{\boldsymbol{k}\lambda} e^{i\boldsymbol{k}\cdot(\boldsymbol{R}_i-\boldsymbol{R}_j)} \\ &\times (\boldsymbol{k}_{\alpha\mu}\cdot\boldsymbol{e}_{\boldsymbol{k}\lambda})\,(\boldsymbol{k}_{\beta\nu}\cdot\boldsymbol{e}_{-\boldsymbol{k}\lambda})\,\frac{\cos\left[\omega_{\boldsymbol{k}\lambda}\,(t-t')\right]}{M\omega_{\boldsymbol{k}\lambda}^2}. \end{aligned} \tag{3.21}$$

So far, the considered spin dynamics are entirely deterministic. However, randomness necessarily enters via the unknown initial values $\tilde{X}_{\boldsymbol{k}\lambda}(0)$ and $P_{\boldsymbol{k}\lambda}(0)$ of the phonon normal modes. As we want the phonons to act as a thermal bath for the spin systems, we will naturally assume that the phonons are initially in thermal equilibrium with temperature T. Then the phonon initial values become classical Gaussian stochastic processes, with statistical properties determined by the equipartition theorem; i.e.,

$$\left\langle \tilde{X}_{\boldsymbol{k}\lambda}(0)\tilde{X}_{\boldsymbol{k}'\lambda'}(0)\right\rangle = N\delta_{\boldsymbol{k},-\boldsymbol{k}'}\delta_{\lambda\lambda'}\frac{T}{M\omega_{\boldsymbol{k}\lambda}^2}, \tag{3.22a}$$

$$\left\langle P_{\boldsymbol{k}\lambda}(0)P_{\boldsymbol{k}'\lambda'}(0)\right\rangle = N\delta_{\boldsymbol{k},-\boldsymbol{k}'}\delta_{\lambda\lambda'}MT, \tag{3.22b}$$

and all other cumulants of $\tilde{X}_{\boldsymbol{k}\lambda}(0)$ and $P_{\boldsymbol{k}\lambda}(0)$ vanish. Under this assumption, the induced magnetic field (3.20) becomes a non-Markovian Gaussian stochastic process with vanishing average,

$$\langle \delta\boldsymbol{h}_i(t)\rangle = 0. \tag{3.23}$$

The covariance of the fluctuating field (3.20) is then directly related to the damping kernel via the fluctuation-dissipation theorem,

$$\left\langle \delta h_i^{\alpha}(t)\delta h_j^{\beta}(t')\right\rangle = T\mathbb{G}_{ij}^{\alpha\beta}(t,t'). \tag{3.24}$$

Collecting all contributions to the equation of motion of the spin vectors, we thus arrive at a non-Markovian generalization of the stochastic Landau-Lifshitz-Gilbert equation (LLG),

$$\begin{aligned}\dot{\boldsymbol{S}}_i(t) =& \boldsymbol{S}_i(t)\times\Big[\boldsymbol{H}(t)+\delta\boldsymbol{h}_i(t)+\sum_j \mathbb{K}_{ij}\boldsymbol{S}_j(t)\Big] \\ &- \boldsymbol{S}_i(t)\times\int_0^t \mathrm{d}t'\sum_j \mathbb{G}_{ij}(t,t')\dot{\boldsymbol{S}}_j(t'). \end{aligned} \tag{3.25}$$

Comparing with the conventional LLG (1.56) presented in Sec. 1.3.2, we notice that the main advantages of our approach is that it provides a microscopic description of the damping (as opposed to a phenomenological constant), and it naturally resolves the ambiguity of the white noise random field by introducing non-Markovian memory effects. Therefore our microscopically derived LLG (3.25) can be expected to give accurate results even on small timescales, which

is fundamentally important for every simulation. Furthermore, since the dissipation kernel (3.21) explicitly retains the information of the phonon dynamics, the non-Markovian LLG (3.25) can also describe magnetoelastic hybridization effects like those discussed in Sec. 2.6 for YIG, where magnon and phonon dynamics occur at the same time scale. Also unlike the conventional LLG (1.56), the damping kernel (3.21) following from the magnon-phonon interactions is in general a tensor in the spin components. Such a tensorial structure has been proposed previously on phenomenological grounds [103]; in our approach it arises naturally because of the nonlinear coupling of the spins to the phonon normal modes in the magnetoelastic Hamiltonian (3.9) and the anisotropy of the phonon modes, which enters via the momentum dependence of the phonon polarization vectors $\boldsymbol{e}_{\boldsymbol{k}\lambda}$. For completeness, let us remark that the conventional LLG (1.56) can be recovered from our non-Markovian equation (3.25) by approximating the damping kernel as $\mathbb{G}_{ij}(t,t') \approx 2\gamma\delta_{ij}\delta^{\alpha\beta}\delta(t-t')$, thereby neglecting all effects of the microscopic phonon dynamics.

Note also that the stochastic process $\delta\boldsymbol{h}_i(t)$ is not stationary, since the the covariance (3.24) explicitly depends on the state of the spin system at times t and t', and not only on the time difference $t-t'$. Hence, the random field cannot be an ergodic process, and it is not possible to extract statistical averages from sufficiently long time samples. However, this stems only from the desire to cast the non-Markovian LLG (3.25) into a form directly comparable to the conventional white noise LLG (1.56), with terms that can be intuitively interpreted as fluctuating magnetic field and dissipation kernel. Indeed, we can factorize the random field (3.20) as

$$\delta\boldsymbol{h}_i(t) = \mathbb{Q}_i(t)\boldsymbol{S}_i(t) \tag{3.26}$$

where the components of the tensor $\mathbb{Q}_i(t)$ are Gaussian stochastic processes which only depend on the phonon degrees of freedom,

$$\begin{aligned}\mathbb{Q}_i^{\alpha\beta}(t) = &-\frac{i}{S^2}\sum_{\alpha\beta} B^{\alpha\beta}\frac{1}{N}\sum_{\boldsymbol{k}\lambda} e^{i\boldsymbol{k}\cdot\boldsymbol{R}_i}\boldsymbol{k}_{\alpha\beta}\cdot\boldsymbol{e}_{\boldsymbol{k}\lambda} \\ &\times\left[\tilde{X}_{\boldsymbol{k}\lambda}(0)\cos\left(\omega_{\boldsymbol{k}\lambda}t\right) + \frac{P_{\boldsymbol{k}\lambda}(0)}{M\omega_{\boldsymbol{k}\lambda}}\sin\left(\omega_{\boldsymbol{k}\lambda}t\right)\right].\end{aligned} \tag{3.27}$$

They themselves satisfy $\langle\mathbb{Q}_i(t)\rangle = 0$, and the fluctuation-dissipation theorem

$$\left\langle \mathbb{Q}_i^{\alpha\mu}(t)\mathbb{Q}_j^{\beta\nu}(t')\right\rangle = T\mathbb{Y}_{ij}^{\alpha\mu\beta\nu}(t-t'). \tag{3.28}$$

Here the components of the fourth-rank damping tensor are explicitly given by

$$\begin{aligned}\mathbb{Y}_{ij}^{\alpha\mu\beta\nu}(t-t') = &\frac{1}{S^4}B^{\alpha\mu}B^{\beta\nu}\frac{1}{N}\sum_{\boldsymbol{k}\lambda} e^{i\boldsymbol{k}\cdot(\boldsymbol{R}_i-\boldsymbol{R}_j)} \\ &\times\left(\boldsymbol{k}_{\alpha\mu}\cdot\boldsymbol{e}_{\boldsymbol{k}\lambda}\right)\left(\boldsymbol{k}_{\beta\nu}\cdot\boldsymbol{e}_{-\boldsymbol{k}\lambda}\right)\frac{\cos\left[\omega_{\boldsymbol{k}\lambda}\left(t-t'\right)\right]}{M\omega_{\boldsymbol{k}\lambda}^2}.\end{aligned} \tag{3.29}$$

As this fourth-rank damping tensor $\mathbb{Y}_{ij}(t-t')$ is only a function of the time difference, the stochastic processes $\mathbb{Q}_i(t)$ are stationary, and hence ergodic. In terms of the fourth-rank tensor, the original damping kernel $\mathbb{G}_{ij}(t,t')$ can be expressed as

$$\mathbb{G}_{ij}^{\alpha\beta}(t,t') = \sum_{\mu\nu} \mathbb{Y}_{ij}^{\alpha\mu\beta\nu}(t-t') S_i^{\mu}(t) S_j^{\nu}(t'). \tag{3.30}$$

3.3 Spin wave approach

In the thin YIG film geometry discussed at length in Sec. 1.2.4, the large bias magnetic field $H_0 \boldsymbol{e}_z$ causes the classical ground state of the spin system to be a saturated ferromagnet, magnetized in z direction. It is then advantageous to work directly with the excitations above the ground state. Thus we separate the ground state from the dynamical variables by setting

$$\boldsymbol{S}_i(t) = S\left[\boldsymbol{e}_z + \boldsymbol{m}_i(t)\right]. \tag{3.31}$$

As the effective spin $S \approx 14$ for YIG is rather large, we expect that thermal fluctuations will induce only comparatively small deviations from the ground state, so that $|\boldsymbol{m}_i(t)| \ll 1$. In the spirit of the conventional LLG and spin wave theory, we may now neglect the state dependence of the stochastic field $\delta\boldsymbol{h}_i(t)$ damping kernel $\mathbb{G}_{ij}(t,t')$ by substituting $\boldsymbol{S}_i(t) \to S\boldsymbol{e}_z$ in the microscopic definitions (3.20) and (3.21). This procedure yields for large S the dominant contributions to random field and dissipation, neglecting only small dynamical corrections. Within this approximation, the damping kernel $\mathbb{G}_{ij}(t,t')$ depends only on the time difference $t-t'$, so that the random field $\delta\boldsymbol{h}_i(t)$ becomes an ergodic process. Furthermore, the spatial dependence of the dissipation kernel $\mathbb{G}_{ij}(t,t')$ is then only on the difference vector $\boldsymbol{R}_{ij} = \boldsymbol{R}_i - \boldsymbol{R}_j$. Thus it is convenient to work in momentum space, and consider the Fourier modes

$$\boldsymbol{m}_{\boldsymbol{k}}(t) = \sum_i e^{-i\boldsymbol{k}\cdot\boldsymbol{R}_i} \boldsymbol{m}_i(t). \tag{3.32}$$

We will frequently refer to the $\boldsymbol{m}_{\boldsymbol{k}}(t)$ as the magnon modes because their linearized equations of motion yields the magnon spectrum; see Eqs. (3.39) and (3.42) below. The Fourier transforms of random field and damping kernel will be defined as

$$\delta\boldsymbol{h}_{\boldsymbol{k}}(t) = \sum_i e^{-i\boldsymbol{k}\cdot\boldsymbol{R}_i} \delta\boldsymbol{h}_i(t) = \sum_\lambda \delta\boldsymbol{h}_{\boldsymbol{k}\lambda}(t), \tag{3.33}$$

$$\mathbb{G}_{\boldsymbol{k}}(t,0) = \sum_i e^{-i\boldsymbol{k}\cdot\boldsymbol{R}_{ij}} \mathbb{G}_{ij}(t,0) = \sum_\lambda \tilde{\mathbb{G}}_{\boldsymbol{k}\lambda} \cos\left(\omega_{\boldsymbol{k}\lambda} t\right). \tag{3.34}$$

Here the contributions of the different phonon polarizations are explicitly given by

$$\delta \boldsymbol{h}_{\boldsymbol{k}\lambda}(t) = -\frac{i}{S}\sum_{\alpha\beta} \boldsymbol{e}_\alpha B^{\alpha z} \boldsymbol{k}_{\alpha z}\cdot \boldsymbol{e}_{\boldsymbol{k}\lambda}\left[\tilde{X}_{\boldsymbol{k}\lambda}(0)\cos\left(\omega_{\boldsymbol{k}\lambda}t\right) + \frac{P_{\boldsymbol{k}\lambda}(0)}{M\omega_{\boldsymbol{k}\lambda}}\sin\left(\omega_{\boldsymbol{k}\lambda}t\right)\right], \tag{3.35}$$

$$\tilde{\mathbb{G}}^{\alpha\beta}_{\boldsymbol{k}\lambda} = B^{\alpha z}B^{\beta z}\frac{\left(\boldsymbol{k}_{\alpha z}\cdot\boldsymbol{e}_{\boldsymbol{k}\lambda}\right)\left(\boldsymbol{k}_{\beta z}\cdot\boldsymbol{e}_{-\boldsymbol{k}\lambda}\right)}{M\omega^2_{\boldsymbol{k}\lambda}S^2}. \tag{3.36}$$

The corresponding momentum space version of the fluctuation-dissipation theorem (3.24) is

$$\left\langle \delta h^\alpha_{\boldsymbol{k}\lambda}(t)\delta h^\beta_{\boldsymbol{k}'\lambda'}(t')\right\rangle = N\delta_{\boldsymbol{k},-\boldsymbol{k}'}\delta_{\lambda\lambda'}T\tilde{\mathbb{G}}^{\alpha\beta}_{\boldsymbol{k}\lambda}\cos\left[\omega_{\boldsymbol{k}\lambda}\left(t-t'\right)\right]. \tag{3.37}$$

The equation of motion of the Fourier modes (3.32) follows directly from the non-Markovian LLG (3.25), and is within our approximation explicitly given by

$$\begin{aligned}\dot{\boldsymbol{m}}_{\boldsymbol{k}}(t) =& \left[\mathbb{L}_{\boldsymbol{k}} + \mathbb{P}(t)\right]\boldsymbol{m}_{\boldsymbol{k}}(t)\\ &+ \boldsymbol{e}_z\times\sum_\lambda\left[\delta\boldsymbol{h}_{\boldsymbol{k}\lambda}(t) - S\tilde{\mathbb{G}}_{\boldsymbol{k}\lambda}\int_0^t \mathrm{d}t'\,\cos\left[\omega_{\boldsymbol{k}\lambda}\left(t-t'\right)\right]\dot{\boldsymbol{m}}_{\boldsymbol{k}}(t')\right]\\ &+ \frac{1}{N}\sum_{\boldsymbol{q}}\boldsymbol{m}_{\boldsymbol{k}-\boldsymbol{q}}(t)\times\Bigg\{S\mathbb{K}_{\boldsymbol{q}}\boldsymbol{m}_{\boldsymbol{q}}(t)\\ &\qquad+\sum_\lambda\left[\delta\boldsymbol{h}_{\boldsymbol{q}\lambda}(t) - S\tilde{\mathbb{G}}_{\boldsymbol{q}\lambda}\int_0^t \mathrm{d}t'\,\cos\left[\omega_{\boldsymbol{q}\lambda}\left(t-t'\right)\right]\dot{\boldsymbol{m}}_{\boldsymbol{q}}(t')\right]\Bigg\},\end{aligned} \tag{3.38}$$

where we introduced the matrices

$$\mathbb{L}_{\boldsymbol{k}} = \begin{pmatrix} 0 & \omega^y_{\boldsymbol{k}} & 0\\ -\omega^x_{\boldsymbol{k}} & 0 & 0\\ 0 & 0 & 0\end{pmatrix}, \tag{3.39}$$

and

$$\mathbb{P}(t) = H_1\cos\left(2\omega_{\mathrm{p}}t\right)\begin{pmatrix} 0 & 1 & 0\\ -1 & 0 & 0\\ 0 & 0 & 0\end{pmatrix}. \tag{3.40}$$

The matrix $\mathbb{L}_{\boldsymbol{k}}$ describes the linear oscillations of the spins around the ground state, i.e., the spin waves, in terms of the frequencies[3]

$$\omega^x_{\boldsymbol{k}} = H_0 + S\left(\mathbb{K}^{zz}_{\boldsymbol{k}=0} - \mathbb{K}^{xx}_{\boldsymbol{k}}\right), \tag{3.41a}$$

$$\omega^y_{\boldsymbol{k}} = H_0 + S\left(\mathbb{K}^{zz}_{\boldsymbol{k}=0} - \mathbb{K}^{yy}_{\boldsymbol{k}}\right), \tag{3.41b}$$

[3]Here we used that the dipole-dipole interaction tensor is diagonal for thin YIG films [6]; see also Sec. 1.2.4. Also note that in terms of the coefficients $A_{\boldsymbol{k}}$ and $B_{\boldsymbol{k}}$ of the quadratic magnon Hamiltonian in Holstein-Primakoff basis given in Eq. (2.5), we have $\omega^x_{\boldsymbol{k}} = A_{\boldsymbol{k}} - B_{\boldsymbol{k}}$ and $\omega^y_{\boldsymbol{k}} = A_{\boldsymbol{k}} + B_{\boldsymbol{k}}$.

whereas $\mathbb{P}(t)$ contains the effect of the parallel parametric pumping field. Note that the magnon dispersion of linear spin wave theory is given by the nonvanishing eigenvalue of the matrix $\mathbb{L}_{\boldsymbol{k}}(t)$,

$$E_{\boldsymbol{k}} = \sqrt{\omega^x_{\boldsymbol{k}}\omega^y_{\boldsymbol{k}}}. \tag{3.42}$$

Using the dipolar matrix elements for thin YIG films given in Eqs. (1.29), we explicitly find in the long-wavelength limit

$$E_{\boldsymbol{k}} = \sqrt{\left[H_0 + \rho_s \boldsymbol{k}^2 + \Delta\left(1 - f_{\boldsymbol{k}}\right)\sin^2\theta_{\boldsymbol{k}}\right]\left[H_0 + \rho_s \boldsymbol{k}^2 + \Delta f_{\boldsymbol{k}}\right]}, \tag{3.43}$$

with the form factor

$$f_{\boldsymbol{k}} = \frac{1 - \exp\left(-|\boldsymbol{k}|d\right)}{|\boldsymbol{k}|d}, \tag{3.44}$$

in accordance with the result of Ch. 2, Eq. (2.12), and as stated in the introductory Sec. 1.2.4. Also, the linear magnon dynamics described by the first line of the LLG (3.38) was used in Sec. 1.2.5 to derive the instability of parametric pumping.

In principle, we could now proceed to set up an ordinary spin wave expansion by noting that the vector $\boldsymbol{m}_i(t)$ has in fact only two independent components. Since the length of the spin vector is conserved, $\boldsymbol{S}_i^2(t) = S^2\left[1 + 2m_i^z(t) + \boldsymbol{m}_i^2(t)\right] = S^2$, we may always express the z component via the x and y components, $m_i^z(t) = \sqrt{1 - \left[m_i^x(t)\right]^2 - \left[m_i^y(t)\right]^2} - 1$. Expanding the squareroot yields an infinite hierarchy of spin wave interaction terms. Provided that the transverse spin components are rather small, i.e., there are only small oscillations around the ground state, such an expansion can be truncated after the first few terms. In this way a perturbative spin wave dynamics can be constructed. This approach is used in App. B.1 to obtain the thermal equilibrium distribution of classical spin waves. However, as it is our goal to explore nonperturbative effects in the spin dynamics, in particular the condensation of magnons, we will not follow this route. Instead, we will keep the full magnon dynamics of Eq. (3.38), thereby taking all spin-spin interactions nonperturbatively into account. As a side remark, let us also note that in momentum space the perturbative approach increases the number of integrations that necessarily have to performed, since the one variable $m_i^z(t)$ is replaced by powers of the products $\left[m_i^x(t)\right]^2$ and $\left[m_i^y(t)\right]^2$. Therefore, the numerical effort is actually reduced by not employing the perturbation expansion for $m_i^z(t)$.

3.4 Exact reduction to Gaussian white noise

The equation of motion (3.38) is still a complicated non-Markovian stochastic integro-differential equation. In order to numerically integrate it, the whole history of the system must be stored, so as to perform the time integration

of the dissipative term at every time step. However, the problem can be considerably simplified because of the harmonic time dependence of the damping kernel (3.34), which allows us to replace the non-Markovian equation (3.38) by a set of Markovian equations of motion [66, 67]. The price we have to pay for this is the introduction of a new set of dynamical variables which absorb all non-Markovian behavior. As a first step we therefore define the auxiliary variables

$$\boldsymbol{u}_{\boldsymbol{k}\lambda}(t) = S\tilde{\mathbb{G}}_{\boldsymbol{k}\lambda} \int_0^t \mathrm{d}t' \, \cos\left[\omega_{\boldsymbol{k}\lambda}\,(t-t')\right] \dot{\boldsymbol{m}}_{\boldsymbol{k}}(t') - S\tilde{\mathbb{G}}_{\boldsymbol{k}\lambda}\boldsymbol{m}_{\boldsymbol{k}}(t). \tag{3.45}$$

These new variables satisfy the equations of motion

$$\ddot{\boldsymbol{u}}_{\boldsymbol{k}\lambda}(t) = -\omega_{\boldsymbol{k}\lambda}^2 \left[\boldsymbol{u}_{\boldsymbol{k}\lambda}(t) + S\tilde{\mathbb{G}}_{\boldsymbol{k}\lambda}\boldsymbol{m}_{\boldsymbol{k}}(t)\right]. \tag{3.46}$$

Since the auxiliary variables $\boldsymbol{u}_{\boldsymbol{k}\lambda}(t)$ are defined in Eq. (3.45) as functionals of the dynamical variables $\boldsymbol{m}_{\boldsymbol{k}}(t)$, their initial conditions cannot be chosen freely; they are fixed to

$$\boldsymbol{u}_{\boldsymbol{k}\lambda}(0) = -\,S\tilde{\mathbb{G}}_{\boldsymbol{k}\lambda}\boldsymbol{m}_{\boldsymbol{k}}(0), \tag{3.47a}$$

$$\dot{\boldsymbol{u}}_{\boldsymbol{k}\lambda}(0) = 0. \tag{3.47b}$$

With the introduction of the new set of variables (3.45), the equation of motion (3.38) becomes

$$\begin{aligned}\dot{\boldsymbol{m}}_{\boldsymbol{k}}(t) = {} & \left[\mathbb{L}_{\boldsymbol{k}} + \mathbb{P}(t)\right]\boldsymbol{m}_{\boldsymbol{k}}(t) \\ & + \boldsymbol{e}_z \times \sum_\lambda \left[\delta\boldsymbol{h}_{\boldsymbol{k}\lambda}(t) - \boldsymbol{u}_{\boldsymbol{k}\lambda}(t) - S\tilde{\mathbb{G}}_{\boldsymbol{k}\lambda}\boldsymbol{m}_{\boldsymbol{k}}(t)\right] \\ & + \frac{1}{N}\sum_{\boldsymbol{q}} \boldsymbol{m}_{\boldsymbol{k}-\boldsymbol{q}}(t) \times \Bigg\{ S\mathbb{K}_{\boldsymbol{q}}\boldsymbol{m}_{\boldsymbol{q}}(t) \\ & \qquad + \sum_\lambda \left[\delta\boldsymbol{h}_{\boldsymbol{q}\lambda}(t) - \boldsymbol{u}_{\boldsymbol{q}\lambda}(t) - S\tilde{\mathbb{G}}_{\boldsymbol{q}\lambda}\boldsymbol{m}_{\boldsymbol{q}}(t)\right] \Bigg\}.\end{aligned} \tag{3.48}$$

Although the time integration has now been hidden in the auxiliary variable $\boldsymbol{u}_{\boldsymbol{k}\lambda}(t)$, above Eq. (3.48) is still not Markovian. This is due to the fact that the random field $\delta\boldsymbol{h}_{\boldsymbol{k}\lambda}(t)$ has to satisfy the fluctuation-dissipation theorem (3.37) and is thus a non-Markovian process. Consequently, as second step we have to simulate a Gaussian stochastic process with covariance given by the fluctuation-dissipation theorem (3.37). Because of the harmonic time dependence of the covariance (3.37), we model the random field dynamics with a driven harmonic oscillator equation of motion [66, 67, 104]:

$$\delta\ddot{\boldsymbol{h}}_{\boldsymbol{k}\lambda}(t) + 2\gamma_{\boldsymbol{k}\lambda}\delta\dot{\boldsymbol{h}}_{\boldsymbol{k}\lambda}(t) + \omega_{\boldsymbol{k}\lambda}^2\delta\boldsymbol{h}_{\boldsymbol{k}\lambda}(t) = \boldsymbol{a}_{\boldsymbol{k}\lambda} f_{\boldsymbol{k}\lambda}(t), \tag{3.49}$$

The external driving function is assumed to be complex Gaussian white noise, with the first two moments given by

$$\langle f_{\boldsymbol{k}\lambda}(t)\rangle = 0, \tag{3.50a}$$

$$\langle f_{\boldsymbol{k}\lambda}(t) f^*_{\boldsymbol{k}'\lambda'}(t')\rangle = N\delta_{\boldsymbol{k}\boldsymbol{k}'}\delta_{\lambda\lambda'}\delta(t-t'). \tag{3.50b}$$

The coupling vector $\boldsymbol{a}_{\boldsymbol{k}\lambda}$ will be determined below by demanding that the random process defined via the above equation of motion (3.49) indeed satisfies the fluctuation-dissipation theorem (3.37). Note also that in order to preserve the Hermiticity $\delta\boldsymbol{h}^*_{\boldsymbol{k}\lambda}(t) = \delta\boldsymbol{h}_{-\boldsymbol{k}\lambda}(t)$ of the random magnetic field both the coupling vector and the random driving have to be Hermitian, i.e., they have to satisfy $\boldsymbol{a}^*_{\boldsymbol{k}\lambda} = \boldsymbol{a}_{-\boldsymbol{k}\lambda}$ and $f^*_{\boldsymbol{k}\lambda}(t) = f_{-\boldsymbol{k}\lambda}(t)$. Since we are interested in oscillatory solutions, the damping rate $\gamma_{\boldsymbol{k}\lambda}$ in the oscillator equation of motion (3.49) must be smaller than the undamped oscillation frequency $\omega_{\boldsymbol{k}\lambda}$. Although we are ultimately interested in generating undamped oscillations, we will see below that the fluctuation-dissipation theorem of the random process (3.49) requires a finite damping in addition to the random driving in the equation of motion. The general solution of the driven oscillator equation (3.49) is

$$\delta\boldsymbol{h}_{\boldsymbol{k}\lambda}(t) = \delta\boldsymbol{h}^{\mathrm{hom}}_{\boldsymbol{k}\lambda}(t) + \boldsymbol{a}_{\boldsymbol{k}\lambda}\int \mathrm{d}t'\, G_{\boldsymbol{k}\lambda}(t-t') f_{\boldsymbol{k}\lambda}(t'), \tag{3.51}$$

where $\delta\boldsymbol{h}^{\mathrm{hom}}_{\boldsymbol{k}\lambda}(t)$ is the solution of the homogeneous system, and the Green function of the damped harmonic oscillator is

$$G_{\boldsymbol{k}\lambda}(t) = \Theta(t) e^{-\gamma_{\boldsymbol{k}\lambda}t}\frac{\sin\left(\sqrt{\omega^2_{\boldsymbol{k}\lambda}-\gamma^2_{\boldsymbol{k}\lambda}}\,t\right)}{\sqrt{\omega^2_{\boldsymbol{k}\lambda}-\gamma^2_{\boldsymbol{k}\lambda}}}. \tag{3.52}$$

Because we want to simulate a process with vanishing average, $\langle\delta\boldsymbol{h}_{\boldsymbol{k}\lambda}(t)\rangle = 0$, we choose

$$\delta\boldsymbol{h}_{\boldsymbol{k}\lambda}(0) = 0, \tag{3.53a}$$

$$\delta\dot{\boldsymbol{h}}_{\boldsymbol{k}\lambda}(0) = 0 \tag{3.53b}$$

for the initial values, so that $\delta\boldsymbol{h}^{\mathrm{hom}}_{\boldsymbol{k}\lambda}(t) = 0$. Fourier transforming to frequency space then yields

$$\delta\boldsymbol{h}_{\boldsymbol{k}\lambda}(\omega) = \int \mathrm{d}t\, e^{i\omega t}\delta\boldsymbol{h}_{\boldsymbol{k}\lambda}(t) = \boldsymbol{a}_{\boldsymbol{k}\lambda} G_{\boldsymbol{k}\lambda}(\omega) f_{\boldsymbol{k}\lambda}(\omega), \tag{3.54}$$

with

$$G_{\boldsymbol{k}\lambda}(\omega) = \frac{1}{\omega^2_{\boldsymbol{k}\lambda} - \omega^2 - 2i\gamma_{\boldsymbol{k}\lambda}\omega}. \tag{3.55}$$

The white noise covariance becomes in frequency space

$$\begin{aligned}\langle f_{\boldsymbol{k}\lambda}(\omega_1) f^*_{\boldsymbol{k}'\lambda'}(\omega_2)\rangle &= \int \mathrm{d}t \int \mathrm{d}t'\, e^{i\omega_1 t - i\omega_2 t'}\langle f_{\boldsymbol{k}\lambda}(t) f^*_{\boldsymbol{k}'\lambda'}(t')\rangle \\ &= N\delta_{\boldsymbol{k}\boldsymbol{k}'}\delta_{\lambda\lambda'}\int \mathrm{d}t\, e^{i(\omega_1-\omega_2)t} \\ &= 2\pi N\delta_{\boldsymbol{k}\boldsymbol{k}'}\delta_{\lambda\lambda'}\delta(\omega_1-\omega_2).\end{aligned} \tag{3.56}$$

Therefore we can evaluate the covariance of the random process $\delta\boldsymbol{h}_{\boldsymbol{k}\lambda}(t)$ as

$$\begin{aligned}\left\langle \delta h^{\alpha}_{\boldsymbol{k}\lambda}(t)\delta h^{\beta}_{\boldsymbol{k}'\lambda'}(t')\right\rangle =&N\delta_{\boldsymbol{k},-\boldsymbol{k}'}\delta_{\lambda\lambda'}a^{\alpha}_{\boldsymbol{k}\lambda}a^{\beta}_{-\boldsymbol{k}\lambda}\int\frac{\mathrm{d}\omega}{2\pi}\,e^{-i\omega(t-t')}|G_{\boldsymbol{k}\lambda}(\omega)|^2\\ =&N\delta_{\boldsymbol{k},-\boldsymbol{k}'}\delta_{\lambda\lambda'}a^{\alpha}_{\boldsymbol{k}\lambda}a^{\beta}_{-\boldsymbol{k}\lambda}\int\frac{\mathrm{d}\omega}{2\pi}\,\frac{e^{-i\omega(t-t')}}{\left(\omega^2_{\boldsymbol{k}\lambda}-\omega^2\right)^2+4\gamma^2_{\boldsymbol{k}\lambda}\omega^2}\\ =&N\delta_{\boldsymbol{k},-\boldsymbol{k}'}\delta_{\lambda\lambda'}\frac{a^{\alpha}_{\boldsymbol{k}\lambda}a^{\beta}_{-\boldsymbol{k}\lambda}}{4\gamma_{\boldsymbol{k}\lambda}\omega^2_{\boldsymbol{k}\lambda}}e^{-\gamma|t-t'|}\Bigg\{\cos\left[\sqrt{\omega^2_{\boldsymbol{k}\lambda}-\gamma^2_{\boldsymbol{k}\lambda}}(t-t')\right]\\ &+\frac{\gamma_{\boldsymbol{k}\lambda}}{\sqrt{\omega^2_{\boldsymbol{k}\lambda}-\gamma^2_{\boldsymbol{k}\lambda}}}\sin\left[\sqrt{\omega^2_{\boldsymbol{k}\lambda}-\gamma^2_{\boldsymbol{k}\lambda}}|t-t'|\right]\Bigg\}.\end{aligned}\tag{3.57}$$

Since our aim is to simulate an undamped random process with covariance (3.37), we introduce the dimensionless damping coefficient $g=\gamma_{\boldsymbol{k}\lambda}/\omega_{\boldsymbol{k}\lambda}$, so that

$$\begin{aligned}\left\langle \delta h^{\alpha}_{\boldsymbol{k}\lambda}(t)\delta h^{\beta}_{\boldsymbol{k}'\lambda'}(t')\right\rangle =&N\delta_{\boldsymbol{k},-\boldsymbol{k}'}\delta_{\lambda\lambda'}\frac{a^{\alpha}_{\boldsymbol{k}\lambda}a^{\beta}_{-\boldsymbol{k}\lambda}}{4g\omega^3_{\boldsymbol{k}\lambda}}e^{-g\omega_{\boldsymbol{k}\lambda}|t-t'|}\Bigg\{\cos\left[\sqrt{1-g^2}\omega_{\boldsymbol{k}\lambda}(t-t')\right]\\ &+\frac{g}{\sqrt{1-g^2}}\sin\left(\sqrt{1-g^2}\omega_{\boldsymbol{k}\lambda}|t-t'|\right)\Bigg\}.\end{aligned}\tag{3.58}$$

Finally, we demand that for vanishing damping the fluctuation-dissipation theorem (3.37) is recovered,

$$\lim_{g\to 0}\left\langle \delta h^{\alpha}_{\boldsymbol{k}\lambda}(t)\delta h^{\beta}_{\boldsymbol{k}'\lambda'}(t')\right\rangle = N\delta_{\boldsymbol{k},-\boldsymbol{k}'}\delta_{\lambda\lambda'}T\tilde{\mathbb{G}}^{\alpha\beta}_{\boldsymbol{k}\lambda}\cos\left[\omega_{\boldsymbol{k}\lambda}\left(t-t'\right)\right].\tag{3.59}$$

This requires that the coupling vector has the form

$$\boldsymbol{a}_{\boldsymbol{k}\lambda}=2\sqrt{g\omega^3_{\boldsymbol{k}\lambda}T}\boldsymbol{b}_{\boldsymbol{k}\lambda},\tag{3.60}$$

with a Hermitian vector $\boldsymbol{b}_{\boldsymbol{k}\lambda}$ satisfying $b^{\alpha}_{\boldsymbol{k}\lambda}b^{\beta}_{-\boldsymbol{k}\lambda}=\tilde{\mathbb{G}}^{\alpha\beta}_{\boldsymbol{k}\lambda}$. A convenient choice is explicitly given by[4]

$$\boldsymbol{b}_{\boldsymbol{k}\lambda}=\sum_{\alpha}\boldsymbol{e}_{\alpha}B^{\alpha z}\frac{i\boldsymbol{k}_{\alpha z}\cdot\boldsymbol{e}_{\boldsymbol{k}\lambda}}{\sqrt{M}\omega_{\boldsymbol{k}\lambda}S},\tag{3.61}$$

Because the vector (3.60) coupling the fluctuating field $\delta\boldsymbol{h}_{\boldsymbol{k}\lambda}(t)$ to the white noise driving $f_{\boldsymbol{k}\lambda}(t)$ scales as $\sqrt{g}$, we cannot take the limit $g\to 0$ exactly in the numerical simulations. However, we can get arbitrarily close to the undamped process by choosing arbitrarily small values of g. Hence we will perform the

[4]Similar as for the calculations of the leading order magnetoelastic hybridization performed in Sec. 2.6, we may collect both transverse phonon branches into a single variable $\delta\boldsymbol{h}_{\boldsymbol{k}\perp}(t)=\delta\boldsymbol{h}_{\boldsymbol{k}\perp 1}(t)+\delta\boldsymbol{h}_{\boldsymbol{k}\perp 2}(t)$. This is possible because in the thin film geometry, the coupling vectors (3.61) are orthogonal, since $\boldsymbol{b}_{\boldsymbol{k}\perp 1}$ always lies in the y-z plane while $\boldsymbol{b}_{\boldsymbol{k}\perp 2}$ points in x direction.

simulations with a small but finite value of g. For our application this is not a serious drawback, since we can readily interpret the dissipation term $+2g\omega_{\boldsymbol{k}\lambda}\delta\dot{\boldsymbol{h}}_{\boldsymbol{k}\lambda}(t)$ on the left-hand side of the equation of motion (3.49) of the fluctuating field as a phenomenological way to take the intrinsic damping of the phonon bath into account; with g being a dimensionless parameter controlling the strength of the phonon dissipation. To be consistent, a similar dissipation term $+2g\omega_{\boldsymbol{k}\lambda}\dot{\boldsymbol{u}}_{\boldsymbol{k}\lambda}(t)$ should also be added to the left-hand side of the equation of motion (3.46) for the auxiliary variable $\boldsymbol{u}_{\boldsymbol{k}\lambda}(t)$, since it inherits the time dependence of the damping kernel $\mathbb{G}_{\boldsymbol{k}}(t,t')$; see the defining Eq. (3.45).

Combining the equations of motion (3.48), (3.46), and (3.49) for the magnon modes, the auxiliary variables, and the random field respectively, we have now achieved our goal of obtaining a completely Markovian set of equations of motion which are equivalent to the single non-Markovian equation (3.38) for the magnon modes. This came at the price of turning both the time integrations and the fluctuating magnetic field in the original non-Markovian equation of motion (3.38) into dynamical variables. However, the situation is not as bad as it seems, for $\boldsymbol{u}_{\boldsymbol{k}\lambda}(t)$ and $\delta\boldsymbol{h}_{\boldsymbol{k}\lambda}(t)$ satisfy the same harmonic oscillator equation (albeit with different driving terms), and only the combination

$$\boldsymbol{v}_{\boldsymbol{k}\lambda}(t) = \delta\boldsymbol{h}_{\boldsymbol{k}\lambda}(t) - \boldsymbol{u}_{\boldsymbol{k}\lambda}(t) \tag{3.62}$$

appears in the magnon equation (3.48). Taking this combination as new auxiliary variable, we end up with the coupled set of Markovian equations of motion

$$\begin{aligned}\dot{\boldsymbol{m}}_{\boldsymbol{k}}(t) = {}& \left[\mathbb{L}_{\boldsymbol{k}} + \mathbb{P}(t)\right]\boldsymbol{m}_{\boldsymbol{k}}(t) + \boldsymbol{e}_z \times \sum_{\lambda}\Big[\boldsymbol{v}_{\boldsymbol{k}\lambda}(t) - S\tilde{\mathbb{G}}_{\boldsymbol{k}\lambda}\boldsymbol{m}_{\boldsymbol{k}}(t)\Big] \\ & + \frac{1}{N}\sum_{\boldsymbol{q}}\boldsymbol{m}_{\boldsymbol{k}-\boldsymbol{q}}(t) \times \left\{S\mathbb{K}_{\boldsymbol{q}}\boldsymbol{m}_{\boldsymbol{q}}(t) + \sum_{\lambda}\Big[\boldsymbol{v}_{\boldsymbol{q}\lambda}(t) - S\tilde{\mathbb{G}}_{\boldsymbol{q}\lambda}\boldsymbol{m}_{\boldsymbol{q}}(t)\Big]\right\}\end{aligned} \tag{3.63a}$$

$$\ddot{\boldsymbol{v}}_{\boldsymbol{k}\lambda}(t) = -2g\omega_{\boldsymbol{k}\lambda}\dot{\boldsymbol{v}}_{\boldsymbol{k}\lambda}(t) - \omega_{\boldsymbol{k}\lambda}^2\Big[\boldsymbol{v}_{\boldsymbol{k}\lambda}(t) - S\tilde{\mathbb{G}}_{\boldsymbol{k}\lambda}\boldsymbol{m}_{\boldsymbol{k}}(t)\Big] + 2\sqrt{gT\omega_{\boldsymbol{k}\lambda}^3}\boldsymbol{b}_{\boldsymbol{k}\lambda}f_{\boldsymbol{k}\lambda}(t) \tag{3.63b}$$

where $f_{\boldsymbol{k}\lambda}(t)$ is complex Gaussian white noise; and the constraints

$$\boldsymbol{v}_{\boldsymbol{k}\lambda}(0) = S\tilde{\mathbb{G}}_{\boldsymbol{k}\lambda}\boldsymbol{m}_{\boldsymbol{k}}(0), \tag{3.64a}$$

$$\dot{\boldsymbol{v}}_{\boldsymbol{k}\lambda}(0) = 0 \tag{3.64b}$$

on the initial values of the auxiliary variables.

The system (3.63) of stochastic differential equations is the final form of the original non-Markovian LLG (3.25) we use in this chapter. The following sections will be devoted to the setup of the numerical simulations performed on this stochastic system (3.63), and the presentation and interpretation of the results obtained in this fashion. Note that the system (3.63) is a conventional Langevin equation (see Sec. 1.5.3) in which the drift vector contains all

nonlinear interactions, and the noise is additive. Therefore there is no ambiguity as to which stochastic calculus should be used despite the noise being white; however, this was to be expected because we set out from the equivalent stochastic differential equation (3.38) which contains colored noise and hence does not entail any ambiguities.

3.5 Numerical implementation

In order to perform meaningful simulations, we first have to fix the parameters determined by the experimental setup; namely the thickness d of the YIG film, the temperature T of the thermal bath, the bias and pumping magnetic field amplitudes H_0 and H_1, and the pumping frequency ω_p. For the simulations presented below, we choose typical experimental values [22, 23, 24, 84]:

$$d = 6.7\,\mu\mathrm{m}, \tag{3.65a}$$
$$T = 300\,\mathrm{K}, \tag{3.65b}$$
$$H_0 = 1710\,\mathrm{Oe} \times \mu, \tag{3.65c}$$
$$H_1 = 0.03 H_0, \tag{3.65d}$$
$$\omega_\mathrm{p} = 2\pi \times 7.046\,\mathrm{GHz}, \tag{3.65e}$$

where $\mu = 2\mu_B$, with the Bohr magneton μ_B. At this point, one should remark that in experiments the actual value of the pumping field H_1 is in general unknown. It is usually generated via a microstrip resonator on top of the YIG film [15, 16, 17, 18, 19, 20, 21, 22, 23, 24], and depends heavily on the particular experimental geometry. Due to this, there is no simple way to determine the magnetic field H_1 from the power supplied to the resonator, which is the quantity measured in experiments. However, since the additional pumping field should not shift the magnon spectrum in any measurable way, we can infer that it can only be a very small percentage of the bias field H_0 used to magnetize the sample. For the set (3.65) of parameters, the minima of the magnon dispersion are located at the momenta $\boldsymbol{k} = \pm k_\mathrm{min} \boldsymbol{e}_z$, where $k_\mathrm{min} = 4.999 \times 10^4\,\mathrm{cm}^{-1}$, and have the frequency $E_\mathrm{min} = 2\pi \times 4.9\,\mathrm{GHz}$. The pumping frequency ω_p has been adjusted such that it is slightly above the ferromagnetic resonance at $E_{\boldsymbol{k}=0} = 2\pi \times 6.824\,\mathrm{GHz}$, as is conventionally done in experiments on magnon condensation [15, 16, 17, 22, 23, 24]. In this case direct transition of parametrically excited magnons to the bottom of the magnon spectrum are kinematically forbidden; thereby setting the stage for the multistep magnon-magnon scattering necessary for thermalization. The resonance energy surface $E_{\boldsymbol{k}} = \omega_\mathrm{p}$ in momentum space on which magnons are parametrically unstable is depicted in Fig. 3.2.

A plot of the magnon and phonon dispersions for a thin YIG film with the parameters (3.65) is shown in Fig. 3.3, for momenta parallel and perpendicular to the external magnetic field. Note that both longitudinal and transverse phonon branches cross the magnon dispersion in the vicinity of the dispersion

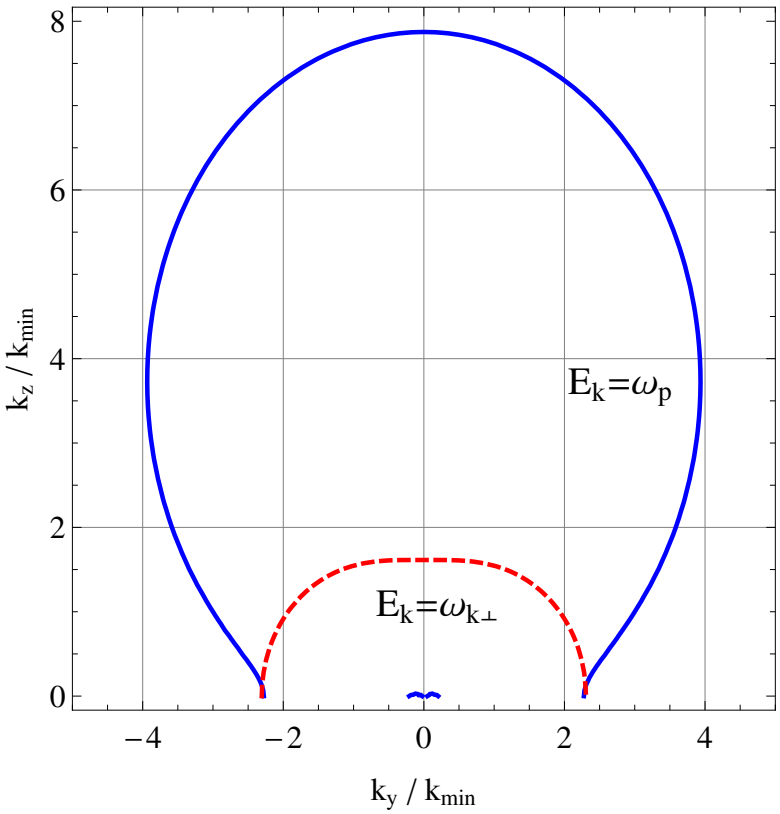

Figure 3.2: *Momentum space contours of the energy surfaces of parametric resonance $E_{\boldsymbol{k}} = \omega_p$ (blue solid line), and transverse magnetoelastic hybridization $E_{\boldsymbol{k}} = \omega_{\boldsymbol{k}\perp}$ (red dashed line), for the parameters given in Eqs. (3.65).*

minimum. Consequently, both spin degrees of freedom and thermal phonon bath can have the same time scales in the momentum range close the minima, which we are most interested in. Therefore an explicitly non-Markovian description is required to also capture hybridization effects between magnons and phonons, which we know to occur from the calculations performed in Sec. 2.6. However, for our simulations we will neglect the longitudinal phonon branch entirely and focus on the effect of the transverse branches. This can be justified in a twofold way: Firstly, the components (3.36) of the damping tensor for different phonon polarizations are proportional to the square of the inverse sound velocity. As the longitudinal sound velocity is larger than the transverse by approximately a factor of two, the longitudinal phonons contribute substantially less than the transverse ones to the overall damping. Secondly, the calculations carried out in Sec. 2.6 showed that to lowest order in the magnetoelastic coupling, there is no hybridization between longitudinal phonon and magnon branches for momenta parallel to the external magnetic field. These momenta are particularly relevant because the magnons there have the lowest energy, and thus magnons usually accumulate in these states

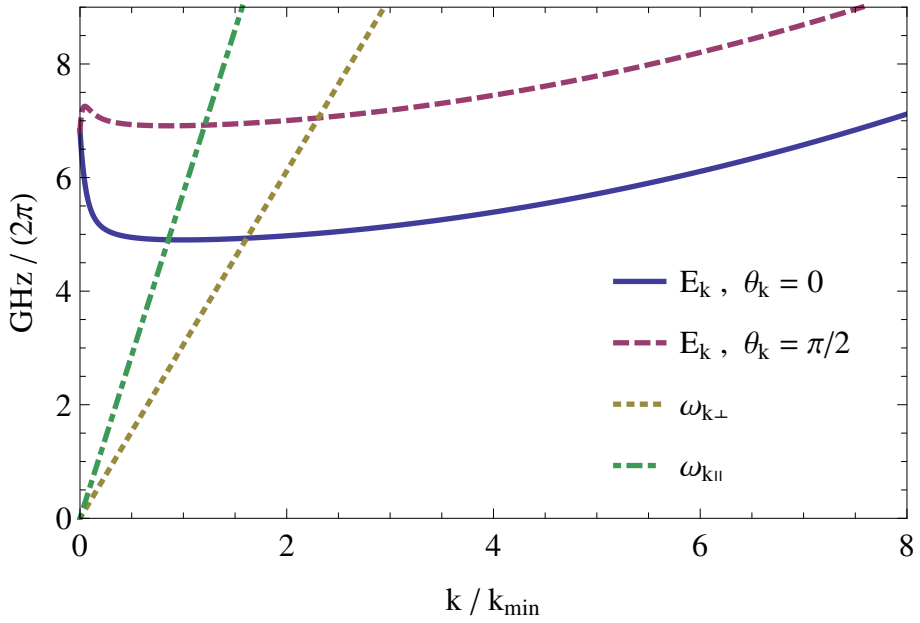

Figure 3.3: *Plot of the magnon and phonon dispersion relations of a YIG film with thickness $d = 6.7\,\mu$m in an external magnetic field $H_0 = 1710\,\mathrm{Oe} \times \mu$, for momenta $\boldsymbol{k}$ parallel ($\theta_{\boldsymbol{k}} = 0$) and perpendicular ($\theta_{\boldsymbol{k}} = \pi/2$) to the in-plane magnetic field.*

[15, 16, 17, 18, 19, 20, 21, 22, 23, 24, 84]. Transverse phonons on the other hand do hybridize for these momenta, and an experimental sign of a nonequilibrium hybridization effect has already been observed [84]. For a plot of the energy surface $E_{\boldsymbol{k}} = \omega_{\boldsymbol{k}\perp}$ of magnon-phonon resonance, and thus possible hybridization effects, in momentum space see Fig. 3.2. Finally, the phonon damping coefficient required for the numerical noise simulation will be set to $g = 10^{-3}$.

For the explicit numerical integration of the stochastic system (3.63) we have to discretize momentum space. Note that we are only interested in systems that are large enough for the thermodynamic limit to be well satisfied[5], this discretization must not be connected to the microscopic physical momentum space lattice. Instead we may choose a discretization convenient for numerics and on the same order as the resolution of the experiments [15, 16, 17, 18, 19, 20, 21, 22, 23, 24] we aim to describe[6]. Thus we work on an equidistant square grid with spacing

$$\Delta k = 0.2\, k_{\mathrm{min}}. \tag{3.66}$$

Because only the long-wavelength part of the magnon spectrum is excited

[5] Recall that the width and length of the YIG stripes used in experiments are of the order of millimeters, whereas the lattice constant is approximately 12 Å.

[6] In Ref. [75], $4490\,\mathrm{cm}^{-1}$ is given as an estimate for the minimal experimental momentum resolution of the BLS setup, which is approximately half of the lattice spacing Δk we choose for our simulation.

(and observed) in the experiments [15, 16, 17, 18, 19, 20, 21, 22, 23, 24, 84] on magnon condensation, we focus our numerics on accurately describing this regime. Therefore we will only work with a truncated momentum space with $125 \times 189 = 23625$ points, such that $|k_y| \leq 12.4\, k_{\min}$ and $|k_z| \leq 18.8\, k_{\min}$. Momentum integrations are then approximated as

$$\frac{1}{N}\sum_{\boldsymbol{k}} = \left(\frac{a}{2\pi}\right)^2 \int \mathrm{d}^2k \approx \left(\frac{a}{2\pi}\right)^2 \sum_{\boldsymbol{k}} (\Delta k)^2 \equiv \frac{1}{N_{\mathrm{eff}}}\sum_{\boldsymbol{k}}, \tag{3.67}$$

where we defined the effective lattice size parameter $N_{\mathrm{eff}} = 4\pi^2/(a\Delta k)^2 \approx 2.6 \times 10^7$. The corresponding delta distributions have to replaced according to $N\delta_{\boldsymbol{k}\boldsymbol{k}'} \to N_{\mathrm{eff}}\delta_{\boldsymbol{k}\boldsymbol{k}'}$, since $\frac{1}{N}\sum_{\boldsymbol{k}} N\delta_{\boldsymbol{k}\boldsymbol{k}'} = 1$ has to hold. Furthermore, inspection of the stochastic system (3.63) reveals that all integrations are convolutions in momentum space. Consequently they can be efficiently calculated using a fast Fourier transform algorithm [105].

To numerically simulate the system (3.63) of stochastic differential equations, a stochastic Heun scheme [47, 106] (see also App. B.2) is used. Note that as for any scheme for integrating stochastic differential equations, the convergence is rather weak and thus very small time steps are needed. For our simulations, an adequate choice for the time step turns out to be

$$\Delta t = 10^{-4}\,\mathrm{ns}. \tag{3.68}$$

Let us also remark that because we have to perform a large number of integrations at each time step, more complicated algorithms which may have higher order of convergence or even adaptive choice of time steps are not suitable for our simulations since they necessarily need to evaluate the integrals more often. The Gaussian random numbers needed at each time step are created via the polar Box-Muller algorithm [107] from independent random numbers distributed uniformly between 0 and 1.

3.6 Simulation results and interpretation

In this central section we will present the simulated stochastic time evolution of the classical magnons in a YIG film subject to parallel parametric pumping at room temperature, with the parameters described in Sec. 3.5 directly above. As we do not want to bias the simulation results in any way, we start the time evolution from a fully polarized ferromagnet state; i.e., a state which does not contain any magnons, so that $\boldsymbol{m}_{\boldsymbol{k}}(0) = 0$. Then we observe how thermal fluctuations, and at later stages the parametric pumping, populate and thermalize the whole magnon spectrum. As main observable, we choose the square of the transverse magnetization,

$$n_{\boldsymbol{k}}(t) = |m^x_{\boldsymbol{k}}(t)|^2 + |m^y_{\boldsymbol{k}}(t)|^2. \tag{3.69}$$

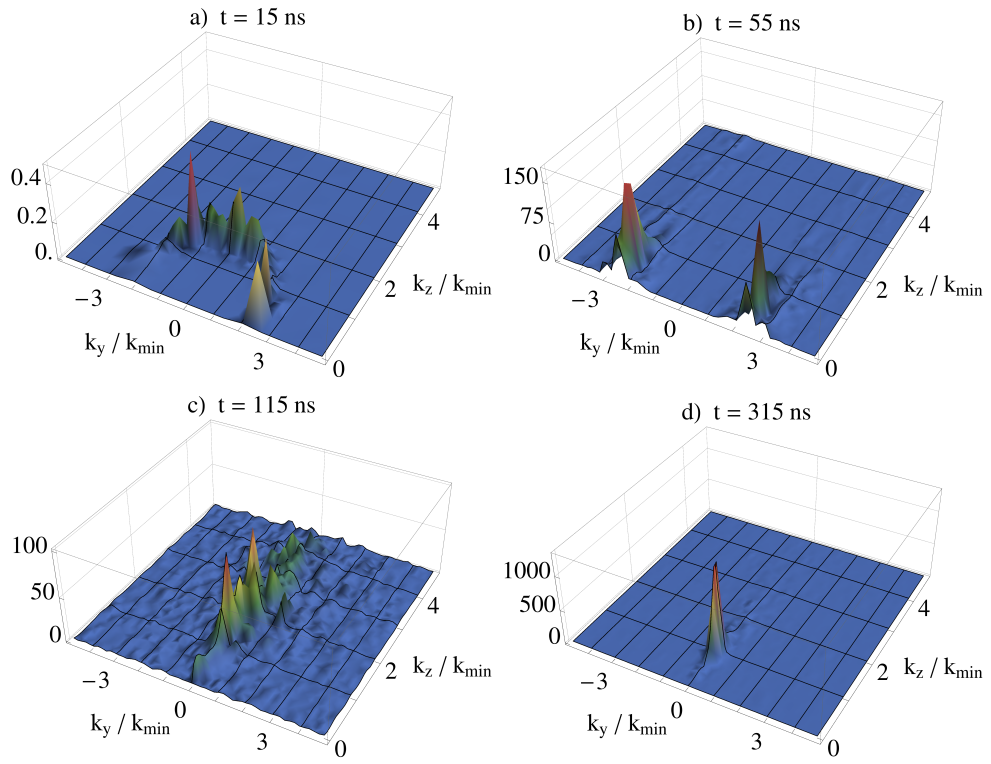

Figure 3.4: *Snapshots of the stochastic time evolution of the magnon distribution $n_{\boldsymbol{k}}(t)/n_{\boldsymbol{k}}^{\mathrm{th}}$ relative to the thermal equilibrium distribution $n_{\boldsymbol{k}}^{\mathrm{th}}$, showing (a) the magnetoelastic hybridization, (b) the parametric instability, (c) the redistribution of magnons in momentum space, and (d) the quasiequilibrium with the magnon condensate.*

This quantity gives the momentum space distribution of the classical magnons, and hence will be referred to as the magnon distribution. The ensemble average $\langle n_{\boldsymbol{k}}(t)\rangle$ is directly proportional to the magnon number of spin wave theory [3]. In particular, as long as spin wave theory is valid, i.e., as long as there are only small oscillations around the ferromagnetic ground state $\boldsymbol{S}_i = S\boldsymbol{e}_z$, the thermal equilibrium ensemble average of the magnon distribution (3.69) is proportional to the classical Rayleigh-Jeans distribution,

$$\langle n_{\boldsymbol{k}}(t)\rangle = n_{\boldsymbol{k}}^{\mathrm{th}} \propto \frac{T}{E_{\boldsymbol{k}}}. \tag{3.70}$$

A derivation of this expression in the framework of classical spin wave theory is given in App. B.1. There the exact prefactor is also given, which depends on the ellipticity of the magnons and the system size and does not play any role for our considerations.

The stochastic time evolution of the magnon distribution $n_{\boldsymbol{k}}(t)$ can be characterized by four distinct stages, which are illustrated in Fig. 3.4. In the first stage, shown in Fig. 3.4 (a), thermal fluctuations begin to populate

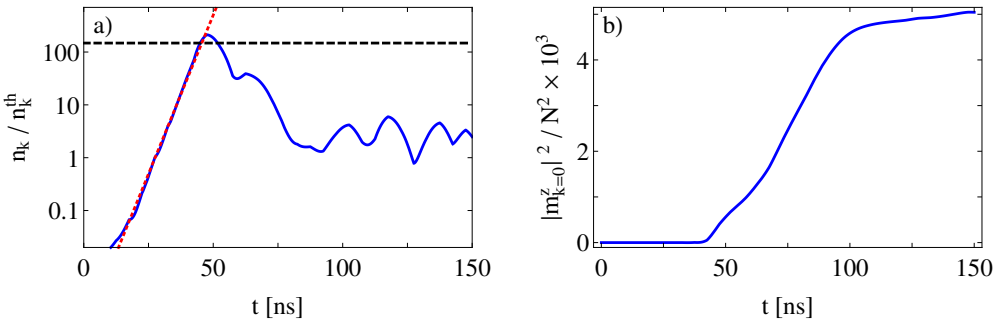

Figure 3.5: *(a) Logarithmic plot of the parametric resonance. The blue solid line shows $n_{\boldsymbol{k}}(t)/n_{\boldsymbol{k}}^{\mathrm{th}}$ for the parametrically unstable magnon with momentum $\boldsymbol{k}/k_{\min} = -2.4\boldsymbol{e}_y + 0.2\boldsymbol{e}_z$. For comparison, the red dotted line is the exponential growth (3.71) predicted by linear spin wave theory. Note that in our nonlinear theory the growth saturates at some finite value close to the S-theory steady state (3.73), which is shown as black dashed line. At later times the magnon distribution relaxes to a quasiequilibrium value. (b) Plot of the stochastic time evolution of the longitudinal uniform mode $|m^z_{\boldsymbol{k}=0}|^2/N^2$, which grows rapidly as soon as the growth of the parametrically unstable modes saturates at $t \approx 50\,\mathrm{ns}$, and saturates itself when the parametric magnons thermalize to quasiequilibrium around $t \approx 100\,\mathrm{ns}$.*

the magnon spectrum. This process is especially effective on the magnon-phonon resonance surface, where magnetoelastic hybridization allows the direct conversion of thermal phonons into magnons, see also Sec. 2.6. Thus, we observe the appearance of distinct peaks in the magnon distribution on the approximately circular resonance surface. Note that taking into account non-Markovian phonon bath correlations of the LLG (3.25) is crucial for obtaining such hybridization effects. Experimentally, this effect is hard to detect because in experiments the initial magnon distribution is already a thermal equilibrium one. In this case one expects that the hybridization effect, which drives the system to thermal equilibrium, is far less pronounced, and usually disappears in the thermal noise background. However, in the experiments [23, 84] there is a slight decrease in the magnon distribution in the overpopulated system on this hybridization surface, which could be related to the same effect.

As soon as the magnon spectrum is somewhat populated, the parametric resonance process takes effect, depicted in Fig. 3.4 (b). One can clearly see the huge increase in magnon population on the resonance surface $E_{\boldsymbol{k}} = \omega_{\mathrm{p}}$, compare also Fig. 3.2. From linear spin wave theory, it is known that the envelope of the occupation of parametrically unstable magnons diverges as [3]

$$n_{\boldsymbol{k}}(t) \propto e^{2\alpha_{\boldsymbol{k}} t}, \tag{3.71}$$

where

$$\alpha_{\boldsymbol{k}}^2 = |V_{\boldsymbol{k}} H_1|^2 - |E_{\boldsymbol{k}} - \omega_{\mathrm{p}}|^2; \tag{3.72}$$

see also Sec. 1.2.5. Here $V_{\boldsymbol{k}} = (\omega^y_{\boldsymbol{k}} - \omega^x_{\boldsymbol{k}})/(4E_{\boldsymbol{k}}) = S(D^{xx}_{\boldsymbol{k}} - D^{yy}_{\boldsymbol{k}})/(4E_{\boldsymbol{k}})$ is proportional to the ellipticity of the spin wave. Thus it is immediately obvious that the threshold of parametric instability is lowest for highly elliptic magnons. For thin YIG films, the elliptic spin waves are those close to $k_z = 0$; and as shown in Fig. 3.4 (b) this is confirmed by our simulation: The huge peaks in magnon occupation arise for those magnons close to $k_z = 0$ which have highest ellipticity; on the rest of the resonance surface, there is only a comparatively small increase. A plot of the stochastic time evolution of one of these parametric magnon modes with high ellipticity is shown as a blue line in Fig. 3.5 (a), with the linear spin wave theory prediction (3.71) as a red dotted line for comparison. One can see that the initial increase in the magnon occupation is well described by linear theory. After approximately 40 ns however, the parametric growth saturates in our simulation, in good agreement with the experiments [16, 18, 19, 22, 23, 24]. This is due the nonlinear spin-spin interactions, which we take nonperturbatively into account in our approach. A comparatively simple way of estimating the saturation value of the parametric modes is given by S-theory [37, 38, 39], which amounts to a self-consistent mean field approach taking the renormalization of the pumping field due to interactions of magnon pairs into account. In this way one obtains [10, 37, 38, 39]

$$\frac{n^{\mathrm{S}}_{\boldsymbol{k}}}{n^{\mathrm{th}}_{\boldsymbol{k}}} = \frac{NSE_{\boldsymbol{k}}}{8T\Delta}\left(|V_{\boldsymbol{k}}H_1| - |E_{\boldsymbol{k}} - \omega_{\mathrm{p}}|\right), \tag{3.73}$$

which is shown as a black dashed line in Fig. 3.5 (a), and agrees reasonably well with our simulations. Also, the interactions processes included in S-theory give a hint to the modes which are responsible for the suppression of the parametric growth: It is the coupling to the longitudinal uniform mode $m^z_{\boldsymbol{k}=0}(t)$ which, in a spin wave expansion, gives rise to the S-theory interaction. In our nonperturbative approach, we should therefore also observe the effect of the parametric pumping on the uniform mode $m^z_{\boldsymbol{k}=0}(t)$, shown in Fig. 3.5 (b). There one can see that the population of the uniform mode begins to grow as soon as the parametric magnons saturate, at $t \approx 50$ ns. Furthermore, in S-theory the saturation value (3.73) corresponds to a stationary state. In contrast to that, our simulation shows that at $t \approx 50$ ns the parametric magnon occupation starts to decay to a quasiequilibrium value although the pumping field is still present, see Fig. 3.5 (a). Such a decrease to quasiequilibrium during the pumping pulse has also been observed in the experiments [18, 19, 22, 23, 24]. Finally, at $t \approx 100$ ns the parametric magnon occupations reach their quasiequilibrium values, and at this time the growth of the longitudinal uniform mode $m^z_{\boldsymbol{k}=0}(t)$ also saturates. Note that the occupation of this uniform mode always remains very small; as it is the correction to the effective spin $S = 14.2$, this confirms that spin waves are indeed the correct description for the excitations of the spin system, even under the strongly nonequilibrium conditions of the parametric pumping. Therefore we expect that thermal equilibrium and also any

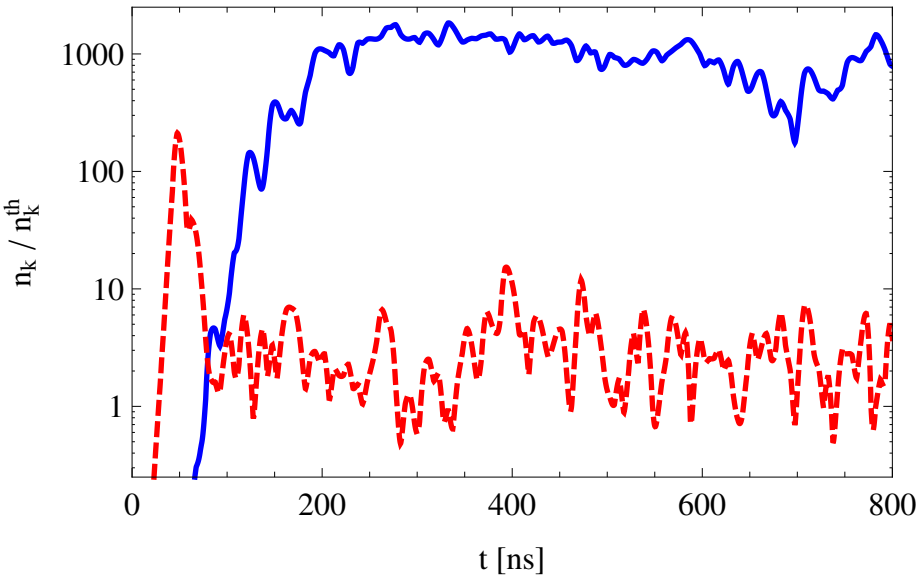

Figure 3.6: *Logarithmic plot of the stochastic time evolution of the magnon distribution $n_{\boldsymbol{k}}(t)/n_{\boldsymbol{k}}^{\mathrm{th}}$ of the condensing mode $\boldsymbol{k} = k_{\mathrm{min}}\boldsymbol{e}_z$ (blue solid line), and of the parametrically unstable mode with momentum $\boldsymbol{k}/k_{\mathrm{min}} = -2.4\boldsymbol{e}_y + 0.2\boldsymbol{e}_z$ (red dashed line). Note that the growth of the condensate begins as soon as the parametrically excited magnons have relaxed to quasiequilibrium.*

quasiequilibrium state is described by the Rayleigh-Jeans distribution (3.2) as predicted by spin wave theory.

After the parametric resonance peaks disappear, the third stage of the nonequilibrium time evolution begins: The thermalization of the highly populated magnon gas generated via the parametric pumping to a quasiequilibrium state, displayed in Fig. 3.4 (c). Due to the nonlinear spin-spin interactions, the excess magnons which arise from the parametric instability are redistributed over the whole momentum space and eventually scattered to the lowest energy states close to $k_y = 0$; again in agreement with the observations in the experiments [20, 23].

In the final stage shown in Fig. 3.4 (d), this redistribution process is finished and a large number of magnons has accumulated precisely at the momenta $\boldsymbol{k} = \pm k_{\mathrm{min}}\boldsymbol{e}_z$ corresponding to the bottom of the magnon spectrum, thereby establishing the Rayleigh-Jeans condensate. Fig. 3.6 displays the stochastic time evolution on the condensing mode, with a parametrically unstable mode for comparison. The formation of the condensate is finished at $t \approx 200\,\mathrm{ns}$; at later times, there are only small oscillations around a quasiequilibrium state for all modes. Let us stress that this time scale of condensate formation agrees very well with the experiments [16, 18, 19, 23]. The quasiequilibrium is stable as long as the parametric pumping field is present. Therefore we may use the ergodic hypothesis presented in Sec. 1.5.2 to obtain ensemble averages by

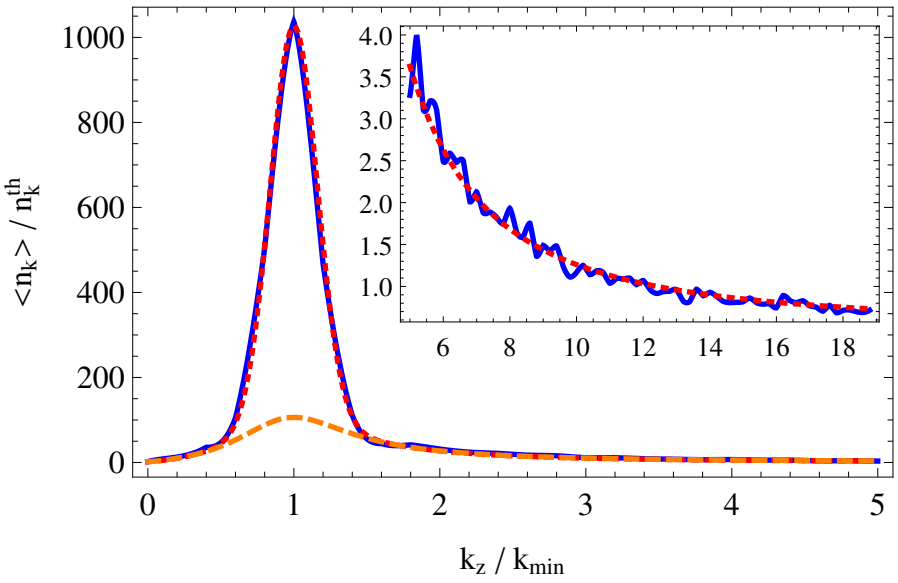

Figure 3.7: *Time-averaged quasiequilibrium magnon distribution function* $\langle n_{\boldsymbol{k}}(t)\rangle/n_{\boldsymbol{k}}^{\mathrm{th}}$ *(blue solid line) on the axis* $k_y = 0$*. The red dotted line shows the fit (3.74) with effective chemical potential* $\mu_{\mathrm{eff}} = 0.995E_{\mathrm{min}}$*, while the orange dashed line is the thermal part alone. The condensate contribution is modeled as a Gaussian centered at* $\boldsymbol{k} = k_{\mathrm{min}}\boldsymbol{e}_z$ *with standard deviations* $\sigma_z = 0.16k_{\mathrm{min}}$ *and* $\sigma_y = 0.1k_{\mathrm{min}}$*, which are both smaller than the lattice spacing* $\Delta k = 0.2k_{\mathrm{min}}$ *of the numerics. The inset shows a magnified view of the fit away from the condensate; axes are the same as in the main plot.*

averaging on time. Choosing the interval between 200 and 800 ns for the time average yields the quasiequilibrium distribution

$$\frac{\langle n_{\boldsymbol{k}}(t)\rangle}{n_{\boldsymbol{k}}^{\mathrm{th}}} \propto \frac{E_{\boldsymbol{k}}}{E_{\boldsymbol{k}} - \mu_{\mathrm{eff}}} + n_c\left[\delta(\boldsymbol{k} - k_{\mathrm{min}}\boldsymbol{e}_z) + \delta(\boldsymbol{k} + k_{\mathrm{min}}\boldsymbol{e}_z)\right]. \tag{3.74}$$

Here the first part describes the thermal magnon cloud and is given by a rescaled Rayleigh-Jeans distribution with effective chemical potential equal to the minimal magnon energy, $\mu_{\mathrm{eff}} \approx E_{\mathrm{min}}$. The second contribution are two delta-like peaks with weight n_c centered at $\boldsymbol{k} = \pm k_{\mathrm{min}}\boldsymbol{e}_z$ that correspond to the condensate. By running the simulations with different resolutions Δk it has been confirmed numerically that the width of the peaks is always on the order of the numerical resolution Δk; i.e., the each condensate is essentially only one point in the discretized momentum space, and thus it exhibits truly a delta-like behavior. In that way we numerically prove that the classical spin dynamics indeed gives rise to Rayleigh-Jeans condensation of magnons at the minima of the energy dispersion. Both the actual numerical time average and our fitting function (3.74) are displayed in Fig. 3.7 for different momentum ranges. Especially note that the condensate peaks are anisotropic,

reflecting the anisotropy of the magnon dispersion; this feature was experimentally observed in Ref. [20]. Also, let us emphasize that the retardation of the dissipation kernel (3.21), i.e., the non-Markovian memory effects, are not essential for the appearance of the Rayleigh-Jeans condensate. However, numerical simulations have shown that a phenomenological damping kernel with shorter correlation time requires unphysical values for the magnetoelastic coupling and the parametric pumping field to achieve a similar condensation.

Microscopically, the quasiequilibrium state (3.74) is well described by the ansatz

$$m_i^x(t) = \sum_{s=\pm} M_s \cos\left[sk_{\min}\boldsymbol{e}_z \cdot \boldsymbol{R}_i + \phi_s(t)\right] + \delta m_i^x(t), \tag{3.75a}$$

$$m_i^y(t) = \sum_{s=\pm} M_s \sin\left[sk_{\min}\boldsymbol{e}_z \cdot \boldsymbol{R}_i + \phi_s(t)\right] + \delta m_i^y(t), \tag{3.75b}$$

for the transverse magnetization. Here the first contribution is the superposition of the two coherent circular spin waves with momenta $\pm k_{\min}\boldsymbol{e}_z$ that is the condensate, with real amplitudes $M_\pm$, and real phases $\phi_\pm(t)$ that contain the time dependence. The second part describes the thermal cloud of uncondensed magnons as Gaussian random processes $\delta m_i^x(t)$ and $\delta m_i^y(t)$ with vanishing mean and a covariance proportional to the classical Rayleigh-Jeans distribution. With the ansatz (3.75) the ensemble average of the magnon distribution is given by

$$\langle n_{\boldsymbol{k}}(t)\rangle = N\frac{M_+^2 + M_-^2}{2}\left[N\delta_{\boldsymbol{k},k_{\min}\boldsymbol{e}_z} + N\delta_{\boldsymbol{k},-k_{\min}\boldsymbol{e}_z}\right] + \langle \delta n_{\boldsymbol{k}}(t)\rangle, \tag{3.76}$$

where $\delta n_{\boldsymbol{k}}(t) = |\delta m_{\boldsymbol{k}}^x(t)|^2 + |\delta m_{\boldsymbol{k}}^y(t)|^2$. In the thermodynamic limit we now have $N\delta_{\boldsymbol{k},\pm k_{\min}\boldsymbol{e}_z} \propto \delta(\boldsymbol{k} \mp k_{\min}\boldsymbol{e}_z)$. Thus we can identify the macroscopic condensate occupation $M_+^2 + M_-^2 \propto n_c$ and the thermal magnon distribution $\langle \delta n_{\boldsymbol{k}}(t)\rangle \propto T/\left(E_{\boldsymbol{k}} - \mu_{\text{eff}}\right)$, thereby completing the connection between the ansatz (3.75) and the actual quasiequilibrium distribution (3.74) obtained from numerical simulations. Instead of the describing the condensate directly with the transverse magnetization components as in the ansatz (3.75), often the circular magnetization component, defined as

$$\psi_i(t) = m_i^x(t) + im_i^y(t) \tag{3.77a}$$

$$= \psi_+(t)e^{ik_{\min}\boldsymbol{e}_z\cdot\boldsymbol{R}_i} + \psi_-(t)e^{-ik_{\min}\boldsymbol{e}_z\cdot\boldsymbol{R}_i} + \delta\psi_i(t), \tag{3.77b}$$

is employed. In this description, the condensate is a complex plane wave with forward and backward traveling amplitudes $\psi_\pm(t) = M_\pm e^{i\phi_\pm(t)}$, and the thermal magnons are contained in the complex Gaussian random process $\delta\psi_i(t) = \delta m_i^x(t) + i\delta m_i^y(t)$. The conventional, quantum approach to magnon condensation claims that the plane wave part of the circular magnetization (3.77) is in fact the quantum mechanical wave function of the condensate [21], hence the letter ψ. This would imply that it is only a probability amplitude,

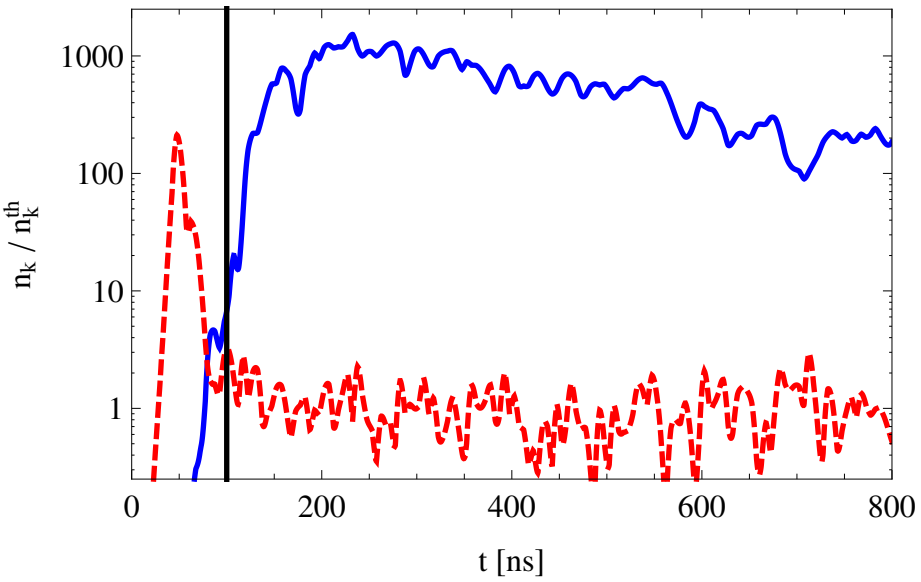

Figure 3.8: *Logarithmic plot of the stochastic time evolution of the magnon distribution $n_{\boldsymbol{k}}(t)/n_{\boldsymbol{k}}^{\mathrm{th}}$ of the condensing mode $\boldsymbol{k} = k_{\min}\boldsymbol{e}_z$ (blue solid line), and of the parametrically unstable mode with momentum $\boldsymbol{k}/k_{\min} = -2.4\boldsymbol{e}_y + 0.2\boldsymbol{e}_z$ (red dashed line), for the case that the pumping is turned off at $t = 100\,\mathrm{ns}$ (black line). For the simulation, the same sequence of random numbers as in Fig. 3.6 has been used. Note that while the parametric magnon decays to thermal equilibrium immediately after the end of the pumping, the condensate appears just as for continuous pumping (compare Fig. 3.6), but it begins to slowly decay around $t \approx 250\,\mathrm{ns}$.*

and consequently the square $|\psi_i(t) - \delta\psi_i(t)|^2$ of the coherent transverse magnetization is identified with the (unnormalized) local probability distribution of the condensate. In contrast, in our classical spin system such an expression for the circular magnetization component (3.77) arises naturally without making any claim about it being a quantum wave function. Instead it is only a classical coherent spin wave, immersed in thermal noise.

In addition to the formation of the condensate and the quasiequilibrium state under pumping, our numerical simulations also allow us to probe the decay of the condensate and eventual thermalization to the phonon bath. Therefore we set up a simulation in which the parametric pumping field is turned off at $t = 100\,\mathrm{ns}$, similar to the experiments [18, 19, 20, 23] where only a short pumping pulse is used to excite the magnons. The resulting stochastic time evolution of the condensate and a parametric mode is shown in Fig. 3.8. In this situation the condensate still forms just as in the continuously pumped case, but starts to decay at $t \approx 250\,\mathrm{ns}$. This behavior is in good agreement with the aforementioned experiments [18, 19, 20, 23], where such an emergence and subsequent decay of the condensate after the end of a short pumping pulse

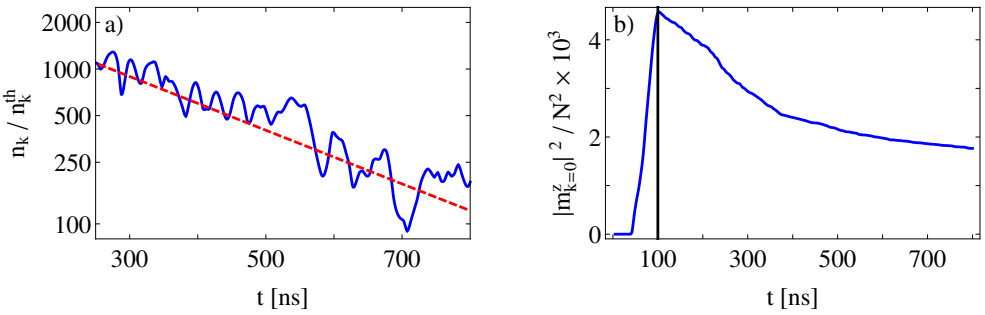

Figure 3.9: *(a) Logarithmic plot of the decay of the condensate, for the case that the parametric pumping is turned off at* $t = 100\,\mathrm{ns}$. *The blue line denotes the magnon distribution* $n_{\boldsymbol{k}}(t)/n^{\mathrm{th}}_{\boldsymbol{k}}$ *at* $\boldsymbol{k} = k_{\mathrm{min}}\boldsymbol{e}_z$, *whereas the red dashed line is an exponential fit with the condensate lifetime* $\tau_{\mathrm{c}} \approx 250\,\mathrm{ns}$. *(b) Plot of the stochastic time evolution of the longitudinal uniform mode* $|m^z_{\boldsymbol{k}=0}|^2/N^2$. *As soon as the pumping is turned off at* $t = 100\,\mathrm{ns}$ *the uniform mode starts to decay.*

is observed. Note that such a condensate formation without applied external pumping is characteristic of a condensation process, which depends only on the overpopulation of the whole system, and rules out direct kinetic instabilities [95, 96, 97, 108, 109] induced by the parametric pumping as explanation. In contrast to the condensate, the longitudinal uniform mode $m^z_{\boldsymbol{k}=0}(t)$, which renormalizes the parametric pumping, decays as soon as the pumping field is turned off, see Fig. 3.9 (b). The decay of the condensate, depicted in Fig. 3.9 (a), turns out to be well fitted by an exponential, with a characteristic lifetime

$$\tau_{\mathrm{c}} \approx 250\,\mathrm{ns}, \tag{3.78}$$

in excellent agreement with the experiments [19, 24].

3.7 Summary and conclusions

In this chapter, we have theoretically investigated the intriguing phenomenon of room temperature magnon condensation in thin films of the magnetic insulator YIG, experimentally observed in Refs. [15, 16, 17, 18, 19, 20, 21, 22, 23, 24]. While current thinking tends to attribute this condensation process to quantum mechanical effects and hence terms it Bose-Einstein condensate, we have proven that a completely classical description is sufficient to achieve the condensation. Inspired by the twin facts that the energy scale of room temperature is very large compared to the energy scale of the condensing spin waves, and that quantum fluctuations in YIG are suppressed by a very large spin, we have proposed that the magnon condensation should be explained as a condensation of classical waves. A similar condensation of classical light waves has been observed recently in photorefractive crystals by Sun *et al.* [100], giving both ex-

perimental and theoretical proof that such classical condensations are possible. As such classical waves are subject to the Rayleigh-Jeans distribution as compared to the Bose-Einstein distribution of quantum mechanics, these classical condensation processes should be referred to as Rayleigh-Jeans condensation. The two necessary requirements for this condensation process to actually occur have been identified as nonlinear wave interactions and randomness.

Starting from the known microscopic Hamiltonian for interacting spins and phonons in YIG films, we have therefore derived a non-Markovian stochastic Landau-Lifshitz-Gilbert equation (LLG) for the classical spins. This equation includes all classical spin-spin interactions nonperturbatively, and also thermal noise generated by the microscopic phonon dynamics. Compared to the conventional LLG, which employs a phenomenological white noise damping, the microscopically derived noise term in our equation is tensorial, nonlocal in space, and contains memory effects. Consequently it suffers from no ambiguities of stochastic calculus, and is reliable even on short time scales and when magnon and thermal phonon bath dynamics have the same time scale, as is the case for the magnon condensation in YIG films. An additional advantage of the non-Markovian LLG comes from the fact that we derived it from a well-characterized microscopic Hamiltonian, so there is no adjustable parameter in our equation that could be used for fitting results.

By performing simulations of the classical spin dynamics generated by the non-Markovian LLG for a thin YIG film in the presence of a parallel parametric pumping field, we have been able to identify four distinct stages of the nonequilibrium time evolution: Magnon-phonon hybridization at early stages, followed by the parametric resonance regime and the thermalization of the magnon system to a quasiequilibrium state, which includes a condensate at the bottom of the magnon spectrum for sufficient pumping. By turning off the parametric pumping at earlier times, we have also confirmed that the emergence of the condensate depends only on the overpopulation of the magnon system, and that it decays exponentially to thermal equilibrium with the thermal bath of phonons without external driving. Finally, using the ergodic hypothesis we have obtained the quasiequilibrium distribution of the pumped magnons, which consists of a thermal magnon cloud and delta-like peaks, i.e., the condensate, located at the momenta where the magnon dispersion acquires its minimum value. The delta-like character of the condensate has been established by comparing the width of the peak with the resolution of the momentum grid chosen for the simulation. For the thermal cloud, it has been shown that a Rayleigh-Jeans distribution with chemical potential equal to the minimal magnon energy emerges as the correct fitting function for the numerical result. Therefore we have concluded that we have indeed numerically observed a Rayleigh-Jeans condensation. It has also been confirmed that the time scales of our simulation are in good agreement with the experiment; in particular, the lifetime of the condensate in our simulation agrees perfectly with measurements. To the best of our knowledge, such a complete description

of the nonequilibrium time evolution of the pumped magnon gas in YIG, which agrees not only qualitatively but also quantitatively with the experiments, has not been achieved before. Thus we have been lead to the conclusion that the experimentally observed condensation of magnons can be explained without resorting to quantum mechanics, as a interaction effect in a random ensemble of classical spins.

An obvious way of extending this work is to optimize the numerical simulation. In particular, it would be desirable to directly calculate ensemble averages and not stochastic trajectories, without introducing any oversimplifying approximations. If one is only interested in qualitative features of the nonequilibrium dynamics and condensation of magnons, it is also reasonable to use a functional integral representation of the stochastic differential equation 3.25. Then one may apply powerful nonperturbative methods like the functional renormalization group [59] to extract generic features of the nonequilibrium dynamics. It might also be worthwhile to investigate the condensation pattern in real space that emerges due to the interference of the two condensing spin waves with finite momenta [21]. Furthermore, it may prove insightful to explore the crossover from the classical to the quantum spin system, which should occur at sufficiently low temperatures.

Appendix A

Magnetoelastic modes and lifetime of magnons

A.1 Magnetoelastic modes from equations of motion

This appendix serves to present an alternative way of obtaining the dispersion relation (2.63) of the magnetoelastic modes by solving the linearized Heisenberg equations of motion for the spin and phonon operators. Although less general than our derivation of Sec. 2.6, this approach is more in the spirit of previous works [3] that employ classical equations of motion.

In order to compute the dispersion relation (2.63) of the magnetoelastic modes, we start by explicitly writing down the linearized Heisenberg equations for the coupled spin-phonon system in the Holstein-Primakoff basis,

$$i\dot{b}_{\boldsymbol{k}} = A_{\boldsymbol{k}} b_{\boldsymbol{k}} + B_{\boldsymbol{k}} b^{\dagger}_{-\boldsymbol{k}} + \boldsymbol{\Gamma}^{*}_{\boldsymbol{k}} \cdot \boldsymbol{X}_{\boldsymbol{k}}, \tag{A.1a}$$

$$-i\dot{b}^{\dagger}_{-\boldsymbol{k}} = A_{\boldsymbol{k}} b^{\dagger}_{-\boldsymbol{k}} + B_{\boldsymbol{k}} b_{\boldsymbol{k}} + \boldsymbol{\Gamma}_{-\boldsymbol{k}} \cdot \boldsymbol{X}_{\boldsymbol{k}}, \tag{A.1b}$$

$$\dot{X}_{\boldsymbol{k}\lambda} = \frac{P_{\boldsymbol{k}\lambda}}{M}, \tag{A.1c}$$

$$\dot{P}_{\boldsymbol{k}\lambda} = -M\omega^{2}_{\boldsymbol{k}\lambda} X_{\boldsymbol{k}\lambda} - \Gamma_{\boldsymbol{k}\lambda} b_{\boldsymbol{k}} - \Gamma^{*}_{-\boldsymbol{k}\lambda} b^{\dagger}_{-\boldsymbol{k}}. \tag{A.1d}$$

Up to leading order in the $1/S$ expansion, we may now identify the Fourier components of the transverse spin operators as

$$S^{x}_{\boldsymbol{k}} = \frac{\sqrt{2S}}{2}\left(b_{\boldsymbol{k}} + b^{\dagger}_{-\boldsymbol{k}}\right), \tag{A.2a}$$

$$S^{y}_{\boldsymbol{k}} = \frac{\sqrt{2S}}{2i}\left(b_{\boldsymbol{k}} - b^{\dagger}_{-\boldsymbol{k}}\right). \tag{A.2b}$$

This allows us to recast the linearized equations of motion (A.1a) and (A.1b) for the transverse spin in the form

$$\dot{S}^{x}_{\boldsymbol{k}} = (A_{\boldsymbol{k}} - B_{\boldsymbol{k}})\, S^{y}_{\boldsymbol{k}} + iB_{\perp}\boldsymbol{k}_{yz} \cdot \boldsymbol{X}_{\boldsymbol{k}}, \tag{A.3a}$$

$$\dot{S}^{y}_{\boldsymbol{k}} = -(A_{\boldsymbol{k}} + B_{\boldsymbol{k}})\, S^{x}_{\boldsymbol{k}} - iB_{\perp}\boldsymbol{k}_{xz} \cdot \boldsymbol{X}_{\boldsymbol{k}}, \tag{A.3b}$$

whereas the equation of motion (A.1d) of the phonon momentum becomes

$$\dot{P}_{\boldsymbol{k}\lambda} = -M\omega_{\boldsymbol{k}\lambda}^2 X_{\boldsymbol{k}\lambda} + i\frac{B_\perp}{S}\boldsymbol{e}_{\boldsymbol{k}\lambda}^* \cdot (\boldsymbol{k}_{xz} S_{\boldsymbol{k}}^x + \boldsymbol{k}_{yz} S_{\boldsymbol{k}}^y)\,. \tag{A.4}$$

Note that the two first order equations of motion (A.1c) and (A.4) for the phonons can be combined into a single second order equation of motion,

$$\ddot{X}_{\boldsymbol{k}\lambda} + \omega_{\boldsymbol{k}\lambda}^2 X_{\boldsymbol{k}\lambda} = i\frac{B_\perp}{MS}\boldsymbol{e}_{\boldsymbol{k}\lambda}^* \cdot (\boldsymbol{k}_{xz} S_{\boldsymbol{k}}^x + \boldsymbol{k}_{yz} S_{\boldsymbol{k}}^y)\,, \tag{A.5}$$

which is a harmonic oscillator externally driven by the spin dynamics.

For vanishing magnetoelastic coupling, the transverse spin equations of motion (A.3) can similarly be reduced to a harmonic oscillator form,

$$\ddot{S}_{\boldsymbol{k}}^\alpha + E_{\boldsymbol{k}}^2 S_{\boldsymbol{k}}^\alpha = 0, \;\; \alpha = x, y, \tag{A.6}$$

with the magnon dispersion $E_{\boldsymbol{k}} = \sqrt{A_{\boldsymbol{k}}^2 - |B_{\boldsymbol{k}}|^2}$. In the case of finite magnetoelastic coupling, the dispersion relations of the magnetoelastic modes is given by the roots of the secular determinant of the above equations of motion (A.3) and (A.5). As in Sec. 2.6 we now assume for simplicity that we are considering a momentum range in which the energy of only one phonon mode $\omega_{\boldsymbol{k}\lambda}$ (either transverse or longitudinal) is close to the magnon energy $E_{\boldsymbol{k}}$. Then it is sufficient to neglect the other phonon polarization and approximate $\boldsymbol{X}_{\boldsymbol{k}} \approx X_{\boldsymbol{k}\lambda}\boldsymbol{e}_{\boldsymbol{k}\lambda}$, and the magnetoelastic dispersion relation may be obtained as roots of the following quartic secular equation:

$$\begin{aligned}\left(\omega^2 - E_{\boldsymbol{k}}^2\right)\left(\omega^2 - \omega_{\boldsymbol{k}\lambda}^2\right) =& \frac{B_\perp^2}{MS}\Big\{(A_{\boldsymbol{k}} + B_{\boldsymbol{k}})\,|\boldsymbol{k}_{yz}\cdot\boldsymbol{e}_{\boldsymbol{k}\lambda}|^2 + (A_{\boldsymbol{k}} - B_{\boldsymbol{k}})\,|\boldsymbol{k}_{xz}\cdot\boldsymbol{e}_{\boldsymbol{k}\lambda}|^2 \\ &+ 2\omega\mathrm{Im}\big[(\boldsymbol{k}_{xz}\cdot\boldsymbol{e}_{\boldsymbol{k}\lambda})\,(\boldsymbol{k}_{yz}\cdot\boldsymbol{e}_{\boldsymbol{k}\lambda}^*)\big]\Big\}.\end{aligned} \tag{A.7}$$

For a thin YIG film, the phonon polarization vectors $\boldsymbol{e}_{\boldsymbol{k}\lambda}$ can always be chosen in such a way that the last term in the above secular equation (A.7) vanishes; see for example the basis given in Sec. 1.2.4 and used throughout this thesis. With this choice of phonon basis, the secular equation (A.7) is biquadratic and has the solutions

$$\Omega_{\boldsymbol{k}\lambda\pm}^2 = \frac{\omega_{\boldsymbol{k}\lambda}^2 + E_{\boldsymbol{k}}^2}{2} \pm \sqrt{\frac{\left(\omega_{\boldsymbol{k}\lambda}^2 - E_{\boldsymbol{k}}^2\right)^2}{4} + \Delta_{\boldsymbol{k}\lambda}^4}, \tag{A.8}$$

where the magnetoelastic hybridization energy scale is

$$\Delta_{\boldsymbol{k}\lambda}^4 = \frac{B_\perp^2}{MS}\Big[(A_{\boldsymbol{k}} + B_{\boldsymbol{k}})\,|\boldsymbol{k}_{yz}\cdot\boldsymbol{e}_{\boldsymbol{k}\lambda}|^2 + (A_{\boldsymbol{k}} - B_{\boldsymbol{k}})\,|\boldsymbol{k}_{xz}\cdot\boldsymbol{e}_{\boldsymbol{k}\lambda}|^2\Big] \tag{A.9a}$$

$$= 2\frac{E_{\boldsymbol{k}}}{M}|\Gamma_{\boldsymbol{k}\lambda}^\beta|^2, \tag{A.9b}$$

as derived by functional integral methods in Sec. 2.6.

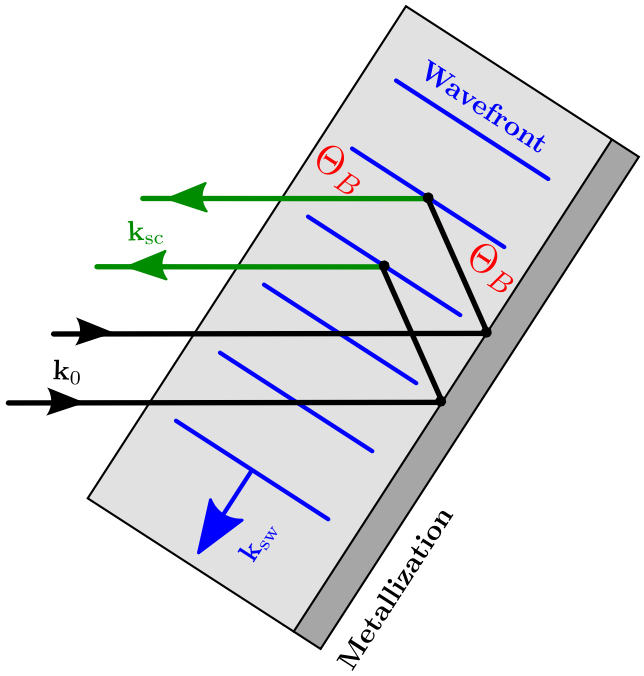

Figure A.1: *Concept of BLS spectroscopy: The incident laser beam with momentum k_0 is reflected at the metalized back-side of the sample and then scatters inelastically from the Bragg grating created by the spin wave with momentum k_{sw}. The scattered light with momentum k_{sc} is collected in the detector (not shown) for different angles of incidence Θ_B.*

A.2 Brillouin light scattering spectroscopy

Brillouin light scattering (BLS) spectroscopy is one of the main experimental tools for investigating magnetization dynamics in thin films and confined elements [13, 75, 78]. Since it is also used in the experimental part of the work presented in Ch. 2, we devote this appendix to a brief introduction to this technique. For a more detailed discussion, see, for example, Ref. [75].

The basic principle of BLS spectroscopy is the inelastic scattering of light, i.e., photons, by spin waves. In the experiment, a probing laser beam with fixed momentum k_0 is focused on the magnetic sample, and the reflected light is usually collected in a tandem Fabry-Pérot interferometer. The inelastic light scattering process can be understood classically as diffraction of the incident light by a moving Bragg-grating generated by the spin wave, as shown in Fig. A.1. In this case, both frequency and momentum of the light are changed. The frequency of the spin wave is then equal to the frequency shift of the reflected light; and the intensity of the reflected light is proportional to the density of magnons with that particular frequency.

The momentum of the spin wave can be extracted from the propagation direction of the inelastically scattered light. In particular, the maximum momentum transfer can be observed when spin wave and incident light satisfy

the Bragg condition

$$k_{\mathrm{sw}} = 2k_0 \sin(\Theta_B). \tag{A.10}$$

Here k_{sw} is the in-plane momentum of the spin wave and Θ_B is the angle of incidence, i.e., the angle between the momenta of spin wave and incident light. From the Bragg condition (A.10), it is also possible to estimate the experimentally achievable momentum resolution as

$$\Delta k_{\mathrm{sw}} = 2k_0 \cos(\Theta_B)\Delta\Theta_B, \tag{A.11}$$

where $\Delta\Theta_B$ is the error in the determination of the angle of incidence Θ_B. The minimal momentum resolution of a given setup is thus achieved for spin waves close to the ferromagnetic resonance at $k_{\mathrm{sw}} = 0$.

A.3 Triangle integration

In this appendix we present the so-called triangle method [110] for the numerical evaluation of two-dimensional integrals on Dirac delta distributions; i.e., we are concerned with integrals of the form

$$I(\epsilon) = \int \frac{\mathrm{d}^2k}{(2\pi)^2}\, F(\boldsymbol{k})\delta(E(\boldsymbol{k}) - \epsilon) \tag{A.12a}$$

$$= \int_{E(\boldsymbol{k})=\epsilon} \frac{\mathrm{d}l}{(2\pi)^2}\, \frac{F(\boldsymbol{k})}{|\nabla E(\boldsymbol{k})|}. \tag{A.12b}$$

The idea of the triangle integration is to cover the Brillouin zone with non-overlapping triangles with neighboring $\boldsymbol{k}$-points at the corners, and calculate the integral (A.12) by adding up the contributions from all triangles.

In each triangle, the functions $F(\boldsymbol{k})$ and $E(\boldsymbol{k})$ are interpolated linearly as

$$F(\boldsymbol{k}) = f_0 + \boldsymbol{f}\cdot\boldsymbol{k}, \tag{A.13a}$$

$$E(\boldsymbol{k}) = e_0 + \boldsymbol{v}\cdot\boldsymbol{k}. \tag{A.13b}$$

Then the contribution of this given triangle to the total integral (A.12) is given by

$$i(\epsilon) = f_0 D(\epsilon) + \boldsymbol{f}\cdot\boldsymbol{d}(\epsilon), \tag{A.14}$$

with coefficients

$$D(\epsilon) = \frac{1}{(2\pi)^2|\boldsymbol{v}|} l, \tag{A.15a}$$

$$\boldsymbol{d}(\epsilon) = \frac{1}{(2\pi)^2|\boldsymbol{v}|} \int_{E(\boldsymbol{k})=\epsilon} \boldsymbol{k}\mathrm{d}l. \tag{A.15b}$$

Here $l = |\boldsymbol{l}|$ is the length of the equipotential line on the triangle.

For the evaluation of the integral in the linear coefficient (A.15b), we will assume that the energies on the corners of the triangle are ordered such that

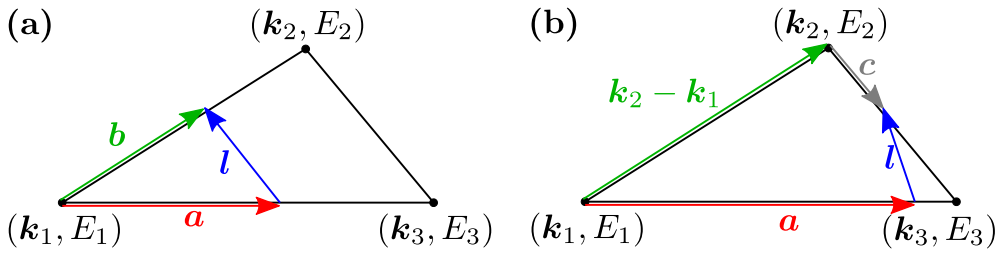

Figure A.2: *Geometry of the triangle for (a) $E_1 < \epsilon \leq E_2$ and (b) $E_2 < \epsilon \leq E_3$. In both cases the length vector $\boldsymbol{l}$ describing the equipotential line can be calculated by simple vector operations.*

$E_1 \leq E_2 \leq E_3$, where we abbreviated $E(\boldsymbol{k}_i) = E_i$. Depending on the value of ϵ, four cases need to be considered, with the two non-trivial ones illustrated in Fig. A.2:

1. $\epsilon \leq E_1$: No contribution, $D(\epsilon) = 0$, $\boldsymbol{d}(\epsilon) = 0$.

2. $E_1 < \epsilon \leq E_2$: The length vector is $\boldsymbol{l} = \boldsymbol{a} - \boldsymbol{b}$, where $\boldsymbol{a} = [(\epsilon - E_1)/(E_2 - E_1)]\,(\boldsymbol{k}_2 - \boldsymbol{k}_1)$ and $\boldsymbol{b} = [(\epsilon - E_1)/(E_3 - E_1)]\,(\boldsymbol{k}_3 - \boldsymbol{k}_1)$. Parametrizing the integral along the curve depicted in Fig. A.2 yields

$$\int_0^l \boldsymbol{k} \mathrm{d}l = l\left(\boldsymbol{b} + \frac{\boldsymbol{l}}{2}\right). \tag{A.16}$$

3. $E_2 < \epsilon \leq E_3$: The length vector is $\boldsymbol{l} = \boldsymbol{k}_2 - \boldsymbol{k}_1 + \boldsymbol{c} - \boldsymbol{b}$, where $\boldsymbol{c} = [(\epsilon - E_2)/(E_3 - E_2)]\,(\boldsymbol{k}_3 - \boldsymbol{k}_2)$, and the integral is again given by

$$\int_0^l \boldsymbol{k} \mathrm{d}l = l\left(\boldsymbol{b} + \frac{\boldsymbol{l}}{2}\right). \tag{A.17}$$

4. $\epsilon > E_3$: No contribution, $D(\epsilon) = 0$, $\boldsymbol{d}(\epsilon) = 0$.

Appendix B

Rayleigh-Jeans condensation of pumped magnons

B.1 Spin waves in thermal equilibrium

In this appendix we apply linear spin wave theory to obtain the classical ensemble average of the magnon distribution in YIG films in thermal equilibrium. Consequently, we neglect the parametric pumping field and all magnetoelastic interactions. As the ground state in this case is ferromagnetic, we may safely assume that the transverse components of the spin deviation vector $\boldsymbol{m}_i = (\boldsymbol{S}_i - S\boldsymbol{e}_z)/S$ are small compared to unity. Then it is possible expand the longitudinal component as

$$m_i^z = \sqrt{1-(m_i^x)^2-(m_i^y)^2} - 1 \approx -\frac{1}{2}\left[(m_i^x)^2 + (m_i^y)^2\right]. \tag{B.1}$$

In this approximation, the magnetic Hamiltonian (3.4) becomes a quadratic form,

$$\begin{aligned}\mathcal{H}_{\mathrm{m}} \approx & -SNH_0 - \frac{S^2}{2}\sum_{ij}\mathbb{K}_{ij}^{zz} \\ & + \frac{S}{2}\sum_{ij}\sum_{\alpha\in\{x,y\}}\left[\delta_{ij}\left(H_0 + S\sum_n \mathbb{K}_{in}^{zz}\right) - S\mathbb{K}_{ij}^{\alpha\alpha}\right] m_i^\alpha m_j^\alpha \\ = & -SNH_0 - \frac{S^2}{2}\mathbb{K}_{\boldsymbol{k}=0}^{zz} + \frac{S}{2N}\sum_{\boldsymbol{k}}\sum_{\alpha\in\{x,y\}}\omega_{\boldsymbol{k}}^\alpha m_{-\boldsymbol{k}}^\alpha m_{\boldsymbol{k}}^\alpha,\end{aligned} \tag{B.2}$$

with $\omega_{\boldsymbol{k}}^\alpha = H_0 + S\left(\mathbb{K}_{\boldsymbol{k}=0}^{zz} - \mathbb{K}_{\boldsymbol{k}}^{\alpha\alpha}\right)$. Because we are now dealing with noninteracting spin waves, it is again advantageous to introduce the complex normal modes

$$\phi_{\boldsymbol{k}} = \left(\frac{\omega_{\boldsymbol{k}}^x}{\omega_{\boldsymbol{k}}^y}\right)^{1/4} m_{\boldsymbol{k}}^x + i\left(\frac{\omega_{\boldsymbol{k}}^y}{\omega_{\boldsymbol{k}}^x}\right)^{1/4} m_{\boldsymbol{k}}^y, \tag{B.3}$$

that were already used in Sec. 1.2.5 to study the parametric instability. In terms of them, the above Hamiltonian (B.2) is given by

$$\mathcal{H}_{\mathrm{m}} = -SNH_0 - \frac{S^2}{2}\mathbb{K}^{zz}_{\boldsymbol{k}=0} + \frac{S}{2N}\sum_{\boldsymbol{k}} E_{\boldsymbol{k}}\phi^*_{\boldsymbol{k}}\phi_{\boldsymbol{k}}, \tag{B.4}$$

which is a sum of the ground state energy and a noninteracting ensemble of classical harmonic oscillators with dispersion relations $E_{\boldsymbol{k}} = \sqrt{\omega^x_{\boldsymbol{k}}\omega^y_{\boldsymbol{k}}}$. In thermal equilibrium at temperature T, each of these oscillators has to satisfy the equipartition theorem [102], which requires

$$\langle \phi^*_{\boldsymbol{k}}\phi_{\boldsymbol{k}'}\rangle = N\delta_{\boldsymbol{k}\boldsymbol{k}'}\frac{2T}{SE_{\boldsymbol{k}}}. \tag{B.5}$$

For the square of the transverse magnetization, i.e., the magnon distribution, $n_{\boldsymbol{k}} = |m^x_{\boldsymbol{k}}|^2 + |m^y_{\boldsymbol{k}}|^2$ this implies the thermal equilibrium ensemble average

$$n^{\mathrm{th}}_{\boldsymbol{k}} = \langle n_{\boldsymbol{k}}\rangle = N\sqrt{1+4|V_{\boldsymbol{k}}|^2}\frac{2T}{SE_{\boldsymbol{k}}}, \tag{B.6}$$

where $V_{\boldsymbol{k}} = \left(\omega^y_{\boldsymbol{k}} - \omega^x_{\boldsymbol{k}}\right)/\left(4E_{\boldsymbol{k}}\right)$ is proportional to the ellipticity of the spin wave. Therefore, as long as spin wave theory is valid, the magnon distribution in thermal equilibrium is directly proportional to the classical Rayleigh-Jeans distribution $T/E_{\boldsymbol{k}}$.

B.2 Stochastic Heun scheme

The numerical integration of a stochastic differential equation (SDE) involves a number of subtleties absent in ordinary differential equations [111]. To illustrate this, we consider a generic Langevin equation for a stochastic process $\boldsymbol{y} = (y_1, \ldots, y_n)^T$, given by

$$\dot{y}_i = A_i(\boldsymbol{y}, t) + \sum_k B_{ik}(\boldsymbol{y}, t)L_k(t), \tag{B.7}$$

with drift vector $\boldsymbol{A} = (A_1, \ldots, A_n)^T$, diffusion matrix B_{ik}, and a Gaussian white noise process $L_k(t)$ satisfying

$$\langle L_k(t)\rangle = 0, \tag{B.8a}$$

$$\langle L_k(t)L_{k'}(t')\rangle = \delta_{kk'}\delta(t-t'). \tag{B.8b}$$

A direct translation of a deterministic integration scheme to the SDE (B.7) is usually problematic for two reasons: As remarked already in Sec. 1.5.3, due to the singular white noise covariance the Langevin equation (B.7) is not uniquely defined, and consequently one has to decide which stochastic calculus should be used to interpret it [52]. The choice of stochastic calculus must then

be reflected in the choice of integration scheme; i.e., it has to be chosen in such a way as to ensure convergence to the correct stochastic calculus. Mere translations of deterministic schemes usually do not fulfill this, and often do not converge to any well-defined solution. Secondly, even when such proper convergence of the integration scheme exists, the order of convergence is usually lower that in the deterministic case.

For our application in Ch. 3, we use the stochastic Heun scheme [47, 106]. It is a predictor-corrector method, in which the information of a given step is used to predict the solution at the next time step; then, this guess is corrected by incorporating derivative information at the new time step. In the Heun method, the predictor values $\tilde{\boldsymbol{y}}$ are computed with the Euler method,

$$\tilde{y}_i = y_i(t) + A_i(\boldsymbol{y}, t)\Delta t + \sum_k B_{ik}(\boldsymbol{y}, t)\Delta W_k, \tag{B.9}$$

where $\boldsymbol{y} = \boldsymbol{y}(t)$. This crude extrapolation is then used to obtain the corrected value at time step $t + \Delta t$:

$$\begin{aligned} y_i(t + \Delta t) =& y_i(t) + \frac{1}{2}\left[A_i(\tilde{\boldsymbol{y}}, t + \Delta t) + A_i(\boldsymbol{y}, t)\right]\Delta t \\ &+ \frac{1}{2}\left[B_{ik}(\tilde{\boldsymbol{y}}, t + \Delta t) + B_{ik}(\boldsymbol{y}, t)\right]\Delta W_k. \end{aligned} \tag{B.10}$$

Here Δt is the (fixed) time step, and ΔW_k is a Wiener process [52] defined as

$$\Delta W_k = \int_t^{t+\Delta t} \mathrm{d}s\, L_k(s); \tag{B.11}$$

i.e., it is a Gaussian random process characterized by

$$\langle \Delta W_k \rangle = 0, \tag{B.12a}$$

$$\langle \Delta W_k \Delta W_{k'} \rangle = \Delta t \delta_{kk'}. \tag{B.12b}$$

The Heun scheme (B.10) converges in quadratic mean to the solution of the Stratonovich interpretation of the Langevin equation (B.7). In contrast, the Euler scheme (B.9) alone converges to the Itô solution of the same Langevin equation (B.7) [47]. To obtain a proper Euler scheme in the Stratonovich sense, one has to add a noise induced correction to the drift vector [52], see Sec. 1.5.3.

Finally, let us remark that for the special case of commutative noise, for which the diffusion matrix obeys the symmetry relation

$$\sum_j B_{jk}\frac{\partial B_{il}}{\partial y_j} = \sum_j B_{jl}\frac{\partial B_{ik}}{\partial y_j}, \tag{B.13}$$

the convergence of the Heun scheme is one order higher than for the corresponding Euler scheme [47]. As we only need to simulate additive noise with $B_{ik}(\boldsymbol{y}, t) = B_{ik}$ in Ch. 3, the above symmetry (B.13) is trivially fulfilled, and we can benefit from the comparatively high convergence.

Appendix C

Deutsche Zusammenfassung

Magnetismus ist das wohl älteste bekannte Beispiel eines makroskopischen Quanteneffekts. Obwohl schon seit Jahrtausenden bekannt, konnte die Entstehung von Magnetismus in Festkörpern doch erst mit dem Aufkommen der Quantenmechanik zu Beginn des 20. Jahrhunderts erklärt werden. Damals erkannte man, dass das Pauli-Prinzip, demzufolge zwei Elektronen nicht den gleichen quantenmechanischen Zustand besetzen können, zu einer effektiven Wechselwirkung zwischen den Spins dieser Elektronen führen kann. In einem Festkörper kann diese sogenannte Austausch-Wechselwirkung die Entstehung eines geordneten Zustands begünstigen, in dem alle Spins parallel bzw. antiparallel ausgerichtet sind. Da mit dem elektronischen Spin ein magnetisches Moment verknüpft ist, ist ein solcherart mikroskopisch geordnetes System makroskopisch magnetisch.

Seiner langen Geschichte zum Trotz ist Magnetismus in Festkörpern auch heute noch ein sehr aktives Forschungsfeld; insbesondere im Hinblick auf neuartige Anwendungen im Bereich der Datenverarbeitung und -Speicherung. In dieser Arbeit beschäftigen wir uns jedoch nicht direkt mit solchen Anwendungsmöglichkeiten. Stattdessen werden wir die mikroskopische Dynamik der Spins, die allen solchen Anwendungen zugrunde liegt, theoretisch untersuchen und modellieren. Dazu konzentrieren wir uns auf ein bestimmtes Material, das aufgrund seiner guten magnetischen Eigenschaften auch von experimenteller Seite eine hohe Aufmerksamkeit genießt: Yttrium-Eisengranat (YIG) [4]. Dabei handelt es sich um einen ferrimagnetischen Isolator mit Curie-Temperatur $T_C = 560\,\mathrm{K}$, dessen niederenergetische magnetische Anregungen sehr gut durch das folgende ferromagnetische Heisenberg-Modell beschrieben werden [6, 8, 11, 12, 13]:

$$\mathcal{H}_{\mathrm{m}}(t) = -\frac{1}{2}\sum_{ij}\sum_{\alpha\beta}\left[J_{ij}\delta^{\alpha\beta} + D_{ij}^{\alpha\beta}\right] S_i^{\alpha} S_j^{\beta} - H_0 \sum_i S_i^z. \tag{C.1}$$

Hierbei sind die S_i^{α} die kartesischen Komponenten des Spinoperators $\boldsymbol{S}_i$ am Gitterplatz $\boldsymbol{R}_i$. J_{ij} ist eine ferromagnetische Austausch-Wechselwirkung zwischen nächsten Nachbarn mit Wert $J \approx 3.19\,\mathrm{K}$ und $D_{ij}^{\alpha\beta}$ ist der Tensor der

Dipol-Dipol Wechselwirkung. Der letzte Term des Hamiltonoperators (C.1) ist die Zeeman-Energie des externen magnetischen Feldes $H_0 \boldsymbol{e}_z/\mu$, mit dem magnetischen Moment des freien Elektrons $\mu = 2\mu_B$. Schließlich sei noch erwähnt, dass das ionische Gitter einfach kubisch mit Gitterkonstante $a = 12.376\,\text{Å}$ ist, und dass sich die effektive Spinquantenzahl aus Messungen der Saturierungsmagnetisierung zu $S \approx 14.2$ ergibt.

Einer der Schwerpunkte dieser Arbeit liegt darin, den Einfluss der elastischen Schwingungen des ionischen Gitters, d.h. der Phononen, auf die magnetischen Anregungen korrekt zu beschreiben. In harmonischer Näherung ist der Hamiltonoperator dieser Phononen als

$$\mathcal{H}_\text{e} = \sum_{\boldsymbol{k}\lambda} \left[\frac{P_{-\boldsymbol{k}\lambda} P_{\boldsymbol{k}\lambda}}{2M} + \frac{M}{2} \omega_{\boldsymbol{k}\lambda}^2 X_{-\boldsymbol{k}\lambda} X_{\boldsymbol{k}\lambda} \right] \tag{C.2}$$

gegeben, wobei $X_{\boldsymbol{k}\lambda}$ der Operator der Normalmoden der elastischen Gitterschwingungen mit Impuls $\boldsymbol{k}$ und Polarisation $\boldsymbol{e}_{\boldsymbol{k}\lambda}$ ist; d.h. die Abweichung der ionischen Positionen von den Ruhelagen $\boldsymbol{R}_i$ ist gegeben durch $\boldsymbol{X}_i = \boldsymbol{X}(\boldsymbol{R}_i) = \frac{1}{\sqrt{N}} \sum_{\boldsymbol{k}\lambda} e^{i\boldsymbol{k}\cdot\boldsymbol{R}_i} X_{\boldsymbol{k}\lambda} \boldsymbol{e}_{\boldsymbol{k}\lambda}$. Der zu $X_{\boldsymbol{k}\lambda}$ kanonisch konjugierte Impulsoperator ist $P_{\boldsymbol{k}\lambda}$. Da wir nur an niederenergetischen Anregungen interessiert sind, betrachten wir hier nur die drei akustischen Phononzweige mit Dispersionsrelation $\omega_{\boldsymbol{k}\lambda} = c_\lambda |\boldsymbol{k}|$, mit den Schallgeschwindigkeiten c_λ. In isotropen Systemen ist einer dieser Phononzweige immer longitudinal, d.h. parallel zu $\boldsymbol{k}$, während die anderen beiden transversal sind. Für YIG bei Raumtemperatur sind die longitudinale und die transversale Schallgeschwindigkeit $c_\parallel = 7.209 \times 10^5\,\text{cm/s}$ und $c_\perp = 3.843 \times 10^5\,\text{cm/s}$ [3]. Die effektive ionische Masse M pro Gitterplatz lässt sich für YIG aus der bekannten Massendichte [3] zu $M = 9.8 \times 10^{-21}\,\text{g}$ bestimmen.

Die Wechselwirkung zwischen magnetischem und elastischem Sektor beruht für kollineare Magneten wie YIG vor allem auf der relativistischen Spin-Bahn Kopplung [3]. Diese hängt von den Ladungsfreiheitsgraden ab und lässt sich folglich nicht auf einfache Weise in unser effektives Spinmodell (C.1) einbinden. Daher nutzen wir einen semiphänomenologischen Zugang [3, 29, 30, 31, 32, 33], der allein auf Symmetrieüberlegungen basiert. Durch Quantisierung und Diskretisierung einer klassischen magnetoelastischen Energie, die alle Symmetrien des Systems korrekt berücksichtigt, erhält man den magnetoelastischen Hamiltonoperator

$$\mathcal{H}_\text{me} = \frac{1}{S^2} \sum_i \sum_{\alpha\beta} B^{\alpha\beta} S_i^\alpha S_i^\beta X_i^{\alpha\beta}, \tag{C.3}$$

wobei $X_i^{\alpha\beta} = \frac{1}{2} \left[\partial X^\alpha(\boldsymbol{r})/\partial r^\beta + \partial X^\beta(\boldsymbol{r})/\partial r^\alpha \right]_{\boldsymbol{r}=\boldsymbol{R}_i}$ der Operator des elastischen Spannungstensors ist. Der magnetoelastische Kopplungstensor $B^{\alpha\beta}$ hat für kubische Gitter die Form $B^{\alpha\beta} = \delta^{\alpha\beta} B_\parallel + \left(1 - \delta^{\alpha\beta}\right) B_\perp$; für YIG bei Raumtemperatur sind die Komponenten als $B_\parallel = 47.8\,\text{K}$ and $B_\perp = 95.6\,\text{K}$ gegeben [3, 34, 35].

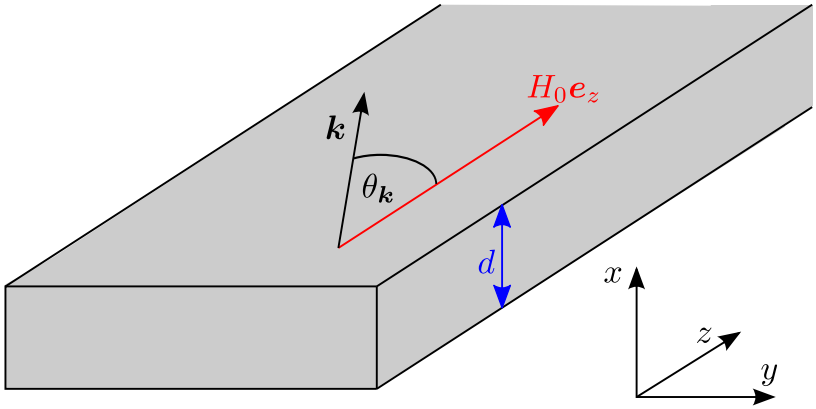

Abbildung C.1: *Geometrie eines dünnen YIG Films der Dicke d, der von einem externen Magnetfeld $\boldsymbol{H}_0 = H_0 \boldsymbol{e}_z$ innerhalb der Filmebene magnetisiert wird. Im Rahmen der Uniform-Mode Näherung werden nur Magnonen mit Impulsen von der Form $\boldsymbol{k} = |\boldsymbol{k}| (\cos\theta_{\boldsymbol{k}} \boldsymbol{e}_z + \sin\theta_{\boldsymbol{k}} \boldsymbol{e}_y)$ innerhalb der Filmebene berücksichtigt.*

Schlussendlich sei noch erwähnt, dass wir uns in dieser Arbeit ausschließlich mit tangential magnetisierten dünnen YIG Filmen befassen, siehe Abb. C.1. In dieser Geometrie haben wir nur in der y-z Ebene Translationsinvarianz, während die Dicke d des Films endlich bleibt. Das niedrigste Magnonband kann dann im Rahmen der sogenannten Uniform-Mode Näherung durch ein effektives zweidimensionales Modell in der Filmebene beschrieben werden, das man durch Mittelung über die Dicke d des Films erhält [6]. Dementsprechend betrachten wir nur Magnonen mit Impulsen der Form $\boldsymbol{k} = |\boldsymbol{k}| (\cos\theta_{\boldsymbol{k}} \boldsymbol{e}_z + \sin\theta_{\boldsymbol{k}} \boldsymbol{e}_y)$ innerhalb der Filmebene. Die Dispersion langwelliger Magnonen in solchen YIG Filmen ist dann durch

$$E_{\boldsymbol{k}} = \sqrt{\left[H_0 + \rho_s \boldsymbol{k}^2 + \Delta\left(1 - f_{\boldsymbol{k}}\right) \sin^2\theta_{\boldsymbol{k}}\right] \left[H_0 + \rho_s \boldsymbol{k}^2 + \Delta f_{\boldsymbol{k}}\right]} \tag{C.4}$$

gegeben, mit der Spin-Steifigkeit $\rho_s = JSa^2$, der dipolaren Energie $\Delta = 4\pi\mu^2 S/a^3$ und dem Formfaktor $f_{\boldsymbol{k}} = \left[1 - \exp\left(|\boldsymbol{k}|d\right)\right] / \left(|\boldsymbol{k}|d\right)$. Hierbei ist insbesondere zu beachten, dass die magnonische Dispersion durch das Zusammenwirken von Austausch-Wechselwirkung, langreichweitiger Dipol-Dipol Wechselwirkung und der endlichen Dicke d des Films zwei entartete Minima bei endlichen Impulsen $\boldsymbol{k} = \pm k_{\min} \boldsymbol{e}_z$ parallel zum externen magnetischen Feld aufweist.

Zur vollständigen Beschreibung der Phononen müssen wir letztlich noch die Polarisationsvektoren angeben; eine günstige Wahl für dünne Filme ist

$$\boldsymbol{e}_{\boldsymbol{k}\parallel} = i\left(\cos\theta_{\boldsymbol{k}} \boldsymbol{e}_z + \sin\theta_{\boldsymbol{k}} \boldsymbol{e}_y\right), \tag{C.5a}$$

$$\boldsymbol{e}_{\boldsymbol{k}\perp 1} = i\left(\sin\theta_{\boldsymbol{k}} \boldsymbol{e}_z - \cos\theta_{\boldsymbol{k}} \boldsymbol{e}_y\right), \tag{C.5b}$$

$$\boldsymbol{e}_{\boldsymbol{k}\perp 2} = \boldsymbol{e}_x. \tag{C.5c}$$

C.1 Magnetoelastische Moden und Lebenszeit von Magnonen

Obwohl die Kopplung von magnetischen und elastischen Freiheitsgraden in magnetischen Isolatoren meist vernachlässigt werden kann [3], ist sie für die korrekte Interpretation mancher Experimente essentiell. So ist es zum Beispiel möglich, in Ultraschallexperimenten aus der Ausbreitung und Dämpfung von Schallwellen Rückschlüsse auf die magnetischen Eigenschaften eines Festkörpers zu ziehen [68]. Desweiteren ist das genaue Verständnis der magnetoelastischen Wechselwirkung von fundamentaler Bedeutung für die neu entstandenen Forschungsfelder der Spintronik und der Spin-Kaloritronik [73, 74], in denen versucht wird, magnetische Freiheitsgrade durch Ladungs- bzw. Wärmeströme zu manipulieren.

Dieses Kapitel wurde durch das Experiment [14] von Agrawal *et al.* motiviert. In diesem Experiment wurde die magnetoelastische Kopplung in dünnen YIG Filmen durch eine räumlich aufgelöste Messung der Temperatur T_m der kurzwelligen Austausch-Magnonen unter Einfluss eines Temperaturgradienten untersucht. Es wurde festgestellt, dass die Temperaturen T_m und T_p der Magnonen und der Phononen fast vollständig identisch waren. Dies wiederum widerspricht früheren Arbeiten über den Spin-Seebeck Effekt [73], bei dem man davon ausgeht, dass ein Spinstrom durch die Differenz $\Delta T = T_\mathrm{m} - T_\mathrm{p}$ von magnonischer und phononischer Temperatur erzeugt wird. Um beide Resultate miteinander in Einklang zu bringen, schlugen die Autoren von [14] vor, dass die Temperatur der Magnonen von ihrem Impuls abhängt, d.h. $T_\mathrm{m} = T_\mathrm{m}(\boldsymbol{k})$. In diesem Fall wäre es möglich, dass die im Experiment nicht beobachtbaren langwelligen dipolaren Magnonen langsamer als die beobachteten kurzwelligen Austausch-Magnonen thermalisieren. Folglich könnte die für den Spin-Seebeck Effekt benötigte Temperaturdifferenz zwischen den langwelligen dipolaren Magnonen und den Phononen für längere Zeiten bestehen. Das Hauptziel dieses Kapitels wird es sein, eine mikroskopische Erklärung für eine solche impulsabhängige magnonische Temperatur zu finden. Dazu berechenen wir die Impulsabhängigkeit der Spin-Gitter Relaxationszeit $\tau(\boldsymbol{k})$, die wir im langwelligen dipolaren Impulsbereich auch mit experimentellen Daten vergleichen können. Desweiteren werden wir auch die Dispersionsrelationen der magnetoelastischen Moden bestimmen und zeigen, dass sie ein charakteristisches Minimum im transversalen Spin-Strukturfaktor zur Folge haben.

Für unsere Berechnungen machen wir uns zunutze, dass der effektive Spin $S = 14.2$ in YIG sehr groß ist. Dies ermöglicht es uns, mittels der sogenannten Holstein-Primakoff Transformation [40] die Spinoperatoren auf Bosonen abzubilden und die Hamiltonoperatoren (C.1) und (C.3) auf kontrollierte Weise nach Potenzen von $1/S$ zu entwickeln. Um den quadratischen Term in der Entwicklung des magnetischen Hamiltonoperators (C.1) zu diagonalisieren, ist es aufgrund der dipolaren Wechselwirkungen nötig, auch noch eine Bogoliubov Transformation [54] zu den magnonischen Erzeugungs- und Vernichtungsope-

ratoren $\beta_{\boldsymbol{k}}^\dagger$ und $\beta_{\boldsymbol{k}}$ auszuführen. Dann erhält man

$$\mathcal{H}_{\mathrm{m}}^{(2)} = \sum_{\boldsymbol{k}} E_{\boldsymbol{k}} \beta_{\boldsymbol{k}}^\dagger \beta_{\boldsymbol{k}}, \tag{C.6}$$

mit der magnonischen Dispersion (C.4).

Analoge Entwicklung des magnetoelastischen Hamiltonoperators (C.3) bis zur quadratischen Ordnung in magnonischen Operatoren ergibt

$$\mathcal{H}_{\mathrm{me}} \approx \mathcal{H}_{\mathrm{me}}^{(2)} + \mathcal{H}_{\mathrm{me}}^{(3)}, \tag{C.7}$$

wobei die hochgestellte Zahl die Anzahl der Operatoren im jeweiligen Ausdruck anzeigt. In $\mathcal{H}_{\mathrm{me}}^{(2)}$ sind jeweils ein magnonischer und ein phononischer Operator enthalten; solche Terme beschreiben die Hybridisierung von Magnonen und Phononen, d.h. das Entstehen von magnetoelastischen Moden. Der kubische Beitrag $\mathcal{H}_{\mathrm{me}}^{(3)}$, der zwei magnonische und einen phononischen Operator enthält, beschreibt im Gegensatz dazu Streuprozesse, durch die die Magnonen eine endliche Lebenszeit erhalten. Die Näherung (C.7) für den magnetoelastischen Hamiltonoperator ist ebenfalls eine Entwicklung nach dem kleinen Parameter $1/S$, mit $\mathcal{H}_{\mathrm{me}}^{(2)} \propto 1/\sqrt{S}$ und $\mathcal{H}_{\mathrm{me}}^{(3)} \propto 1/S$.

Wir werden uns nun zuerst mit der magnetoelastischen Hybridisierung befassen, die durch $\mathcal{H}_{\mathrm{me}}^{(2)}$ beschrieben wird. Dieser Beitrag zum Hamiltonoperator hat explizit die Form

$$\mathcal{H}_{\mathrm{me}}^{(2)} = \sum_{\boldsymbol{k}\lambda} X_{-\boldsymbol{k}\lambda} \left[\Gamma_{\boldsymbol{k}\lambda}^{\beta} \beta_{\boldsymbol{k}} + \Gamma_{-\boldsymbol{k}\lambda}^{\bar{\beta}} \beta_{-\boldsymbol{k}}^\dagger \right], \tag{C.8}$$

mit impulsabhängiger Vertexfunktion $\Gamma_{\boldsymbol{k}\lambda}^{\beta} = (\Gamma_{\boldsymbol{k}\lambda}^{\bar{\beta}})^*$. Entweder durch explizites Lösen der linearisierten Heisenberg-Bewegungsgleichungen für die magnonischen und phononischen Operatoren oder aber durch Ausintegrieren der phononischen Freiheitsgrade mittels Funktionalintegral-Methoden ist es nun möglich, die Dispersionsrelationen $\Omega_{\boldsymbol{k}\lambda\pm}$ der magnetoelastischen Moden zu führender Ordnung in $1/S$ analytisch zu berechnen,

$$\Omega_{\boldsymbol{k}\lambda\pm}^2 = \frac{\omega_{\boldsymbol{k}\lambda}^2 + E_{\boldsymbol{k}}^2}{2} \pm \sqrt{\frac{\left(\omega_{\boldsymbol{k}\lambda}^2 - E_{\boldsymbol{k}}^2\right)^2}{4} + \Delta_{\boldsymbol{k}\lambda}^4}, \tag{C.9}$$

wobei die Hybridisierungsenergie durch $\Delta_{\boldsymbol{k}\lambda}^4 = 2\frac{E_{\boldsymbol{k}}}{M} |\Gamma_{\boldsymbol{k}\lambda}^{\beta}|^2$ gegeben ist. Bei der Herleitung der magnetoelastischen Dispersion (C.9) wurde angenommen, dass entweder die Energie der longitudinalen oder der transversalen Phononen nahe an der der Magnonen liegt, sodass man den jeweils anderen Phononzweig vernachlässigen kann. Dass dies für YIG sehr gut erfüllt ist, kann man in Abb. C.2 sehen, die die magnetoelastischen Dispersionen für Impulse $\boldsymbol{k} = k\boldsymbol{e}_z$ parallel zum externen Magnetfeld zeigt. Tatsächlich hybridisieren für diese Ausbreitungsrichtung die longitudinalen Phononen überhaupt nicht, da der relevante Hybridisierungsvertex $\Gamma_{\boldsymbol{k}\parallel}^{\beta}$ verschwindet.

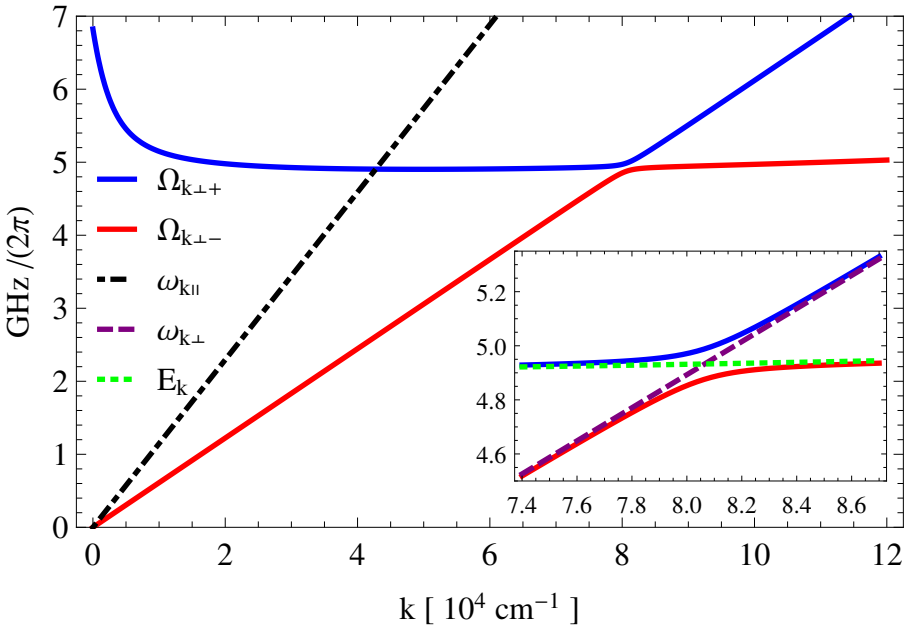

Abbildung C.2: *Plot der magnetoelastischen Dispersionsrelationen (C.9) eines YIG Films der Dicke* $d = 6.7\,\mu\mathrm{m}$ *in einem externen Magnetfeld* $H_0 = 1710\,\mathrm{Oe} \times \mu$*, für Impulse* $\boldsymbol{k} = k\boldsymbol{e}_z$ *parallel zum magnetischen Feld. Die eingebettete Grafik zeigt eine vergrößerte Sicht auf den Kreuzungspunkt der Dispersionen von Magnonen und transversalen Phononen; die Achsen sind dieselben wie im Hauptplot.*

Im Rahmen derselben Näherungen haben wir ebenfalls den transversalen dynamischen Spin-Strukturfaktor analytisch berechnet, der als

$$S_\perp(\boldsymbol{k},\omega) = \int_{-\infty}^{\infty} \frac{\mathrm{d}t}{2\pi}\, e^{i\omega t} \left\langle S^x_{-\boldsymbol{k}}(0) S^x_{\boldsymbol{k}}(t) + S^y_{-\boldsymbol{k}}(0) S^y_{\boldsymbol{k}}(t) \right\rangle \tag{C.10}$$

definiert ist. Dieser Strukturfaktor ist direkt proportional zur Intensität der Brillouin-Lichtstreuung [75], die in vielen Experimenten zur Beobachtung magnetischer Freiheitsgrade benutzt wird [77, 78]. Ein Intensitätsplot unseres Ergebnisses für Impulse $\boldsymbol{k} = k\boldsymbol{e}_z$ parallel zum externen Magnetfeld ist in Abb. C.3 dargestellt; darin ist deutlich zu erkennen, dass das spektrale Gewicht in der Nähe des Kreuzungspunkts $E_{\boldsymbol{k}} \approx \omega_{\boldsymbol{k}\perp}$ von den Magnonen auf die transversalen Phononen übertragen wird.

Zur Berechnung der Spin-Gitter Dämpfung benötigen wir die Magnon-Phonon Streuprozesse, die durch den Hamiltonoperator $\mathcal{H}^{(3)}_{\mathrm{me}}$ beschrieben wer-

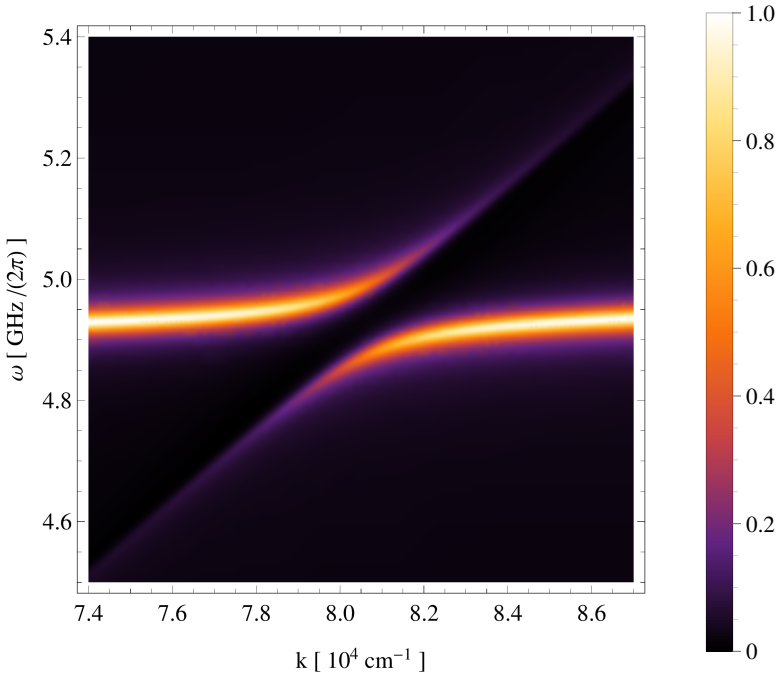

Abbildung C.3: *Normierter Intensitätsplot des transversalen dynamischen Spin-Strukturfaktors eines YIG Films der Dicke* $d = 6.7\,\mu\mathrm{m}$ *in einem externen Magnetfeld* $H_0 = 1710\,\mathrm{Oe} \times \mu$ *und bei Temperatur* $T = 300\,\mathrm{K}$*, für Impulse* $\boldsymbol{k} = k\boldsymbol{e}_z$ *parallel zum magnetischen Feld.*

den. Dieser ist explizit durch

$$\mathcal{H}_{\mathrm{me}}^{(3)} = \frac{1}{\sqrt{N}} \sum_{\boldsymbol{k}\boldsymbol{k}'} \Bigg[\boldsymbol{\Gamma}_{\boldsymbol{k},\boldsymbol{k}'}^{\bar{\beta}\beta} \cdot \boldsymbol{X}_{\boldsymbol{k}-\boldsymbol{k}'} \beta_{\boldsymbol{k}}^{\dagger} \beta_{\boldsymbol{k}'} + \frac{1}{2!} \left(\boldsymbol{\Gamma}_{\boldsymbol{k},\boldsymbol{k}'}^{\beta\beta} \cdot \boldsymbol{X}_{-\boldsymbol{k}-\boldsymbol{k}'} \beta_{\boldsymbol{k}} \beta_{\boldsymbol{k}'} + \boldsymbol{\Gamma}_{\boldsymbol{k},\boldsymbol{k}'}^{\bar{\beta}\bar{\beta}} \cdot \boldsymbol{X}_{\boldsymbol{k}+\boldsymbol{k}'} \beta_{\boldsymbol{k}}^{\dagger} \beta_{\boldsymbol{k}'}^{\dagger} \right) \Bigg] \tag{C.11}$$

gegeben und enthält sowohl Terme, die die Magnonenanzahl erhalten, als auch solche, die sie nicht erhalten. Die Magnonenanzahl erhaltenden Prozesse mit der Vertexfunktion $\boldsymbol{\Gamma}_{\boldsymbol{k},\boldsymbol{k}'}^{\bar{\beta}\beta} = (\boldsymbol{\Gamma}_{\boldsymbol{k}',\boldsymbol{k}}^{\bar{\beta}\beta})^*$ beschreiben die Streuung eines Magnons an einem Phonon und werden Cherenkov-Prozesse genannt [3]. Die Vertices $\boldsymbol{\Gamma}_{\boldsymbol{k},\boldsymbol{k}'}^{\beta\beta} = (\boldsymbol{\Gamma}_{\boldsymbol{k},\boldsymbol{k}'}^{\bar{\beta}\bar{\beta}})^*$, die die Anzahl der Magnonen nicht erhalten, beschreiben die Konfluenz zweier Magnonen zu einem Phonon bzw. den inversen Prozess, den Zerfall eines Phonons in zwei Magnonen.

In führender Ordnung im kleinen Parameter $1/S$ lässt sich dann auch die Dämpfungsrate der Magnonen durch magnetoelastische Wechselwirkungen als Summe von drei Termen schreiben:

$$\gamma_2(\boldsymbol{k}) = \gamma_{2a}^{\mathrm{Che}}(\boldsymbol{k}) + \gamma_{2b}^{\mathrm{Che}}(\boldsymbol{k}) + \gamma_2^{\mathrm{con}}(\boldsymbol{k}), \tag{C.12}$$

wobei die einzelnen Beiträge für den experimentell relevanten Fall hoher Temperaturen $T \gg E_{\boldsymbol{k}}$ als

$$\gamma_{2a}^{\mathrm{Che}}(\boldsymbol{k}) = \frac{\pi T E_{\boldsymbol{k}}}{2MN} \sum_{\boldsymbol{q}\lambda} \frac{|\Gamma^{\bar{\beta}\beta}_{\boldsymbol{k},\boldsymbol{k}+\boldsymbol{q},\lambda}|^2}{E_{\boldsymbol{k}+\boldsymbol{q}}\omega^2_{\boldsymbol{q}\lambda}} \delta\left(E_{\boldsymbol{k}} - E_{\boldsymbol{k}+\boldsymbol{q}} + \omega_{\boldsymbol{q}\lambda}\right), \tag{C.13a}$$

$$\gamma_{2b}^{\mathrm{Che}}(\boldsymbol{k}) = \frac{\pi T E_{\boldsymbol{k}}}{2MN} \sum_{\boldsymbol{q}\lambda} \frac{|\Gamma^{\bar{\beta}\beta}_{\boldsymbol{k},\boldsymbol{k}-\boldsymbol{q},\lambda}|^2}{E_{\boldsymbol{k}-\boldsymbol{q}}\omega^2_{\boldsymbol{q}\lambda}} \delta\left(E_{\boldsymbol{k}} - E_{\boldsymbol{k}-\boldsymbol{q}} - \omega_{\boldsymbol{q}\lambda}\right), \tag{C.13b}$$

$$\gamma_{2}^{\mathrm{con}}(\boldsymbol{k}) = \frac{\pi T E_{\boldsymbol{k}}}{2MN} \sum_{\boldsymbol{q}\lambda} \frac{|\Gamma^{\beta\beta}_{\boldsymbol{k},\boldsymbol{q}-\boldsymbol{k},\lambda}|^2}{E_{\boldsymbol{q}-\boldsymbol{k}}\omega^2_{\boldsymbol{q}\lambda}} \delta\left(E_{\boldsymbol{k}} + E_{\boldsymbol{q}-\boldsymbol{k}} - \omega_{\boldsymbol{q}\lambda}\right) \tag{C.13c}$$

gegeben sind. $\gamma_{2a}^{\mathrm{Che}}(\boldsymbol{k})$ und $\gamma_{2b}^{\mathrm{Che}}(\boldsymbol{k})$ beschreiben Cherenkov-Prozesse, bei denen ein Magnon mit Energie $E_{\boldsymbol{k}}$ ein Phonon mit Energie $\omega_{\boldsymbol{q}\lambda}$ absorbiert bzw. emittiert und dabei in ein Magnon mit Energie $E_{\boldsymbol{k}\pm\boldsymbol{q}}$ zerfällt. Der letzte Term $\gamma_{2}^{\mathrm{con}}(\boldsymbol{k})$ entsteht durch die Konfluenz zweier Magnonen mit den Energien $E_{\boldsymbol{k}}$ und $E_{\boldsymbol{q}-\boldsymbol{k}}$ in ein Phonon mit Energie $\omega_{\boldsymbol{q}\lambda}$.

Wir haben nun die Dämpfungsintegrale (C.13) sowohl im Rahmen analytischer Näherungen als auch direkt numerisch gelöst, zunächst für Impulse im langwelligen dipolaren Bereich und dann auch im kurzwelligen Austauschbereich; diese Lösungen werden grafisch in Abb. C.4 bzw. Abb. C.5 gezeigt. Die solcherart bestimmten Dämpfungsraten zeigen sehr unterschiedliches Verhalten in den beiden Impulsbereichen: Im langwelligen dipolaren Bereich ist die Impulsabhängigkeit nur schwach ausgeprägt und die Konfluenzprozesse geben den größten Beitrag zur gesamten Dämpfung, siehe Abb. C.4. Im Gegensatz dazu dominiert im in Abb. C.5 gezeigten Austauschbereich der Cherenkov-Prozess und die Dämpfungsrate zeigt eine komplexe Impulsabhängigkeit, mit Peaks in der Nähe der Kreuzungspunkte von magnonischen und phononischen Dispersionen und Geschwindigkeiten. Es ist ebenfalls zu beachten, dass die Dämpfungsrate vom dipolaren zum Austausch dominierten Impulsbereich um zwei Größenordnungen zunimmt. Dies impliziert für die Spin-Gitter Relaxationszeit $\tau(\boldsymbol{k}) = 1/\gamma_2(\boldsymbol{k})$ Werte von der Ordnung $50\,\mu$s für langwellige dipolare Magnonen; für kurzwellige Austausch-Magnonen andererseits kann sie bis auf 480 ns abfallen. Damit passt unser Resultat sehr gut zu der von Agrawal *et al.* zur Erklärung ihres Experiments [14] vorgeschlagenen Hypothese, wonach die Spin-Gitter Relaxationszeit im dipolaren Impulsbereich wesentlich langsamer als im Austausch dominierten Impulsbereich ist.

Als Teil dieser Arbeit wurde die magnonische Dämpfungsrate in einem YIG Film bei Raumtemperatur ebenfalls experimentell mittels zeit- und impulsaufgelöster Brillouin-Lichtstreuung [75] gemessen. Dazu wurde das magnonische Spektrum durch parametrisches Pumpen [13] angeregt und die freie Thermalisierung der Magnonen mit Impuls- und Zeitauflösung beobachtet. Die Relaxationszeit der Magnonen als Funktion des Impulses wurde dann durch exponentielles Fitten der Relaxation verschiedener Magnonengruppen bestimmt. Allerdings war es aufgrund von technischen Beschränkungen

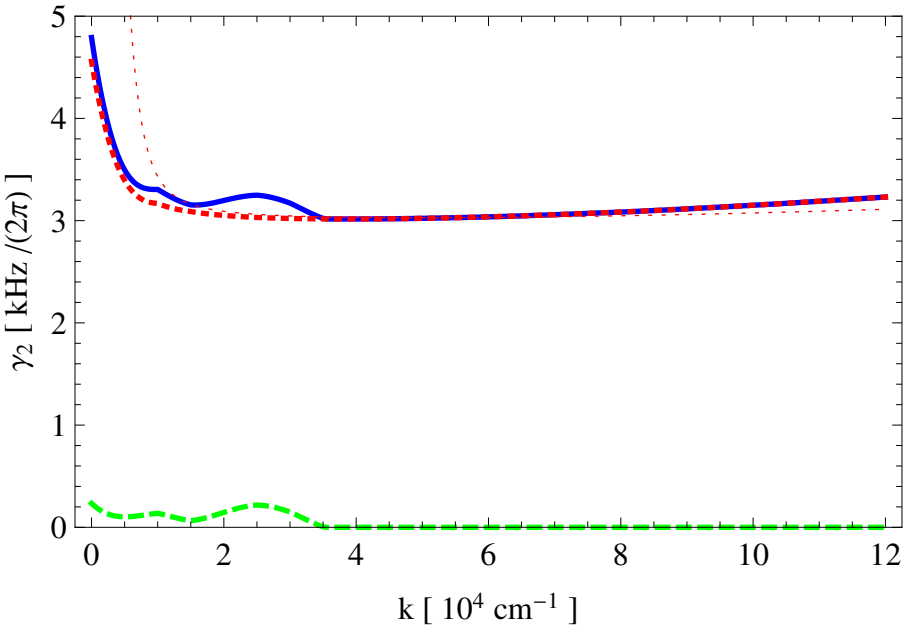

Abbildung C.4: *Numerische Auswertung der magnonischen Dämpfungsraten (C.13) für einen YIG Film mit Temperatur $T = 300\,\mathrm{K}$, im dipolaren Impulsbereich. Der Plot ist für einen Film der Dicke $d = 6.7\,\mu\mathrm{m}$ in einem externen Magnetfeld $H_0 = 1710\,\mathrm{Oe} \times \mu$ und für Impulse $\boldsymbol{k} = k\boldsymbol{e}_z$ parallel zum magnetischen Feld. Die durchgezogene blaue Linie entspricht der gesamten Dämpfungsrate, während die gestrichelte grüne und die gepunktete rote Linie die Beiträge von Cherenkov- und Konfluenzprozessen repräsentieren. Die dünne gepunktete rote Linie ist eine analytische Näherung für die Konfluenzdämpfungsrate im dipolaren Impulsbereich; die Cherenkov-Prozesse geben in derselben Näherung keinen Beitrag.*

nur möglich, den langwelligen dipolaren Impulsbereich zu untersuchen. Die derartig experimentell bestimmte Dämpfungsrate zeigt zwar als Funktion des Impulses qualitativ das gleiche Verhalten wie die theoretisch bestimmte Spin-Gitter Dämpfungsrate, die in Abb. C.4 gezeigt ist, ist aber etwa drei Größenordnungen größer. Dies ist allerdings auch nicht sehr überraschend, da experimentell immer nur die gesamte Dämpfungsrate bestimmt werden kann, die insbesondere auch Beiträge von Magnon-Magnon- und Störstellen-Streuung enthält. Daher kommen wir zu dem Schluss, dass die von uns betrachteten Magnon-Phonon Streuprozesse im dipolaren Bereich bei Raumtemperatur nicht der dominante Relaxationskanal der Magnonen ist. Für die in dem Experiment [14] untersuchte Equilibration der Temperaturen von Magnonen und Phononen ist allerdings allein die hier berechnete Spin-Gitter Relaxationszeit relevant.

Der theoretische Teil der in diesem Kapitel vorgestellten Arbeit wurde zu-

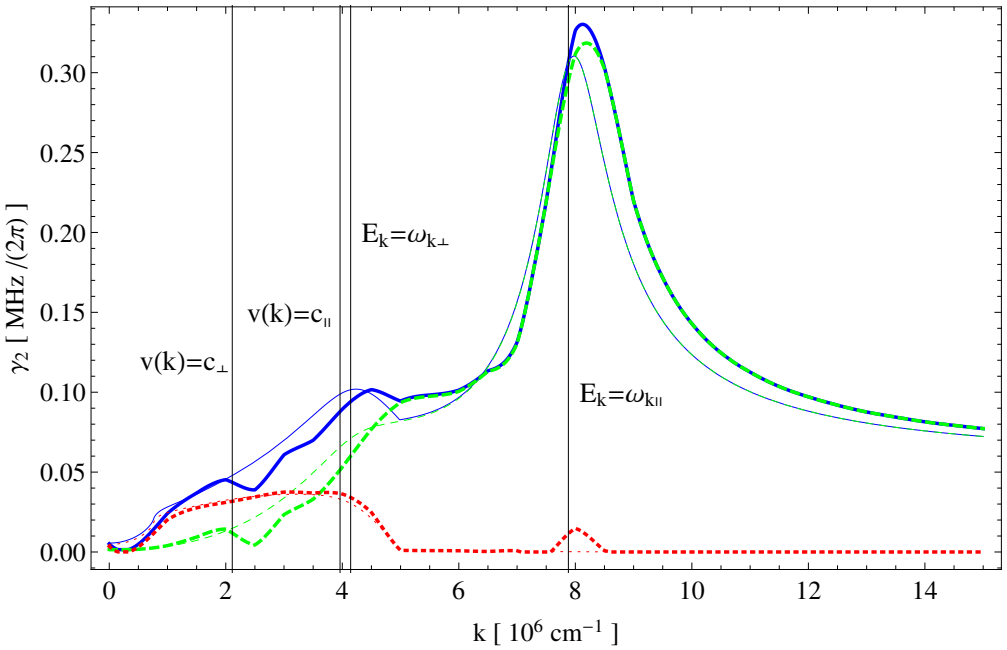

Abbildung C.5: *Numerische Auswertung der magnonischen Dämpfungsraten (C.13) für einen YIG Film mit Temperatur $T = 300\,\mathrm{K}$, im Austausch dominierten Impulsbereich. Der Plot ist für einen Film der Dicke $d = 6.7\,\mu\mathrm{m}$ in einem externen Magnetfeld $H_0 = 1710\,\mathrm{Oe} \times \mu$ und für Impulse $\boldsymbol{k} = k\boldsymbol{e}_z$ parallel zum magnetischen Feld. Durchgezogene blaue Linien entsprechen der gesamten Dämpfungsrate, während die gestrichelte grüne und die gepunktete rote Linie die Beiträge von Cherenkov- und Konfluenzprozessen repräsentieren. Die korrespondierenden dünnen Linien sind semianalytische Näherungen im Austausch-Impulsbereich. $v(\boldsymbol{k}) = |\nabla_{\boldsymbol{k}} E_{\boldsymbol{k}}|$ bezeichnet die Gruppengeschwindigkeit der Magnonen.*

sammen mit Peter Kopietz durchgeführt, während der experimentelle Anteil von Dmytro A. Bozhko, Alexander A. Serga und Burkard Hillebrands beigesteuert wurde. Diese Arbeit wurde in [P2] veröffentlicht.

C.2 Rayleigh-Jeans Kondensation von gepumpten Magnonen

Im Laufe des letzten Jahrzehnts rückte die Nichtgleichgewichtsdynamik von Magnonen in YIG Filmen bei Raumtemperatur immer mehr in den Fokus experimenteller Studien [15, 16, 17, 18, 19, 20, 21, 22, 23, 24]. In dem bahnbrechenden Experiment [15] wurde die Technik des parametrischen Pumpens [13] benutzt, um Magnonen mit wohldefinierter Energie und Impuls in das Magnonengas zu injizieren. Die Nichtgleichgewichtsdynamik dieser überschüssigen

Magnonen wurde dann mithilfe frequenzaufgelöster Brillouin-Lichtstreuungs Spektroskopie untersucht. Dabei wurde festgestellt, dass das Magnonengas zu einem Quasigleichgewicht thermalisiert, das durch ein endliches chemisches Potential charakterisiert wird. Für hinreichend starke Pumpleistung erreichte dieses chemische Potential seinen maximalen Wert, der der minimalen Energie der Magnonen entspricht. In diesem Fall entstand auch ein zusätzlicher, scharf gepeakter Beitrag an jener minimalen magnonischen Energie: Ein Magnon-Kondensat war entstanden. Da Magnonen Bosonen sind, wurde diese Kondensation sofort als Bose-Einstein Kondensation (BEC) [85] von Magnonen bei Raumtemperatur interpretiert. Seitdem haben zahlreiche Experimente [16, 17, 18, 19, 20, 21, 22, 23, 24] die Existenz dieser Kondensation von Magnonen im Nichtgleichgewicht bestätigt und unser Wissen darüber erweitert. Insbesondere ist es mithilfe von zeit- und impulsaufgelöster Brillouin-Lichtstreuungs Spektroskopie [75] möglich geworden, die Nichtgleichgewichtsdynamik der Magnonen im Impulsraum direkt zu beobachten.

Diese Entdeckungen führten zu einer Neubelebung des Interesses an parametrisch gepumpten Magnonen und hatten ebenfalls viele theoretische Arbeiten zur Magnon-Kondensation zur Folge [8, 9, 10, 11, 12, 76, 86, 87, 88, 89, 90]. Bis jetzt war allerdings keine dieser Theorien in der Lage, eine vollständig befriedigende theoretische Beschreibung der Nichtgleichgewichts-Zeitentwicklung und letztendlichen Kondensation der Magnonen zu geben. Während die in den 1960er und 70er Jahren entwickelte sogenannte S-Theorie [37, 38, 39, 91] und ihre Erweiterungen [9, 10, 11, 92, 93, 94] das exponentielle Wachstum und die Saturation desselben bei parametrischer Resonanz gut beschreiben kann, werden bei ihr Magnon-Magnon Wechselwirkungen doch nur in einer Art von Molekularfeld-Näherung berücksichtigt; dementsprechend ist sie nicht in der Lage, die Kaskade von Relaxationsprozessen, die zur Entstehung eines Kondensats führen, korrekt zu beschreiben. Im Gegensatz dazu ignorieren Theorien, die sich mit dem Kondensat befassen, in der Regel die Pumpdynamik völlig und benutzen einen Quasigleichgewichtszustand als Ausgangspunkt, der mit dem Grundzustand eines effektiven quantenmechanischen Hamiltonoperators identifiziert werden kann [8, 12, 86, 88, 89]. Zur Beschreibung der Dynamik des Kondensats wurden ebenfalls phänomenologische Ginzburg-Landau Theorien aufgestellt [87]. Schließlich wurde von Theorien, die sich mit Relaxationsprozessen und der Kinetik angeregter Magnonen befassen, die Möglichkeit einer tatsächlichen Kondensation von Magnonen nicht berücksichtigt [76, 90, 95, 96, 97].

In diesem Kapitel folgen wir einer radikal anderen Herangehensweise: Ausgangspunkt unserer Betrachtungen ist die Tatsache, dass die Magnonen in YIG sich bei Raumtemperatur wie klassische Wellen verhalten. Insbesondere ist Raumtemperatur etwa drei Größenordnungen höher als die Energie der kondensierenden Magnonen; folglich ist die thermische Gleichgewichtsverteilung nicht von der Rayleigh-Jeans Verteilung zu unterscheiden, die man aus dem klassischen Gleichverteilungssatz erhält. Darüber hinaus ist der effektive Spin $S \approx 14$ in YIG so groß, dass alle Quantenfluktuationen, die in Spinsy-

stemen bekanntlich mit Potenzen von $1/S$ skalieren [46], vernachlässigbar sein sollten. Wenn die Magnonen allerdings klassische Wellen sind, kann es sich bei der experimentell beobachteten Kondensation nicht um BEC handeln, da BEC ein reiner Quanteneffekt ist. Daher interpretieren wir diesen Kondensationsprozess als ein neues Beispiel der noch relativ unbekannten kinetischen Kondensation von klassischen Wellen [98, 99, 100], die wir als Rayleigh-Jeans Kondensation bezeichnen [101]. Die beiden grundlegenden Voraussetzungen für eine solche klassische Kondensation sind ein stochastisches Ensemble von Wellen und nichtlineare Wechselwirkungen. Für YIG bei Raumtemperatur sind diese beiden Bedingungen erfüllt: Die klassische Spindynamik ist intrinsisch nichtlinear und bei hohen Temperaturen gibt es natürlich thermische Fluktuationen, die das System stochastisch machen. Experimentell wurde diese klassische Rayleigh-Jeans Kondensation bis jetzt nur von Sun *et al.* durch Abbildung von klassischem Licht in einem photorefraktiven Kristall nachgewiesen [100]. Das Ziel dieses Kapitels wird es sein, zu zeigen, dass die in den Experimenten [15, 16, 17, 18, 19, 20, 21, 22, 23, 24] beobachtete Kondensation von Magnonen bei Raumtemperatur tatsächlich ein weiteres Beispiel für klassische Rayleigh-Jeans Kondensation ist.

Dazu betrachten wir wieder die Hamiltonoperatoren für den magnetischen Sektor (C.1), den elastischen Sektor (C.2) und für die magnetoelastische Kopplung (C.3); zusätzlich erweitern wir das externe Magnetfeld durch das parametrische Pumpfeld, sodass $\boldsymbol{H}(t) = [H_0 + H_1 \cos(2\omega_\mathrm{p} t)]\, \boldsymbol{e}_z$ (mit der Pumpfrequenz ω_p), und wir reskalieren die phononischen Normalmoden gemäß $X_{\boldsymbol{k}\lambda} \to X_{\boldsymbol{k}\lambda}/\sqrt{N}$ und $P_{\boldsymbol{k}\lambda} \to P_{\boldsymbol{k}\lambda}/\sqrt{N}$, um einen wohldefinierten thermodynamischen Limes in allen Ausdrücken zu erhalten. Die Dynamik der Spinoperatoren gehorcht dann der Heisenberg-Bewegungsgleichung

$$\dot{\boldsymbol{S}}_i = \boldsymbol{S}_i \times \Big[\boldsymbol{H}(t) + \sum_j \mathbb{K}_{ij} \boldsymbol{S}_j\Big] + \frac{1}{2}\Big[\boldsymbol{S}_i \times \boldsymbol{F}_i(t) - \boldsymbol{F}_i(t) \times \boldsymbol{S}_i\Big], \tag{C.14}$$

mit dem sowohl Austausch- als auch Dipol-Dipol Wechselwirkungen enthaltenden Spin-Spin Wechselwirkungstensor $\mathbb{K}_{ij}$ mit kartesischen Komponenten $\mathbb{K}_{ij}^{\alpha\beta} = J_{ij}\delta^{\alpha\beta} + D_{ij}^{\alpha\beta}$ und dem Vektoroperator

$$\boldsymbol{F}_i(t) = -\frac{2}{S^2} \sum_{\alpha\beta} \boldsymbol{e}_\alpha B^{\alpha\beta} X_i^{\alpha\beta}(t) S_i^\beta(t), \tag{C.15}$$

der das durch die magnetoelastische Kopplung induzierte magnetische Feld beschreibt. Die entsprechende Heisenberg-Bewegungsgleichung für die Phononen lautet

$$\ddot{X}_{\boldsymbol{k}\lambda} + \omega_{\boldsymbol{k}\lambda}^2 X_{\boldsymbol{k}\lambda} = A_{\boldsymbol{k}\lambda}(t), \tag{C.16}$$

wobei die Kraft, die die Spinfreiheitsgrade auf die Phononen ausüben, durch

$$A_{\boldsymbol{k}\lambda}(t) = \frac{i}{2MS^2} \sum_i \sum_{\alpha\beta} e^{-i\boldsymbol{k}\cdot\boldsymbol{R}_i} B^{\alpha\beta} \boldsymbol{k}_{\alpha\beta} \cdot \boldsymbol{e}_{-\boldsymbol{k}\lambda} S_i^\alpha(t) S_i^\beta(t) \tag{C.17}$$

gegeben ist.

An dieser Stelle vollziehen wir nun den Übergang von Quanten- zur klassischen Mechanik, d.h. wir ersetzen alle quantenmechanischen Vektoroperatoren durch klassische Vektoren. Wie in Ref. [48] im Detail ausgeführt, ist es nun möglich, die phononischen Freiheitsgrade aus der Bewegungsgleichung (C.14) der Spins exakt zu eliminieren. Dies wird erreicht, indem man die formale Lösung der phononischen Bewegungsgleichung (C.16) in die Spin-Bewegungsgleichung (C.14) einsetzt. Auf diese Weise erhält man die folgende nicht-Markovsche stochastische Landau-Lifshitz-Gilbert Gleichung (LLG):

$$\begin{aligned}\dot{\boldsymbol{S}}_i(t) =& \boldsymbol{S}_i(t) \times \Big[\boldsymbol{H}(t) + \boldsymbol{h}_i(t) + \sum_j \mathbb{K}_{ij}\boldsymbol{S}_j(t)\Big] \\ &- \boldsymbol{S}_i(t) \times \int_0^t \mathrm{d}t' \sum_j \mathbb{G}_{ij}(t,t')\dot{\boldsymbol{S}}_j(t'). \end{aligned} \tag{C.18}$$

Der Effekt der magnetoelastischen Wechselwirkungen mit den Phononen manifestiert sich hier durch das induzierte Magnetfeld $\boldsymbol{h}_i(t)$ und den nicht-Markovschen Dämpfungstensor $\mathbb{G}_{ij}(t,t')$; explizit ist dieser als

$$\begin{aligned}\mathbb{G}_{ij}^{\alpha\beta}(t,t') =& \frac{1}{S^4}\sum_{\mu\nu} B^{\alpha\mu}B^{\beta\nu}S_i^{\mu}(t)S_j^{\nu}(t')\frac{1}{N}\sum_{\boldsymbol{k}\lambda} e^{i\boldsymbol{k}\cdot(\boldsymbol{R}_i-\boldsymbol{R}_j)} \\ &\times (\boldsymbol{k}_{\alpha\mu}\cdot\boldsymbol{e}_{\boldsymbol{k}\lambda})\,(\boldsymbol{k}_{\beta\nu}\cdot\boldsymbol{e}_{-\boldsymbol{k}\lambda})\,\frac{\cos\left[\omega_{\boldsymbol{k}\lambda}\,(t-t')\right]}{M\omega_{\boldsymbol{k}\lambda}^2} \end{aligned} \tag{C.19}$$

gegeben, mit $\boldsymbol{k}_{\alpha\beta} = k_\alpha \boldsymbol{e}_\beta + k_\beta \boldsymbol{e}_\alpha$. Das induzierte Magnetfeld $\boldsymbol{h}_i(t)$ in der LLG (C.18) ist ein lineares Funktional der Anfangswerte der Phononkoordinaten; nimmt man an, dass diese im thermischen Gleichgewicht bei Temperatur T sind, so sind die $\boldsymbol{h}_i(t)$ Gaußsche nicht-Markovsche stochastische Prozesse. Während der Mittelwert $\langle \boldsymbol{h}_i(t)\rangle = \bar{\boldsymbol{h}}_i(t)$ nur eine kleine Korrektur zum externen Magnetfeld $\boldsymbol{H}(t)$ darstellt (die wir vernachlässigen werden), ist der fluktuierende Anteil $\delta\boldsymbol{h}_i(t) = \boldsymbol{h}_i(t) - \bar{\boldsymbol{h}}_i(t)$ entscheidend für die Thermalisierung und das Entstehen eines magnonischen Kondensats. Desweiteren ist die Kovarianz des induzierten Magnetfeldes auf die übliche Art mit dem Dämpfungstensor über das Fluktuations-Dissipations Theorem verknüpft, d.h.

$$\left\langle \delta h_i^{\alpha}(t)\delta h_j^{\beta}(t')\right\rangle = T\mathbb{G}_{ij}^{\alpha\beta}(t,t'). \tag{C.20}$$

Die LLG (C.18) beschreibt die Präzession der klassischen Spins um ein effektives Magnetfeld, das sowohl den Effekt von Spin-Spin Wechselwirkungen als auch thermische Fluktuationen und Dämpfung beinhaltet. Im Gegensatz zur konventionellen stochastischen LLG enthält unsere LLG (C.18) einen Dämpfungstensor $\mathbb{G}_{ij}(t,t')$, der aufgrund der nichtlokalen Spin-Spin Wechselwirkungen, die durch den Austausch von Phononen induziert werden, und der Gedächtniseffekte des thermischen Phononenbads sowohl im Ort als auch in

der Zeit nichtlokal ist. Eine solche nicht-Markovsche Dämpfung korrespondiert wegen des Fluktuations-Dissipations Theorems (C.20) zu einem thermischen Rauschen mit einem farbigen Spektrum, das von der mikroskopischen Dynamik der Phononen erzeugt wird. Anders als das weiße Rauschen in der konventionellen LLG kann dieses farbige Rauschen die physikalische Realität auch auf kurzen Zeitskalen und für den Fall beschreiben, dass Spin- und Phononendynamik dieselbe Zeitskala haben [48, 67]. Es ist ebenfalls zu beachten, dass der über die Kovarianz (C.20) definierte stochastische Prozess aufgrund der expliziten Abhängigkeit des Dämpfungstensors (C.19) von den Spinvariablen nicht ergodisch ist. Zwar ließe sich ein zugrunde liegender ergodischer Prozess definieren [48]; wir werden hier jedoch stattdessen eine physikalisch motivierte Näherung durchführen: Wir sind nur an Systemen interessiert, deren Grundzustand ein saturierter Ferromagnet ist, sodass alle Spins ausschließlich in z-Richtung zeigen. Dann ist es nützlich, die Spins als

$$\boldsymbol{S}_i(t) = S\left[\boldsymbol{e}_z + \boldsymbol{m}_i(t)\right] \tag{C.21}$$

zu schreiben. Da der effektive Spin $S \approx 14$ in YIG sehr groß ist, erwarten wir, dass thermische Fluktuationen nur vergleichsweise kleine Abweichungen vom Grundzustand induzieren, sodass $|\boldsymbol{m}_i(t)| \ll 1$. Um den führenden Beitrag zu thermischen Fluktuationen und Dämpfung zu erhalten, können wir in der Definition des Dämpfungstensors (C.19) dann $\boldsymbol{S}_i(t) \to S\boldsymbol{e}_z$ substituieren, wodurch $\delta\boldsymbol{h}_i(t)$ seine Abhängigkeit vom Zustand des Spinsystems verliert und folglich ein ergodischer Prozess wird. Ein weiterer Vorteil dieser Näherung ist, dass der Dämpfungstensor $\mathbb{G}_{ij}(t,t')$ dann nur noch eine Funktion der Differenzen $\boldsymbol{R}_i - \boldsymbol{R}_j$ und $t-t'$ ist. In diesem Fall ist es sinnvoll, im Impulsraum zu arbeiten und direkt die Zeitentwicklung der Fouriermoden

$$\boldsymbol{m}_{\boldsymbol{k}}(t) = \sum_i e^{-i\boldsymbol{k}\cdot\boldsymbol{R}_i}\boldsymbol{m}_i(t) \tag{C.22}$$

zu berechnen. Nach dieser Vereinfachung können wir unsere LLG (C.18) numerisch ohne weitere Näherungen direkt lösen. Ohne weiter auf die Details solch einer numerichen Lösung einzugehen, werden wir im Folgenden nur noch unsere Ergebnisse präsentieren.

Um den direkten Kontakt mit den Experimenten [15, 16, 17, 18, 19, 20, 21, 22, 23, 24] herzustellen, wählen wir die Parameter unserer Simulation so, dass sie ein typisches Experiment beschreiben [22, 23, 24, 84]: Wir betrachten einen dünnen YIG Film der Dicke $d = 6.7\,\mu$m bei Temperatur $T = 300\,\mathrm{K}$ in einem statischen Magnetfeld der Stärke $H_0 = 1710\,\mathrm{Oe} \times \mu$; Stärke und Frequenz des Pumpfeldes werden zu $H_1 = 0.03H_0$ und $\omega_\mathrm{p} = 2\pi \times 7.046\,\mathrm{GHz}$ festgesetzt. Für diese Wahl der Parameter hat die magnonische Dispersion ihr Minimum $E_\mathrm{min} = 2\pi \times 4.9\,\mathrm{GHz}$ bei den Impulsen $\boldsymbol{k} = \pm k_\mathrm{min}\boldsymbol{e}_z$, mit $k_\mathrm{min} = 4.999 \times 10^4\,\mathrm{cm}^{-1}$. Außerdem ist die Pumpfrequenz ω_p nur wenig größer als die Frequenz der ferromagnetischen Resonanz $E_{\boldsymbol{k}=0} = 2\pi \times 6.824\,\mathrm{GHz}$; dies verhindert direkte Übergänge der parametrisch angeregten Magnonen zu den

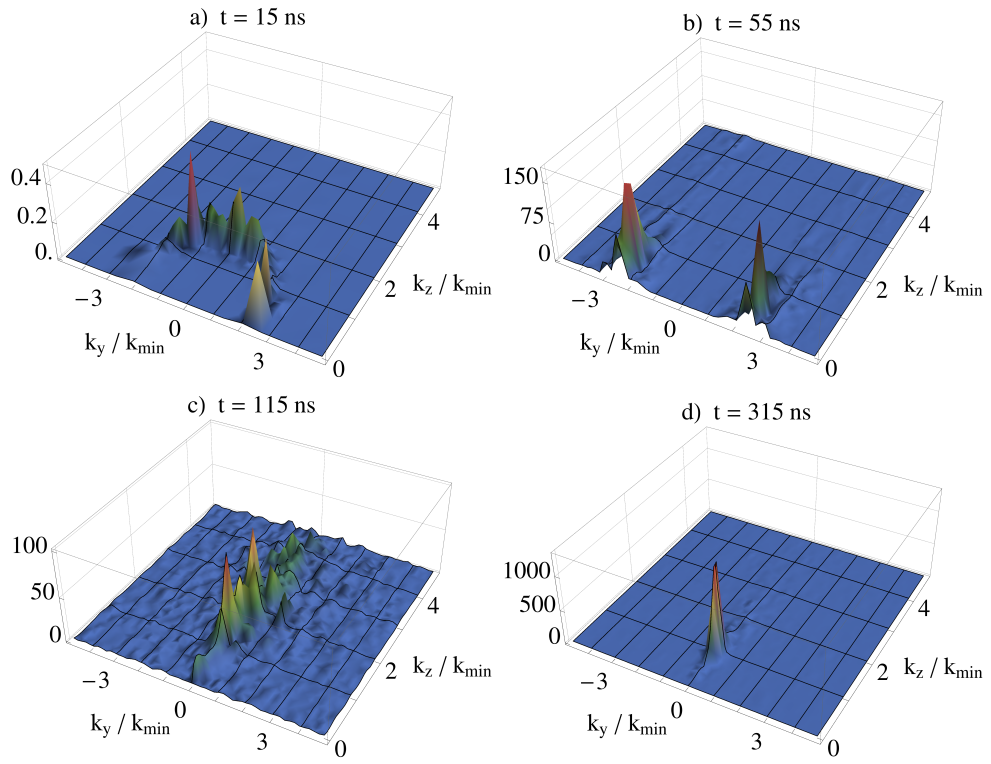

Abbildung C.6: *Momentaufnahmen der stochastischen Zeitentwicklung der Magnonverteilung $n_{\boldsymbol{k}}(t)/n_{\boldsymbol{k}}^{\mathrm{th}}$ relativ zur thermischen Gleichgewichtsverteilung $n_{\boldsymbol{k}}^{\mathrm{th}}$; (a) zeigt die magnetoelastische Hybridisierung, (b) die parametrische Instabilität, (c) die Umverteilung der Magnonen im Impulsraum und (d) das Quasigleichgewicht mit dem Magnon-Kondensat.*

Zuständen niedrigster Energie und ermöglicht daher die Thermalisierung über mehrstufige Magnon-Magnon Streuung [15, 16, 17, 22, 23, 24].

Unsere Observable ist das Quadrat der transversalen Magnetisierung $n_{\boldsymbol{k}}(t) = |m_{\boldsymbol{k}}^x(t)|^2 + |m_{\boldsymbol{k}}^y(t)|^2$, deren Mittelwert $\langle n_{\boldsymbol{k}}(t)\rangle$ direkt proportional zur Magnonenanzahl ist [3]. Solange Spinwellen eine gute Näherung sind, d.h. solange die Abweichung $\boldsymbol{m}_i(t)$ vom ferromagnetischen Grundzustand klein ist, gilt im thermischen Gleichgewicht insbesondere $\langle n_{\boldsymbol{k}}(t)\rangle = n_{\boldsymbol{k}}^{\mathrm{th}} \propto T/E_{\boldsymbol{k}}$. In Abb. C.6 zeigen wir die wichtigsten Abschnitte der Zeitentwicklung von $n_{\boldsymbol{k}}(t)$, unter der Annahme, dass das System zur Zeit $t = 0$ in einem vollständig polarisierten ferromagnetischen Zustand präpariert ist. Diese Zeitentwicklung gliedert sich in vier unterschiedliche Bereiche: In Abb. C.6 (a) ist zu sehen, dass die Bevölkerung des Magnonspektrums auf der Energieoberfläche beginnt, auf der magnetische und elastische Moden hybridisieren; diese Hybridisierung wurde schon in Kap. C.1 behandelt. An dieser Stelle ist zu beachten, dass unsere nicht-Markovsche Beschreibung essentiell für die korrekte Berücksichtigung einer solchen Hybridisierung ist. Im nächsten, in Abb. C.6 (b) gezeigten Abschnitt der Zeitentwicklung dominiert die parametrische Instabilität der Magnonen mit

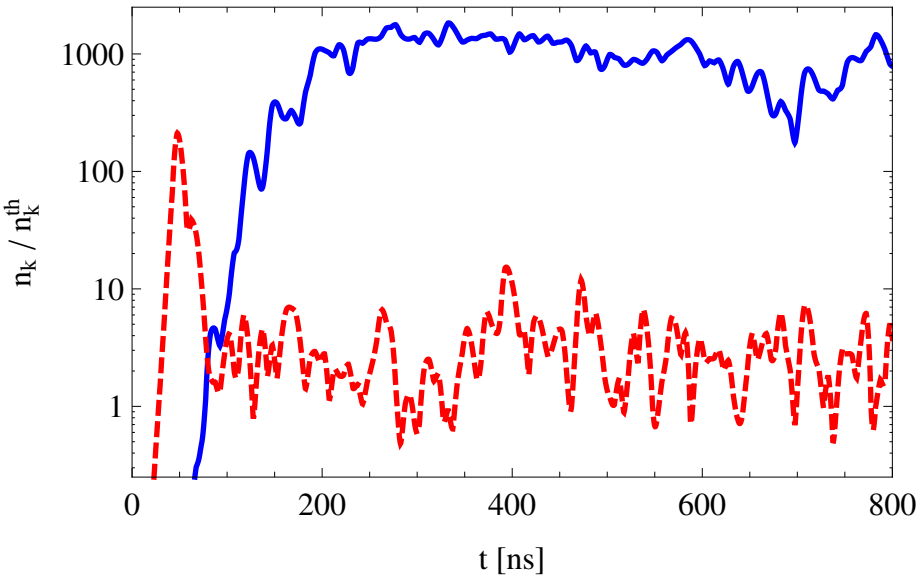

Abbildung C.7: *Logarithmischer Plot der stochastischen Zeitentwicklung der Magnonverteilung $n_{\boldsymbol{k}}(t)/n_{\boldsymbol{k}}^{\mathrm{th}}$ der kondensierenden Mode $\boldsymbol{k} = k_{\mathrm{min}}\boldsymbol{e}_z$ (durchgezogene blaue Linie) und der parametrisch instabilen Mode mit Impuls $\boldsymbol{k}/k_{\mathrm{min}} = -2.4\boldsymbol{e}_y + 0.2\boldsymbol{e}_z$ (gestrichelte rote Linie). Hierbei ist zu beachten, dass das Wachstum des Kondensats beginnt, sobald die parametrischen Moden zum Quasigleichgewicht relaxiert sind.*

$E_{\boldsymbol{k}} \approx \omega_{\mathrm{p}}$ und hoher Elliptizität (d.h. $k_z \approx 0$). Das exponentielle Wachstum der parametrisch instabilen Moden wird sehr gut durch lineare Spinwellentheorie beschrieben; allerdings saturiert es in unserer Simulation aufgrund der nichtperturbativ berücksichtigten Wechselwirkungen nach ungefähr 40 ns. Darüber hinaus beginnen die parametrischen Magnonen bei $t \approx 50$ ns trotz des externen Pumpfeldes zu einem Quasigleichgewicht zu relaxieren. Dies ist der in Abb. C.6 (c) gezeigte dritte Abschnitt der Zeitentwicklung, in dem die durch die parametrische Instabilität erzeugten angeregten Magnonen zu den Zuständen niedriger Energie mit $k_y = 0$ gestreut werden. Im vierten Abschnitt, gezeigt in Abb. C.6 (d), ist diese Umverteilung schließlich abgeschlossen und eine große Anzahl Magnonen hat sich an exakt den Impulsen $\boldsymbol{k} = \pm k_{\mathrm{min}}\boldsymbol{e}_z$ angesammelt, für die die Magnondispersion minimal wird; d.h. ein Rayleigh-Jeans Kondensat ist entstanden.

Die stochastische Zeitentwicklung der kondensierenden Mode ist in Abb. C.7 gezeigt, mit einer parametrisch instabilen Mode zum Vergleich. Die Bildung des Kondensats ist zur Zeit $t \approx 200$ ns beendet; für spätere Zeiten sind, solange das externe Pumpen beibehalten wird, für alle Moden nur noch Oszillationen um einen Quasigleichgewichtszustand zu beobachten. Dies erlaubt es uns, Ensemble-Mittelwerte durch Zeitmittelung zu erhalten. Wählen wir das Intervall zwischen 200 und 800 ns für die Mittelung, so erhalten wir die

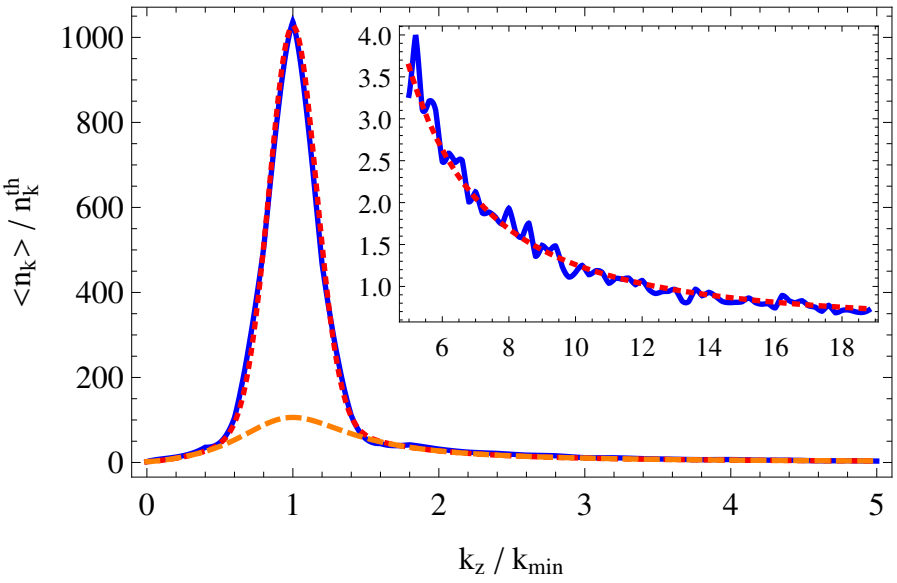

Abbildung C.8: *Zeitgemittelte Quasigleichgewichtsverteilung* $\langle n_{\boldsymbol{k}}(t)\rangle/n^{\mathrm{th}}_{\boldsymbol{k}}$ *der Magnonen (durchgezogene blaue Linie) auf der Achse* $k_y = 0$*. Die gepunktete rote Linie zeigt die Fit-Funktion (C.23) mit effektivem chemischem Potential* $\mu_{\mathrm{eff}} = 0.995E_{\mathrm{min}}$*, während die gestrichelte orange Linie der thermische Anteil alleine ist. Der Beitrag des Kondesats ist als Gaußkurve um* $\boldsymbol{k} = k_{\mathrm{min}}\boldsymbol{e}_z$ *modelliert; mit Standardabweichungen* $\sigma_z = 0.16k_{\mathrm{min}}$ *und* $\sigma_y = 0.1k_{\mathrm{min}}$*, die beide kleiner als der Gitterabstand* $\Delta k = 0.2k_{\mathrm{min}}$ *der Numerik sind. Die eingebettete Grafik zeigt eine vergrößerte Ansicht der Fit-Funktion abseits des Kondensats; die Achsen sind dieselben wie im Hauptplot.*

Quasigleichgewichtsverteilung

$$\frac{\langle n_{\boldsymbol{k}}(t)\rangle}{n^{\mathrm{th}}_{\boldsymbol{k}}} \propto \frac{E_{\boldsymbol{k}}}{E_{\boldsymbol{k}} - \mu_{\mathrm{eff}}} + n_c\left[\delta(\boldsymbol{k} - k_{\mathrm{min}}\boldsymbol{e}_z) + \delta(\boldsymbol{k} + k_{\mathrm{min}}\boldsymbol{e}_z)\right]. \tag{C.23}$$

Der erste Beitrag entspricht einer reskalierten Rayleigh-Jeans Verteilung mit effektivem chemischem Potential $\mu_{\mathrm{eff}} \approx E_{\mathrm{min}}$, die für alle Moden mit Ausnahme der Moden an den Dispersionsminima gültig ist; für diese Moden ist es nötig, einen Delta-artigen Beitrag mit Gewicht n_c und einer mit der Auflösung Δk des für die Numerik gewählten Impulsgitters vergleichbaren Breite hinzuzufügen. Dies beweist, dass die klassische Spindynamik tatsächlich die Rayleigh-Jeans Kondensation von Magnonen ermöglicht. Sowohl die zeitgemittelte Verteilungsfunktion als auch unsere Fit-Funktion (C.23) sind in Abb. C.8 dargestellt. Obwohl die Retardierung des Dämpfungstensors (C.19) nicht entscheidend für das Entstehen des Kondensats ist, so ist sie doch notwendig, um die Kondensation für realistische Werte von magnetoelastischer Kopplung und parametrischem Pumpen zu beobachten.

Schlussendlich haben wir auch den Zerfall des Kondensats untersucht. Dazu haben wir die Simulation mit dem Unterschied wiederholt, dass das

parametrische Pumpen zum Zeitpunkt $t = 100\,\mathrm{ns}$ abgeschaltet wird. In diesem Fall entsteht das Kondensat zwar immer noch (im Einklang mit den Experimenten [18, 19, 20, 23]), aber es beginnt bei $t \approx 250\,\mathrm{ns}$ zu zerfallen. Dieser Zerfall des Kondensats lässt sich in guter Näherung exponentiell beschreiben, mit einer charakteristischen Zerfallszeit $\tau_\mathrm{c} \approx 250\,\mathrm{ns}$, in hervorragender Übereinstimmung mit dem Experiment [19, 24].

Die in diesem Kapitel vorgestellte Arbeit wurde in Zusammenarbeit mit Peter Kopietz durchgeführt und in [P3] veröffentlicht.

Publications

[P1] Andreas Rückriegel, Andreas Kreisel, and Peter Kopietz, *Time-dependent spin-wave theory*, Phys. Rev. B **85**, 054422 (2012).

[P2] Andreas Rückriegel, Peter Kopietz, Dmytro A. Bozhko, Alexander A. Serga, and Burkard Hillebrands, *Magnetoelastic modes and lifetime of magnons in thin yttrium iron garnet films*, Phys. Rev. B **89**, 184413 (2014).

[P3] Andreas Rückriegel and Peter Kopietz, *Rayleigh-Jeans Condensation of Pumped Magnons in Thin-Film Ferromagnets*, Phys. Rev. Lett. **115**, 157203 (2015).

[P4] Carsten Bauer, Andreas Rückriegel, Anand Sharma, and Peter Kopietz, *Nonperturbative renormalization group calculation of quasiparticle velocity and dielectric function of graphene*, Phys. Rev. B **92**, 121409(R) (2015).

([P1] resulted from my Bachelor project; [P4] is not relevant for this thesis.)

Bibliography

[1] W. Nolting, *Quantentheorie des Magnetismus 1. Grundlagen*, Teubner, Stuttgart (1986).

[2] N. W. Ashcroft and N. D. Mermin, *Solid State Physics*, Brooks/Cole, Cengage Learning (1976).

[3] A. G. Gurevich and G. A. Melkov, *Magnetization Oscillations and Waves*, CRC Press, Boca Raton (1996).

[4] V. Cherepanov, I. Kolokolov, and V. L'vov, *The saga of YIG: spectra, thermodynamics, interaction and relaxation of magnons in a complex magnet*, Phys. Reports **229**, 81 (1993).

[5] M. A. Gilleo and S. Geller, *Magnetic and Crystallographic Properties of Substituted Yttrium-Iron Garnet,* $3Y_2O_3 \cdot xM_2O_3 \cdot (5-x)Fe_2O_3$, Phys. Rev. **110**, 73 (1958).

[6] A. Kreisel, F. Sauli, L. Bartosch, and P. Kopietz, *Microscopic spin-wave theory for yttrium-iron garnet films*, Eur. Phys. J. B **71**, 59 (2009).

[7] A. Kreisel, F. Sauli, L. Bartosch, and P. Kopietz, *Spin-waves in Yttrium-iron garnet*, Europhysics News **40/6**, 18 (2009)

[8] I. S. Tupitsyn, P. C. E. Stamp, and A. L. Burin, *Stability of Bose-Einstein Condensates of Hot Magnons in Yttrium Iron Garnet Films*, Phys. Rev. Lett. **100**, 257202 (2008).

[9] S. M. Rezende, *Theory of microwave superradiance from a Bose-Einstein condensate of magnons*, Phys. Rev. B **79**, 060410(R) (2009).

[10] S. M. Rezende, *Theory of coherence in Bose-Einstein condensation phenomena in a microwave-driven interacting magnon gas*, Phys. Rev. B **79**, 174411 (2009).

[11] T. Kloss, A. Kreisel, and P. Kopietz, *Parametric pumping and kinetics of magnons in dipolar ferromagnets*, Phys. Rev. B **81**, 104308 (2010).

[12] J. Hick, F. Sauli, A. Kreisel, and P. Kopietz, *Bose-Einstein condensation at finite momentum and magnon condensation in thin film ferromagnets*, Eur. Phys. J. B **78**, 429 (2010).

[13] A. A. Serga, C. W. Sandweg, V. I. Vasyuchka, M. B. Jungfleisch, B. Hillebrands, A. Kreisel, P. Kopietz, and M. P. Kostylev, *Brillouin light scattering spectroscopy of parametrically excited dipole-exchange magnons*, Phys. Rev. B **86**, 134403 (2012).

[14] M. Agrawal, V. I. Vasyuchka, A. A. Serga, A. D. Karenowska, G. A. Melkov, and B. Hillebrands, *Direct Measurement of Magnon Temperature: New Insight into Magnon-Phonon Coupling in Magnetic Insulators*, Phys. Rev. Lett. **111**, 107204 (2013).

[15] S. O. Demokritov, V. E. Demidov, O. Dzyapko, G. A. Melkov, A. A. Serga, B. Hillebrands, and A. N. Slavin, *Bose-Einstein condensation of quasi-equilibrium magnons at room temperature under pumping*, Nature (London) **443**, 430 (2006).

[16] V. E. Demidov, O. Dzyapko, S. O. Demokritov, G. A. Melkov, and A. N. Slavin, *Thermalization of a Parametrically Driven Magnon Gas Leading to Bose-Einstein Condensation*, Phys. Rev. Lett. **99**, 037205 (2007).

[17] O. Dzyapko, V. E. Demidov, S. O. Demokritov, G. A. Melkov, and A. N. Slavin, *Direct observation of Bose-Einstein condensation in a parametrically driven gas of magnons*, New J. Phys. **9**, 64 (2007).

[18] V. E. Demidov, O. Dzyapko, S. O. Demokritov, G. A. Melkov, and A. N. Slavin, *Observation of Spontaneous Coherence in Bose-Einstein Condensate of Magnons*, Phys. Rev. Lett. **100**, 047205 (2008).

[19] S. O. Demokritov, V. E. Demidov, O. Dzyapko, G. A. Melkov, and A. N. Slavin, *Quantum coherence due to Bose-Einstein condensation of parametrically driven magnons*, New J. Phys. **10**, 045029 (2008).

[20] V. E. Demidov, O. Dzyapko, M. Buchmeier, T. Stockhoff, G. Schmitz, G. A. Melkov, and S. O. Demokritov, *Magnon Kinetics and Bose-Einstein Condensation Studied in Phase Space*, Phys. Rev. Lett. **101**, 257201 (2008).

[21] P. Nowik-Boltyk, O. Dzyapko, V. E. Demidov, N. G. Berloff, and S. O. Demokritov, *Spatially non-uniform ground state and quantized vortices in a two-component Bose-Einstein condensate of magnons*, Sci. Rep. **2**, 482 (2012).

[22] A. A. Serga, V. S. Tiberkevich, C. W. Sandweg, V. I. Vasyuchka, D. A. Bozhko, A. V. Chumak, T. Neumann, B. Obry, G. A. Melkov, A. N.

Slavin, and B. Hillebrands, *Bose-Einstein condensation in an ultra-hot gas of pumped magnons*, Nat. Commun. **5**, 3452 (2014).

[23] P. Clausen, D. A. Bozhko, V. I. Vasyuchka, B. Hillebrands, G. A. Melkov, and A. A. Serga, *Stimulated thermalization of a parametrically driven magnon gas as a prerequisite for Bose-Einstein magnon condensation*, Phys. Rev. B **91**, 220402(R) (2015).

[24] P. Clausen, D. A. Bozhko, V. I. Vasyuchka, G. A. Melkov, B. Hillebrands, and A. A. Serga, *Magnon Supercurrent in a Magnon Bose-Einstein Condensate subject to a Thermal Gradient*, arXiv:1503.00482v1 [cond-mat.quant-gas] 2 Mar 2015.

[25] B. R. Tittmann, *Possible identification of magnetostatic surface spin wave modes in ferromagnetic resonance on epitaxial yttrium-iron-garnet films*, Solid State Commun. **13**, 463 (1973).

[26] N. Kumar and K. P. Sinha, *Spin-phonon relaxation due to transverse optical modes*, Physica **34**, 387 (1967).

[27] N. Kumar and K. P. Sinha, *A new mechanism of magnon-phonon relaxation process in ferrimagnetic insulators*, Physica **36**, 655 (1967).

[28] A. Kreisel, P. Kopietz, P. T. Cong, B. Wolf, and M. Lang, *Elastic constants and ultrasonic attenuation in the cone state of the frustrated antiferromagnet* Cs_2CuCl_4, Phys. Rev. B **84**, 024414 (2011).

[29] E. Abrahams and C. Kittel, *Spin-Lattice Relaxation in Ferromagnets*, Phys. Rev. **88**, 1200 (1952).

[30] C. Kittel and E. Abrahams, *Relaxation Processes in Ferromagnetism*, Rev. Mod. Phys. **25**, 233 (1953).

[31] C. Kittel, *Interaction of Spin Waves and Ultrasonic Waves in Ferromagnetic Crystals*, Phys. Rev. **110**, 836 (1958).

[32] M.I. Kaganov and V.M. Tsukernik, *Phenomenological Theory of Kinetic Processes in Ferromagnetic Dielectrics. II. Interaction of Spin Waves with Phonons*, Sov. Phys. JETP **9**, 151 (1959).

[33] A. E. Lord, Jr., *Sound wave attenuation due to the magnon-phonon interaction*, Phys. Kondens. Mater. **7**, 232 (1968).

[34] W. Strauss, *Magnetoelastic Properties of Yttrium-Iron Garnet*, Physical Acoustics **4**, 211 (1968).

[35] P. Hansen, *Magnetostriction of Ruthenium-Substituted Yttrium Iron Garnet*, Phys. Rev. B **8**, 246 (1973).

[36] M. P. Marder, *Condensed Matter Physics*, Wiley, New York (2000).

[37] V. S. L'vov, *Wave Turbulence under Parametric Excitations*, Springer, Berlin (1994).

[38] V. E. Zakharov, V. S. L'vov, and S. S. Starobinets, *Stationary Nonlinear Theory of Parametric Excitation of Waves*, Sov. Phys. JETP **32**, 656 (1971).

[39] V. E. Zakharov, V. S. L'vov and S. S. Starobinets, *Spin-wave turbulence beyond the parametric excitation threshold*, Sov. Phys. Usp. **17**, 896 (1975).

[40] T. Holstein and H. Primakoff, *Field Dependence of the Intrinsic Domain Magnetization of a Ferromagnet*, Phys. Rev. **58**, 1098 (1940).

[41] S. V. Maleev, *Scattering of Slow Neutrons in Ferromagnets*, Sov. Phys. JETP **6**, 776 (1958).

[42] D. P. Arovas and A. Auerbach, *Functional integral theories of low-dimensional quantum Heisenberg models*, Phys. Rev. B **38**, 316 (1988).

[43] W. Nolting, *Quantentheorie des Magnetismus 2. Modelle*, Teubner, Stuttgart (1986).

[44] C. Herring and C. Kittel, *On the Theory of Spin Waves in Ferromagnetic Media*, Phys. Rev. **81**, 869 (1951).

[45] N. D. Mermin, *Absence of Ordering in Certain Classical Systems*, J. Math. Phys. **8**, 1061 (1967).

[46] A. Polkovnikov, *Phase space representation of quantum dynamics*, Annals of Physics **325**, 1790 (2010).

[47] J. L. García-Palacios and F. J. Lázaro, *Langevin-dynamics study of the dynamical properties of small magnetic particles*, Phys. Rev. B **58**, 14937 (1998).

[48] E. Rossi, O. G. Heinonen, and A. H. MacDonald, *Dynamics of magnetization coupled to a thermal bath of elastic modes*, Phys. Rev. B **72**, 174412 (2005).

[49] W. F. Brown, Jr., *Thermal Fluctuations of a Single-Domain Particle*, Phys. Rev. **130**, 1677 (1963).

[50] R. Kubo and N. Hashitsume, *Brownian Motion of Spins*, Prog. Theor. Phys. Suppl. **46**, 210 (1970).

[51] R. Kubo, *The fluctuation-dissipation theorem*, Rep. Prog. Phys. **29**, 255 (1966).

[52] N.G. Van Kampen, *Stochastic Processes in Physics and Chemistry* (Third Edition), North-Holland Personal Library, North Holland (2007).

[53] J. W. Negele and H. Orland, *Quantum Many-Particle Systems*, Advanced Books Classics, Perseus Books (1998).

[54] A. L. Fetter and J. D. Walecka, *Quantum Theory of Many-Particle Systems*, McGraw-Hill, San Francisco (1971).

[55] W. Nolting, *Grundkurs Theoretische Physik Band 7: Viel-Teilchen-Theorie* (Fünfte Auflage), Springer (2001).

[56] R. D. Mattuck, *A Guide to Feynman Diagrams in the Many-Body problem*, Dover, N. Y. (1992).

[57] A. A. Abrikosov, L. P. Gorkov, and I. E. Dzyaloshinskii, *Methods of Quantum Field Theory in Statistical Physics*, Dover, N. Y. (1975).

[58] A. Altland and B. Simons, *Condensed Matter Field Theory* (Second Edition), Cambridge (2010).

[59] P. Kopietz, L. Bartosch, and F. Schütz, *Introduction to the Functional Renormalization Group*, Springer, Berlin (2010).

[60] C. W. Gardiner, *Stochastic Methods: A Handbook for the Natural and Social Sciences* (Fourth Edition), Springer, Berlin (2009).

[61] Pottier, Noelle, *Nonequilibrium Statistical Physics: Linear Irreversible Processes* Oxford University Press, Oxford (2010).

[62] P. C. Martin, E. D. Siggia, and H. A. Rose, *Statistical Dynamics of Classical Systems*, Phys. Rev. A **8**, 423 (1973).

[63] H. K. Janssen, *On a Lagrangean for classical field dynamics and renormalization group calculations of dynamical critical properties*, Z. Phys. B **23**, 377 (1976).

[64] C. De Dominicis, *Techniques de renormalisation de la théorie des champs et dynamique des phénomenès critiques*, J. Phys. Colloques **37** C1, 247 (1976).

[65] E. Wong and M. Zakai, *On the Convergence of Ordinary Integrals to Stochastic Integrals*, Annals Mathem. Statistics **36**, 1560 (1965).

[66] R. L. S. Farias, R. O. Ramos, and L. A. da Silva, *Numerical solutions for non-Markovian stochastic equations of motion*, Comput. Phys. Commun. **180**, 574 (2009).

[67] R. L. S. Farias, R. O. Ramos, and L. A. da Silva, *Stochastic Langevin equations: Markovian and non-Markovian dynamics*, Phys. Rev. E **80**, 031143 (2009).

[68] B. Lüthi, *Physical Acoustics in the Solid State*, Springer, Berlin (2005).

[69] H. F. Tiersten, *Coupled Magnetomechanical Equations for Magnetically Saturated Insulators*, J. Math. Phys. **5**, 1298 (1964).

[70] C. M. Bandari and G. S. Verma, *Scattering of Magnons and Phonons in the Thermal Conductivity of Yttrium Iron Garnet*, Phys. Rev. **152**, 731 (1966).

[71] T. Kobayashi, R. C. Barker, J. L. Bleustein, and A. Yelon, *Ferromagnetoelastic Resonance in Thin Films. I. Formal Treatment*, Phys. Rev. B **7**, 3273 (1973).

[72] L. Dreher, M. Weiler, M. Pernpeintner, H. Huebl, R. Gross, M. S. Brandt, and S. T. B. Goennenwein, *Surface acoustic wave driven ferromagnetic resonance in nickel thin films: Theory and experiment*, Phys. Rev. B **86**, 134415 (2012).

[73] Hiroto Adachi, Ken-ichi Uchida, Eiji Saitoh, and Sadamichi Maekawa, *Theory of the spin Seebeck effect*, Rep. Prog. Phys. **76**, 036501 (2013).

[74] A. Kamra and G. E. W. Bauer, *Actuation, propagation, and detection of transverse magnetoelastic waves in ferromagnets*, Solid State Commun. (2013).

[75] C. W. Sandweg, M. B. Jungfleisch, V. I. Vasyuchka, A. A. Serga, P. Clausen, H. Schultheiss, B. Hillebrands, A. Kreisel, and P. Kopietz, *Wide-range wavevector selectivity of magnon gases in Brillouin light scattering spectroscopy*, Rev. Sci. Instrum. **81**, 073902 (2010).

[76] J. Hick, T. Kloss, and P. Kopietz, *Thermalization of magnons in yttrium-iron garnet: Nonequilibrium functional renormalization group approach*, Phys. Rev. B **86**, 184417 (2012).

[77] M. G. Cottam and D. J. Lockwood, *Light Scattering in Magnetic Solids*, Wiley, New York (1986).

[78] J. Jorzick, S. O. Demokritov, C. Mathieu, B. Hillebrands, B. Bartenlian, C. Chappert, F. Rousseaux, and A. N. Slavin, *Brillouin light scattering from quantized spin waves in micron-size magnetic wires*, Phys. Rev. B **60**, 15194 (1999).

[79] M. Sparks, *Ferromagnetic-Relaxation Theory*, McGraw-Hill, New York (1964).

[80] M. J. Hurben and C. E. Patton, *Theory of two magnon scattering microwave relaxation and ferromagnetic resonance linewidth in magnetic thin films*, J. Appl. Phys. **83**, 4344 (1998).

[81] A. V. Chumak, A. A. Serga, B. Hillebrands, G. A. Melkov, V. Tiberkevich, and A. N. Slavin, *Parametrically stimulated recovery of a microwave signal using standing spin-wave modes of a magnetic film*, Phys. Rev. B **79**, 014405 (2009).

[82] A. V. Chumak, A. A. Serga, M. B. Jungfleisch, R. Neb, D. A. Bozhko, V. S. Tiberkevich, and B. Hillebrands, *Direct detection of magnon spin transport by the inverse spin Hall effect*, Appl. Phys. Lett. **100**, 082405 (2012).

[83] A. L. Chernyshev, *Field dependence of magnon decay in yttrium iron garnet thin films*, Phys. Rev. B **86**, 060401(R) (2012).

[84] B. Hillebrands *et al.*, Annual Report 2012.

[85] L. P. Pitaevskii and S. Stringari, *Bose-Einstein condensation*, Clarendon Press, Oxford (2003).

[86] A. I. Bugrij and V. M. Loktev, *On the theory of BoseEinstein condensation of quasiparticles: on the possibility of condensation of ferromagnons at high temperatures*, Low Temp. Phys. **33**, 37 (2007).

[87] B. A. Malomed, O. Dzyapko, V. E. Demidov, and S. O. Demokritov, *Ginzburg-Landau model of Bose-Einstein condensation of magnons*, Phys. Rev. B **81**, 024418 (2010).

[88] F. Li, W. M. Saslow, and V. L. Pokrovsky, *Phase Diagram for Magnon Condensate in Yttrium Iron Garnet Film*, Sci. Rep. **3**, 1372 (2013).

[89] A. I. Bugrij and V. M. Loktev, *On the theory of inhomogeneous Bose-Einstein condensation of magnons in yttrium garnet*, Low Temp. Phys. **39**, 1037 (2013).

[90] F. S. Vannucchi, Á. R. Vasconcellos, and R. Luzzi, *Dynamics of a Bose-Einstein condensate of excited magnons*, Eur. Phys. J. B **86**, 463 (2013).

[91] S. P. Lim and D. L. Huber, *Microscopic theory of spin-wave instabilities in parallel-pumped easy-plane ferromagnets*, Phys. Rev. B **37**, 5426, (1988).

[92] V. M. Tsukernik and R. P. Yankelevich, *Stationary distribution of magnons following parametric excitation in ferromagnetic substances*, Sov. Phys. JETP **41**, 1059 (1975).

[93] I. A. Vinikovetskii, A. M. Frishman, and V. M. Tsukernik, *Kinetic equation for a system of parametrically excited spin waves*, Sov. Phys. JETP **49**, 1067 (1979).

[94] Yu. D. Kalafati and V. L. Safanov, *Thermodynamic approach in the theory of paramagnetic resonance of magnons*, Sov. Phys. JETP **68**, 1162 (1989).

[95] A. V. Lavrinenko, V. S. L'vov, G. A. Melkov, and V. B. Cherepanov, *"Kinetic" instability of a strongly nonequilibrium system of spin waves and tunable radiation of a ferrite*, Sov. Phys. JETP **54**, 542 (1981).

[96] V. S. Lutovinov, G. A. Melkov, A. Yu. Taranenko, and V. B. Cherepanov, *Kinetic instability of first order spin waves in ferrite*, Sov. Phys. JETP **68**, 432 (1989).

[97] A. Yu. Taranenko and V. B. Cherepanov, *Energy absorption in a ferrite beyond the kinetic instability threshold*, Sov. Phys. JETP **68**, 1046 (1989).

[98] C. Connaughton, C. Josserand, A. Picozzi, Y. Pomeau, and S. Rica, *Condensation of Classical Nonlinear Waves*, Phys. Rev. Lett. **95**, 263901 (2005).

[99] G. Düring, A.Picozzi, and S. Rica, *Breakdown of weak-turbulence and nonlinear wave condensation*, Physica D (Amsterdam) **238**, 1524 (2009).

[100] C. Sun, S. Jia, C. Barsi, S. Rica, A. Picozzi, and J. W. Fleischer, *Observation of the kinetic condensation of classical waves*, Nat. Phys. **8**, 470 (2012).

[101] P. Kirton and J. Keeling, *Thermalization and breakdown of thermalization in photon condensates*, Phys. Rev. A **91**, 033826 (2015).

[102] K. Huang, *Statistical Mechanics* (Second Edition), Wily, New York (1987).

[103] N. Smith, *Modeling of thermal magnetization fluctuations in thin-film magnetic devices*, J. Appl. Phys. **90**, 5768 (2001).

[104] T. Munakata and T. Kawakatsu, *Resonance in Non-Markovian Activation Processes*, Prog. Theor. Phys. **74**, 262 (1985).

[105] *The NAG Library*, The Numerical Algorithms Group (NAG), Oxford, United Kingdom.

[106] D. García-Álvarez, *A comparison of a few numerical schemes for the integration of stochastic differential equations in the Stratonovich interpretation*, arXiv:1102.4401v1 [physics.comp-ph] 22 Feb 2011.

[107] D. B. Thomas, W. Luk, P. H. W. Leong, and J. D. Villasenor, *Gaussian random number generators*, ACM Comput. Surv. **39**, 11 (2007).

[108] G. A. Melkov and S. V. Sholom, *Kinetic instability of spin waves in thin ferrite films*, Sov. Phys. JETP **72**, 341 (1991).

[109] G.A. Melkov, V.L. Safonov, A.Y. Taranenko, and S.V. Sholom, *Kinetic instability and bose condensation of nonequilibrium magnons*, J. Magn. Magn. Mater. **132**, 180 (1994).

[110] O. Jepsen, J. Madsen, and O. K. Andersen, *Band structure of thin films by the linear augmented-plane-wave method*, Phys. Rev. B **18**, 605 (1978).

[111] P. E. Kloeden and E. Platen, *Numerical Solution of Stochastic Differential Equations*, Springer, Berlin (1992).

Danksagung

Zum Abschluss möchte ich noch den Personen danken, die einen wesentlichen Beitrag zum Gelingen dieser Arbeit hatten.

Der größte Dank gebührt meinem Betreuer Prof. Dr. Peter Kopietz, der es mir ermöglichte, an interessanten Problemstellungen zu forschen. Sowohl von seiner Intuition und seinem Wissen als auch von seiner Herangehensweise an komplexe physikalische Probleme habe ich in großem Maße profitiert. Insbesondere möchte ich ihm auch für die angenehme und produktive Arbeitsatmosphäre in seiner Gruppe und dafür, dass er immer ein offenes Ohr für Fragen und Probleme hat, danken. Ich bin ebenfalls dankbar dafür, dass ich ihn bei seinem Forschungssemester an die University of Florida in Gainesville begleiten konnte.

Priv.-Doz. Dr. Axel Pelster danke ich für seine Bereitschaft, das Zweitgutachten für diese Arbeit anzufertigen. Außerdem danke ich ihm für sein Engagement im Graduiertenkolleg des Sonderforschungsbereichs TRR 49, insbesondere für die Organisation vieler Seminare und für die interessanten Diskussionen, die wir bei diesen führten.

Diese Arbeit wurde erst durch die direkte Zusammenarbeit mit der Arbeitsgruppe von Prof. Dr. Burkard Hillebrands und durch die finanzielle Unterstützung der DFG im Rahmen des Sonderforschungsbereichs TRR 49 möglich. Besonders danken möchte ich neben Prof. Dr. Burkard Hillebrands auch Dr. Alexander A. Serga und Dmytro A. Bozhko für die anregenden Diskussionen und die detaillierte Erklärung ihrer Experimente.

Dank gebührt auch sämtlichen Mitgliedern der Arbeitsgruppe Kopietz für die gute Zusammenarbeit und kollegiale Atmosphäre. Der University of Florida in Gainesville, an der der erste Teil dieser Arbeit entstand, danke ich für ihre Gastfreundschaft.

Zu guter Letzt möchte ich mich bei meinen Eltern und meinem Bruder Christian für ihre fortwährende Unterstützung bedanken.

Lebenslauf

Persönliche Daten

Name	Andreas Rückriegel
Staatsangehörigkeit	Deutsch
Geburtsdatum und -ort	27.02.1989 in Gelnhausen

Bildung und beruflicher Werdegang

10.2013 - heute	Doktorand am Institut für Theoretische Physik, Goethe Universität Frankfurt am Main Betreuer: Prof. Dr. Peter Kopietz
08.2013 - 02.2014	Forschungsaufenthalt an der University of Florida in Gainesville, USA
10.2011 - 08.2013	Masterstudium Physik, Goethe Universität Frankfurt am Main Abschluss: Master of Science, Note: 1,0 Titel der Abschlussarbeit: *Kinetic equations for parametrically excited spin waves* Betreuer: Prof. Dr. Peter Kopietz
10.2008 - 09.2011	Bachelorstudium Physik, Goethe Universität Frankfurt am Main Abschluss: Bachelor of Science, Note: 1,1 Titel der Abschlussarbeit: *Spin-waves in ferromagnets with time-dependent classical ground states* Betreuer: Prof. Dr. Peter Kopietz
1999 - 2008	Grimmelshausen Gymnasium Gelnhausen Abschluss: Abitur, Note: 2,0